# On GPS Based Attitude Determination

Von der Naturwissenschaftlich-Technischen Fakultät der
Universität Siegen
zur Erlangung des akademischen Grades

**Doktor der Ingenieurwissenschaften**
(Dr.-Ing.)

von

**M.Sc. Zhen Dai**

1. Gutachter: Professor Dr. -Ing. habil. Otmar Loffeld

2. Gutachter: Privatdozent Dr.-Ing. habil. Stefan Knedlik

Datum der mündlichen Prüfung: 1.Feb.2013

# Acknowledgments

My gratitude goes first to Prof. Dr. -Ing. habil. Otmar Loffeld for supporting my work all through. I have been impressed not only with his deep knowledge and scientific rigorousness in estimation theory and signal processing, but also with his elegant leading temperament. His confidence on everyone and his active personality allow a free and comfortable research atmosphere in the institute.

I am also greatly indebted to PD Dr. -Ing. habil. Stefan Knedlik. As an active researcher in the navigation area, he has successfully navigated not only a GPS/INS system but also a young research group during the past four years. I will never forget his introduction into the GPS, his encouragement in publications and his guidance into a correct research behavior. I also profit from his helps in various non-scientific matters and his management in the IPP and MOSES programs.

My thanks would go to Dr. Yu Wang. He motivated me to bridge GPS and SAR by taking my GPS knowledge into SAR motion compensation. Meanwhile, he kindly offered associated intellectual supports.

Many thanks for my friends M.Sc. Jieying Zhang, M.Sc. Jinshan Ding, M.Sc. Junchuan Zhou and M.E. Miao Zhang for helpful comments and revisions on my thesis. I also would like to thank all the members of the navigation group for useful discussions in our group meetings.

I gained numerous kind helps from the colleagues of ZESS during my PhD studies, from the technical supports to administrative services, from scientific activities to social events. Your helps are sincerely acknowledged. It is my special gratitude to all the IPP members for constructing an intercultural atmosphere which I really enjoyed. The time with you worth recalling all the life time.

Finally, I dedicate this thesis to my beloved family. Your love, approval and encouragement have accompanied me until today, giving me strength and confidence to live abroad. It is also my belief that my mother, who is seeing me from paradise all the while, is now smiling with gratification.

# Kurzfassung

Das TerraSAR-X/PAMIR Experiment ist ein Raum- und Luftfahrt basiertes bistatisches Synthetisches-Apertur-Radar (SAR) Experiment, in welchem der deutsche Erdbeobachtungssatellit TerraSAR-X als Sender und das Fraunhofer-FHR Flugradarsystem PAMIR als Empfänger fungieren. Durch den unabhängigen Betrieb von Sender und Empfänger bildet die hochgenaue Bestimmung der Position, Geschwindigkeit und Lage insbesondere des Empfängers auf dem Flugzeug eine zwingend notwendige Vorraussetzung für die Synchronisierung, als auch für die nachfolgende Radarbildererstellung. Die genannten Parameter können unter Nutzung von GPS (Global Positioning System) bestimmt werden. Diese Dissertation beschäftigt sich mit der Lagebestimmung durch ein GPS-Mehrantennensystem unter der zusätzlichen Verwendung eines konstanten Drehratenmodells.

Die trägerphasenbasierte differenzielle Positionierung stellt ein typisches Verfahren zur hochgenauen Positionierung dar. Eine Vorraussetzung für die Verwendung von Trägerphasendaten ist die Erkennung und Korrektur von Cycle-Slips. Basierend auf einer Analyse von traditionellen Zweifrequenz-Ansätzen wurde in dieser Arbeit ein neuartiger Algorithmus für die Cycle-Slip Erkennung, Bestimmung und Validierung für ein Dreifrequenz-GPS entwickelt.

Die differentielle Positionierung kann für die Lagebestimmung mit einem GPS-Mehrantennensystem erweitert werden. Hierfür wurde eine Software für die Postprozessierung von GPS Rohdaten entwickelt. Um die, aufgrund eines relativ kleinen Antennenabstandes auf dem Flugzeugrumpf, eingeschränkte Genauigkeit zu erhöhen, kann das GPS Mehrantennensystem zusammen mit einem konstanten Drehratenmodell innerhalb eines Kalman-Filters integriert werden. Nach Vergleich unterschiedlicher nichtlinearer Kalman-Filter in Bezug auf Genauigkeit und Rechenlast, wurde das erweiterte Kalman-Filter als geeignete Methode für diese Anwendung ausgewählt. Allerdings kann die Approximation der realen Dynamik durch ein konstantes Drehratenmodell zu Fehlern führen. Daher wird ein adaptiver Interaktiv-Multiple-Modell-Ansatz vorgeschlagen, um die von Modellübergängen verursachten Fehler zu reduzieren und das Prozessrauschen autonom zu optimieren.

Die Genauigkeit der Positions-, Lage- und Geschwindigkeitsparameter aus GPS wird bestimmt, um die Fortpflanzung dieser Fehler auf die Parameter der Radar-Bewegungskompensation zu analysieren. Basierend auf einer geometrischen Darstellung des Radar-Antennen-Phasenzentrum (APC) in Bewegungs-/ und Querrichtungen wurde eine Reihe von Fehleranalysen durchgeführt, um die potentiellen Fehler der Dopplermittelfrequenz und des APC Positionsfehler abzuleiten.

# Abstract

The TerraSAR-X/PAMIR experiment is a spaceborne/airborne hybrid bistatic synthetic aperture radar (SAR) experiment using the German earth-observation satellite TerraSAR-X as transmitter and the Fraunhofer-FHR's airborne radar system PAMIR as receiver. Due to the independent operation of the transmitter and receiver, accurate position, attitude and velocity parameters of the airborne platform serve as necessary parameters for the synchronization procedure and the subsequent generation of radar images. All these parameters can be obtained by using Global Positioning System (GPS) system. This thesis highlights the attitude determination technique using GPS multi-antenna system augmented by a constant angular rate model.

Differential positioning technique with carrier phase data is usually applied for accurate positioning. Cycle-slip detection and repair are prerequisites for processing the carrier phase data. By analyzing and refining the traditional dual-frequency approaches, a novel algorithm is elaborated for cycle-slip detection, determination and validation in triple-frequency GPS.

The differential positioning technique can be expanded onto the multiple GPS antennas for attitude determination. Regarding to this technique, a software package is developed and presented to process the GPS raw data in a post-processing. In order to improve the accuracy limited by the short antenna space on the airplane fuselage, the GPS multi-antenna system can be incorporated with a constant angular rate model through Kalman filters for less-maneuvering airplanes. By comparing different nonlinear Kalman filters in terms of the estimation accuracy and the computational burden, the extended Kalman filter is identified as a proper choice for this application. However, approximating the real dynamics by a constant angular rate model might lead to mismodeling errors. An adaptive interacting multiple-model approach is proposed to reduce the model transition errors as well as to tune the process noise online for an improved accuracy.

The precision of position, attitude and velocity parameters obtained from GPS is calculated first in order to analyze the error propagation from GPS measurements to the parameters for radar motion compensation. Based on a geometric representation of the radar Antenna Phase Center (APC) in the along/cross-track frame, a series of error analysis is carried out to derive the potential errors on the Doppler centroid frequency and the positioning error of the APC.

# Table of Contents

# List of Figures

# List of Tables

# Abbrevations

| | |
|---|---|
| ABF | Antenna Body Frame |
| ACU | Along-track/Cross-track/Up |
| AEKF | Adaptive Extended Kalman Filter |
| AIMM | Adaptive Interacting Multiple Model |
| APC | Antenna Phase Center |
| DCF | Doppler Centroid Frequency |
| DCM | Direction Cosine Matrix |
| DGPS | Differential GPS positioning |
| DOP | Dilution Of Precision |
| ECEF | Earth Centered Earth Fixed |
| EKF | Extended Kalman Filter |
| FMKF | Fading Memory Kalman Filter |
| GLONASS | GLObal NAvigation Satellite System |
| GNSS | Global Navigation Satellite System |
| GPS | Global Positioning System |
| HDOP | Horizontal Dilution Of Precision |
| IEKF | Iterated Extended Kalman Filter |
| IGS | International GNSS Service |
| IMM | Interacting Multiple Model |
| KF | Kalman Filter |
| LAMBDA | Least-squares AMBiguity Decorrelation Adjustment |
| LLF | Local Level Frame |
| LSAD | Least-Squares Attitude Determination |
| PBF | Plane Body Frame |
| PDOP | Position Dilution Of Precision |
| PRF | Pulse Repetition Frequency |
| PRN | PseudoRandom Noise code |
| RMSE | Root Mean Square Error |
| SAR | Synthetic Aperture Radar |
| SOEFK | Second-Order Extended Kalman Filter |
| SPP | Single-Point Positioning |
| TEC | Total Electron Content |
| UKF | Unscented Kalman Filter |
| UTC | Coordinated Universal Time |
| ZESS | Zentrum für Sensorsysteme |

# 1. Introduction

## 1.1 Motivation

The Bistatic Synthetic Aperture Radar (BiSAR) is characterized by the spatial separation between transmitter and receiver and hence offers a considerable flexibility in designing remote sensing missions. Recently, a spaceborne/airborne hybrid configuration has become an interesting research field. Such a configuration offers more robustness to deliberate jamming than both the spaceborne and the airborne radar systems operated monostatically. Additionally, its performance, for equivalent synthetic apertures, is better than the monostatic spaceborne SAR in terms of radar resolution and signal-to-noise-ratio (SNR). Such a hybrid experiment has been under investigation in German radar community, where the TerraSAR-X (the German high-resolution radar satellite) serves as the illuminator in the sliding spotlight mode and the airborne SAR system (Fraunhofer-FHR's Phased Array Multifunctional Imaging Radar, abbreviated as PAMIR) as the passive receiver in the inverse sliding spotlight mode. The basic configuration of the TerraSAR/PAMIR experiment is illustrated in Figure 1-1, where the point "P" represents a point target within the composite footprint.

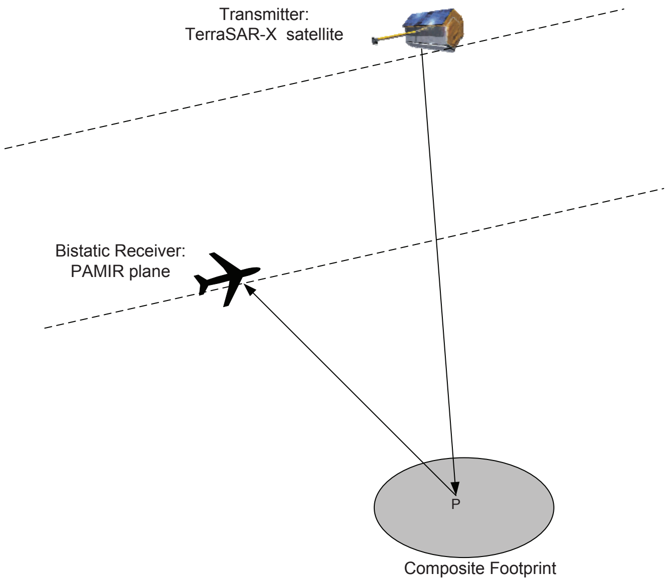

**Figure 1-1 Bistatic configuration in the TerraSAR-X/PAMIR experiment**

One crucial problem in this experiment is to accurately determine the flight trajectory, the attitude and velocity parameters of the airplane. These parameters can be obtained by using the Global Positioning System (GPS). The trajectory of the PAMIR airplane can be determined using differential positioning technique, where a ground station or a station network needs to be established to transfer the correction values to the onboard rover antenna(s). Usually, the attitude parameters are provided by inertial sensors. However, the results offer only short-term accuracy, if there are no aiding sensors available (e.g., GPS signals) for the detection and compensation of inertial sensor errors over time. As an alternative method, a GPS multi-antenna system can be used for attitude determination. This technique employs off-the-shelf devices and offers long-term accurate attitude solutions. In this thesis, the existing techniques for GPS multi-antenna systems are extended to obtain a more reliable and accurate attitude estimation. The overview scheme of system design proposed in the thesis is depicted in Figure 1-2.

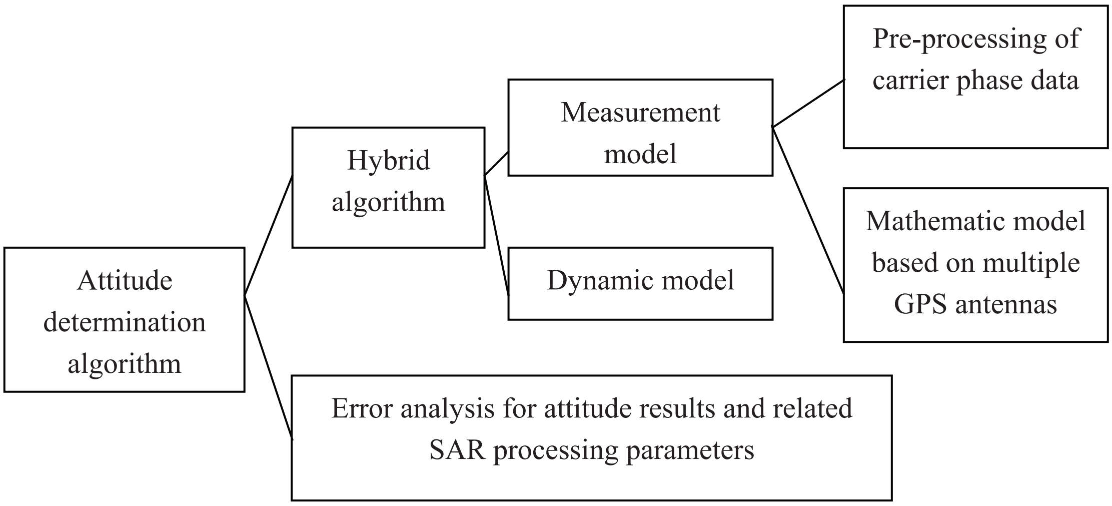

**Figure 1-2 Overview scheme of system design**

Such a system does not only employ the GPS measurements for attitude determination, but also takes advantages of the attitude dynamic information. The measurement model refers to the calculation of attitude using GPS carrier phase measurements, and hence the pre-processing of GPS carrier phase should be carried out first for resolving the integer ambiguities. Then, the attitude can be derived using proper mathematic models and GPS measurements. The attitude dynamics is subject to the application scenario and can be integrated with the measurement model by an optimal and robust data fusion algorithm. Last but not least, the potential errors in SAR processing parameters introduced by GPS need to be investigated.

The use of carrier phases is the basis for accurate position and attitude determination. The preprocessing should be performed to quantify and monitor the integer phase ambiguities, namely the ambiguity resolution and cycle-slip fixing. The cycle-slip fixing is still a challenging task, leaving space for innovation. Firstly, the published materials show great efforts in the cycle-slip detection for single- and dual-frequency GPS, but the research regarding to triple-frequency GPS is missing so far. Although the developed cycle-slip detection algorithms for single- or dual-frequency GPS can be applied to triple-frequency GPS, this method cannot take full advantages of triple-frequency signals and needs a large computational burden. A new approach is therefore desired especially for triple-frequency signals. Secondly, in the previous research, once the cycle-slips are detected, the ambiguity resolution procedure is normally restarted. However, once the cycle-slips can be quantified and removed from carrier phase raw data, the restart of ambiguity resolution might be replaced by the determination of cycle-slip sizes. Due to the similarity in the integer properties of cycle-slips and ambiguities, the technique for ambiguity resolution can be applied to determine cycle-slip sizes as well. However, it is not thoroughly discussed in the existing literature. Thirdly, the determined cycle-slip values need to be validated. There is still a research gap in the cycle-slip validation for a stand-alone receiver. A fast and reliable approach for cycle-slip validation is required as well.

With the resolved ambiguities, GPS carrier phase measurements acquired from multiple antennas can be fused to estimate attitude parameters. The applied strategy is mainly software-oriented, making it possible to implement a receiver independent software package for attitude determination. It is not only the framework for carrying out research activities, but also builds up a basis for further expansion and integration with other sensor systems. Driven by these motivations, such a software package has been implemented and will be presented in the thesis.

The estimation accuracy of attitude parameters deteriorates with short baselines between antennas. In this case, coupling with the attitude dynamics might help to improve the accuracy. For the less-maneuvering airplanes with high GPS data rate, a constant angular rate model can be used when the inertial sensors are not available. Though the integration of the GPS measurements and such a dynamic model using an extended Kalman filer has been studied, this technique still needs to be refined and improved in the following aspects: (1) There are some other nonlinear Kalman filters theoretically providing better performance than the extended Kalman filter, but they are always more time-consuming. A comparison of these filters in terms of accuracy and computational time should be carried out in order to select a proper filter in this application. (2) Due to the changing dynamics of airplanes, a constant angular rate model cannot fully reflect the variation of attitudes during the entire trajectory, yielding the mismodeling errors. The first type of mismodeling errors occurs when the airplane transits the motion models. In this case, the errors introduced by the model transition may not be correctly described by the predefined process noise parameters, leading to a temporary failure of the dynamic model. Solutions to the model transition should be sought for. The second type of mismodeling errors lies in the fixed and conservatively initialized process noise parameters. In order to benefit more from the dynamic model, the filter should identify the process noises online. Thus, a hybrid algorithm is needed to deal with both types of mismodeling errors.

Although GPS technique has been successfully applied in the motion compensation of many SAR experiments, a rigorous error analysis is in demand to quantify the effect of GPS measurement errors on the bistatic SAR motion compensation, especially when multiple onboard GPS antennas are used. The relevant studies are missing and need to be investigated.

## 1.2 Outline

This thesis includes six chapters. Some fundamentals of GPS positioning are discussed in Chapter 1, including single-point positioning and differential positioning. GPS modernization and multiple GNSS integration are briefly explained as well.

Chapter 2 highlights cycle-slip processing. Firstly, the popular algorithms for ambiguity resolution and cycle-slip detection using single/dual-frequency GPS are reviewed. After that, novel algorithms for cycle-slip detection, determination and validation using triple-frequency GNSS are elaborated. Simulations in different scenarios demonstrate the reliability of the algorithms.

Chapter 3 introduces the attitude determination approaches, i.e. the least-squares attitude estimation and direct attitude computation. Both algorithms are categorized into dual-antenna and triple/more antennas cases. A self-developed software package for attitude determination using GPS raw data is also presented.

Based on the techniques given in Chapter 3, Chapter 4 presents an augmented system based on the integration of GPS measurements with attitude dynamics. The major objective is to improve the accuracy limited by the short antenna baselines. With a less-maneuvering platform and a high GPS data rate, a constant angular rate model can approximate the dynamics very well. In order to choose a proper filter to integrate the GPS measurements with the dynamic model, different nonlinear Kalman filters are compared in terms of accuracy and computational burden. Simulations with different initialization errors are conducted to evaluate these filters.

Chapter 5 refers to the solutions of inherent mismodeling errors. Two kinds of mismodeling errors caused by the constant angular model are introduced at first. In order to handle the model transition problem, several approaches are presented and then compared, e.g. using different nonlinear filters, fading-memory filter and interacting multiple-model approach. In order to automatically identify the changing dynamics, the adaptive tuning of process noises is analyzed. In the end, an adaptive interacting multiple-model approach is proposed, which integrates the robustness of multiple-model approach to the model transition and the adaptive tuning of process noises.

In Chapter 6, error analysis is carried out to show the error propagation from GPS carrier phase measurements onto the parameters related to the SAR motion compensation, including the position of SAR antenna phase center in the along/cross track directions and Doppler centroid frequency. Finally, conclusions are drawn and future works are proposed.

## 1.3 GPS Principles

The Global Positioning System (GPS) is a radio-based Global Navigation Satellite System (GNSS) established by the U.S. Department of Defense. GPS satellites offer three kinds of measurements for positioning and navigation, including the pseudorange, the carrier phase and the instantaneous Doppler. We will firstly introduce the basic observation equations of pseudorange measurements and carrier phase measurements. Then, the models for ionospheric errors and multipath errors will be highlighted due to their importance in the simulation generation in the latter chapters. The GPS modernization and the integration of GPS with other GNSS will also be briefly presented in this chapter.

### 1.3.1 Observation equations

GPS observation equations are the basis for the GPS data processing. The pseudorange measurements reflect the time difference between the signal transmission from the satellite and the signal reception at the antenna. It can obtained by "multiplying the speed of light with the time shift needed for aligning the receiver-replicated code with the real code received from a GPS satellite" (Wells et al. 1986). For this reason, the pseudorange data is always simply referred to as the code measurements. The pseudorange observation equation at epoch $t$ can be expressed as:

$$R(t)=\rho(t)+\frac{\lambda_{Li}^{2}}{\lambda_{L1}^{2}}I_{L1}(t)+T(t)+S(t)+c\cdot t_{r}(t)+c\cdot t^{s}(t)+e_{Li,code}(t)+M_{Li,code}(t) \qquad (1\text{-}1)$$

where

$L_i$ (subscript) indicates the corresponding signal;

$\lambda$ is the wavelength of the corresponding GPS signal;

$R$ is the pseudorange measurement;

$\rho$ is the geometric distance from the GPS receiver's antenna phase center at the epoch of signal reception to the GPS satellite's antenna phase center at the epoch of signal transmission;

$I$ is the ionospheric delay;

$T$ is the tropospheric delay;

$S$ is the satellite orbit bias;

$c$ is the speed of light;

$t^s$ is the satellite clock bias in units of time;

$t_r$ is the receiver clock bias in units of time;

$e$ is the thermal noise contained in the pseudorange data;

$M$ is the multipath error.

Note that all terms except for clock biases are given in units of length.

The carrier phase measurements reflect the difference between the phase of the incoming signal from a GPS satellite and the generated signal in the receiver. A carrier phase measurement is composed of four parts:

$$\Phi_{output}(t) = \Phi_f(t) + \Phi_i(t) + N(t) + e(t) \tag{1-2}$$

where $\Phi_{output}$ represents the carrier phase measurements from the receiver; $\Phi_f$ is the fractional part of the measured carrier phase, whereas $\Phi_i$ is the number of integer cycles accumulated from the first observation epoch to the current epoch; $e$ is the error term; $N$ is the integer phase ambiguity. "This integer refers to the first epoch of observation and remains constant during the period of observation. During this period, the receiver accumulates the phase differences between arriving phases and internally generated receiver phases. The receiver, therefore, effectively generates an accumulate carrier phase observables that reflects the changes in distance to the satellite"(Leick 2004). The integer ambiguity should be resolved *a priori* and subtracted from the carrier phase measurements obtained from the receiver. As the integer ambiguity remains constant epoch by epoch, the time dependence can therefore be dropped. The carrier phase observation equation can be formulated as:

$$\lambda_{Li}\Phi_{Li}(t) = \rho(t) + \lambda_{Li}N_{Li} - \frac{\lambda_{Li}^2}{\lambda_{L1}^2} I_{L1}(t) + T(t) + S(t) + c \cdot t_r(t) + c \cdot t^s(t) + e_{Li}(t) + M_{Li}(t) \tag{1-3}$$

Note that terms $\Phi$ and $N$ are expressed in units of cycles. In comparison with Eq. (1-1), the carrier phase observation equation has the following differences:

1. The ionospheric error $I$ has the same magnitude but opposite sign.
2. Thermal noise $e$ on carrier phase is three or four orders of magnitude lower than that of code measurements. "The precision of a pseudorange derived from code measurements has been traditionally about 1% of the chip length. Therefore, a chip length of 300 m for a coarse code would yield a precision of 3 m and an assumed chip length of 30m for a precise code would yield a precision of 0.3m. The phase of an electromagnetic wave can be measured to better than 0.01 cycles which corresponds to millimeter precision for a frequency in the gigahertz range" (Hofmann-Wellenhof et al. 2003).
3. Multipath errors $M$ on the carrier phases are normally several orders of magnitude lower than that on the pseudoranges in the measurement domain. Maximal multipath error can reach 150m on pseudoranges with a wide correlator and 4.75 cm on carrier phases with wide or narrow correlator (Ray 2000). This allows a reduction of multipath effects on pseudoranges by a smoothing the pseudorange measurements with the previous carrier phases (Hatch 1982).

### 1.3.2 Observation errors

The prerequisite of an accurate GPS positioning is to reduce the errors contained in the GPS measurements. Error modeling and signal combinations are commonly used techniques for the error reduction or the error removal. In this section, we will highlight the error models for ionospheric error and multipath error because these models will be used to generate the simulation scenarios in the following parts of the thesis. Other error sources will also be overviewed.

#### 1.3.2.1.The modeling of ionospheric error

The ionospheric delay can be modeled as a function of the electron density represented by the Total Electron Content (TEC). A simplified Klobuchar model can be used to simulate the TEC. This model assumes that the vertical ionospheric delay can be approximated by half a cosine function of the local time during daytime and by a constant level during nighttime (Kaplan and Hegarty 2006). During the daytime the maximal TEC occurs at 14:00 local time. The simulated TEC is subject to the following model (Kaplan and Hegarty 2006):

$$\begin{aligned}
&\varphi = \left(t-14\right)/28\cdot 2\pi \\
&TEC = \begin{cases} \left|\varphi\right| < \pi/2, & min + max\cdot\cos\varphi \quad Daytime \\ \left|\varphi\right| \geq \pi/2, & min \qquad\qquad\qquad\quad Nighttime \end{cases}
\end{aligned} \tag{1-4}$$

where *min* and *max* are the predefined minimal and maximal values of TEC in units of number of electrons per square-meter; *t* is the local time; $\varphi$ indicates the time phase in a 28-hour period. The obtained TEC is assumed at the ionosphere point, namely the intersection point of the signal propagation path and the ionospheric layer. In order to explore the ionospheric error in the measurement domain of a GPS antenna, the geometric relation between the GPS antenna and the ionospheric point should be employed (Kaplan and Hegarty 2006):

$$\begin{aligned}
&\Delta I_{phase} = -40.3\sqrt{1-\left(\frac{R_e\cos\theta}{R_e+h}\right)^2}\cdot TEC \Big/ f^2 \\
&\Delta I_{code} = -\Delta I_{phase}
\end{aligned} \tag{1-5}$$

where $\Delta I_{phase}$ and $\Delta I_{code}$ denote the generated ionospheric error of phase and code measurements, respectively; $R_e$ is the mean radius of the earth; $h$ is the mean height of the ionosphere to the earth surface; $\theta$ is the azimuth angle at the ionospheric point; $f$ is the carrier frequency of GPS signals. The ionospheric error contributes the same magnitude but different signs to the carrier phase and code noise. The ionospheric delay is related to the signal frequency and hence can be eliminated by a proper combination of the carrier signals, and this is an important reason why GPS satellites transmit on two or more carrier frequencies.

### 1.3.2.2.The modeling of multipath error

The multipath effect describes “the phenomenon whereby a satellite-emitted signal arrives at a receiver’s antenna by more than one path” (Hofmann-Wellenhof et al. 2001). The difference in path lengths causes the signal interferes at the antenna. For GPS, multipath is usually noted when the antenna is operating near large reflecting obstacles. If the antenna is located at a fixed position, the periodical variation of multipath effects can be estimated by long-term observation (Teunissen and Kleusberg 1998). Referring to dynamic applications in unknown environments, there is no general model of the multipath effect because of the time- and location-dependent geometric situation (Hofmann-Wellenhof et al. 2001). In a simulation, the zero-angle multipath error for GPS code measurements is usually generated using an autoregressive model (Braasch 1999):

$$\mathbf{m}_t^0 = \sum_{i=1}^{nb} \mathbf{b}_i \mathbf{x}_{t-i} + \sum_{j=1}^{na} \mathbf{a}_j \mathbf{m}_{t-j} \tag{1-6}$$

where $\mathbf{m}_t^0$ represents the multipath error to be generated at epoch $t$; **b** and **a** are predefined index vectors with the length of *nb* and *na*, respectively; **x** is a vector with each component having a time-uncorrelated white Gaussian noise. Index vectors **a** and **b** can be obtained as the numerator and denominator of the coefficients of a 1-order Butterworth filter with a cut-off frequency of 0.007 (Yang 1998), respectively. In (1-6), the second sum operation reflects the correlation of multipath errors over time. The multipath error obtained from (1-6) is under the assumption that the satellite is vertical to the antenna. Considering the motion of satellites, the multipath error on the code measurements will be scaled by the cosine of the satellite elevation angle $\theta_t$ as follows:

$$\mathbf{m}_t^{code} = \alpha \cos\left(\theta_t\right) \mathbf{m}_t^0 \tag{1-7}$$

where $\alpha$ is the scaling factor used to identify a high-multipath environment or a low-multipath environment. The multipath errors on the code measurements are significantly larger than that on the phase measurements. The following equation reflects the difference and will be used for the simulation (Leick 2004):

$$\mathbf{m}_t^{phase} = 0.5\% \cdot \lambda \cdot \mathbf{m}_t^{code} \tag{1-8}$$

where $\lambda$ is the wavelength of the associated GPS signal.

### 1.3.2.3.Reduction of other observation errors

The GPS data processing algorithms presented in this thesis mainly rely on the signal combinations or differential positioning. Both techniques aim at reducing or eliminating the

GPS observation errors. Non-dispersive errors, including the tropospheric error, the satellite clock error, the satellite orbit error and the receiver clock error, can be eliminated by differencing the observations of different signals per satellite, because they contribute with the same amount to the observation of each signal. The error reduction using differential positioning will be discussed in section 1.3.3.2. The thermal noises arise randomly on each signal and each satellite, and hence they cannot be eliminated by signal combinations or the differential positioning technique. The thermal noises are normally modeled as Gaussian errors, which will be elaborated in the following chapters.

### 1.3.3 GPS positioning modes

The GPS positioning modes can be categorized according to the number of antennas involved. Providing a stand-alone receiver, we have Single Point Positioning (SPP) and precise point positioning. The former one uses the GPS code measurements and the latter one mainly relies on the carrier phase measurements. Once two or more antennas are used, we have Differential GPS positioning (DGPS) and relative positioning, where both code measurements and carrier phase measurements can be processed.

### 1.3.3.1.Single-point positioning

In the SPP, the receiver clock error is taken as another unknown value besides the three dimensional positioning parameters, and hence the observations from at least 4 satellites are needed. The mathematic model for SPP is given below:

$$\begin{gathered}\sqrt{\left(x^{s1}-x_u\right)^2+\left(y^{s1}-y_u\right)^2+\left(z^{s1}-z_u\right)^2}-t_r\cdot c=r_u^{s1}+e_u^{s1}\\ \sqrt{\left(x^{s2}-x_u\right)^2+\left(y^{s2}-y_u\right)^2+\left(z^{s2}-z_u\right)^2}-t_r\cdot c=r_u^{s2}+e_u^{s2}\\ \vdots\\ \sqrt{\left(x^{sn}-x_u\right)^2+\left(y^{sn}-y_u\right)^2+\left(z^{sn}-z_u\right)^2}-t_r\cdot c=r_u^{sn}+e_u^{sn}\end{gathered}\tag{1-9}$$

where all terms are related to a certain epoch so that the time dependence is dropped from the equation; the subscript $u$ denotes the user position (namely the antenna position); the superscript $sn$ denotes the $n$-th satellite position; $t_r$ is the receiver clock error; $r$ is the original or corrected pseudorange measurement; $e$ contains the remaining errors of Eq. (1-1). After the linearization we obtain the following equation given in a vector form:

$$\mathbf{A}\cdot\begin{bmatrix}x_u & y_u & z_u & t_r\end{bmatrix}^T=\mathbf{r}+\mathbf{e}\tag{1-10}$$

where **A** is the design matrix. Eq. (1-10) can be solved by the least-squares adjustment initialized with a position near the earth surface.

### 1.3.3.2. Differential and relative positioning

The differential and relative positioning techniques are based on the idea that some common errors can be cancelled or reduced by differencing the measurements between the satellites and the receivers. For this purpose, two or more receivers are involved. A simple example for the differential positioning is illustrated in Figure 1-3.

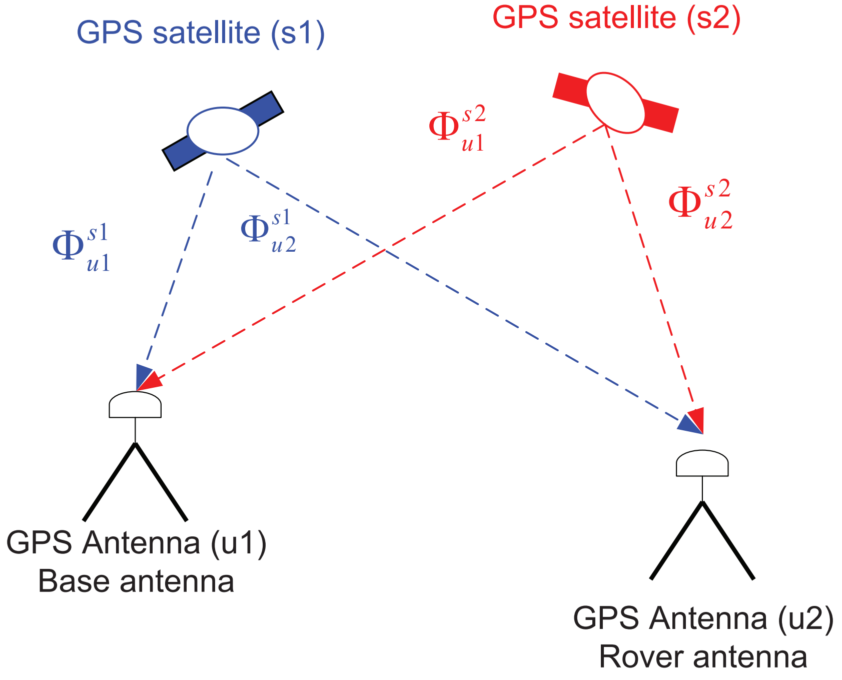

**Figure 1-3: An illustration for differential/relative positioning**

Using the observation equation (1-3) to express the carrier phase measurements of both antennas to a common satellite s1, we have:

$$\begin{aligned}\lambda_{Li}\Phi_{u1}^{s1} &= \rho_{u1}^{s1} + \lambda_{Li}N_{u1,Li}^{s1} - \frac{\lambda_{Li}^{2}}{\lambda_{L1}^{2}} I_{u1,Li}^{s1} + T_{u1}^{s1} + S^{s1} + c\cdot t_{u1} + c\cdot t^{s1} + e_{u1}^{s1} + M_{u1}^{s1} \\ \lambda_{Li}\Phi_{u2}^{s1} &= \rho_{u2}^{s1} + \lambda_{Li}N_{u2,Li}^{s1} - \frac{\lambda_{Li}^{2}}{\lambda_{L1}^{2}} I_{u2,Li}^{s1} + T_{u2}^{s1} + S^{s1} + c\cdot t_{u2} + c\cdot t^{s1} + e_{u2}^{s1} + M_{u2}^{s1}\end{aligned} \tag{1-11}$$

where the subscript $u1$ and $u2$ indicate the user (antenna); $s1$ indicate the satellite. In both equations of (1-11), the satellite clock error $t^{s1}$ and orbits error $S^{s1}$ are common errors. Thus, differencing both equations yields:

$$\begin{aligned}\lambda_{Li}\Delta\Phi_{u1-u2}^{s1} &= \Delta\rho_{u1-u2}^{s1} + \lambda_{Li}\Delta N_{u1-u2,Li}^{s1} - \frac{\lambda_{Li}^{2}}{\lambda_{L1}^{2}} \Delta I_{u1-u2,Li}^{s1} \\ &\quad + \Delta T_{u1-u2}^{s1} + c\cdot\Delta t_{u1-u2} + \Delta e_{u1-u2}^{s1} + \Delta M_{u1-u2}^{s1}\end{aligned} \tag{1-12}$$

where the operator $\Delta$ indicates the differencing, for example $\Delta\rho_{u1-u2}^{s1}$ stands for $\Delta\rho_{u1}^{s1} - \Delta\rho_{u2}^{s1}$.

If both antennas are located closely to each other, for example less than 10 kilometers on the ground plane, the atmospheric effects on the observation equations in (1-11) are approximately same, so that the differenced tropospheric error $\Delta T$ and ionospheric error $\Delta I$ might be neglected. In this case, Eq. (1-12) can be further simplified to:

$$\lambda_{Li}\Delta\Phi_{u1-u2}^{s1} = \Delta\rho_{u1-u2}^{s1} + \lambda_{Li}\Delta N_{u1-u2}^{s1},_{Li} + c\cdot\Delta t_{u1-u2} + \Delta e_{u1-u2}^{s1} + \Delta M_{u1-u2}^{s1} \qquad (1\text{-}13)$$

Such a differential processing is referred to as the "***single-differential positioning***", namely differencing the measurements of two receivers with respect to a common satellite. However, the receiver clock error $\Delta t_{u1-u2}$ still exists. In order to eliminate it, we first apply the single-differential positioning to satellite s2:

$$\lambda_{Li}\Delta\Phi_{u1-u2}^{s2} = \Delta\rho_{u1-u2}^{s2} + \lambda_{Li}\Delta N_{u1-u2}^{s2},_{Li} + c\cdot\Delta t_{u1-u2} + \Delta e_{u1-u2}^{s2} + \Delta M_{u1-u2}^{s2} \qquad (1\text{-}14)$$

The receiver clock error ($\Delta t_{u1-u2}$) is a common error term in (1-13) and (1-14) and hence can be eliminated by further differencing both equations, so that we have:

$$\lambda_{Li}\Delta\nabla\Phi_{u1-u2}^{s1-s2} = \Delta\nabla\rho_{u1-u2}^{s1-s2} + \lambda_{Li}\Delta\nabla N_{u1-u2}^{s1-s2},_{Li} + \Delta\nabla e_{u1-u2}^{s1-s2} + \Delta\nabla M_{u1-u2}^{s1-s2} \qquad (1\text{-}15)$$

The operator $\Delta\nabla$ denotes a further difference between the "single-differential" measurements associated to a common receiver. For example, $\Delta\nabla\rho_{u1-u2}^{s1-s2}$ stands for $\left(\Delta\rho_{u1}^{s1} - \Delta\rho_{u2}^{s1}\right) - \left(\Delta\rho_{u1}^{s2} - \Delta\rho_{u2}^{s2}\right)$. This procedure is called "***double-differential positioning***". So far, the satellite clock error, satellite orbit error and receiver clock error have been eliminated. In case of short antenna baseline, the remaining ionospheric and tropospheric errors can also be neglected. For these reasons, the differential positioning leads to the accuracy improvement. However, a drawback of the differential positioning is that the thermal noise and multipath errors will be accumulated.

The relative positioning is also based on the same idea of differential positioning. However, both techniques have some differences. Firstly, the differential positioning mode (e.g. DGPS) aims at determining the precise position of the rover receiver, whereas the relative positioning aims at determining a precise baseline vector between two receivers. In DGPS, a reference receiver (also called reference station) is stationary and located at a known position. In relative positioning, both receivers can be moving and their individual position might not be precisely determined. The second difference lies in the latency. The relative positioning needs the simultaneous and synchronized observations from both receivers, whereas in DGPS, "the reference station commonly calculates pseudorange correction and range rate correction which are transmitted to the remote receiver in real-time" (Hofmann-Wellenhof et al. 2003). The range rate correction is actually introduced to correct the errors caused by the time delay in the data transmission.

The real-time relative positioning based on the carrier phase measurements is usually termed as Real-Time Kinematic (RTK) technique. The RTK technique needs the simultaneous processing of carrier phase measurements of the base and rover stations. The RTK is the basis for multi-antenna attitude determination and real-time precise positioning. The following experiment shows the different accuracies of SPP and RTK. As seen in Figure 1-4, a platform with a GPS antenna moves from P1 to P2 and then back to P3 in front of the building of Center for Sensorsystems (ZESS). The whole trajectory is close to a straight line. A base station marked as solid rectangular is located near P1. The trajectories processed using the single-point positioning and RTK are depicted in different colors. The base station is built using a Novatel ProPak-V3 receiver and a Novatel 702GG antenna, and the rover station is built using a Novatel DL-4 receiver and a Novatel 702 antenna. The code measurements on L1 signal are employed in the single-point positioning. Ionospheric and tropospheric errors are estimated using the Klobuchar model and Hopfield model (Hofmann-Wellenhof et al. 2001), respectively. The carrier phase ambiguities are resolved using the signal combination technique (Horemuž and Sjöberg 2002).

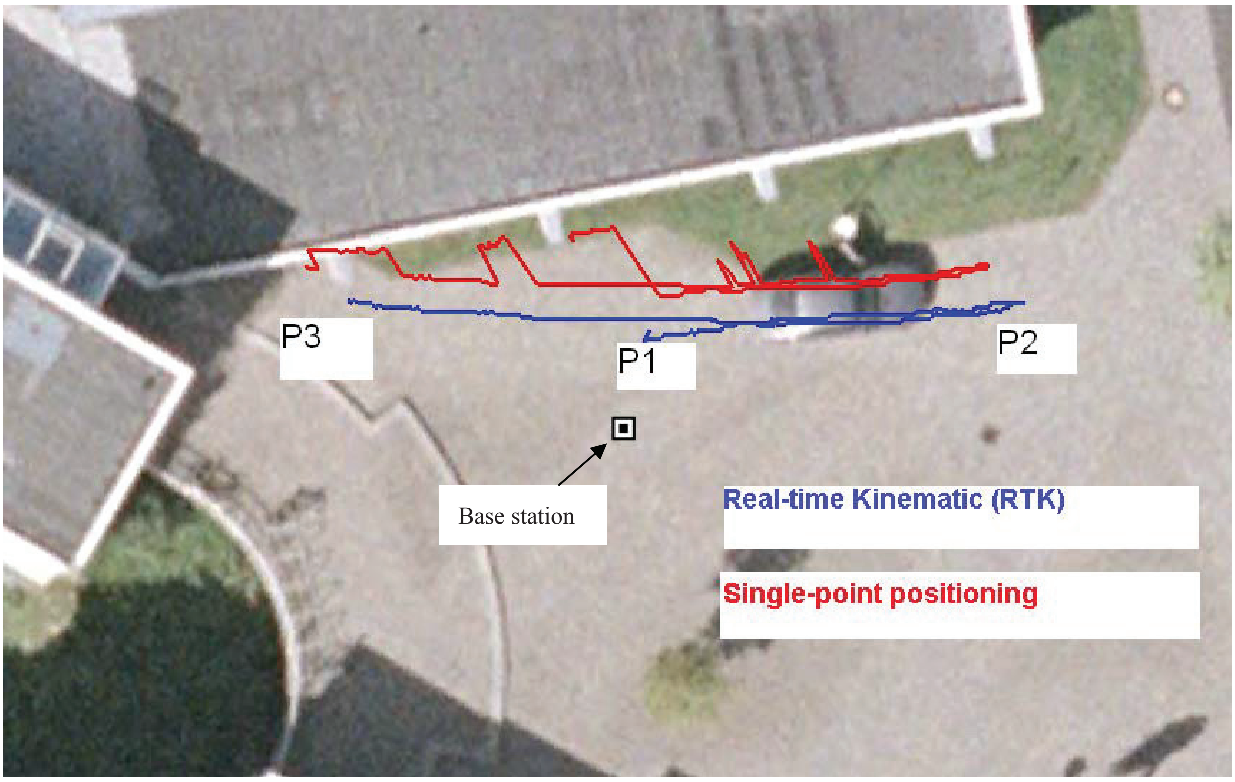

**Figure 1-4: Trajectories made by SPP and RTK**[1]

The trajectory generated using RTK is clearly closer to the reality. Large jumps can be observed in the trajectory generated using SPP. These are mainly due to the multipath effects caused by the surrounding environments and the large thermal noises of code measurements.

---

[1] The map information is obtained on 8-Feb-2011 from Google Map. The presented map reflects the situation when the map was captured rather than the situation when the experiments were carried out. The car seen in the map did not really exist in the experiments.

We can also observe biases between the two trajectories. These biases are mainly due to the remaining atmospheric errors in the SPP.

### 1.3.4 GPS modernization

The GPS modernization manifests itself in the new civilian code measurements (L2C), new carrier frequencies (L5), new signal structures and the increased signal availability and power from GPS spacecraft, etc (McDonald 2002). As an important improvement, a new civilian L5 signal centered at 1176.45 MHz will be available at the first GPS IIF satellite as an addition to the L1 signal at 1575.42 MHz and the L2 signal at 1227.60 MHz. The triple-frequency signal results in a faster ambiguity resolution (Han and Rizos 1999; Hatch 1996; Julien et al. 2004), better estimation of the multipath error (Simsky 2006) and ionospheric refection (Wang et al. 2005). Another significant advantage of triple-frequency signal manifests itself in the improvement of success rate of the cycle-slip detection (Dai et al. 2009a), which will be elaborated in the thesis.

### 1.3.5 Integration of GPS with other GNSS

Besides GPS, there are other coexisting GNSS, including the Russian GLONASS system, the European GALILEO which is still in experimental phase and the second generation of the Chinese COMPASS system. Integrating GPS with other GNSS will bring in improved availability, satellite coverage, interference susceptibility, accuracy and safety (Hofmann-Wellenhof et al. 2003). An example is given below to show the benefit of the multiple GNSS constellations. The GPS and GLONASS measurements are collected from the “UNGJ” station of International GNSS Service (IGS). Note that only the satellites simultaneously providing P1 and P2 code measurements are employed. The settings for the positioning algorithm are listed in Table 1-1.

**Table 1-1: Parameters used for SPP**

| Measurement used | Code measurements |
|---|---|
| Cut-off angle | 15º |
| GPS orbit determination | broadcast ephemeris |
| GLONASS orbit determination | IGS final precise orbit data |
| Starting time (Coordinated Universal Time, or UTC) | 10:00 30. April. 2009 |
| Epoch interval | 30 s |
| Ionospheric correction | dual-frequency correction |
| Tropospheric correction | Hopfield model |

Figure 1-5 shows the positioning accuracy and Dilution of Precision (DOP) with (solid line) or without GLONASS (dashed line). The calculation of DOP values for SPP is formulated in Appendix I.

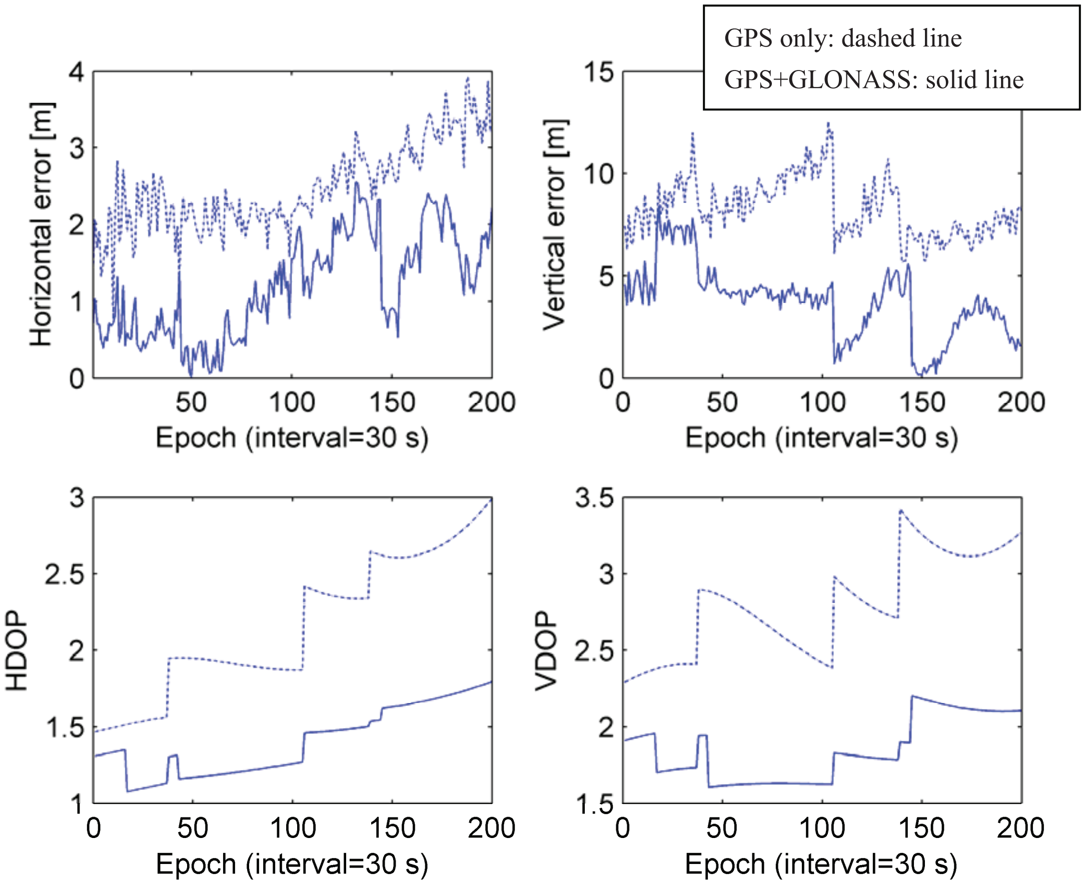

**Figure 1-5: Positioning error from GPS and GPS+GLONASS**

From Figure 1-5 it can be seen that the GLONASS satellites will apparently enlarge the satellite sky coverage, so that the DOP values are decreased. The horizontal and vertical errors from the integrated GPS/GLONASS system are lower than that in the GPS-only case.

The reduced DOP values from the multiple GNSS constellations in a global area can be simulated using predefined satellite orbits. Figure 1-6 shows DOP values under integrated GNSS constellations. The resolution for each grid is 1 degree for longitude and latitude. At each grid point, the DOP values are calculated using all satellites viewed at the corresponding location. At each grip point, the DOP values are firstly collected for 14 hours with a sampling interval of 15 minutes, and then the averaged DOP value is calculated and presented. We assume that all GNSS are operating under full constellation. This means 24 satellites for GPS, 24 satellites for GLONASS and 30 satellites for GALILEO.

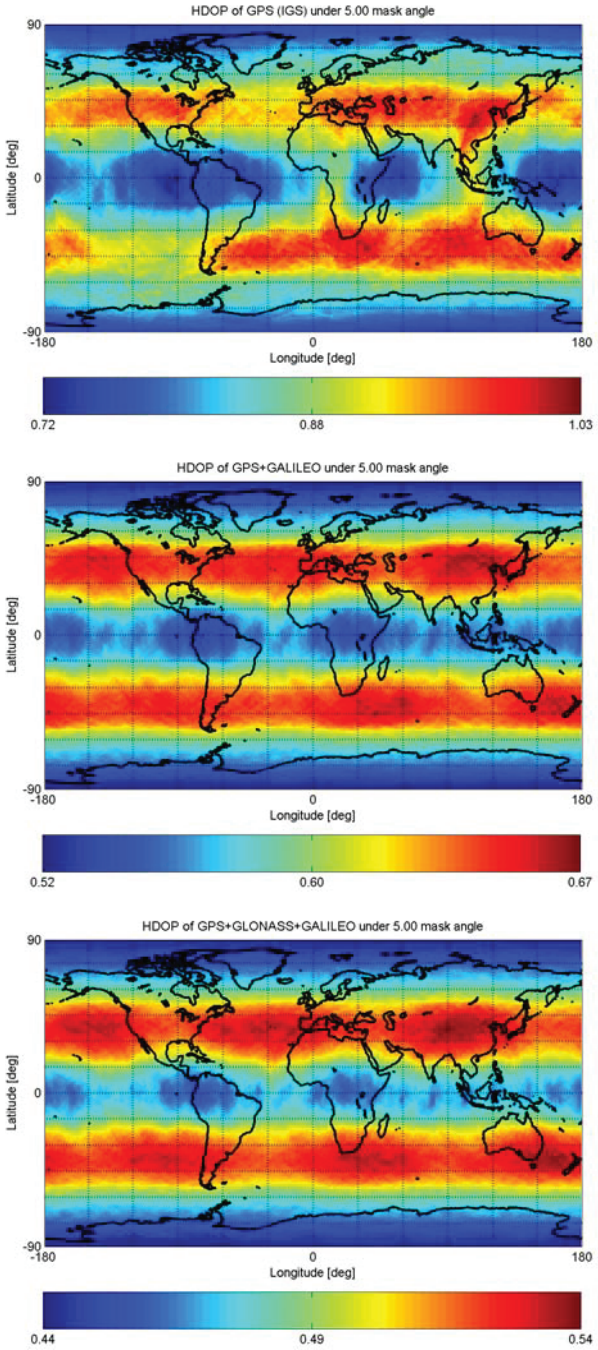

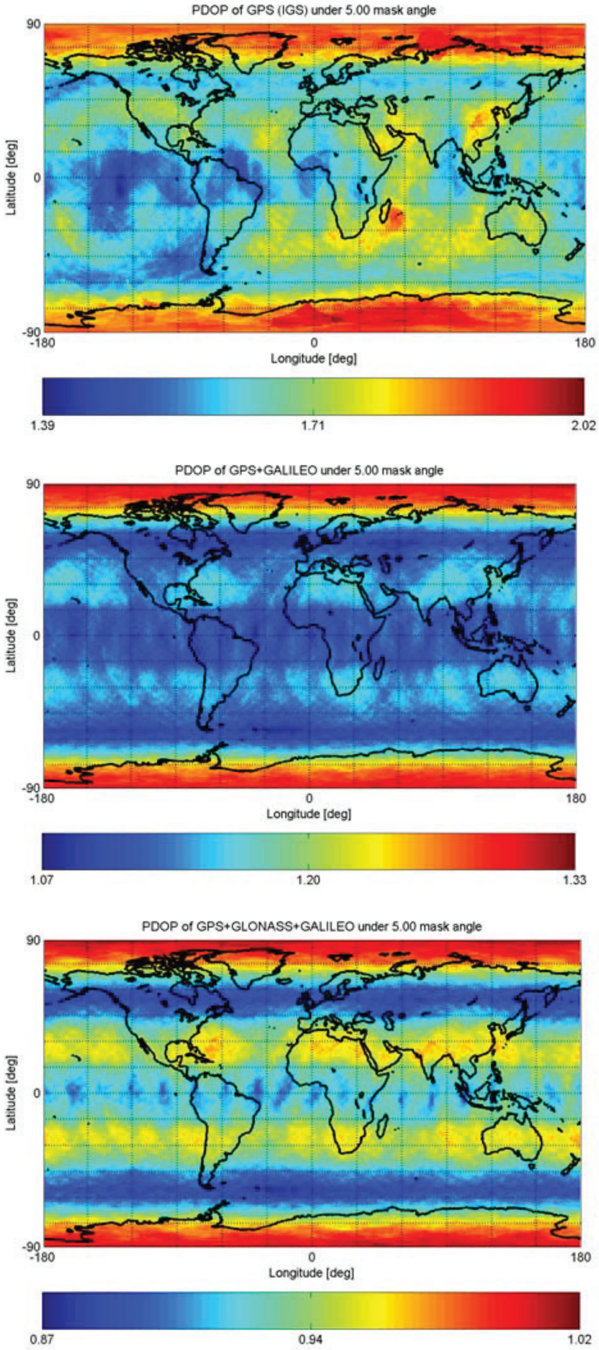

**Figure 1-6: HDOP for GNSS combinations**

**Figure 1-7: PDOP for GNSS combinations**

By integrating more GNSS systems, the DOP values are remarkably decreased. It does not only imply the potential improvement in the positioning accuracy, but also means the increased safety and availability. In this thesis, we will focus on the use of GPS. Due to the similarity of positioning model for different GNSS systems, the algorithms referred in the thesis can be augmented to other GNSS systems.

# 2. GPS data pre-processing

The pre-processing of carrier phase mainly comprises two steps, namely the ambiguity resolution and the cycle-slip fixing. In this chapter, both techniques will be overviewed at first, and the cycle-slip detection and repair for triple-frequency GPS are highlighted in the following.

## 2.1 Overview of ambiguity resolution approaches

Resolving the integer ambiguities *N*(*t*) is a prerequisite of positioning applications based on GPS carrier phase measurements. As seen from Eq. (1-15), the double-differenced carrier phase observation equation is an underdetermined equation and the ambiguities cannot be solved directly. When coupling with GPS code measurements, the non-dispersive terms can be eliminated. However, the remaining high thermal noises of pseudorange measurements, the ionospheric errors as well as the multipath errors make it difficult to derive the true integer values of ambiguities instantaneously.

The ambiguity resolution aims at defining a search space for ambiguity candidates and identifying the correct candidate. It mainly involves three sequential steps (Hofmann-Wellenhof et al. 2001). The first step is to resolve the float ambiguities, namely to calculate the float values of ambiguities through a proper mathematic model. The second step is to generate integer candidates around the float values and choose the best one. The first two steps determine the center and the size of the search space. The final step is the ambiguity validation, namely to verify whether or not the best ambiguity candidate is the correct one.

### 2.1.1 Generation of float ambiguities

In the single-frequency GPS, the float ambiguities can be calculated by incorporating the code measurements. The double-differenced code and carrier phase observation equations can be simplified as:

$$\begin{aligned}&\text{Carrier phase: } \lambda_{L1}\cdot\Delta\nabla\mathbf{\Phi}_{L1}(t)-\lambda_{L1}\cdot\Delta\nabla\mathbf{N}_{L1}(t)=\Delta\nabla\boldsymbol{\rho}(t)+\Delta\nabla\mathbf{e}_{phase,L1}(t)\\&\text{Code: } \Delta\nabla\mathbf{R}_{L1}(t)=\Delta\nabla\boldsymbol{\rho}(t)+\Delta\nabla\mathbf{e}_{code,L1}(t)\end{aligned} \tag{2-1}$$

where $\Delta\nabla\mathbf{\Phi}_{L1}$ and $\Delta\nabla\mathbf{R}_{L1}$ are the double-differenced carrier phase and code measurements on L1 signal in a vector form; $\Delta\nabla\mathbf{e}_{phase,L1}$ and $\Delta\nabla\mathbf{e}_{code,L1}$ are remaining errors for carrier phase and code measurements, respectively. Although the ambiguity term is identified with the time dependence, it should be constant value without cycle-slips or loss of lock. The geometric term $\boldsymbol{\rho}$ is equivalent for both equations, and hence it can be computed firstly using code measurements and then substituted into the carrier phase equation. After that, the float ambiguity is ready to be calculated.

Compared to single-frequency receivers, dual-/multi-frequency receivers allow a much faster ambiguity resolution by using linear phase combinations. Commonly used combinations include the ionosphere-free combination, the geometry-free combination and the time-variance combination (Teunissen and Kleusberg 1998). The combined signals may present much longer wavelengths than each individual signal and hence the integer solution of ambiguities on the combined signals can be immediately achieved. Following that, the candidates of $\mathbf{N}_{L1}$ can be restricted to a smaller search space by the decorrelation (Horemuž and Sjöberg 2002).

### 2.1.2 Search of ambiguity candidates

The float ambiguities determine the center of the search space for integer ambiguity candidates, whereas the size of the search space is another important factor. Referring to a certain observation epoch *t*, the search space for each ambiguity can be expressed by:

$$\Delta\nabla\hat{N}_i(t) - \delta_{Ni}(t) < \Delta\nabla N_i(t) < \Delta\nabla\hat{N}_i(t) + \delta_{Ni}(t) \tag{2-2}$$

where $\Delta\nabla\hat{N}_i$ is the float ambiguity and $\Delta\nabla N_i$ is an integer ambiguity candidate; $\delta$ is the size of the search space in one dimensional case. A proper choice of the term $\delta$ is a crucial step for ambiguity resolution. If the search range is too small, the true value might be excluded and the ambiguity resolution might fail. If the search range is too large, it yields huge computational burden and severely delays the ambiguity resolution. A correct set of ambiguities should offer the minimal sum of residuals. Here the term “residuals” means the deviation between the estimated double-differenced GPS carrier phase measurements and the actual measurements. In this case, the search of the ambiguity candidates can be considered as a minimization procedure as follows (Teunissen and Kleusberg 1998):

$$\sum_{i=1}^{n}(\hat{\mathbf{z}}_i - \mathbf{z}_i)^T\, Cov(\hat{\mathbf{z}})^{-1}(\hat{\mathbf{z}}_i - \mathbf{z}_i) \rightarrow \min \text{ at epoch } t \tag{2-3}$$

where $\hat{\mathbf{z}}_i$ is the *i*-th double-differenced phase measurements related to the ambiguity candidate $\Delta\nabla\hat{N}_i$; $\mathbf{z}_i$ is the actual double-differenced phase measurements; $Cov(\hat{\mathbf{z}})$ is the error covariance matrix of measurements. The size of the search range can be determined through the following approaches:

- Using the fixed variance of each ambiguity

Assuming that the ambiguities have a covariance matrix $Cov(\mathbf{N})$ and neglecting the correlation between the ambiguities, the search range for each ambiguity candidate is then:

$$\begin{aligned}
&\Delta\nabla\hat{N}_1 - \eta_1\sqrt{Cov(\mathbf{N})_{1,1}} \le \Delta\nabla N_1 \le \Delta\nabla\hat{N}_1 + \eta_1\sqrt{Cov(\mathbf{N})_{1,1}} \\
&\Delta\nabla\hat{N}_2 - \eta_2\sqrt{Cov(\mathbf{N})_{2,2}} \le \Delta\nabla N_2 \le \Delta\nabla\hat{N}_2 + \eta_2\sqrt{Cov(\mathbf{N})_{2,2}} \\
&\ldots\ldots \\
&\Delta\nabla\hat{N}_n - \eta_n\sqrt{Cov(\mathbf{N})_{n,n}} \le \Delta\nabla N_n \le \Delta\nabla\hat{N}_n + \eta_n\sqrt{Cov(\mathbf{N})_{n,n}}
\end{aligned} \tag{2-4}$$

where $\eta$ is a scaling factor determining the confidence level used for searching. All terms given above are referred to a specific epoch. The determination of ambiguity covariance matrix is a quite flexible task, which can be affected by the observation model used, the satellite geometry, the measurement qualities, etc (Abidin 1993; Kim and Langley 2000; Teunissen and Kleusberg 1998).

- The reduction of the search space by the search domain transformation

The reduction of the search space can be realized by transforming the original ambiguity sets into a decorrelated space (Kim and Langley 2000; Teunissen 1995).

- The sequential conditional search

Due to the integer properties of ambiguities and the correlation in $Cov(\mathbf{N})$, once the ambiguities $\hat{N}_1,\ldots,\hat{N}_i$ have been fixed, the variance of the next ambiguity $Cov(\mathbf{N})_{i+1,i+1}$ may be reduced in comparison with its original value. Starting from 1990, it becomes the most popular approach for the ambiguity resolution, and many studies have been investigated based on this idea, for example the Fast Ambiguity Resolution Approach (Frei and Beuler 1990), the Least-Squares Ambiguity Search Technique (Hatch 1990) and the LAMBDA (Least-squares AMBiguity Decorrelation Adjustment) technique (Teunissen 1995), where the LAMBDA approach provides not only the highest success rate of the ambiguity resolution but also an effective ambiguity validation (Teunissen 1999; Verhagen 2004).

- The reduction of the search space using constraints

In some specific applications, the geometry and the distance between the base and rover antennas serve as constraints for ambiguity searching and might significantly reduce the searching time. In a GPS multi-antenna system, the baseline lengths between antennas can be used. Considering a general model for ambiguity resolution:

$$\mathbf{Ax} = \lambda_{L1}\Delta\nabla\mathbf{\Phi}_{L1} - \lambda_{L1}\Delta\nabla\mathbf{N}_{L1} \text{ at epoch } t \tag{2-5}$$

where **A** is the design matrix containing line-of-sight vectors; **x** is the antenna coordinate to be estimated. The squared baseline length $l$ is equal to the state vector multiplied by its transpose.

$$l^2 = \mathbf{x}^T\mathbf{x} = \left(\lambda_{L1}\Delta\nabla\mathbf{\Phi}_{L1} - \lambda_{L1}\Delta\nabla\mathbf{N}_{L1}\right)^T \left(\mathbf{A}\mathbf{A}^T\right)^{-1} \left(\lambda_{L1}\Delta\nabla\mathbf{\Phi}_{L1} - \lambda_{L1}\Delta\nabla\mathbf{N}_{L1}\right) \text{ at epoch } t \qquad (2\text{-}6)$$

By applying the decomposition to the design matrix **A**, the relation between the ambiguity candidates $\Delta\nabla\mathbf{N}$ and the baseline length $l$ can be established. Lu proposed the use of Cholesky decomposition (Lu et al. 1994) for the primary four satellites. The application of QR decomposition (Sutton 1997) and Singular Value Decomposition (Park et al. 1996) have already been studied. These algorithms sequentially add constraints to each ambiguity candidate. The shorter the baseline is, the fewer candidates lie in the search scope, and hence the faster the ambiguity resolution will be. However, a short baseline yields less precise attitude parameters. For these reasons, a trade-off between the precision and the efficiency is usually in need.

### 2.1.3 Ambiguity validation

The ambiguity candidate that leads to the minimal sum of squared residuals can be identified as the best candidate within the search space. However, the best candidate does not implicitly mean the correct one. In order to judge the success of the ambiguity resolution, the ambiguity validation is needed. The ambiguity validation comprises two steps. Firstly, the best candidate should make the carrier phase measurements obey the stochastic behavior of the adjustment procedure. Secondly, the best candidate should contribute significantly lower sum of squared residuals than the second best one. More details can be found in (Verhagen 2004).

Once the ambiguities are resolved, they should keep unchanged if the associated carrier phase measurements are still available. However, anomalies might occur on the carrier phase measurements, so that a one-time ambiguity resolution cannot guarantee the safe use of carrier phase measurements during the entire observation session. In many GPS positioning applications, especially for single-frequency receivers, the real-time ambiguity resolution is still a challenging task. It is therefore not applicable to carry out the ambiguity resolution epoch by epoch to exclude these phase anomalies. Instead, we can implement rapid and sensitive approaches to detect and repair these anomalies. This technique is called “cycle-slip detection and repair”, which will be elaborated in the following sections.

## 2.2 Overview of cycle-slip detection and repair

“A cycle-slip is a sudden jump in the carrier phase observable by an integer number of cycles” (Leick 2004). Reasons of cycle-slips come from the failure of GPS receivers, the signal interruption, the low signal-to-noise ratio, or the high receiver dynamics. Cycle-slips may occur independently on each carrier frequency per GPS satellite and remain in the phase measurements. The handling of cycle-slips is conventionally composed of four sequential stages:

(1) cycle-slip detection, which checks the occurrence of cycle-slips.

(2) cycle-slip determination, which quantifies the sizes of cycle-slips.

(3) cycle-slip validation, which tests whether the cycle-slips are correctly resolved (Kim and Langley 2001).

(4) cycle-slip removal, which removes the cycle-slips from the associated phase measurement.

The occurrence of cycle-slips is a random event, and therefore the cycle-slip detection should be applied epoch by epoch. For this reason, it should be a rapid algorithm with small computational burden. Cycle-slip determination and validation will be performed on the phase measurements contaminated by cycle-slips. After the cycle-slip values are calculated and validated, the cycle-slips can be simply removed by subtracting the cycle-slip values from the original phase measurements.

The processing of cycle-slips can be applied either to the stand-alone positioning or to the differential positioning. In each case, the cycle-slip detection and determination can be further categorized according to the number of available signals. Listed below are the commonly used cycle-slip detection and determination methods and their application scenarios:

**Table 2-1: Application scenarios of cycle-slip detection/determination algorithms**

| Method | Stand-alone positioning | | Differential positioning | |
|---|---|---|---|---|
| | Single-Freq. | Dual-Freq. | Single-Freq. | Dual-Freq. |
| polynomial fitting (Beutler et al. 1984) | x | x | x | x |
| high order differences (Hofmann-Wellenhof et al. 2001) | x | x | x | x |
| Kalman filter prediction (De Jong 1998) | | x | | x |
| phase combinations (Bisnath and Langley 2000; Blewitt 1990) | | x | | x |
| phase/code combination (Hofmann-Wellenhof et al. 2001) | | x | | x |
| quality control (Kim and Langley 2001; Teunissen and Kleusberg 1998) | | | | x |

The algorithms oriented to stand-alone receivers can also be applied to differential positioning and therefore have a wide range of application scenarios. For this reason, the techniques presented in the following text are dedicated to stand-alone receivers.

## 2.3 Cycle-slip detection for triple-frequency GPS

In this section, we will firstly overview the cycle-slip detection techniques for single- and dual-frequency GPS and then elaborate the approach for triple-frequency GPS.

### 2.3.1 Cycle-slip detection for single/dual-frequency GPS

Considering the carrier phase measurements of a satellite tracked by a stand-alone GPS receiver, a general formulation for cycle-slips can be obtained by differencing the carrier phase observation equations between two adjacent epochs:

$$\lambda_{Li}\Delta_t\Phi_{Li} = \Delta_t\rho + \lambda_{Li}\Delta_t N_{Li} - \frac{\lambda_{Li}^2}{\lambda_{L1}^2}\Delta_t I_{L1} + \Delta_t T + \Delta_t S + \Delta_t t_r \cdot c + \Delta_t t_s \cdot c + \lambda_{Li}\Delta_t e_{Li} + \Delta_t M_{Li} \qquad (2\text{-}7)$$

where the operator $\Delta_t$ stands for the between-epoch differencing made between epoch $t$ and $t-1$. The cycle-slip term is denoted by $\Delta_t N_{Li}$, namely the between-epoch difference of integer ambiguity. The other notations were clarified in (1-1) and (1-3). Note that the thermal noise **e** is given in units of cycles. In (2-7), the only output from the GPS receiver is the carrier phase measurement, and therefore the foundation for cycle-slip detection is to derive the relation between the cycle-slip term $\Delta_t N_{Li}$ and the carrier phase measurements $\Delta_t\Phi_{Li}$. For this reason, the other errors should be eliminated or reduced.

For single-frequency GPS receivers, the cycle-slip detection faces a problem because the geometry term $\rho$ is unknown. If the GPS antenna is not moving, the geometry term is mainly affected by the satellite motion. In this case, the phase measurements could obey a high-order polynomial. This allows a cycle-slip detection approach by testing whether or not the high-order differenced phase measurements agree with a Gaussian distribution. An example for third-order differencing is illustrated below:

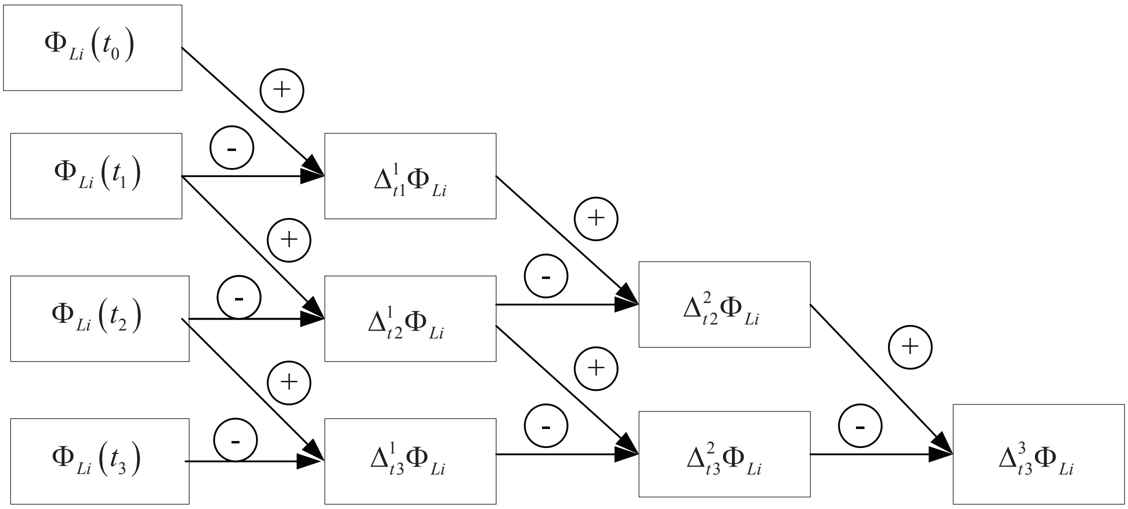

(2-8)

The operator $\Delta_t^n$ represents a $n$-order differencing ended at epoch $t$. If the antenna is stationary or moving with low maneuver and the epoch interval is not large, the remaining geometric term, the atmospheric and clock errors approach zero-values after differencing, so that the effect of cycle-slips can be remarkably demonstrated. A static experiment is carried out in order to show the performance of this approach. The GPS antenna is mounted on the roof of the institute building. The L1 phase measurements of the satellite PRN 16 are collected starting from 16:00 on the 11th April 2008 (UTC time) with a sampling frequency of 1 Hz. The original and differenced phase measurements are plotted versus time in Figure 2-1, where the last two subplots are the histograms for the second- and the third-order differenced phase measurements.

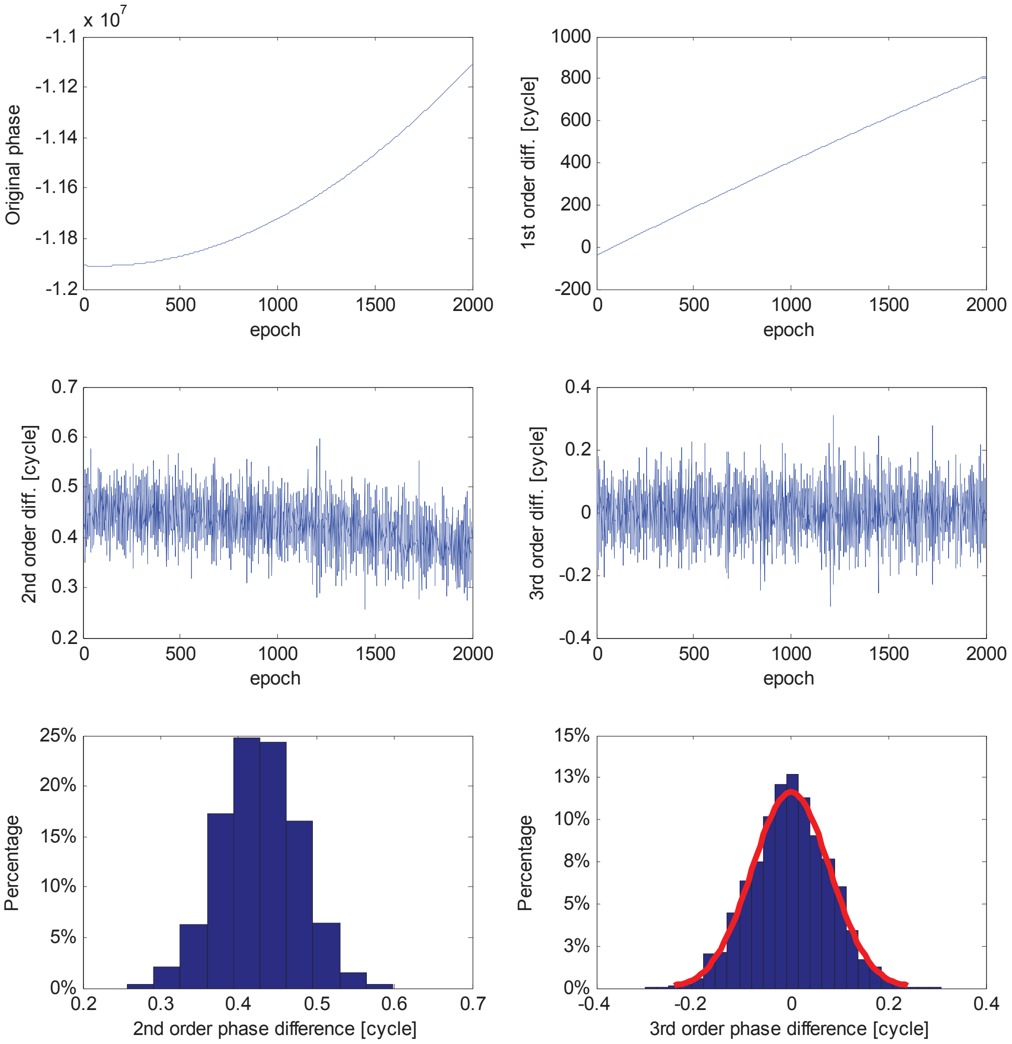

**Figure 2-1: Differenced phase measurements without cycle-slips**

Denoting the second- and third-order differenced phase measurements as $\Phi_{2d}$ and $\Phi_{3d}$, respectively, the experimental results show that $\Phi_{3d}$ obeys a Gaussian distribution with a zero-valued mean value and standard deviation of 0.08 cycles, if no cycle-slip occurs.

Suppose that a cycle-slip with the magnitude of 1 cycle arises at 500th epoch, we have the following second- and third-order differenced phase measurements.

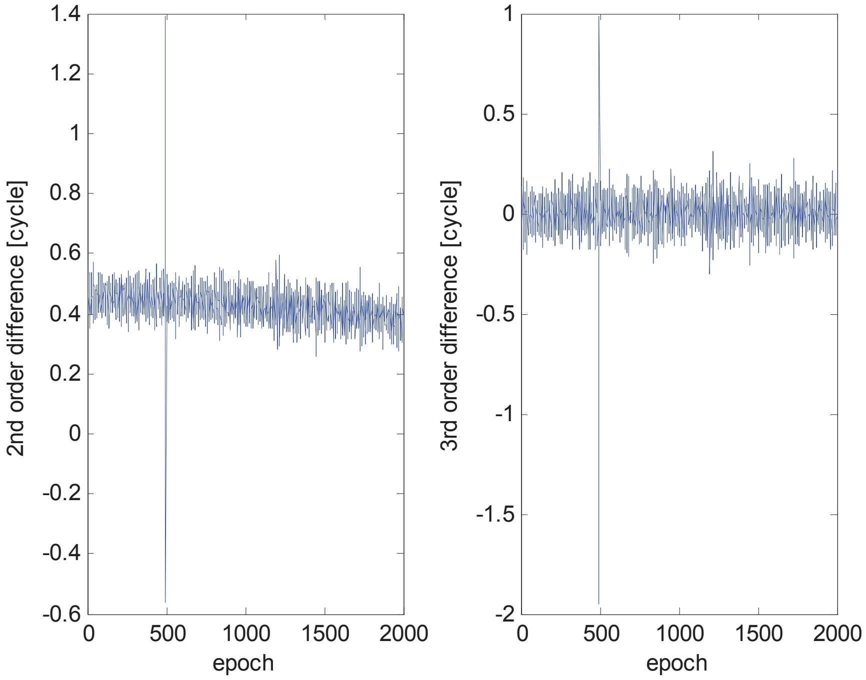

**Figure 2-2: Differenced phase measurements with cycle-slips**

There is an apparent jump at 500th epoch due to the cycle-slip, even if the magnitude of the slip is only 1 cycle. The previous discussions shows that the occurrence of a cycle-slip can be probably identified by checking whether the third-order differenced phase measurements agree with a predefined zero-mean Gaussian distribution. This algorithm employs only the phase measurements and hence it is less affected by the thermal noises and the multipath errors. However, the results given above are obtained from a static antenna, where the variation of the carrier phase measurement mainly reflects the motion of the GPS satellite along its orbit. If the antenna is moving, the third-order differenced phase measurements might lose the Gaussian behavior. Some techniques have then been developed to incorporate a proper dynamic model into a Kalman filter (Jia and Wu 2001). However, when the antenna is undergoing a complex motion, like a sharp change in the moving direction, the dynamic model may not fit well the actual maneuver. For this reason, the single-frequency cycle-slip detection is still challenging in dynamic scenarios.

Dual-frequency GPS receivers have a distinct superiority over the single-frequency receivers in the cycle-slip detection, because the geometry term and the non-dispersive errors can be fully eliminated by a geometry-free phase combination (Leick 2004):

$$\begin{aligned}&\lambda_{L1}\Delta_t\Phi_{L1}-\lambda_{L2}\Delta_t\Phi_{L2}=\\&\lambda_{L1}\Delta_t N_{L1}-\lambda_{L2}\Delta_t N_{L2}-\frac{\lambda_{L1}^2-\lambda_{L2}^2}{\lambda_{L1}^2}\Delta_t I_{L1}+\lambda_{L1}\Delta_t e_{L1}+\lambda_{L2}\Delta_t e_{L2}+\Delta_t M_{L1}+\Delta_t M_{L2}\end{aligned} \tag{2-9}$$

The remaining errors include the ionospheric error $\Delta_t I$ , the phase thermal noise $\Delta_t e$ and the multipath error $\Delta_t M$ . The thermal noise can be considered as a zero mean white Gaussian noise and its standard deviation is dependent on the quality of the receiver. The variation of ionospheric errors is just at sub-millimeter level if the GPS data rate is high (Borre 2003). Moreover, the geometry-free combination furthermore reduces the magnitude of the L1 ionospheric error by 35% due to the term $\left(\lambda_{L1}^2-\lambda_{L2}^2\right)/\lambda_{L1}^2$ . For theses reasons, we can often neglect the ionospheric error in case of a high GPS data rate. The multipath errors depend on the environment nearby and normally do not obey a Gaussian distribution. Its effect on the cycle-slip detection and determination for triple-frequency cases will be demonstrated with numerical results in section 2.7.3 and section 2.7.4. If we first neglect the multipath terms, Eq. (2-9) can be simplified to:

$$\underbrace{\lambda_{L1}\Delta_t\Phi_{L1}-\lambda_{L2}\Delta_t\Phi_{L2}}_{\Delta_t\Phi}=\underbrace{\lambda_{L1}\Delta_t N_{L1}-\lambda_{L2}\Delta_t N_{L2}}_{\Delta_t N}+\underbrace{\lambda_{L1}\Delta_t e_{L1}+\lambda_{L2}\Delta_t e_{L2}}_{\Delta_t e} \tag{2-10}$$

If no cycle-slip arises, $\Delta_t N$ term should be zero, implying that the value of $\Delta_t\Phi$ term should fall within the error range bounded by $\Delta_t e$, otherwise we can confirm an occurrence of the cycle-slips either on L1 or L2 or simultaneously on both signals. Due to the elimination of the geometry term, the cycle-slip detection for a dual-frequency GPS receiver is applicable for any dynamic application. A major limitation lies in the insensitive cycle-slip pairs, for example when the cycle-slip on L1 ($\Delta_t N_{L1}$) is 9 cycles and on L2 ($\Delta_t N_{L2}$) is 7 cycles. Since their ratio is approximately equal to the ratio of their corresponding carrier frequencies, the right-hand side of Eq. (2-10) is close to zero. These insensitive cycle-slips leave a hidden danger for cycle-slip detection.

## 2.3.2 Cycle-slip detection for triple frequency GPS

Due to the introduction of the new GPS L5 signal, the traditional approaches dealing with cycle-slip problems should be expanded to triple-frequency cases. Literature regarding triple-frequency cycle-slip detection and correction is still scarce, leaving a space for innovation. It is quite straightforward to construct the geometry-free combination for cycle-slip detection, as already presented for dual-frequency GPS. A general phase combination for triple-frequency GPS signals can be formulated as:

$$\begin{aligned}
& w_1 \lambda_{L1} \Delta_t \Phi_{L1} + w_2 \lambda_{L2} \Delta_t \Phi_{L2} + w_5 \lambda_{L5} \Delta_t \Phi_{L5} \\
& = \underbrace{\left(w_1 + w_2 + w_5\right)\left(\Delta_t \rho + \Delta_t T + \Delta_t S + \Delta_t t_r + \Delta_t t_s\right)}_{f(d)} \\
& +(w_1 \lambda_{L1} \Delta_t N_{L1} + w_2 \lambda_{L2} \Delta_t N_{L2} + w_5 \lambda_{L5} \Delta_t N_{L5}) \\
& \underbrace{+\left[w_1 \quad w_2 \quad w_5\right] \begin{bmatrix} -\Delta_t I_{L1} + \lambda_{L1} \Delta_t e_{L1} + \Delta_t M_{L1} \\ -\lambda_{L2}^2 / \lambda_{L1}^2 \cdot \Delta_t I_{L1} + \lambda_{L2} \Delta_t e_{L2} + \Delta_t M_{L2} \\ -\lambda_{L5}^2 / \lambda_{L1}^2 \cdot \Delta_t I_{L1} + \lambda_{L5} \Delta_t e_{L5} + \Delta_t M_{L5} \end{bmatrix}}_{f(e)}
\end{aligned} \qquad (2\text{-}11)$$

In order to adapt the model (2-11) to the cycle-slip detection, the non-dispersive error *f(d)*, including the geometric term, the tropospheric error, the satellite orbit and clock errors as well as the receiver clock error, can be eliminated by assuring $w_1 + w_2 + w_5 = 0$. Meanwhile, the dispersive error term *f(e)* needs to be minimized, which will be detailed in section 2.3.3. Let us first assume that *f(e)* has be optimally minimized and the remaining value is ignorable, the following relation holds true:

$$\begin{aligned}
& w_1 \lambda_{L1} \left(\Delta_t \Phi_{L1} - \Delta_t e_{L1}\right) + w_2 \lambda_{L2} \left(\Delta_t \Phi_{L2} - \Delta_t e_{L2}\right) + w_5 \lambda_{L5} \left(\Delta_t \Phi_{L5} - \Delta_t e_{L5}\right) \\
& = w_1 \lambda_{L1} \Delta_t N_{L1} + w_2 \lambda_{L2} \Delta_t N_{L2} + w_5 \lambda_{L5} \Delta_t N_{L5}
\end{aligned} \qquad (2\text{-}12)$$

The carrier phase noise $\Delta_t e_{Li}$ is assumed to be white Gaussian noise. It is further assumed that the signals have the same resolution in units of cycles (Leick 2004), i.e. $\sigma_{L1,cycle} = \sigma_{L2,cycle} = \sigma_{L5,cycle}$ where $\sigma$ stands for the standard deviation. Applying the variance propagation law yields the noise of the left-hand side of Eq. (2-12), expressed by $\sigma_c$:

$$\sigma_c = \sqrt{2} \cdot \sqrt{w_1^2 \cdot \lambda_{L1}^2 + w_2^2 \lambda_{L2}^2 + w_5^2 \lambda_{L5}^2} \cdot \sigma_{L1,cycle} \qquad (2\text{-}13)$$

where $\sqrt{2}$ reflects the between-epoch differencing.

By choosing a proper confidence level, we have a critical value $f\sigma_c$ to test the occurrence of the cycle-slips, where the scalar $f$ is a multiplication factor usually chosen as 3 (99.7% confidence level) or 4 (99.9% confidence level) in GPS applications. Summarizing the discussions above, we can conclude the occurrence of a cycle-slip if the following inequality holds true,

$$\frac{\left|w_1 \lambda_{L1} \Delta_t \Phi_{L1} + w_2 \lambda_{L2} \Delta_t \Phi_{L2} + w_5 \lambda_{L5} \Delta_t \Phi_{L5}\right|}{\sqrt{2} \cdot \sqrt{w_1^2 \cdot \lambda_{L1}^2 + w_2^2 \lambda_{L2}^2 + w_5^2 \lambda_{L5}^2}} \geq f \cdot \sigma_{L1,cycle} \qquad (2\text{-}14)$$

As there are more geometry-free combinations available for triple-frequency signals, there are two questions to be considered, one is how to find the optimal combination(s), the other one is how to benefit from the increased number of geometry-free combinations. These two questions will be explored in section 2.3.3 and section 2.3.4, respectively.

### 2.3.3 Selection of the optimal geometry-free combinations

The optimization of the geometry-free phase combination focuses on minimizing the dispersive term $f\left(e\right)$ in Eq. (2-11). Substituting the complete dispersive terms identified in (2-11) into (2-14) yields a rigorous cycle-slip detection model:

$$\frac{\left|w_1\lambda_{L1}\Delta_t\Phi_{L1}+w_2\lambda_{L2}\Delta_t\Phi_{L2}+w_5\lambda_{L5}\Delta_t\Phi_{L5}-f\left(e\right)\right|}{\sqrt{2}\cdot\sqrt{w_1^{\,2}\cdot\lambda_{L1}^{\;\,2}+w_2^{\,2}\lambda_{L2}^{\;\,2}+w_5^{\,2}\lambda_{L5}^{\;\,2}}}\geq f\cdot\sigma_{L1,cycle} \tag{2-15}$$

Denoting the denominator as $S_{comb}$, we can see that the term to be minimized is actually not $f\left(e\right)$ itself but $f\left(e\right)/S_{comb}$, namely the error with respect to the combined carrier wavelength. Such a minimization procedure for the thermal noise, the ionospheric delay and the multipath error can be formulated from (2-16) to (2-18), respectively.

$$\text{Thermal noise:}\quad \left\{\left(w_1^{\,2}\cdot\lambda_{L1}^{\;\,2}+w_2^{\,2}\lambda_{L2}^{\;\,2}+w_5^{\,2}\lambda_{L5}^{\;\,2}\right)/S_{comb}\right\}\rightarrow\min \tag{2-16}$$

$$\text{Ionospheric delay:}\quad \left\{\left(w_1+w_2\cdot\lambda_{L2}^2/\lambda_{L1}^2+w_5\cdot\lambda_{L5}^2/\lambda_{L1}^2\right)/S_{comb}\right\}\rightarrow\min \tag{2-17}$$

$$\text{Multipath error:}\quad \left\{\left(w_1\Delta_tM_{L1}+w_2\Delta_tM_{L2}+w_5\Delta_tM_{L5}\right)/S_{comb}\right\}\rightarrow\min \tag{2-18}$$

Relation (2-16) is obtained under the assumption that the carrier phase has the same standard deviation for each signal. Due to the known difficulties in the modeling of multipath errors, we will not explore the effect of multipath on the cycle-slip detection mathematically. The performance of cycle-slip detection under a high-multipath environment will be shown later using simulations. A similar determination procedure for scalars can be read from (Fan et al. 2006), where only the reduction of thermal noise is considered.

The thermal noise reduction shown in (2-16) requires that the scalars $w_i\big|_{i=1,2,5}$ are small and therefore we fix the search range of each scalar from -4 to +4 cycles. Within this range, the scalars presented in Table 2-2 yield the geometry-free combinations having relatively small ionospheric residuals, where the title “ionospheric residuals” represents the result of the left-hand side of (2-17).

**Table 2-2: Geometry-free combinations with small ionospheric residuals**

| $(w_1, w_2, w_5)$ | Ionospheric residuals | $(w_1, w_2, w_5)$ | Ionospheric residuals |
|---|---|---|---|
| (-1, 4, -3) | $0.166\Delta I_{L1}$ | (-2, 3, -1) | $1.328\Delta I_{L1}$ |
| (-1, 3, -2) | $0.388\Delta I_{L1}$ | (-3, 4, -1) | $1.547\Delta I_{L1}$ |
| (-1, 2, -1) | $0.859\Delta I_{L1}$ | (-1, -1, 2) | $1.576\Delta I_{L1}$ |
| (-1, -3, 4) | $0.971\Delta I_{L1}$ | (-2, -1, 3) | $1.951\Delta I_{L1}$ |
| (-1, -2, 3) | $1.171\Delta I_{L1}$ | (-3, -1, 4) | $2.116\Delta I_{L1}$ |

Based on the scalars presented in Table 2-2 we can make a trade-off between the reduction of thermal noise and ionospheric errors. It should be stressed that the scalars should be non-zero values. A zero-valued scalar implies the exclusion of the cycle-slip detection on the corresponding signal.

### 2.3.4 Detection of the insensitive cycle-slips

Similar as dual-frequency signals, there are also insensitive cycle-slips for triple-frequency signals. These cycle-slips usually fulfill the relation:

$$\frac{\left|w_1\lambda_{L1}\Delta_t\Phi_{L1} + w_2\lambda_{L2}\Delta_t\Phi_{L2} + w_5\lambda_{L5}\Delta_t\Phi_{L5}\right|}{\sqrt{2}\cdot\sqrt{w_1^{\;2}\cdot\lambda_{L1}^{\;\;2} + w_2^{\;2}\lambda_{L2}^{\;\;2} + w_5^{\;2}\lambda_{L5}^{\;\;2}}} < f\cdot\sigma_{L1,cycle} \tag{2-19}$$

It can be understood that the insensitive cycle-slips are related to the scalars $w_i\big|_{i=1,2,5}$. The insensitive cycle-slips ranging from 0 to 10 cycles belonging to the combination ($w_1 = -1, w_2 = -1, w_5 = 2$) are given in Table 2-3, where the "detection value" indicates the value of the left-hand side of (2-19).

**Table 2-3: Insensitive cycle-slips**

| Cycle-slips | Detection values |
|---|---|
| (0, 2, 1) | 0.0213 |
| (3, 4, 3) | 0.0188 |
| (3, 6, 4) | 0.0025 |
| (3, 8, 5) | 0.0237 |
| (4, 1, 2) | 0.0139 |
| (6, 10, 7) | 0.0163 |
| (7, 5, 5) | 0.0048 |
| (7, 7, 6) | 0.0164 |
| (8, 0, 3) | 0.0066 |
| (10, 9, 8) | 0.0236 |

In case of dual-frequency GPS, these insensitive cycle-slips are usually ignored due to their low probability. In triple-frequency GPS, the number of insensitive cycle-slips can be reduced due to the fact that the insensitive cycle-slips associated to a specific geometry-free combination could be detected by applying other geometry-free combinations. Nevertheless, the following cycle-slips are immune to geometry-free combinations as they are proportional to their individual frequencies:

$$\left\{\left(\Delta N_{L1},\Delta N_{L2},\Delta N_{L5}\right) \mid \Delta N_{L1}=154a,\Delta N_{L2}=120a,\Delta N_{L5}=115a,a\in\mathbb{N}\right\} \tag{2-20}$$

We define the cycle-slips in (2-20) as ***the most insensitive cycle-slips***. For the sake of computational efficiency, it is expected to detect maximal number of cycle-slips using minimal number of geometry-free combinations. The study reveals that all the cycle-slips except for the most insensitive ones can be detected by properly choosing two geometry-free combinations from Table 2-2. These phase combinations are presented in Table 2-4, where the last column shows the sum of the ionospheric residuals.

**Table 2-4: Two geometry-free phase combinations for cycle-slip detection**

| No | First combination | Second combination | Sum of ionospheric residuals |
|---|---|---|---|
| 1 | (-1, -1, 2) | (-1, 4, -3) | $1.7414\Delta I_{L1}$ |
| 2 | (-1, 2, -1) | (-1, -3, 4) | $1.9639\Delta I_{L1}$ |
| 3 | (-1, -1, 2) | (-1, 3, -2) | $1.8295\Delta I_{L1}$ |
| 4 | (-1, 2, -1) | (-1, -2, 3) | $2.0305\Delta I_{L1}$ |

By comparison, we use the geometry-free combinations constructed by scalars (-1, -1, 2) and (-1, 4, -3) simultaneously for cycle-slip detection, because they contribute the smallest ionospheric residuals. We define them as the ***first optimal phase combination*** and ***the second***

***optimal phase combination***, respectively.

Such a selection criteria for scalars can also be applied to GALILEO system, where the scalars (-1, 2, -1) and (-1, -4, 5) can be used for E1, E5a and E5b signals (Dai et al. 2008).

## 2.4 Cycle-slip validation for triple-frequency GPS

Traditionally, the cycle-slip validation is the next step following the cycle-slip determination. But in this study, the cycle-slip validation is embedded into the cycle-slip determination to test the cycle-slip candidates. For this reason, we will firstly introduce the cycle-slip validation in this section and then the cycle-slip determination afterwards.

The aforementioned cycle-slip detection approach can serve as the cycle-slip validation approach with a slight modification:

$$\frac{\left|w_1\lambda_{L1}\Delta_t\Phi_{L1}^{repair}+w_2\lambda_{L2}\Delta_t\Phi_{L2}^{repair}+w_5\lambda_{L5}\Delta_t\Phi_{L5}^{repair}\right|}{\sqrt{2}\cdot\sqrt{w_1^2\cdot\lambda_{L1}^2+w_2^2\lambda_{L2}^2+w_5^2\lambda_{L5}^2}}<f\cdot\sigma_{L1,cycle} \tag{2-21}$$

In comparison with formula (2-14), the difference of (2-21) lies in the superscript "repair", which implies that the carrier phase measurements is already corrected by subtracting the calculated cycle-slip values from the original phase measurements. Once the repaired phase measurements do not agree with (2-21), it means that this cycle-slip candidate under test is not the correct one.

## 2.5 Cycle-slip determination for triple-frequency GPS

Once the cycle-slips on a satellite have been detected, the next step is to quantify the sizes of the slips. A general model for cycle-slip determination can be formulated as:

$$\underbrace{\begin{bmatrix}\lambda_{L1}\Delta_t\Phi_{L1}-\Delta_t\rho\\ \lambda_{L2}\Delta_t\Phi_{L2}-\Delta_t\rho\\ \lambda_{L5}\Delta_t\Phi_{L5}-\Delta_t\rho\end{bmatrix}_t}_{\mathbf{l}_t}=\underbrace{\begin{bmatrix}\lambda_{L1}&0&0\\0&\lambda_{L2}&0\\0&0&\lambda_{L5}\end{bmatrix}}_{\mathbf{A}_t}\underbrace{\begin{bmatrix}\Delta_t\hat{N}_{L1}\\ \Delta_t\hat{N}_{L2}\\ \Delta_t\hat{N}_{L5}\end{bmatrix}_t}_{\Delta_t\hat{\mathbf{N}}}+\mathbf{e}_t \tag{2-22}$$

where the non-dispersive errors, including the tropospheric delay, satellite and receiver clock bias, are put into the term $\Delta_t\rho$, since they contribute the same amount to all signals; the column vector $\mathbf{e}$ contains the thermal noise, multipath error and the remaining ionospheric error after being differenced. It is worth noting that the $\Delta_t\hat{\mathbf{N}}$ represents the float cycle-slips rather than its integer counterpart to be determined. The term $\Delta_t\rho$ is shifted to the left-hand side of the equation as a known value in order to avoid an underdetermined model. However, this term is still unknown and should be estimated *a priori* using additional measurements immune to cycle-slips. Referring to stand-alone receivers, the following data can be employed to estimate $\Delta_t\rho$ : (a) the predicted phase measurements based on a polynomial fitting; (b) the code measurements; (c) the Doppler frequency data. The Doppler frequency data, however, are not available for some receivers. For this reason, we mainly focus on the first two types of measurements.

### 2.5.1 Measurements used for cycle-slip determination

The predicted phase based on a polynomial fitting can be used for cycle-slip determination. The phase at epoch *t* is assumed to fit a *n*-order polynomial as:

$$\hat{\Phi}_t = a_n t^n + a_{n-1} t^{n-1} + \ldots + a_1 t + a_0 \tag{2-23}$$

so that the $\Delta_t\rho$ of Eq. (2-22) can be estimated by $\Delta_t\rho = \hat{\Phi}_t - \Phi_t$ , where $\hat{\Phi}_t$ denotes the predicted phase; $\Phi_t$ is the received phase measurement; $a_{i|i=1,2\ldots n}$ are the coefficients of the polynomial. The coefficients can be estimated using the least-squares principle based on the previous phase measurements of at least *n*+1 epochs.

We can also use the code measurements to estimate the $\Delta_t\rho$ term from the following relation:

$$\begin{bmatrix}\Delta_t R_{L1} & \Delta_t R_{L2} & \Delta_t R_{L5}\end{bmatrix}^T = \mathbf{I}_{3\times1}\Delta_t\rho + \mathbf{e}_{t,code} \tag{2-24}$$

where the symbol $\Delta_t R$ represents the between-epoch code measurements; **I** stands for $[1\ 1\ 1]^T$; $\mathbf{e}_{t,code}$ contains the thermal noises of the code measurement.

Both kinds of measurements fit different scenarios. The phase prediction based on the polynomial fitting employs only the phase measurements, and hence it provides high quality phase estimation in static or low dynamic case and is less affected by multipath errors. If the antenna undergoes a complex motion, this method might provide unexpected results. The $\Delta_t\rho$ related to the code measurements is not affected by the maneuver of the antenna, but using code measurements might cause the problems in the following two aspects. Firstly, the large thermal noises of code measurements might severely enlarge the search space. Secondly, in a rich-multipath environment, the multipath error contained in the code measurements might bias the center of the search space and moreover excluded the true cycle-slip value from the search space. For these reasons, both measurements can be adaptively used in order to take their advantages in different scenarios. The first choice is the predicted carrier phase measurements. If the cycle-slip values cannot be determined in this case, the code measurements can be used instead. If the true cycle-slip values are still not resolvable, it can be concluded that the cycle-slip determination cannot offer a reliable estimation of cycle-slips, and hence the phase measurements of the current epoch cannot be further used for positioning. In this case, either the ambiguity resolution should be performed again or the handling of cycle-slips should be shifted to the next epoch.

### 2.5.2 Search of cycle-slip candidates

After $\Delta_t\rho$ is determined, we can invoke the Least-squares AMBiguity Decorrelation Adjustment (LAMBDA) technique (Teunissen 1995) to determine the cycle-slip values. The covariance matrix of cycle-slips and the estimated float cycle-slip values are required by the LAMBDA technique. In Eq. (2-22), the covariance matrix of known values $Cov(\mathbf{l}_t)$ and that of float cycle-slips $Cov\left(\Delta_t\hat{\mathbf{N}}\right)$ read:

$$\begin{aligned} Cov(\mathbf{l}_t) &= 2\cdot\mathbf{A}_t Cov(\mathbf{\Phi}_t)\mathbf{A}_t^T + \mathbf{I}\cdot Cov(\Delta_t\rho) \\ Cov\left(\Delta_t\hat{\mathbf{N}}\right) &= (\mathbf{A}_t^T Cov(\mathbf{l}_t)^{-1}\mathbf{A}_t)^{-1} \end{aligned} \tag{2-25}$$

where $Cov(\Delta_t\rho)$ is the variance of $\Delta_t\rho$ and depends on the measurements used, as presented in (2-23) and (2-24); $Cov(\mathbf{\Phi}_t)$ is the error covariance matrix of the carrier phase measurements on the triple-frequency signals; $\mathbf{I}$ is a three-dimensional identity matrix; the factor 2 in the expression of $Cov(\mathbf{l}_t)$ reflects the between-epoch differencing; the other short-hand notations are introduced in model (2-22).

The estimated float cycle-slips $\Delta_t\hat{\mathbf{N}}$ can be obtained following the least-squares principle:

$$\Delta_t\hat{\mathbf{N}} = \begin{bmatrix}\Delta_t\hat{N}_{L1} & \Delta_t\hat{N}_{L2} & \Delta_t\hat{N}_{L5}\end{bmatrix}^T = Cov\left(\Delta_t\hat{\mathbf{N}}\right)\mathbf{A}_t^T Cov(\mathbf{l}_t)^{-1}\mathbf{l}_t \tag{2-26}$$

The three-dimensional cycle-slip search space is defined as:

$$C = \left\{\Delta_t\mathbf{N}\left|\left(\Delta_t\mathbf{N}-\Delta_t\hat{\mathbf{N}}\right)^T Cov\left(\Delta_t\hat{\mathbf{N}}\right)^{-1}\left(\Delta_t\mathbf{N}-\Delta_t\hat{\mathbf{N}}\right)\le\chi^2;\Delta_t\mathbf{N}\in\mathbb{Z}^3;\Delta_t\hat{\mathbf{N}}\in\mathbb{R}^3\right.\right\} \tag{2-27}$$

where $\mathbf{x}_t$ contains the cycle-slip candidates at epoch *t*; $\Delta_t\hat{\mathbf{N}}$ represent the float cycle-slip values and $\Delta_t\mathbf{N}$ is the integer cycle-slips to be searched. The search space might contain more than one cycle-slip candidate. These cycle-slip candidates should be tested individually by the cycle-slip validation criteria given in (2-21). If just one candidate passes the validation, it can be concluded that the cycle-slip is correctly resolved.

The original search space usually manifests itself as an elongated ellipsoid due to the correlation between cycle-slips of different signals. In order to reduce the search time, the search space should be decorrelated. The decorrelation is achieved by iteratively applying the integer approximations of the conditional least-squares transformations (Teunissen 1995). An example for decorrelation of the search space is illustrated in Figure 2-3, where the ellipsoid represents the three dimensional search space and the ellipse represents the search area projected onto each two-dimensional plane:

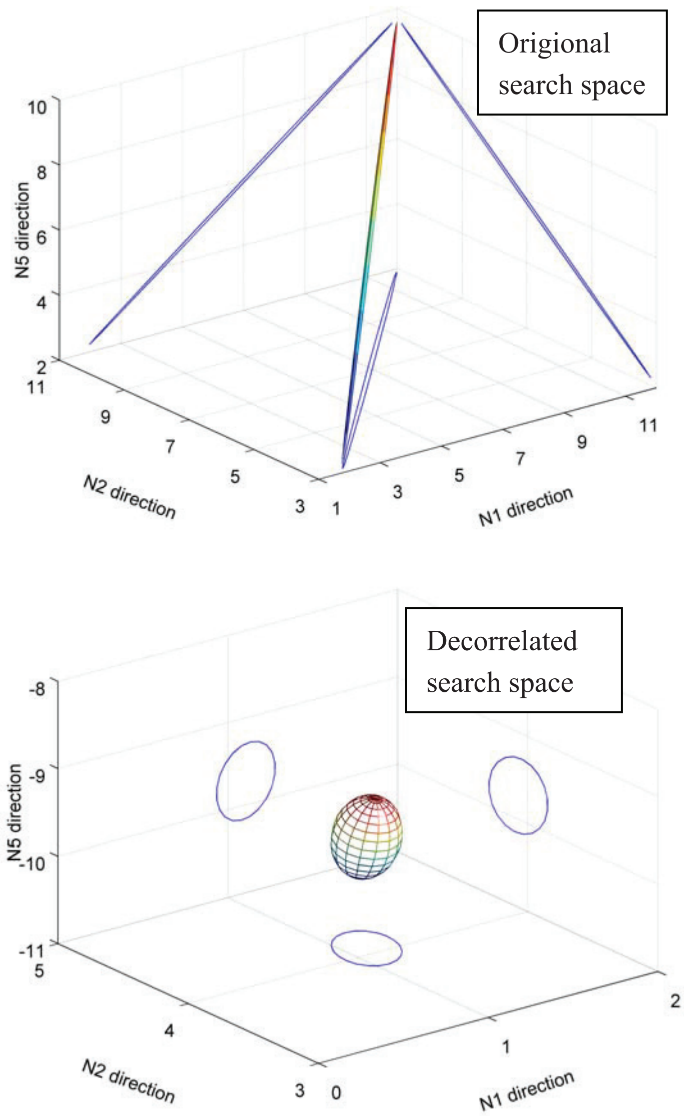

**Figure 2-3: Original and decorrelated ellipsoidal search space of cycle-slip candidates**

It can be seen that the originally elongated search space has been flattened by the decorrelation. Note that the center of search space is also shifted by the decorrelation, and hence the selected cycle-slip candidates need to be retransformed into the original space.

## 2.6 Flowchart of cycle-slip handling for triple-frequency GPS

A flowchart of the proposed cycle-slip detection, determination, and validation approaches for triple-frequency GPS is presented in Figure 2-4.

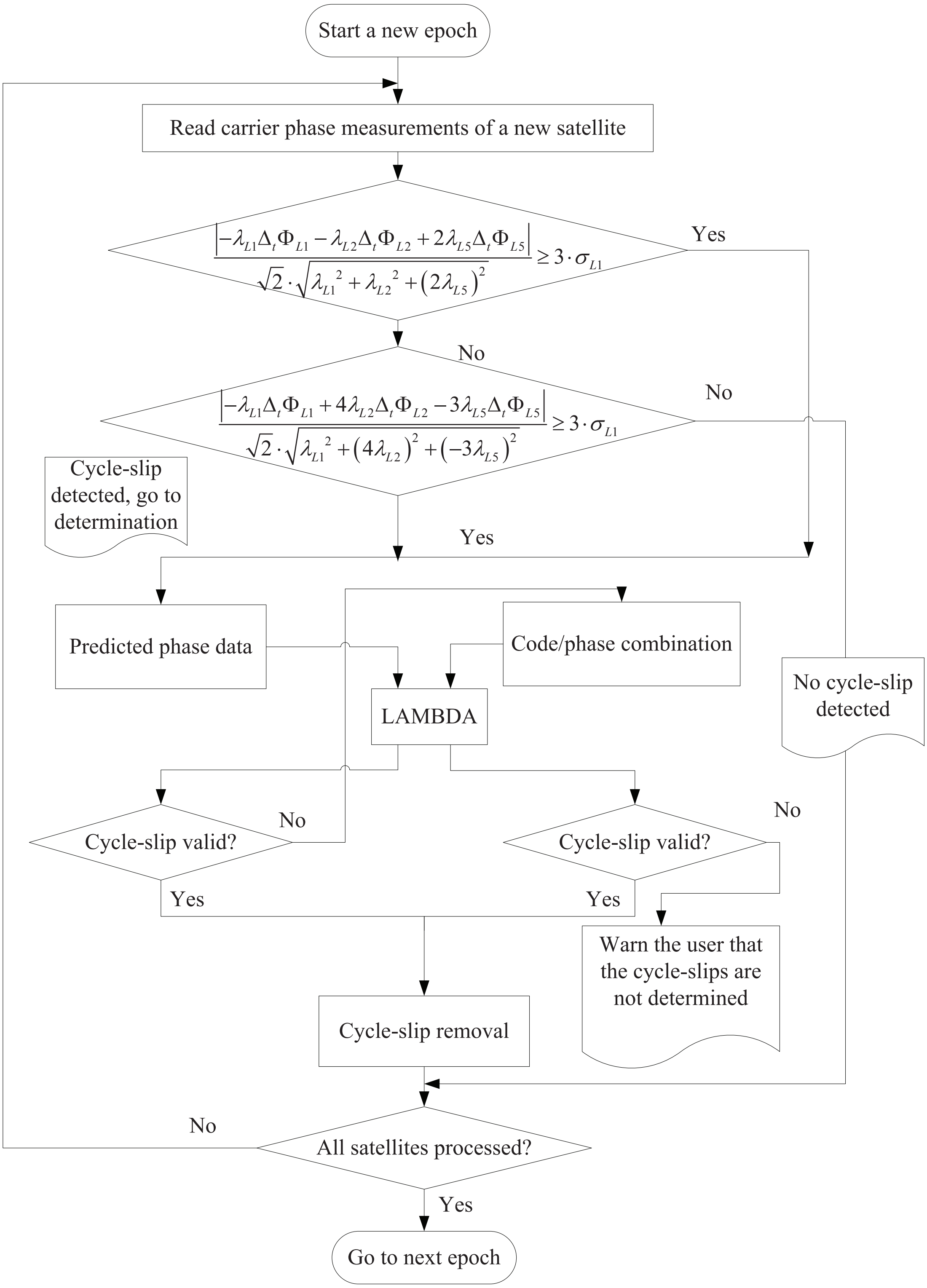

**Figure 2-4: Flowchart of triple-frequency cycle-slip detection and repair**

## 2.7 Test of cycle-slip detection and repair approaches using synthetic data

Simulations are carried out to test the proposed cycle-slip detection, determination and validation approaches. The code and carrier phase measurements are generated using the commercial GNSS software simulator SatNav Toolbox 3.0 for MATLAB® by GPSoft®. The ionospheric and multipath errors are generated using the models given in section 1.3.2. Tropospheric errors are neglected as they will be totally removed by geometry-free combinations. The satellite trajectory is calculated using the ephemeris data of GPS satellites. The error-free phase and code measurements are generated at first according to the satellite coordinates and the antenna location. Then the errors are added to the phase and code measurements, where the thermal noises are produced as white Gaussian noises. The standard deviation of the code noise is related to the carrier phase noise by (Leick 2004):

$$\begin{aligned} \sigma_{\Phi_{Li}} &= \lambda_{Li} / \lambda_{L1} \cdot \sigma_{\Phi_{L1}} \\ \sigma_{R_{Li}} &= \lambda_{Li} / \lambda_{L1} \cdot k \cdot \sigma_{\Phi_{L1}} \end{aligned} \qquad (2\text{-}28)$$

where *k* is a constant multiplication factor indicating the error level of the code measurements.

The antenna is undergoing a movement along a trajectory illustrated in Figure 2-5. Given in the axes are the coordinates in X and Y direction in the Earth-Centered-Earth-Fixed (ECEF) frame. We assume that the antenna is always moving at the ellipsoidal height of 360 m, i.e. Z value is a constant value. The numbers marked in the figure represent the epochs.

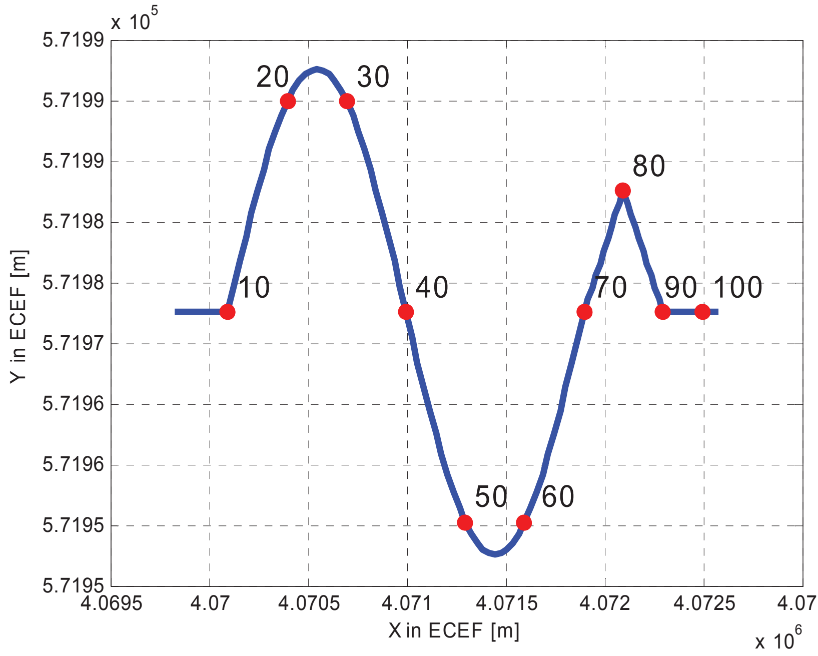

**Figure 2-5: Motion trajectory of the antenna**

Figure 2-6 shows the multipath errors contained in the carrier phase measurements and the code measurements in a low-multipath environment, whereas Figure 2-7 shows the multipath errors in a high-multipath environment. They have the same pattern but different magnitudes.

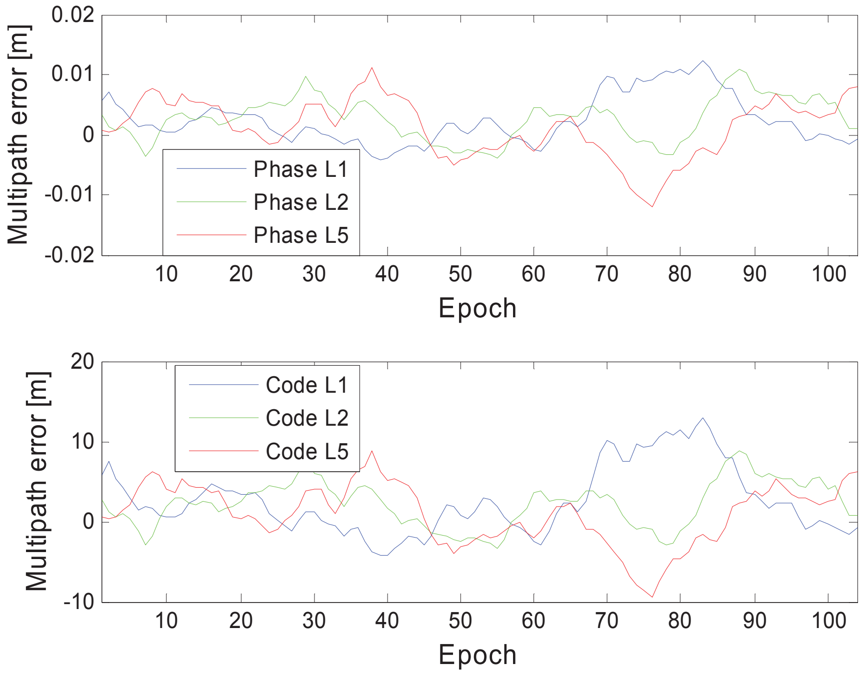

**Figure 2-6: Generated low multipath errors**

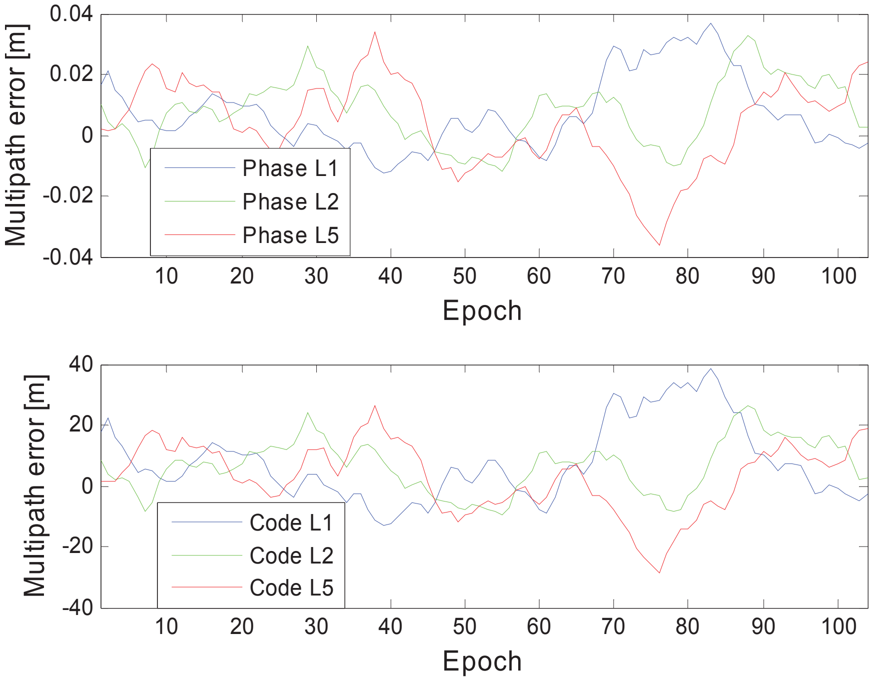

**Figure 2-7: Generated high multipath errors**

Other parameters for the simulation are listed in Table 2-5:

**Table 2-5: Parameters for the simulation**

| Parameter | value | Remarks |
|---|---|---|
| $f$ in (2-14), the multiplication factor for cycle-slip detection | 3 | 3-sigma standard deviation is adopted to detect the cycle-slips. |
| $n$ in (2-23), the order of polynomial | 3 | 3-order polynomial is used to predict the carrier phase of current epoch, namely the previous 4 epochs are involved. |
| $k$ in (2-28) | 154 | It corresponds to the P code chipping rate on L1 signal. For C/A code, this value should be enlarged depending on the technique used. |
| Sampling rate of GPS | 1 Hz | The problem with low sampling rate will be shown in the later context. |
| $\sigma_{\Phi_{L1}}$ in (2-28) | 0.01 cycles | The standard deviation of the carrier phase noise is set as 1% of the wavelength. |

The original phase measurements signal are proven to be cycle-slip free, and hence some cycle-slips should be deliberately added to the original carrier phase measurements in order to test the algorithms. After the cycle-slips are fixed, they will be removed directly from the original phase measurements and hence will not affect the following epochs any more. Therefore, even when the cycle-slips occur epoch by epoch, the algorithms still works properly.

### 2.7.1 Cycle-slip detection in a low-multipath environment

Small cycle-slips ranging from 0 to 2 cycles, i.e. from (0, 0, 1) to (2, 2, 2), have been added to the phase measurements starting from the 2nd epoch with an interval of 4 epochs. Figure 2-8 shows the detection values of cycle-slips using only the first optimal phase combination. According to the parameters given in Table 2-5, the threshold for cycle-slip detection is 0.03 cycles.

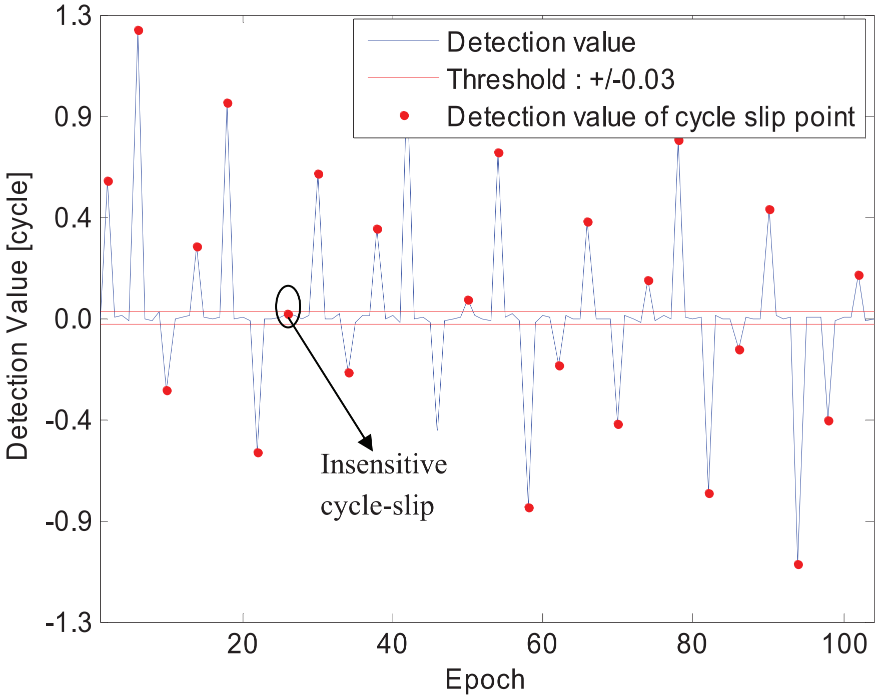

**Figure 2-8: Cycle-slip detection results in low-multipath environment**

Except for the cycle-slip (0, 2, 1) at the 26th epoch, the detection value of the other small cycle-slips exceed the threshold. Thus, this detection algorithm is sensitive to small cycle-slips.

Problems with detection are shown by using the cycle-slips given in Table 2-3. According to the previous analysis, these cycle-slips cannot be detected by using the first optimal phase combination. This also explains why the cycle-slip (0, 2, 1) lies within the thresholds in Figure 2-8. We add these insensitive cycle-slips into the original phase measurements at the epochs marked in Figure 2-9. Figure 2-10 demonstrates the different detection values when detecting cycle-slips using the aforementioned two optimal phase combinations.

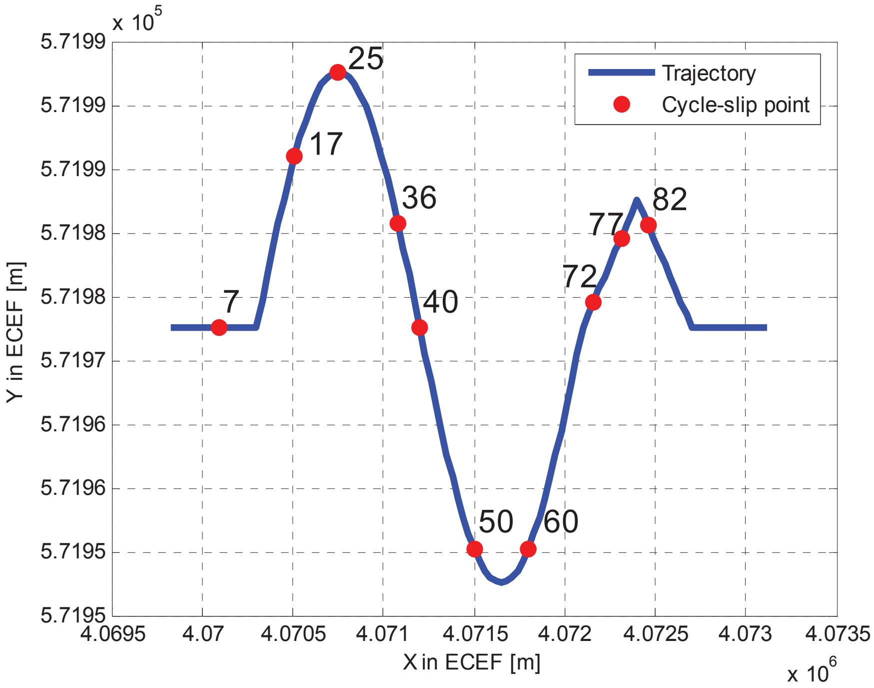

**Figure 2-9: Trajectory with cycle-slip epochs identified**

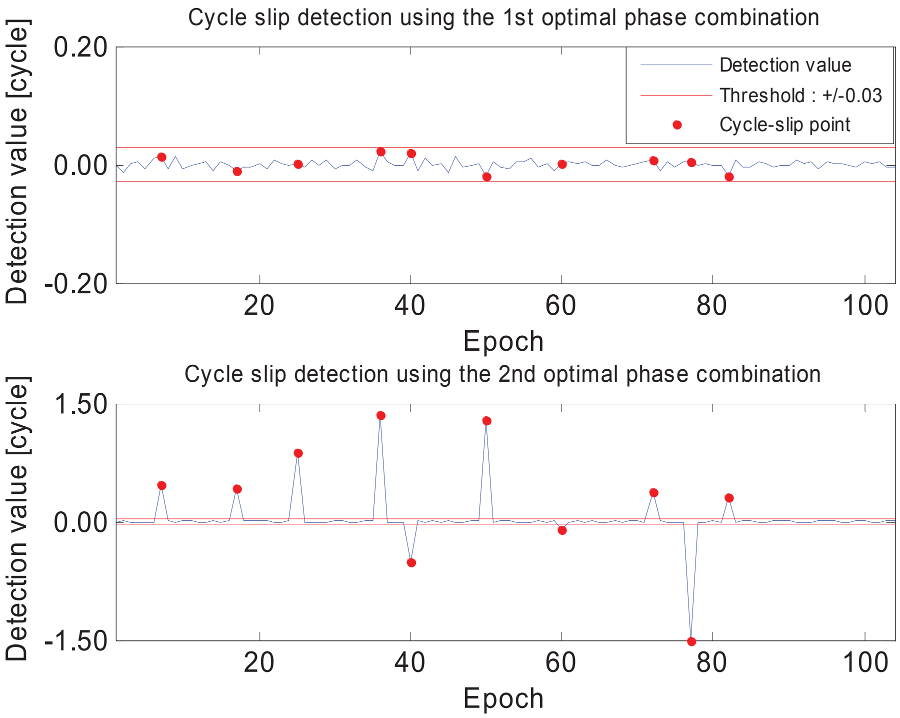

**Figure 2-10: Detection values using both optimal phase combinations**

The lower figure indicates that the detection values from the second optimal phase combination apparently exceed the threshold of ±0.03 cycles. It implies that these cycle-slips insensitive to the first optimal phase combination have been detected by the second optimal phase combination.

## 2.7.2 Test of cycle-slip determination in a low-multipath environment

We use the cycle-slips in Table 2-3 again to test the cycle-slip determination and add them to the phase measurements at the epochs given in Figure 2-9. Multipath errors are illustrated in Figure 2-6. The results obtained using the predicted phase measurements and the code measurements are given in Table 2-6, where the notation "None" implies that none of the results from LAMBDA has passed the cycle-slip validation, or in other words, this cycle-slip is not correctly determined.

**Table 2-6: Cycle-slip determination results under a low-multipath environment**

| Epoch | True Value | Float value (phase prediction) | Float value (code measurements) | Integer value(phase prediction) | Integer value (code measurements) |
|---|---|---|---|---|---|
| 7 | 0,2,1 | 0.015,1.953,0.925 | 3.442,4.678,3.560 | 0,2,1 | 0,2,1 |
| 17 | 3,4,3 | 3.007,4.020,2.984 | 1.734,3.023,2.063 | 3,4,3 | 3,4,3 |
| 25 | 3,6,4 | 3.020,6.047,4.090 | 2.336,5.489,3.508 | 3,6,4 | 3,6,4 |
| 36 | 3,8,5 | 2.948,7.994,5.085 | 6.224,10.508,7.425 | 3,8,5 | 3,8,5 |
| 40 | 4,1,2 | 3.991,1.055,2.047 | 2.923,0.183,1.230 | 4,1,2 | 4,1,2 |
| 50 | 6,10,7 | 6.064,9.990,6.945 | 6.338,10.236,7.216 | 6,10,7 | 6,10,7 |
| 60 | 7,5,5 | 6.957,4.966,5.017 | 11.495,8.505,8.376 | 7,5,5 | 7,5,5 |
| 72 | 7,7,6 | -27.197,-19.627,-19.565 | -0.426,1.207,0.438 | None | 7,7,6 |
| 77 | 8,0,3 | 7.897,-0.093,2.918 | 9.215,0.957,3.910 | 8,0,3 | 8,0,3 |
| 82 | 10,9,8 | 15.084,13.039,11.830 | 1.513,2.390,1.658 | None | 10,9,8 |

It can be seen that the method based on the phase prediction fails at the 72nd and 82nd epochs. At the 72nd epoch, the antenna is changed from a sinuous motion to a straight line motion. At the 82nd epoch, the antenna has just made a sharp turn between two straight line motions. Since we use a three-order polynomial fitting, once the antenna has undergone a significant change in the motion direction in the previous four epochs, the phase prediction may provide a wrong result. However, the incorrectly estimated cycle-slips can be filtered out by the cycle-slip validation.

As discussed before, the cycle-slip determination based on the code measurements is independent of the motion status of the antenna. Under the low-multipath environments, the multipath errors on the code measurements will not severely bias the float cycle-slip estimates, so that the LAMBDA technique will output the correct integer cycle-slip values. The results listed in the last column of Table 2-6 reveal that these cycle-slips are correctly identified since the estimated integer values equal the corresponding true values.

### 2.7.3 Test of the cycle-slip detection in high-multipath environment

The multipath errors on the carrier phase measurements are several orders of magnitude lower than that on the code measurements. The detection part is mainly related to carrier phase measurements and hence less affected by the multipath.

We use insensitive cycle-slips given in Table 2-3 to check the different detection values in different multipath environments. The detection results using the first optimal phase combination are depicted in Figure 2-11.

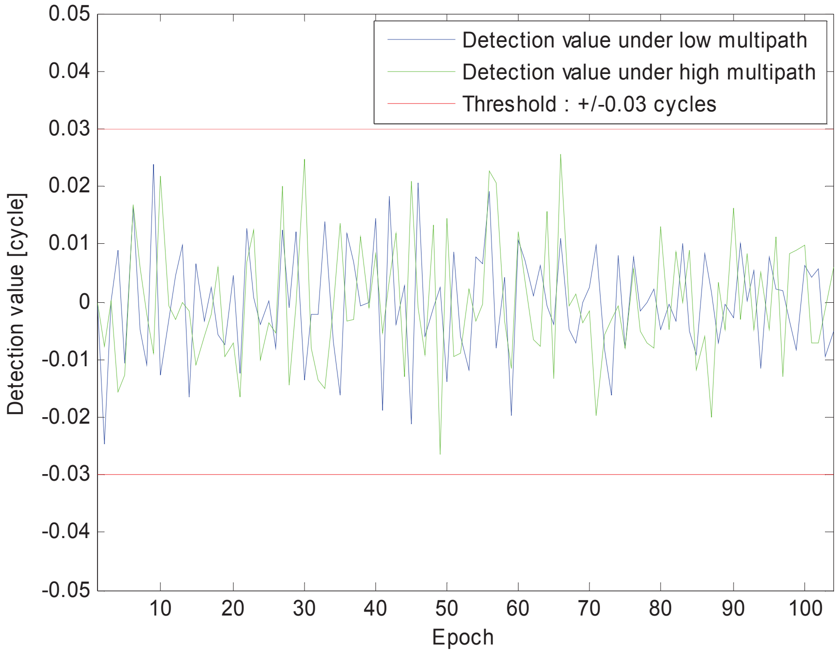

**Figure 2-11: Cycle-slip detection under low multipath**

The "detection values" refers to the left-hand side Eq. (2-19). Although different multipath errors yield different detection values, these detection values are still limited within the thresholds. Figure 2-12 shows the detection values when adding small cycle-slips ranging from (0, 0, 1) to (2, 2, 2) into the original phase measurements with the interval of 4 epochs.

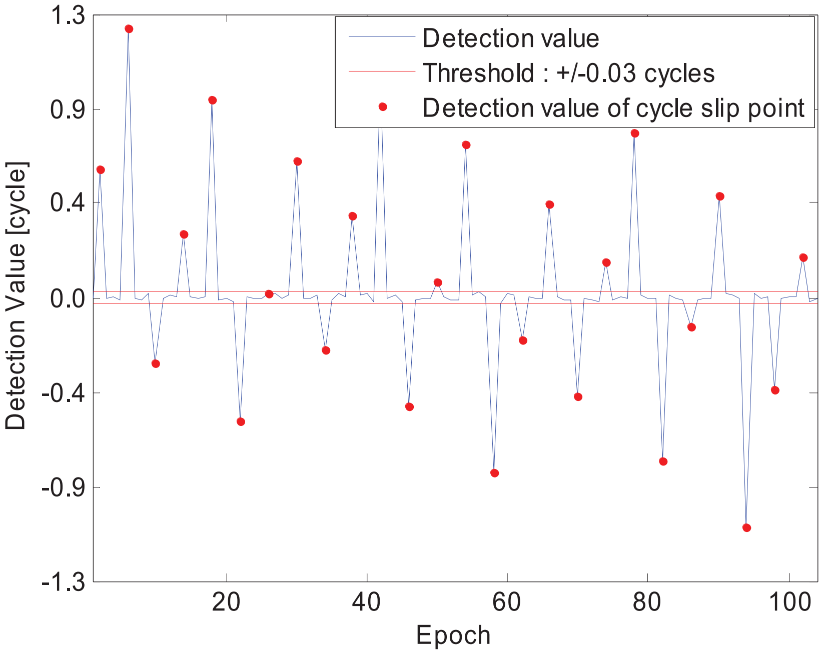

**Figure 2-12: Cycle-slip detection under high multipath**

Comparing with Figure 2-10 we can observe similar detection values in low- and high-multipath environments. These results agree with our analysis that the multipath errors do not affect the cycle-slip detection significantly.

### 2.7.4 Test of the cycle-slip determination in a high-multipath environment

The cycle-slip determination will employ either the predicted phase measurements or the code measurements. The predicted phase is less affected by the multipath, whereas the large multipath on the code measurements may severely bias the center of the search space, so that the initial search space might not contain the true cycle-slip value.

We utilize again the same insensitive cycle-slips used in low-multipath environment. The multipath errors are depicted in Figure 2-7. The determination results are given in Table 2-7.

Table 2-7: Cycle-slip determination under a high-multipath environment

| Epoch | True Value | Float value (phase prediction) | Float value (code measurements) | Integer value(phase prediction) | Integer value (code) |
|---|---|---|---|---|---|
| 7 | 0,2,1 | 0.038,1.971,0.939 | 26.081,22.334,20.464 | 0,2,1 | None |
| 17 | 3,4,3 | 2.967,4.036,2.983 | 3.097,4.089,3.094 | 3,4,3 | 3,4,3 |
| 25 | 3,6,4 | 2.989,6.063,4.122 | 18.039,17.741,15.238 | 3,6,4 | 3,6,4 |
| 36 | 3,8,5 | 2.946,8.010,5.106 | 24.371,24.653,20.988 | 3,8,5 | None |
| 40 | 4,1,2 | 4.014,1.033,2.046 | -20.327,-17.950,-16.158 | 4,1,2 | None |
| 50 | 6,10,7 | 6.017,10.013,6.907 | 21.938,22.402,18.875 | 6,10,7 | 6,10,7 |
| 60 | 7,5,5 | 6.946,4.980,4.971 | 27.186,20.740,20.095 | 7,5,5 | 7,5,5 |
| 72 | 7,7,6 | -27.114,-19.593,-19.551 | -5.201,-2.526,-3.108 | None | 7,7,6 |
| 77 | 8,0,3 | 7.892,-0.093,2.896 | 1.297,-5.210,-2.021 | 8,0,3 | 8,0,3 |
| 82 | 10,9,8 | 15.092,13.051,11.819 | -1.531,0.013,-0.628 | None | 10,9,8 |

By comparing with Table 2-6 we can see that the cycle-slip determination based on the predicted phase measurements shows a similar performance in low- and high-multipath environments. When using the code measurements, the cycle-slips at the 7th, 36th and 40th epoch cannot be fixed in the high-multipath environment, whereas these cycle-slips can be correctly identified in the low-multipath environment.

### 2.7.5 Test of the cycle-slip detection with long observation intervals

The cycle-slip detection criterion is established under a slight ionospheric change between adjacent epochs. This assumption is valid for a short observation interval. For a long observation interval, the change of the ionospheric delay can be large and remarkably affect the cycle-slip detection. We design a static scenario to show the effects of the observation interval on the cycle-slip detection. The antenna is fixed at the initial position as given in Figure 2-5 and the observation takes 60 epochs. The ionospheric delay on L1 signal under different observation intervals is plotted versus time in Figure 2-13. As we are only interested in the variation of the ionospheric delay over time, the presented results are in fact obtained with respect to the value of the initial epoch. In Figure 2-14, the detection results based on the first optimal phase combination are depicted.

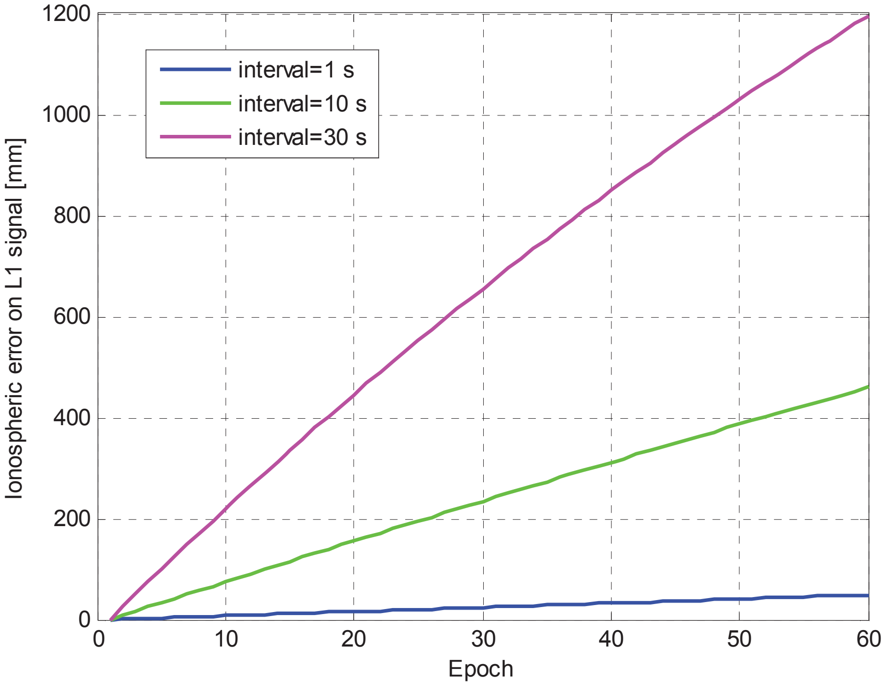

**Figure 2-13: Variation of ionospheric error for different observation intervals**

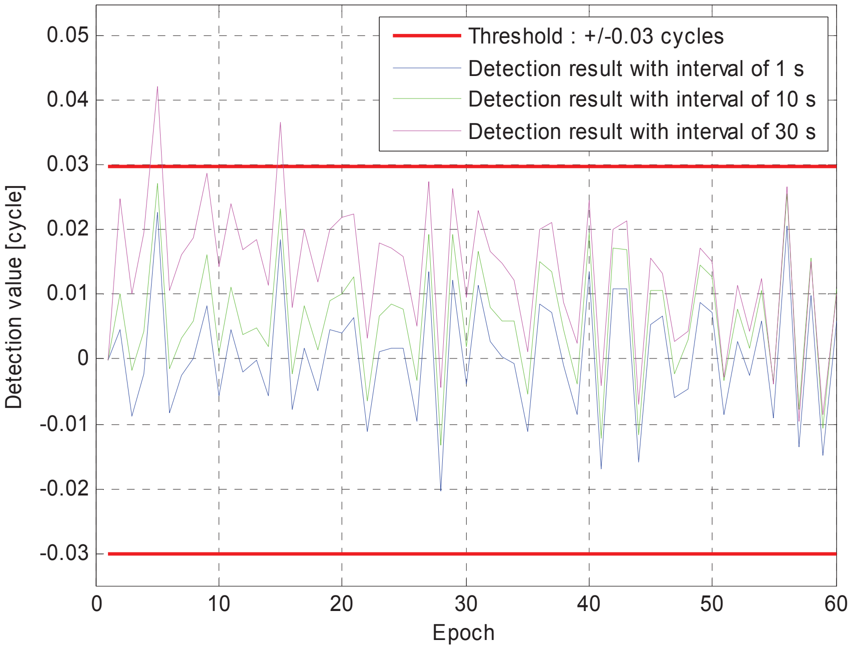

**Figure 2-14: Cycle-slip detection values under different observation intervals**

With the increasing observation intervals, the detection values are closer to the threshold. For the observation interval of 30 seconds, some detection values even exceed the threshold, resulting in a wrong judgment on the cycle-slip occurrence. In this sense, the proposed cycle-slip detection method is only applicable under high data rate.

## 2.8 Conclusions

In this chapter, a novel method for cycle-slip detection, determination and validation for triple-frequency GPS has been highlighted. This technique is designed for a stand-alone GPS receiver and suitable for real-time static or dynamic applications.

The cycle-slip detection is implemented using two geometry-free phase combinations constructed by the scalars (-1, -1, 2) and (-1, 4, -3) in order to detect a larger number of insensitive cycle-slips. The proper performance of the cycle-slip detection relies on the small change of ionospheric delay between two adjacent epochs, and hence this approach is only applicable given a high GPS data sampling rate. In some extreme cases, for example, magnetic storm, the detection approach may provide unexpected results.

In the cycle-slip determination, the float cycle-slip values can be estimated either from the predicted phase measurements or from the code measurements. The phase prediction technique is less affected by multipath errors but will probably fail in a complex motion of the antenna. The use of code measurements is independent of the antenna motion but will be contaminated by large multipath errors. In order to improve the robustness, both techniques can be adaptively applied.

With the improvement of the GPS receiver technology, a phase noise of 1% cycles or even lower can be achieved. At such a noise level, the cycle-slip validation allows a sensitive test criterion to the cycle-slip candidates.

# 3. Attitude determination using GPS

After the ambiguities are resolved and the cycle-slips are checked, the carrier phase measurements can be used for attitude determination. In this chapter, we will at first explain the coordinate frames and the commonly-used attitude representations. Following that, the algorithms dedicated to the GPS multi-antenna systems will be overviewed and the least-squares attitude determination approach (LSAD) will be highlighted. Finally, the results from a site experiment will be presented to evaluate the performance of the system.

## 3.1 Introduction to GPS multi-antenna systems

The GPS multi-antenna systems for attitude determination can be categorized into dedicated and non-dedicated systems (Lu 1995). In a dedicated system, the antennas are connected with a specially designed receiver with a common oscillator synchronizing the signals. A non-dedicated system is composed of several antenna-receiver pairs. The output of the code and phase measurements from the receivers will be transferred to a common processing unit which performs the synchronization and the signal processing. Compared with dedicated systems, non-dedicated systems provide not only comparable results, but also cost-effectiveness (since off-the-shelf components can be used) and flexibility. In a dedicated system, a common oscillator is used for all antennas, and hence the receiver clock error can be cancelled by a single-differential processing. For non-dedicated systems, double-differential processing is required to cancel the satellite and receiver clock errors. Figure 3-1 is an illustration of a non-dedicated system.

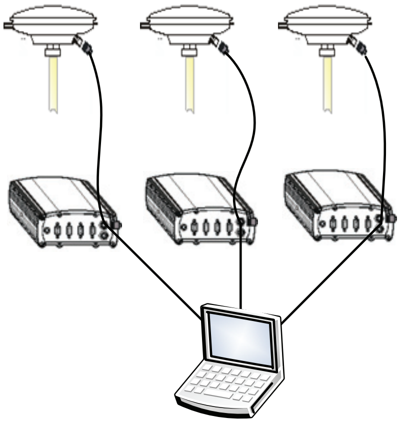

**Figure 3-1: Non-dedicated GPS multi-antenna system**

The basic idea behind the GPS multi-antenna system is to calculate the baselines between antennas using RTK technique and then to derive the attitude parameters. Carrier phase measurements are employed for high-accurate attitude solutions. Although only processing the pseudorange measurements also yields attitude parameters as well, the accuracy will be much lower.

## 3.2 Coordinate frames

In order to clarify the attitude determination using GPS multi-antenna systems, several coordinate frames needs to be distinguished, including the Earth-Centered-Earth-Fixed (ECEF) frame, the Local Level Frame (LLF), the Antenna Body Frame (ABF) and the Plane Body Frame (PBF). The ECEF and the LLF are depicted in Figure 3-2.

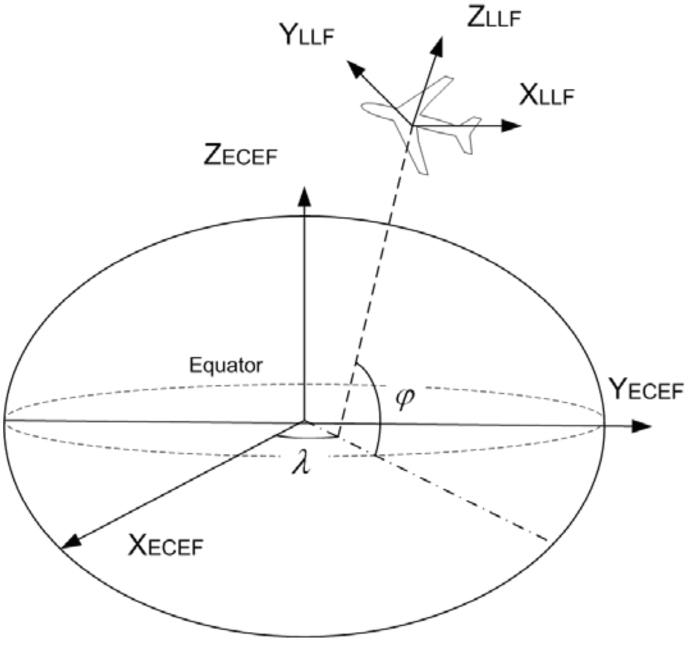

**Figure 3-2: ECEF and LLF**

The ECEF, also referred to as terrestrial equatorial system, is defined as follows: the origin is the geocenter; $X_{ECEF}$ is located in the equatorial plane and points towards the Greenwich meridian; $Z_{ECEF}$ is the rotation axis of the earth; $Y_{ECEF}$ completes the right-handed Cartesian system along with $Z_{ECEF}$ and $X_{ECEF}$.

The LLF describes the local coordinate of a point with respect to a reference point, and it is usually expressed in East-North-Up (ENU) directions. The origin of the LLF is chosen as the reference point. $X_{LLF}$ points to ellipsoidal east and $Y_{LLF}$ to north; $Z_{LLF}$ is along with the ellipsoidal norm and points upwards. LLF is usually adopted as the reference frame in the attitude determination frame.

The ABF and PBF are described in Figure 3-3.

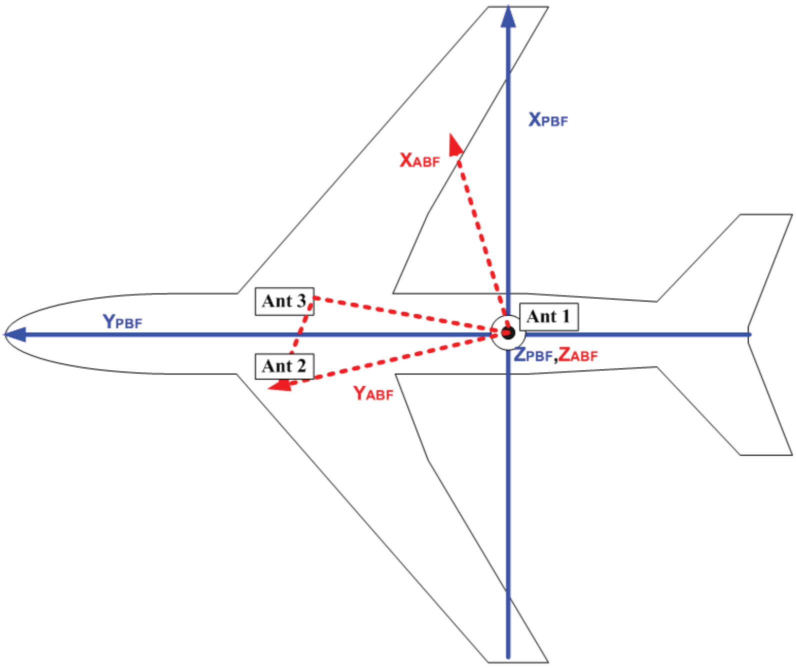

Figure 3-3: ABF and PBF

The ABF is formed by the GPS antennas. We assume that the antennas are mounted on a rigid platform, i.e. the relative distances between antennas remain unchanged. One antenna is chosen as the master antenna, and the other antennas are called slave antennas. Actually, three antennas are sufficient to determine the ABF. The origin is chosen as the phase center of antenna 1, namely the master antenna. $Y_{ABF}$ is assumed along with the baseline from antenna 1 to antenna 2. $X_{ABF}$ is perpendicular to $Y_{ABF}$ and lies in the plane defined by antenna 1, 2 and 3. $Z_{ABF}$ is perpendicular to both of the $X_{ABF}$ and $Y_{ABF}$ axis and points upwards. It should be stressed that we define the ABF using a configuration of three antennas, however, it does not mean that three antennas are prerequisites for attitude determination. Three or more antennas give us three-dimensional attitude parameters, whereas a dual-antenna configuration yields two-dimensional attitude parameters. Related information can be found in section 3.5.

The PBF is defined according to the body architecture of an airplane. In the PBF frame, the $Y_{PBF}$ axis is drawn along the center line of the airborne fuselage from tail to front. The $X_{PBF}$ axis is perpendicular $Y_{PBF}$ and parallel to the line from the left wing tip to the right wing tip. The $Z_{PBF}$ points upwards and is perpendicular to both of the $X_{PBF}$ and $Y_{PBF}$. The origin of the PBF can be simply assumed to be overlapped with ABF.

## 3.3 Theoretical background for attitude determination

The three-dimensional coordinate transformation from a-frame to b-frame can be expressed using Helmert formulation (Hofmann-Wellenhof et al. 2003):

$$\mathbf{x}^b = \mathbf{x}_{0,a}^b + \mu \mathbf{R}_a^b \left(\alpha_1, \alpha_2, \alpha_3\right) \mathbf{x}^a \tag{3-1}$$

where vectors $\mathbf{x}^a$ and $\mathbf{x}^b$ represent the coordinates in a-frame and b-frame, respectively; $\mathbf{x}_{0,a}^b$ is the origin of *b*-frame expressed in a-frame; $\mathbf{R}_a^b$ is the rotation matrix from *a*-frame to *b*-frame; $\alpha$ represents the three-dimensional attitude parameters; $\mu$ is the scaling factor. The complete transformation is composed of three components:

1. Rotations reflected by $\mathbf{R}_a^b$;
2. Translations reflected by $\mathbf{x}_{0,a}^b$;
3. Scaling reflected by $\mu$.

In the GPS multi-antenna systems, the attitude represents the misalignment between the ABF and the LLF. As a result of the overlapped origin and the same scale of ABF and LLF, the only remaining transformation component is rotation. We therefore rewrite (3-1) as:

$$\mathbf{b}_n = \mathbf{R}_{LLF}^{ABF} \left(\alpha_1, \alpha_2, \alpha_3\right) \mathbf{l}_n \tag{3-2}$$

where $\mathbf{b}_n$ and $\mathbf{l}_n$ represent the baseline vector from antenna *n* to antenna 1 (master antenna) expressed in ABF and LLF, respectively. For example, $\mathbf{b}_2$ represents the coordinate of antenna 2 in ABF with respect to the master antenna (namely the origin of ABF), which can be expressed as $\mathbf{b}_2 = [x_{2,b} \quad y_{2,b} \quad z_{2,b}]^T$.

## 3.4 Attitude representation

The three-dimensional attitude parameters can be represented using different parameterization frames, including Direction Cosine Matrix (DCM), Euler angles, quaternions, Euler Axis/Angle and Gibbs vectors (Wertz 1978). The DCM provides a general mathematical model for attitude determination. The Euler angles allow a clear view of the attitude information. In comparison with the Euler angles, the quaternions offer a very abstract but more robust expression of the attitude information. Different attitude parameterization schemes play different roles in attitude determination. The Euler angles are usually used as inputs and outputs of an attitude determination system. In some special applications, the quaternions can be used instead of Euler angles to yield a robust performance, especially when singularity problems take place. Figure 3-4 clarifies a general flow of attitude determination with different attitude representations.

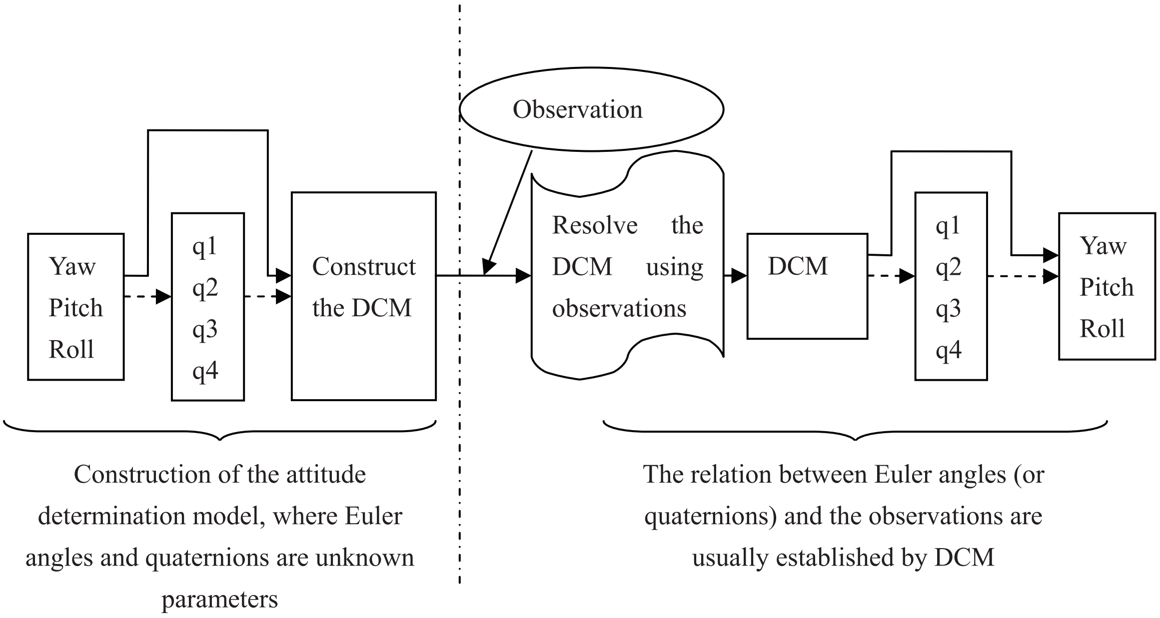

**Figure 3-4: A general flow of attitude determination**

### 3.4.1 Direction Cosine Matrix

The rotation can be expressed by specifying the coordinates of the body frame with respect to the reference coordinate frame. Each component of a DCM represents the cosine angle between a specific axis in the body frame and its correspondence in the reference frame. Therefore, a DCM has nine parameters given in a form of $3\times3$ matrix. A vector $x$ with the components $a_u$, $a_v$ and $a_w$ along the reference axes can be projected into the body frame with axes $x_a$, $x_b$ and $x_c$ by:

$$\begin{bmatrix} x_u \\ x_v \\ x_w \end{bmatrix} = \begin{bmatrix} u_a & u_b & u_c \\ v_a & v_b & v_c \\ w_a & w_b & w_c \end{bmatrix} \begin{bmatrix} x_a \\ x_b \\ x_c \end{bmatrix} \tag{3-3}$$

Each component of a DCM indicates a cosine angle. For example, $u_a$ is the cosine of the angle between the $u$ axis of the reference frame and the $a$ axis of the body frame. DCM is a fundamental quantity specifying the orientation of a rigid body and a convenient product rule for successive rotations (Wertz 1978).

### 3.4.2 Euler angles

A three-dimensional rotation can be decomposed into three individual rotations with each around a single axis. Euler angles, which are often called yaw, pitch and roll angles, represent the rotation angles with respect to three axes, as shown in Figure 3-5. In physics and engineering, the right-handed frame is usually used, where the Euler angles describe counter-clockwise rotations when seeing from the end of the positive axes and clockwise rotation when seeing from the origin of the positive axes.

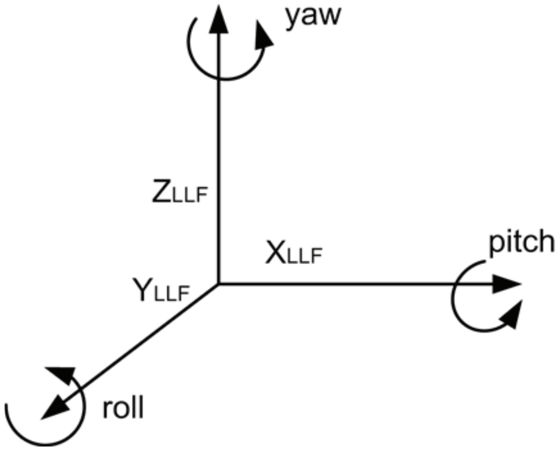

LLF=Local Level Frame

**Figure 3-5: Euler angles**

Each rotation can be described by a DCM. A three-dimensional rotation can be obtained by multiplying the three DCMs in a specific order, yielding the combined rotation matrix. An example using the yaw-pitch-roll sequence is given below (Hofmann-Wellenhof et al. 2001):

$$\mathbf{b}_n = \mathbf{R}_2'\{r\}\mathbf{R}_1'\{p\}\mathbf{R}_3'\{y\}\mathbf{l}_n = \underbrace{\begin{bmatrix} c_r c_y - s_r s_p s_y & c_r s_y + s_r s_p c_y & -s_r c_p \\ -c_p s_y & c_p c_y & s_p \\ s_r c_y + c_r s_p s_y & s_r s_y - c_r s_p c_y & c_r c_p \end{bmatrix}}_{\mathbf{R}} \mathbf{l}_n \tag{3-4}$$

where $\mathbf{b}_n$ and $\mathbf{l}_n$ represent the baseline vector from antenna $n$ to antenna 1 (master antenna) expressed in ABF and LLF, respectively; $\mathbf{R}'\{\cdot\}$ is the DCM related to each Euler angle; $y$, $p$ and $r$ are short-hand notations for yaw, pitch and roll angles, respectively; $c$ and $s$ denote the cosine and sine operators, respectively. Based on the combined rotation matrix $\mathbf{R}$, the attitude determination can be generalized by solving the $\mathbf{R}$ firstly and then calculating each Euler angle from the implicit relations:

$$\begin{aligned} pitch &= \tan^{-1}\left(\mathbf{R}_{23} \Big/ \sqrt{\mathbf{R}_{21}^2 + \mathbf{R}_{22}^2}\right) = \sin^{-1}\left(\mathbf{R}_{23}\right) \\ yaw &= -\tan^{-1}\left(\mathbf{R}_{21}/\mathbf{R}_{22}\right) \\ roll &= -\tan^{-1}\left(\mathbf{R}_{13}/\mathbf{R}_{33}\right) \end{aligned} \tag{3-5}$$

The above formula works only for the Euler angles ranging from –π/2 to π/2. For an interval from –π to π, the quadrant of Euler angles cannot be directly determined. For example, as *sin(pitch)* is equal to *sin (π - pitch)*, we cannot distinguish the true pitch value and its ambiguous counterpart. This hidden problem can be solved by checking the compatibility of the original DCM with the new DCM constructed by Euler angles obtained from (3-5). If both are not compatible, one or more Euler angles must lie in wrong quadrants. In this case, we have to try possible ambiguous counterparts until both DCMs match each other.

A combined rotation matrix is subject to the rotation sequence. The selection of a proper order should take the singularity issue into account. Model (3-4) shows a singularity when pitch angle is ±90 degrees, as it results in a zero-valued denominator for the expression of yaw and roll. A pitch angle of 90 degrees manifests itself in a vertically upward motion. This means that the yaw-pitch-roll sequence is not suitable for rockets or missiles, but should be applicable for civilian airplanes. Each Euler angle sequence has at least one singularity point. Moreover, in the neighborhood of its singular point, the systemic behavior of tracking sequence application is, in general, erratic and often troubled with serious transient errors (Kuipers 2002). In order to solve the singularity problem, quaternion representation is usually adopted. In the TerraSAR/PAMIR experiment, the singularity problem does not likely occur due to the maneuver output of the PAMIR airplane. We therefore consider the use of Euler angles in this thesis due to its clear physical interpretation.

## 3.5 Attitude determination based on Euler angles

The attitude determination based on multiple GPS antennas follows the same rule of attitude determination based on vector measurements. A general model can be formulated to find a rotation matrix yielding the minimized least-squares residuals (Wertz 1978):

$$\sum_{i=2}^{n} w_i \left| \mathbf{b}_n - \mathbf{R}_{LLF}^{ABF} \mathbf{l}_n \right|^2 \rightarrow \min \tag{3-6}$$

where $w_i$ is the weighting factor for each baseline vector from the LLF to the ABF. Several methods have been studied since the early 1960s in order to resolve this model. A early version is based on the singular value decomposition (Wahba 1965) and further refined by (Markley 1988; Markley 1993). Another method utilizes the pseudo-inverse of the rotation matrix, so that the rotation matrix can be resolved by (Grass and Braasch 1991):

$$\mathbf{R}_{LLF}^{ABF} = \left[ \mathbf{b}_2 \;\vdots\; \cdots \;\vdots\; \mathbf{b}_n \right] \begin{bmatrix} \mathbf{l}_2^T \\ \hdashline \vdots \\ \hdashline \mathbf{l}_n^T \end{bmatrix} \left( \left[ \mathbf{l}_2 \;\vdots\; \cdots \;\vdots\; \mathbf{l}_n \right] \begin{bmatrix} \mathbf{l}_2^T \\ \hdashline \vdots \\ \hdashline \mathbf{l}_n^T \end{bmatrix} \right)^{-1} \tag{3-7}$$

As stated in chapter 3.4.2, the “re-check” procedure should be applied to determine the quadrant of each Euler angle.

The aforementioned algorithms employ all available measurements and hence yield an optimal solution. However, it is not easy to incorporate the covariance matrix of GPS measurements into the model. In order to overcome this drawback, some dedicated models are developed. Cohen refined the loss function by substituting the GPS carrier phase measurement into the model (Cohen 1992). However, the potential measuring errors contained in the ABF are not considered. Lu proposed a explicit least-squares model to fully incorporate all potential errors (Lu et al. 1994). The model proposed by Lu simplifies the error analysis for attitude parameters, and moreover, it facilitates a possibility to integrate with proper dynamic models or other sensors. A shortcoming is that the Jacobin matrix has to be calculated.

Another commonly used method is referred to as Direct Attitude Computation (Lu et al. 1994). This is also a dedicated method for multi-antenna system as it smartly using the properties of the ABF and the rotation matrix. On the one hand, there are some zero-valued components in the ABF according to the definition. On the other hand, the Euler angles can be calculated in a one-step wise as shown in Eq. (3-5). These properties allow a direct computation of the Euler angles.

The prerequisite for the attitude determination is to accurately measure the ABF and estimate the LLF. The ABF can be determined by its definition given in chapter 3.1, as long as the magnitude of antenna baselines can be accurately measured. This can be done by using other measuring sensors or by performing a long-term differential positioning. The LLF relies on the estimated three-dimensional baseline vectors between the master antenna and slave antennas. In most applications, accurate baseline estimation is achieved by RTK technique.

### 3.5.1 Least-squares attitude determination approach (LSAD)

In order to apply the least-squares method to the model (3-6), this model should be linearized at first around the Euler angles. Taking the measurement errors into account, Eq. (3-2) can be rewritten as:

$$\left(\mathbf{b}_i - \mathbf{e}_{\mathbf{b}_i}\right) = \mathbf{R}_{LLF}^{ABF}\left(\mathbf{l}_i - \mathbf{e}_{\mathbf{l}_i}\right) \tag{3-8}$$

where $\mathbf{e}_{\mathbf{b}_i}$ and $\mathbf{e}_{\mathbf{l}_i}$ indicate the measurement errors of $\mathbf{b}_i$ and $\mathbf{l}_i$, respectively; the unknown Euler angle estimates are included in the rotation matrix $\mathbf{R}_{LLF}^{ABF}$. Linearizing the right-hand side with respect to the Euler angles yields:

$$\mathbf{b}_i - \mathbf{e}_{\mathbf{b}_i} = \left[\begin{array}{c:c:c} \frac{\partial\left[\mathbf{R}_{LLF}^{ABF}\left(\mathbf{l}_i - \mathbf{e}_{\mathbf{l}_i}\right)\right]}{\partial y} & \frac{\partial\left[\mathbf{R}_{LLF}^{ABF}\left(\mathbf{l}_i - \mathbf{e}_{\mathbf{l}_i}\right)\right]}{\partial p} & \frac{\partial\left[\mathbf{R}_{LLF}^{ABF}\left(\mathbf{l}_i - \mathbf{e}_{\mathbf{l}_i}\right)\right]}{\partial r} \end{array}\right]\begin{bmatrix} \partial y \\ \partial p \\ \partial r \end{bmatrix} \tag{3-9}$$

Based on this relation, the least-squares adjustment can be performed around the initial Euler angle values:

$$\mathbf{b}_i - \mathbf{R}_0\mathbf{l}_i = \left[\begin{array}{c|c|c} \dfrac{\partial(\mathbf{R}_0\mathbf{l}_i)}{\partial y} & \dfrac{\partial(\mathbf{R}_0\mathbf{l}_i)}{\partial p} & \dfrac{\partial(\mathbf{R}_0\mathbf{l}_i)}{\partial r} \end{array}\right]\Bigg|_{y_0,p_0,r_0} \begin{bmatrix} \Delta y \\ \Delta p \\ \Delta r \end{bmatrix} + \left(\mathbf{e}_{\mathbf{b}_i} - \mathbf{R}_0\mathbf{e}_{\mathbf{l}_i}\right) \tag{3-10}$$

where $\mathbf{R}_0$ is an approximated DCM determined by the initial values of Euler angles $y_0$, $p_0$ and $r_0$; $\mathbf{b}_i - \mathbf{R}_0\mathbf{l}_i$ is the measurement vector; $\left[\begin{array}{c|c|c} \dfrac{\partial(\mathbf{R}_0\mathbf{l}_i)}{\partial y} & \dfrac{\partial(\mathbf{R}_0\mathbf{l}_i)}{\partial p} & \dfrac{\partial(\mathbf{R}_0\mathbf{l}_i)}{\partial r} \end{array}\right]$ is the design matrix; $[\Delta y \quad \Delta p \quad \Delta r]^T$ is the correction values of the Euler angle estimates; $\left(\mathbf{e}_{\mathbf{b}_i} - \mathbf{R}_0\mathbf{e}_{\mathbf{l}_i}\right)$ is the measurement error vector. The relation given in (3-10) is only valid for a single baseline vector composed of two antennas. Assuming that we have totally $n$ antennas, there are $n$-1 antenna baseline vectors with respect to the master antenna (antenna 1). Thus, (3-10) can be expanded to all baseline vectors:

$$\left[\begin{array}{c} \mathbf{z}_2 \\ \hline \mathbf{z}_3 \\ \hline \vdots \\ \hline \mathbf{z}_n \end{array}\right] = \left[\begin{array}{c} \mathbf{A}_2 \\ \hline \mathbf{A}_3 \\ \hline \vdots \\ \hline \mathbf{A}_n \end{array}\right] \times \begin{bmatrix} \Delta y \\ \Delta p \\ \Delta r \end{bmatrix} + \left[\begin{array}{c} \mathbf{v}_2 \\ \hline \mathbf{v}_3 \\ \hline \vdots \\ \hline \mathbf{v}_n \end{array}\right]$$

$$\left[\begin{array}{c} \mathbf{z}_2 \\ \hline \mathbf{z}_3 \\ \hline \vdots \\ \hline \mathbf{z}_n \end{array}\right] = \left[\begin{array}{c} \mathbf{b}_2 - \mathbf{R}_0\mathbf{l}_2 \\ \hline \mathbf{b}_3 - \mathbf{R}_0\mathbf{l}_3 \\ \hline \vdots \\ \hline \mathbf{b}_n - \mathbf{R}_0\mathbf{l}_n \end{array}\right]; \left[\begin{array}{c} \mathbf{A}_2 \\ \hline \mathbf{A}_3 \\ \hline \vdots \\ \hline \mathbf{A}_n \end{array}\right] = \left[\begin{array}{c|c|c} \dfrac{\partial(\mathbf{R}_0\mathbf{l}_2)}{\partial y} & \dfrac{\partial(\mathbf{R}_0\mathbf{l}_2)}{\partial p} & \dfrac{\partial(\mathbf{R}_0\mathbf{l}_2)}{\partial r} \\ \hline \dfrac{\partial(\mathbf{R}_0\mathbf{l}_3)}{\partial y} & \dfrac{\partial(\mathbf{R}_0\mathbf{l}_3)}{\partial p} & \dfrac{\partial(\mathbf{R}_0\mathbf{l}_3)}{\partial r} \\ \hline \vdots & \vdots & \vdots \\ \hline \dfrac{\partial(\mathbf{R}_0\mathbf{l}_n)}{\partial y} & \dfrac{\partial(\mathbf{R}_0\mathbf{l}_n)}{\partial p} & \dfrac{\partial(\mathbf{R}_0\mathbf{l}_n)}{\partial r} \end{array}\right]; \left[\begin{array}{c} \mathbf{v}_2 \\ \hline \mathbf{v}_3 \\ \hline \vdots \\ \hline \mathbf{v}_n \end{array}\right] = \left[\begin{array}{c} \mathbf{e}_{\mathbf{b}_2} - \mathbf{R}_0\mathbf{e}_{\mathbf{l}_2} \\ \hline \mathbf{e}_{\mathbf{b}_3} - \mathbf{R}_0\mathbf{e}_{\mathbf{l}_3} \\ \hline \vdots \\ \hline \mathbf{e}_{\mathbf{b}_n} - \mathbf{R}_0\mathbf{e}_{\mathbf{l}_n} \end{array}\right] \tag{3-11}$$

where **z** is the measurement vector; **A** is the design matrix; **v** is the measurement error vector. The model (3-11) describes the Least-Squares Attitude Determination approach (LSAD) (Lu 1995). The correction values for Euler angles associated to a rotation matrix $\mathbf{R}_0$ are computed by:

$$\begin{aligned} [\Delta y \quad \Delta p \quad \Delta r]^T &= -\left[\sum_{i=2}^{n} \mathbf{A}_i^T \mathbf{P}_i \mathbf{A}_i\right]^{-1} \times \left[\sum_{i=2}^{n} \mathbf{A}_i^T \mathbf{P}_i \mathbf{z}_i\right] \\ \mathbf{P}_i &= \left(\mathbf{R}_0^T Cov(\mathbf{l}_i)\mathbf{R}_0 + Cov(\mathbf{b}_i)\right)^{-1} \end{aligned} \tag{3-12}$$

where the short-hand notation $Cov(\cdot)$ denotes the error covariance matrix; **P** is the weight matrix determined by the measurement errors. A detailed derivation of the design matrix $\mathbf{A}_i$ can be seen in Appendix II. The least-squares adjustment proceeds until the correction values converge to a certain threshold or the maximal iteration number is reached.

The LSAD aims at determine the attitude of the ABF with respect to the LLF using the GPS carrier phase measurements. The measurement errors in both LLF and ABF are also taken into account. If the attitude dynamics can be described by a proper mathematic model or measured by other sensors, the LSAD model can be furthermore integrated with the attitude dynamics using proper data fusion techniques, such as Kalman filters, where the LSAD model serves as the measurement model. Related content will be presented in Chapter 4 and Chapter 5.

### 3.5.2 Direct attitude computation

Based on the definition of ABF, the coordinates of antenna 2 (see Figure 3-3) in the ABF can be expressed as $\mathbf{b}_2 = \begin{bmatrix} 0 & b_{12} & 0 \end{bmatrix}^T$, where $b_{12}$ is the baseline length from the master antenna to the slave antenna (antenna 2). Substituting the ABF coordinate of the slave antenna into (3-4) and using the orthogonality of the rotation matrix yields the LLF coordinate of the slave antenna (Lu 1995):

$$\underbrace{\begin{bmatrix} x_{2,l} \\ y_{2,l} \\ z_{2,l} \end{bmatrix}}_{\mathbf{l}_2} = b_{12} \begin{bmatrix} -c_p s_y \\ c_p c_y \\ s_p \end{bmatrix} \tag{3-13}$$

where the baseline vector of antenna 2 in LLF ($\mathbf{l}_2$) is expressed with the concrete three-dimensional components $[x_{2,l}, y_{2,l}, z_{2,l}]^T$. Then, the yaw angle and pitch angle can be directly calculated:

$$\begin{aligned} yaw &= -\tan^{-1}\left(\frac{x_{2,l}}{y_{2,l}}\right) \\ pitch &= \sin^{-1}\left(\frac{z_{2,l}}{b_{12}}\right) = \tan^{-1}\left(\frac{z_{2,l}}{\sqrt{x_{2,l}^2 + y_{2,l}^2}}\right) \end{aligned} \tag{3-14}$$

From both expressions of pitch it is clear that the pitch angle is acquirable using only the LLF coordinate of the slave antenna instead of using the baseline length $b_{12}$. This reveals a significant advantage of the direct attitude computation that the baseline length does not need to be measured in advance.

The direct attitude computation can also be expended to calculate the roll angle once three or more antennas are available. We can firstly rotate antenna 3 by yaw and pitch obtained from (3-14) in order to obtain the rotation matrix including roll:

$$\begin{bmatrix} x'_{3,l} \\ y'_{3,l} \\ z'_{3,l} \end{bmatrix} = \begin{bmatrix} 1 & 0 & 0 \\ 0 & c_p & s_p \\ 0 & -s_p & c_p \end{bmatrix} \begin{bmatrix} c_y & s_y & 0 \\ -s_y & c_y & 0 \\ 0 & 0 & 1 \end{bmatrix} \begin{bmatrix} x_{3,l} \\ y_{3,l} \\ z_{3,l} \end{bmatrix} \tag{3-15}$$

Then following relationship holds by employing the ABF coordinate of antenna 3:

$$\begin{bmatrix} x_{3,b} \\ y_{3,b} \\ 0 \end{bmatrix} = \begin{bmatrix} c_r & 0 & -s_r \\ 0 & 1 & 0 \\ s_r & 0 & c_r \end{bmatrix} \begin{bmatrix} x'_{3,l} \\ y'_{3,l} \\ z'_{3,l} \end{bmatrix} \tag{3-16}$$

where the scalars $x_{3,b}$ and $y_{3,b}$ represent the x- and y-coordinate of antenna 3 in the ABF and they do not need to be explicitly specified. From the zero-valued components we can simply derive the roll angle:

$$r = -\tan^{-1}\left( \frac{z'_{3,l}}{x'_{3,l}} \right) \tag{3-17}$$

The direct attitude computation and least-squares approaches apply to different scenarios. Even if the baselines are not measured in advance, the direct attitude computation can still yield the attitude results. However, it does not take all the measurements into calculation and hence leads to a sub-optimal solution (Lu 1995).

### 3.5.3 Attitude determination using a dual-antenna configuration

Three-dimensional Euler angles may not be concerned in some applications. For example in the maritime application, only the yaw angle (or heading angle) is of great interest. In these cases, the single-baseline configuration composed of two GPS antennas can fulfill the requirement. From such a configuration we can obtain yaw and pitch angles. The LSAD can be applied to this case with a slight modification. The DCM with a yaw-pitch sequence can be formulated as:

$$\mathbf{b}_2 = \mathbf{R}'_1\{p\}\mathbf{R}'_3\{y\}\mathbf{l}_2 = \begin{bmatrix} c_y & s_y & 0 \\ -s_y c_p & c_p c_y & s_p \\ s_y s_p & -c_y s_p & c_p \end{bmatrix} \mathbf{l}_2 \tag{3-18}$$

The LSAD model can be constructed as:

$$\mathbf{z}_2 = \mathbf{A}_2 \times \begin{bmatrix} \Delta y \\ \Delta p \end{bmatrix} + \mathbf{v}_2$$

with

$$\begin{aligned} &\mathbf{z}_2 = \mathbf{b}_2 - \mathbf{R}_0 \mathbf{l}_2 \\ &\mathbf{A}_2 = \left[ \frac{\partial(\mathbf{R}_0 \mathbf{l}_2)}{\partial y} \;\vdots\; \frac{\partial(\mathbf{R}_0 \mathbf{l}_2)}{\partial p} \right] \\ &\mathbf{v}_2 = \mathbf{e}_{\mathbf{b}_2} - \mathbf{R}_0 \mathbf{e}_{\mathbf{l}_2} \end{aligned} \tag{3-19}$$

The derivation of the design matrix $\mathbf{A}_2$ can be is found in Appendix III. This model can be solved by least-squares adjustment. Besides that, the direct attitude computation can be directly used for the single-baseline case, which has been clearly shown in Eq. (3-14).

### 3.5.4 Error due to non-rigidity of antenna body frame

A GPS multi-antenna system often aims at measuring the attitude of a vehicle body frame, whereas its output is the attitude of the ABF. If both of the ABF and vehicle body frame are rigid, the attitude derivations between both frames can be measured *a priori*, so that the attitude information based on the ABF can be simply related to that on the vehicle body frame. If the ABF loses the rigidity, the attitude information cannot correctly describe the attitude of the vehicle.

Regarding to an airplane, the attitude of the fuselage is of great interest. If the antennas are mounted on the wings of the airplane, the vibration of the wings during the flight will bring in errors into the pre-measured ABF. In order to identify this problem, we use a simple example illustrated in Figure 3-6. We assume that two antennas are mounted on the wings with same baseline length $l$ to the middle line of fuselage. As explained before, a dual-antenna configuration can measure the pitch and yaw of the ABF and we will only consider the pitch angle in this example. Referring to the airplane, the pitch angle of the ABF corresponds to the roll angle of the airplane body. The wings at rest have an elevation angle $\theta$ with respect to the level plane. The flexure of wings is expressed using deviation angles $\alpha$ and $\beta$, respectively.

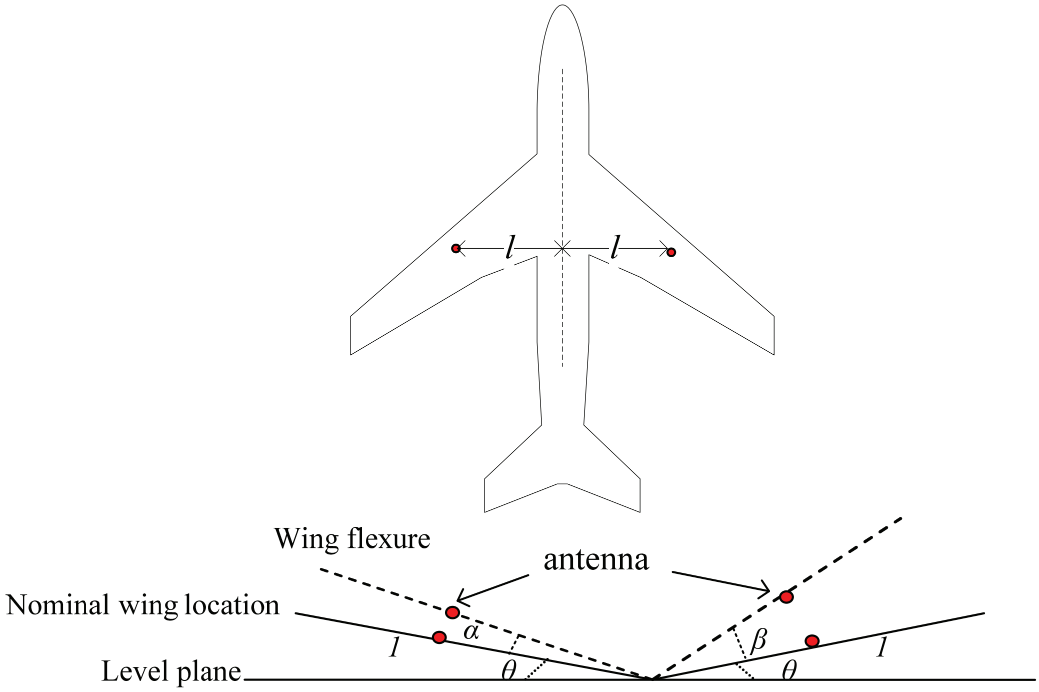

**Figure 3-6 An illustration of the airplane with two GPS antennas on the wings**

It is assumed that both antennas are levelly mounted on the wings in a stationary state, yielding a zero-valued roll angle for the body frame of fuselage (namely also zero-valued pitch angle for the ABF). As reported in the literature, "most of fuselage is fairly rigid; however, the position of the wing tips of an aircraft may move more than a meter vertically relative to the fuselage during flight. Most of the variation of wing flexure is due to changes in fuel loading, but turbulence and varying flight conditions also cause wing movements" (Gustafsson et al. 1996 ). For a wing length of 10 meters, one meter vertical movement corresponds to about 5 degrees for $\alpha$ and $\beta$ angles. Assuming the wings have a flexure angle ranging from -5 to 5 degrees, the roll angle will deviate from its nominal value as follows:

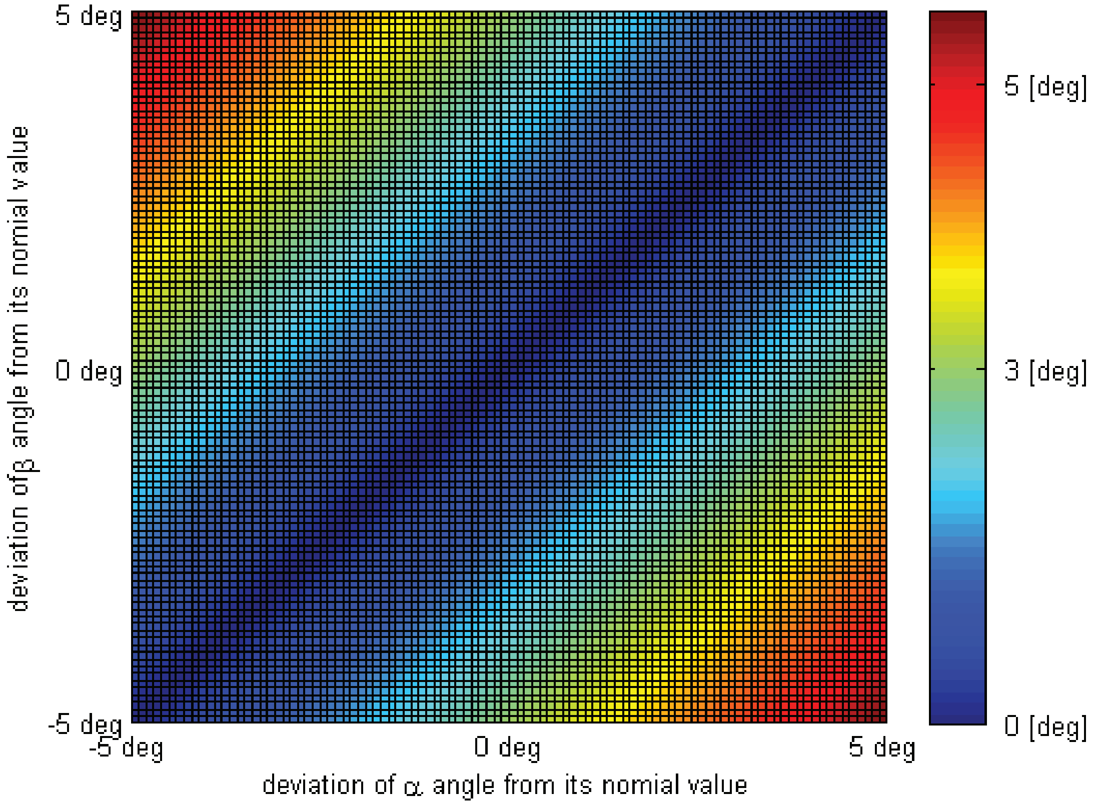

**Figure 3-7 Deviation of roll angle from its nomial value**

It can be seen that the wing flexure can result in several degrees errors to the attitude related to the fuselage. It is therefore recommended to mount the antennas on the fuselage instead of on the wing tips.

## 3.6 A toolbox for GPS-based attitude determination

A MATLAB toolbox has been implemented to process the data from multiple GPS antennas (Dai et al. 2009b). This toolbox is used for post-processing of the RINEX data from all receivers. The interface of the toolbox is depicted below:

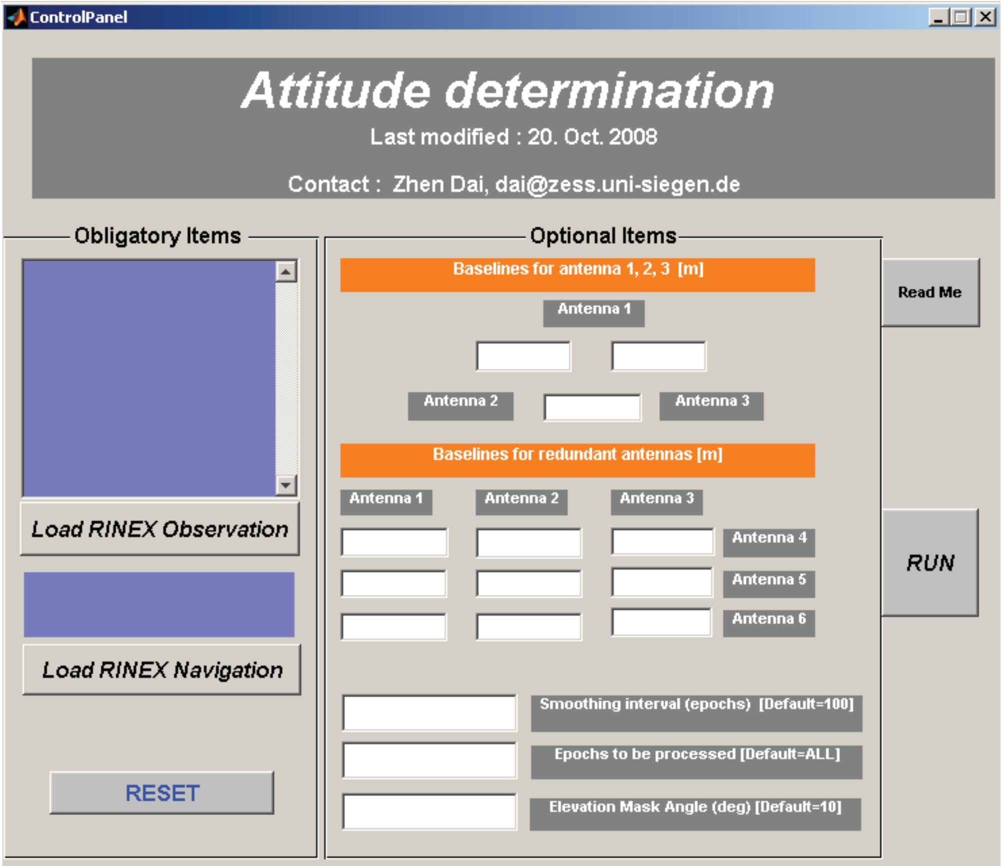

**Figure 3-8: MATLAB Toolbox for attitude determination**

Attitude determination starts with the data synchronization. The GPS measurements of all antennas at the same receipt epoch are picked up to implement the data synchronization. The position of the master antenna should be calculated prior to performing the differential positioning. If there is no ground station available, the position of the master antenna can be computed by single-point positioning. Although the associated positioning accuracy can range from several meters to several tens of meters with Selective Availability (SA) turned off, it will only affect the LLF of the slave antennas at millimeter level (Lu 1995). It implies that the accuracy of the attitude parameters will not be significantly degraded due to the application of SPP to the master antenna. A proof to this conclusion can be found in Appendix IV.

Having known the position of the master antenna, the differential positioning can be performed in order to derive the baseline vectors between antennas. For this purpose, we need to resolve the integer phase ambiguities and detect the phase cycle-slips. Both techniques have been addressed in chapter 2.

In order to apply the LSAD, the ABF should be fixed at first. With two or three antennas, the ABF can be determined based on the definition given in chapter 3.1, whereby the length of each master-slave antenna pair should be accurately measured. Once more than three antennas are available, the redundant antenna(s) can be projected into the ABF. For this operation, the distances from redundant antenna(s) to the first three antennas should be given as well. Nevertheless, there will be a multiple-solution problem, since we cannot uniquely identify whether the redundant antenna(s) are above or under the ABF. However, taking the redundant antenna(s) into calculation should yield compatible attitude parameters with those from other algorithms. For this reason, the attitude parameters can be firstly resolved by applying the direct attitude computation or the LSAD involving only the first three antennas. The computed attitude parameters are then employed to solve this multiple-solution problem. Note that the ABF needs to be fixed only one time before the experiment starts.

The flowchart for the data processing in a GPS multi-antenna system is presented below:

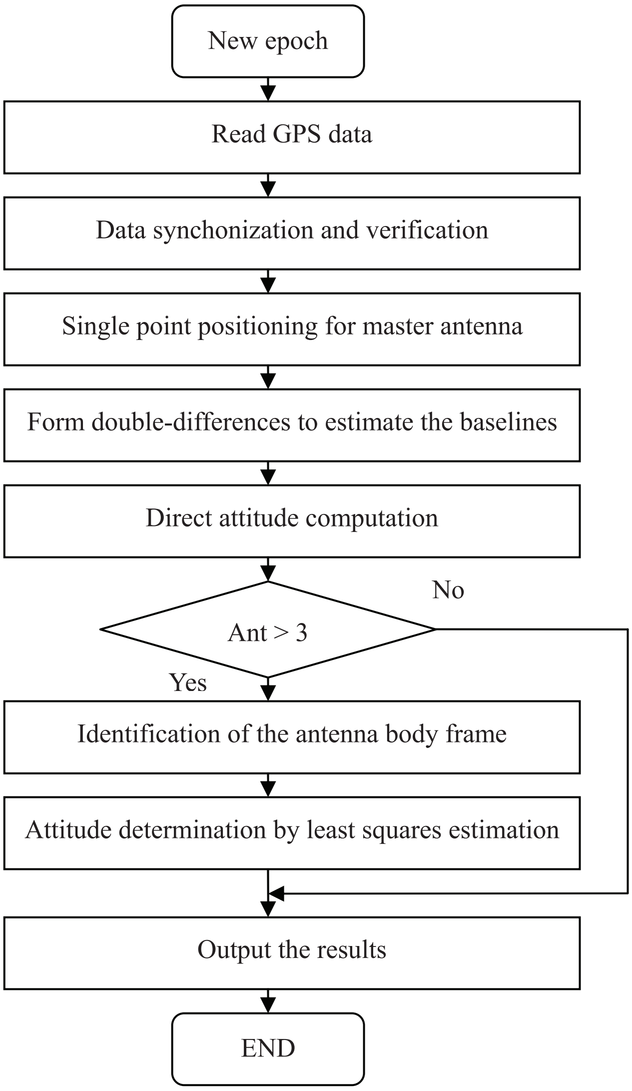

**Figure 3-9: Flowchart for attitude determination algorithm**

## 3.7 Experimental results

A static experiment has been carried out in order to show the performance of the GPS multi-antenna system. The hardware configuration is shown in Figure 3-10.

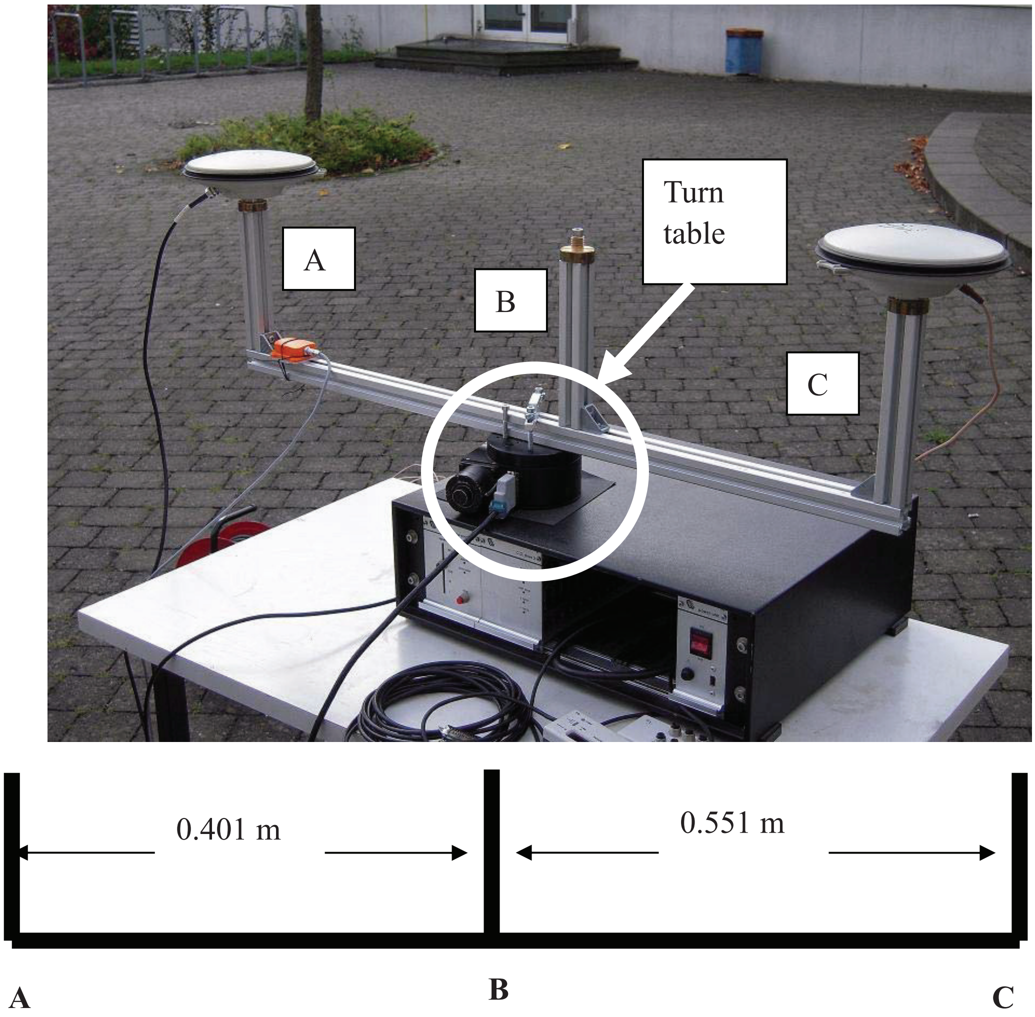

**Figure 3-10: Test devices for GPS dual-antenna experiments**

A frame with three antenna holders is fixed on a turn table. The space between antenna holders A, B and C are labeled in the lower part of Figure 3-10. The length of the baseline is determined using differential positioning for more than one hour observation. Two dual-frequency receiver/antenna pairs are used in this experiment. One is a Novatel DL-4 receiver with a GPS-702 antenna, the other one is a Novatel ProPak-V3 receiver with a GPS-702 GG antenna.

In the static experiment, the turn table is switched off and the Euler angles should be constant values. For each baseline, we record the measurement for 20 minutes at 5Hz sampling rate. Integer ambiguities should be resolved prior to the attitude computation. To do this, the rapid dual-frequency ambiguity resolution technique is applied (Horemuž and Sjöberg 2002). The Novatel receivers output the C1 (on L1 signal) and P2 (on L2 signal) code measurements with a root mean square error of 30 cm, which allows the instantaneous ambiguity resolution. After smoothing the code measurements with carrier phase for 400 epochs, the ambiguities can be correctly resolved epoch by epoch. The satellite constellation tracked by the master antenna at the first epoch for the long-baseline (0.952 m) experiment is illustrated in Figure 3-11. The red satellites are used for the attitude determination, whereas the bright blue satellites are excluded due to their low elevation angles. The key satellite is satellite PRN 6 having highest elevation angle. Considering the short distances between both antennas, the slave antenna is also tracking the same satellites.

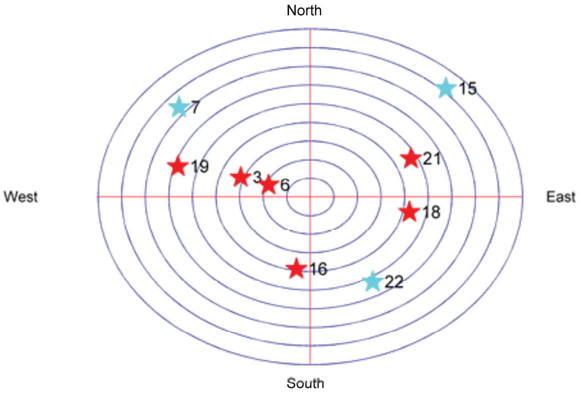

**Figure 3-11: Satellite constellation at the first epoch of experiment**

The least-squares residuals for each double-differenced carrier phase measurement can be used to judge whether or not the integer ambiguities are correctly resolved. Due to the close-spaced antennas, the atmospheric errors can be almost eliminated. Without large multipath errors, the correctly resolved integer ambiguities should lead to Gaussian-form carrier phase residuals. Figure 3-12 shows the residuals for three double-differenced carrier phase measurements:

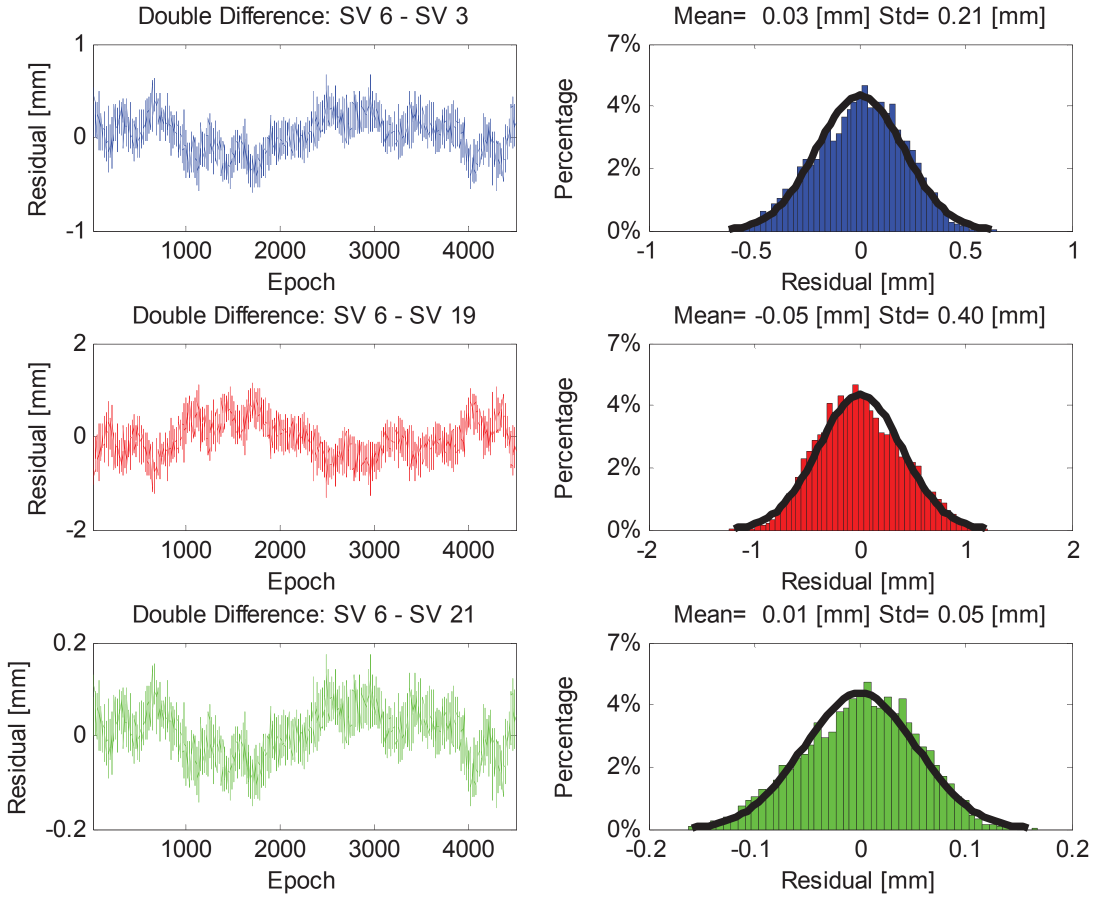

**Figure 3-12: Least-squares residuals with correctly resolved integer ambiguities**

As indicated by Figure 3-12, the double-differenced carrier phase residuals approximately obey zero-mean Gaussian distributions with standard deviations at millimeter level. If the ambiguities are not correctly resolved, the Gaussian-form error distribution will no longer exist. Given below are the residuals once the ambiguity PRN 6-PRN 19 is deliberately added with one cycle.

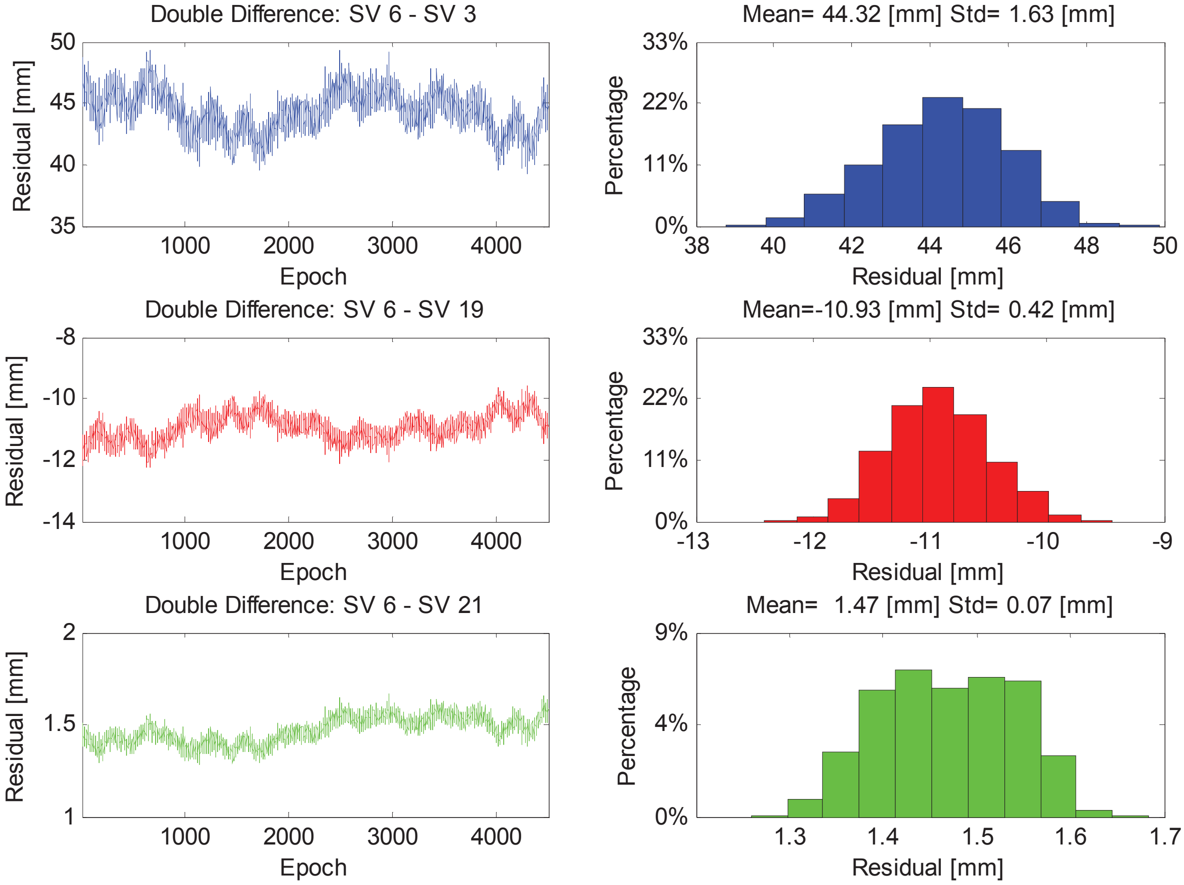

**Figure 3-13: Least-squares residuals with incorrectly resolved ambiguities**

Although a one-cycle shift in the ambiguity contributes only 20 centimeters error to the measurements, it brings large biases into the residuals. Besides, the pair SV6-SV21 (in green) clearly lost the Gaussian-form distribution.

Based on the correctly resolved integer ambiguities, the baseline vector between both antennas can be estimated, and then the LSAD approach is carried out to calculate the yaw and pitch angles. Both angles estimated at the first 2500 epochs are depicted in Figure 3-14. Note that there might be some small variation of both angles when changing the antennas from one holder to another.

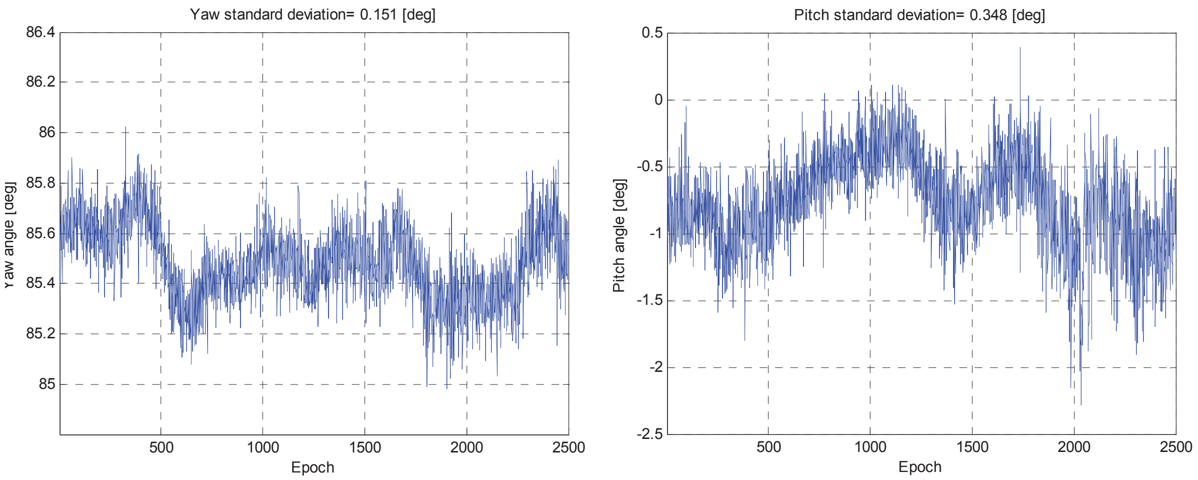

Results of long baseline

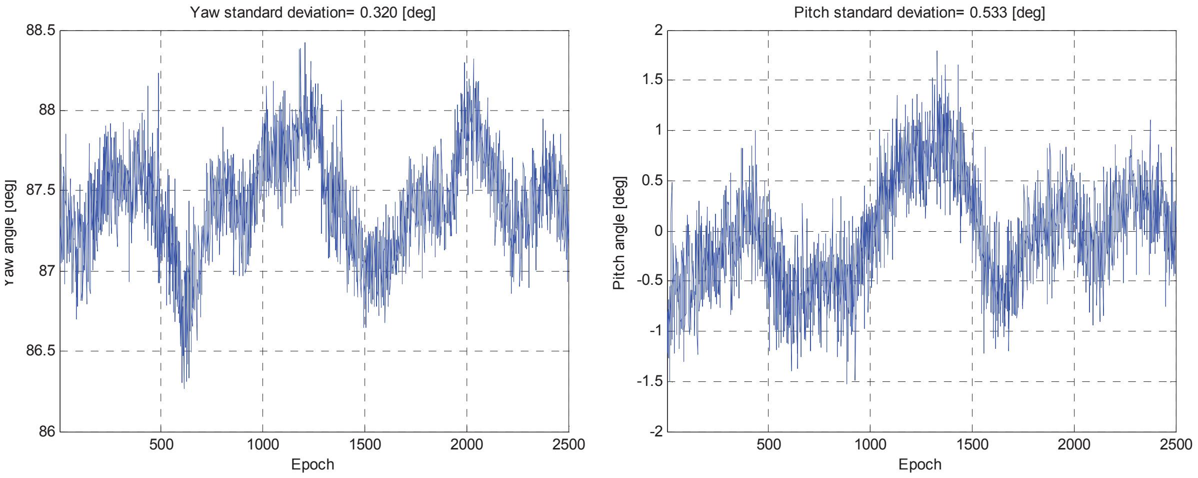

Results of medium baseline

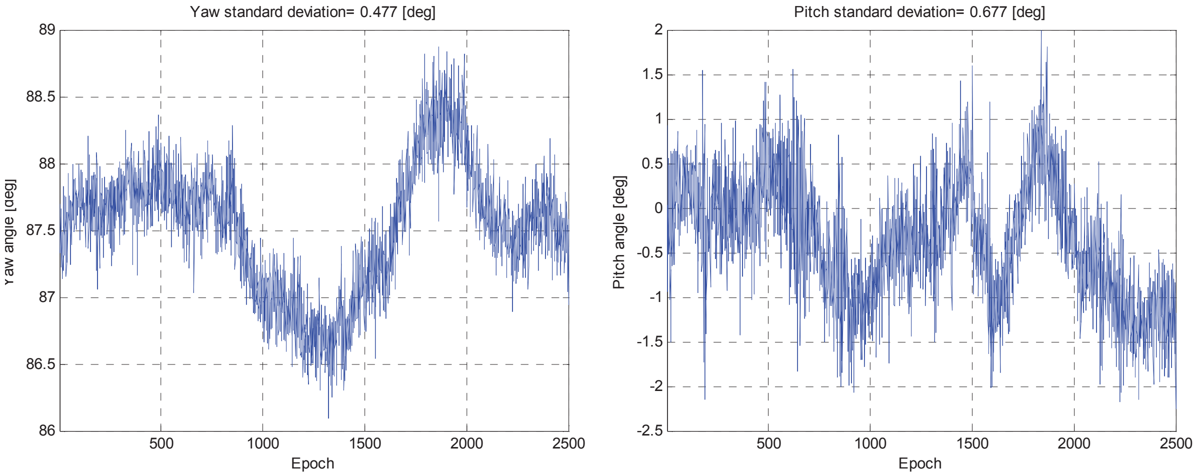

Results of short baseline

**Figure 3-14: Yaw and pitch values with correctly resolved ambiguities**

Comparing the standard deviations presented at the head of each figure it can be seen that, a longer baseline yields a smaller standard deviation of the attitude error. A detailed illustration showing the relation between the attitude precision and baseline length will be given in chapter 6.

The baseline length is a fixed value and can serve as an evaluation of the positioning accuracy. The estimated baseline lengths are given in Figure 3-15.

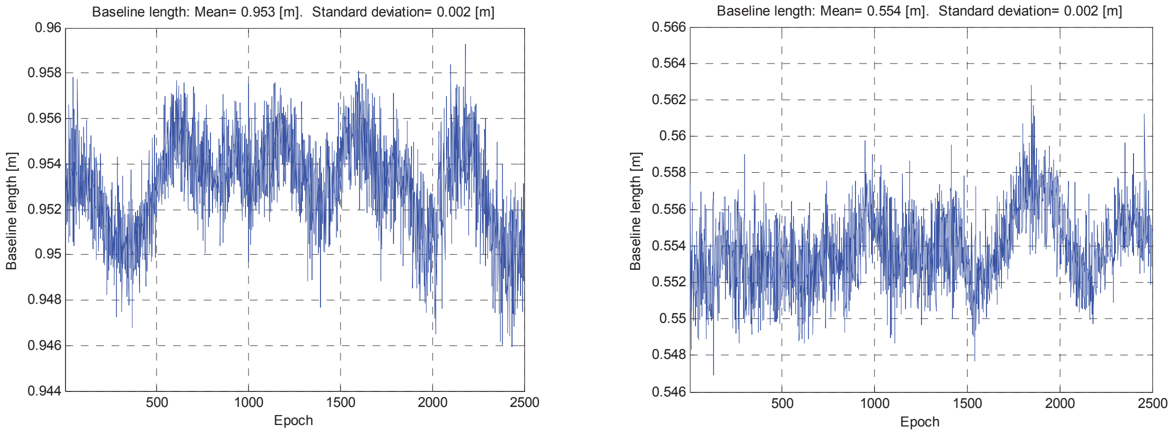

Long baseline

Medium baseline

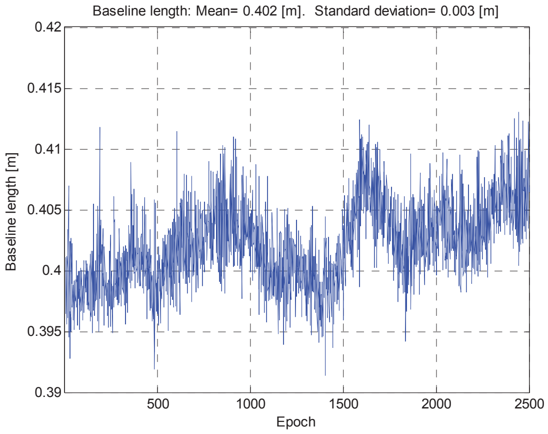

Short baseline

**Figure 3-15: Estimated baselines with correctly resolved ambiguities**

Figure 3-15 shows the compatibility between the estimated baseline lengths and the associated reference values given in Figure 3-10. The standard deviation of the estimated baseline lengths is of millimeter level.

When the turn table is turned on, it forces the antennas to rotate at a angular rate set in advance. The turn table used in this experiment does not allow a digital display and hence the accurate angular rate is not known. Nevertheless, different rotation rates can be clearly seen from the increment of the yaw angle. The curves in Figure 3-16 represent the variation of yaw angle until it completes the first 360 degrees. The short antenna baseline (0.401 m) is used in this experiment. Three different angular rates are set and the corresponding results are depicted in different colors, respectively. As we only want to show the increment of yaw angle, all the results are shifted with respect to the first epoch.

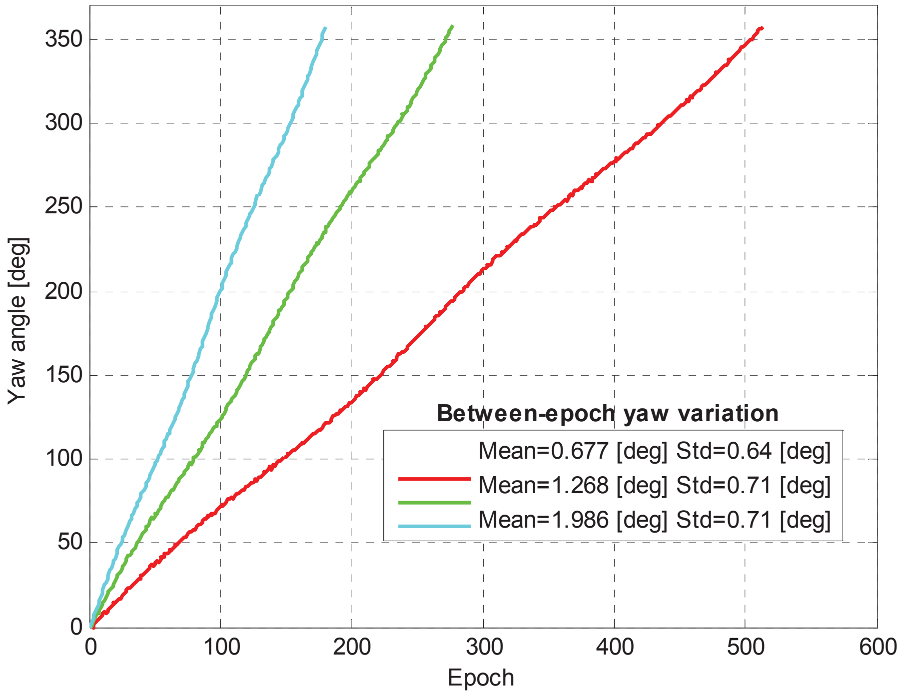

**Figure 3-16: Estimated yaw values under different angular rates**

Different angular rates can be clearly seen from the inclination angles of the curves. In Figure 3-16, the statistical results for between-epoch yaw variations are also presented. Different mean values indicate different angular rates. Similar standard deviations are due to the same baseline length used in the experiment.

## 3.8 Conclusions

In this chapter, techniques for attitude determination using multiple GPS antennas have been presented. Euler angles reflect the misalignment between the LLF and the ABF, whereby both frames refer to the coordinates of slave antennas with respect to the master antenna. The ABF coordinates are constant values for a rigid platform, whereas the LLF coordinates are determined based on the precise baseline estimation using RTK technique. By linearizing DCM with respect to Euler angles we have the LSAD for optimal attitude estimates. By exploiting the properties of the ABF we have the direct attitude computation approach for a fast but sub-optimal attitude solution. With three or more antennas, three dimensional Euler angles can be obtained. With two antennas, the yaw and pitch angles are resolvable. The baseline length is a crucial limiting factor for the precision of estimated attitude parameters. Considering the overall structure of the thesis, a detailed interpretation of limiting factors for attitude parameters will be given in chapter 6.

# 4. GPS based attitude determination using Kalman filters and a constant angular rate model

In chapter 3, the mathematic models for GPS multi-antenna systems have been presented. They serve as the measurement model to determine the attitude parameters epoch by epoch from GPS measurements. However, it does not take information of attitude dynamics into account. If gyroscopes are available, attitude dynamics can be acquired and a dynamic model can be constructed. This is known as the integration of GPS and gyros for attitude determination (Barrows et al. 1996; Hirokawa and Ebinuma 2009; Knedlik et al. 2009). If the inertial sensors are not available, it will be difficult to gain the knowledge about vehicle dynamics for high-maneuvering vehicles. However, the dynamic model can be described by a random walk process in some specific applications (El-Mowafy and Mohamed 2005). The use of such a dynamic model normally needs the following prerequisites:

1. The airplane is of low maneuver, for example, a civilian airplane.
2. The GPS sampling rate is high enough, for example, higher than 5 Hz.
3. The airplane has to maintain a relatively level and stable flight in order to fulfill the requirement of some particular experiments, for example, the PAMIR airplane in the bistatic SAR mission.

In comparison with the LSAD stated in chapter 3, introducing a dynamic model can improve the performance in at least the following cases. The first case arises when the GPS observation is lost or cycle-slip occurs. In these cases, the phase ambiguity resolution or cycle-slip correction may not be accomplished within one epoch. Consequently the GPS phase measurements cannot be used and the dynamic model is the only source to obtain the attitude information. Another superiority of introducing a dynamic model manifests itself in the accuracy improvement. In a GPS multi-antenna system, the quality of attitude parameters will be restricted by many factors, for example the baseline lengths between the antennas. A longer baseline results in a higher precision. Nevertheless, long baselines are usually not applicable in the real aviation application due to the limited place on the fuselage. In this case, the improvement of accuracy can benefit from an appropriate dynamic model.

Starting from 1960s, the Kalman Filter (KF) becomes one of the most widely used methods for sensor data fusion. The Kalman filter has initially been developed for linear systems. However, most of engineering applications have nonlinear measurements or dynamic models. Thus, some modified versions have been implemented in order to adapt the Kalman filter to nonlinear systems, including the Extended Kalman Filter (EKF), the Iterated

Extended Kalman Filter (IEKF), the Second-Order Extended Kalman Filter (SOEFK) and the Unscented Kalman Filter (UKF), etc. The utilization of the EKF in the GPS-based attitude determination system with a random walk process have been investigated (El-Mowafy and Mohamed 2005; Wang 2003). The use of other nonlinear filters is still missing and hence will be explored in this chapter and chapter 5.

## 4.1 Fundamentals of nonlinear Kalman filtering

A discrete-time Kalman type filter comprises a dynamic model and a measurement model, as formulated below:

$$\text{Dynamic model}: \mathbf{x}_k = f_{k-1}\left(\mathbf{x}_{k-1}\right) + g_{k-1}\left(\mathbf{w}_{k-1}\right) \tag{4-1}$$

$$\text{Measurement model: } \mathbf{z}_k = h_k\left(\mathbf{x}_k, \mathbf{v}_k\right) \tag{4-2}$$

where **x** is the state vector to be estimated; *k* is the time variable; **z** is the vector of observables; $f(\cdot)$ represents the state transition function; $h(\cdot)$ is the observation function; $g(\cdot)$ is the noise gain function; **w** indicates the process noise; **v** reflects the measurement noise. The process and measurement noise are assumed to be time-uncorrelated white Gaussian noise and have the covariance matrices $\mathbf{Q}_k$ and $\mathbf{R}_k$, respectively:

$$\mathbf{w}_k \sim N\left(0, \mathbf{Q}_k\right) \text{ and } \mathbf{v}_k \sim N(0, \mathbf{R}_k) \tag{4-3}$$

In practice, the adaption of Kalman filter to nonlinear systems will lose the accuracy due to the inherent approximation. The approximations can be made either to the nonlinear models or to the state error distributions. Both approaches will be discussed in section 4.1.1 and 4.1.2.

### 4.1.1 Nonlinear Kalman filters with model approximation

The nonlinear model can be approximated by truncating its Taylor series expansion:

$$h(x_k) = h(x_k') + \left.\frac{\partial h}{\partial x}\right|_{x=x_k'} \left(x_k - x_k'\right) + \frac{1}{2}\left(x_k - x_k'\right)^T \left.\frac{\partial^2 h}{\partial x^2}\right|_{x=x_k'} \left(x_k - x_k'\right) + H.O.T \tag{4-4}$$

where $x_k'$ is the reference point for the Taylor series expansion; short-hand notation *H.O.T* stands for higher order terms. The discrepancy between the approximated and original model lies in the following aspects:

- The order of expansion

Assuming that the Taylor expansion is carried out in the same computational environment and the reference point is fixed, the accuracy of the approximated Taylor series depends on the orders of expansion applied. The most computationally efficient way is to truncate the second and the higher orders, leaving only the first order term. The conventional EKF is developed based on this idea. Once the nonlinearity is high, a first order truncation might lead to large remaining errors. In this case, we can also take the second order term into consideration, namely the SOEKF.

- The selected reference point for expanding the Taylor series

The closer the reference point is to the true value, the smaller the error due to the nonlinearity. If the nominal values are known, the linearization can be performed at the nominal values. This is referred to as the Linearized Kalman Filter (Simon 2006). Without the nominal values, the reference points can be initially chosen at the *a priori* estimates $x_k^-$. When the measurements of epoch *k* are available, the *a posteriori* estimates $x_k^+$ can be obtained. Theoretically speaking, choosing $x_k^+$ instead of $x_k^-$ as the linearization reference point might reduce the linearization error, because the measurements of current epoch are taken into consideration. This procedure can be iteratively applied to gradually improve the accuracy of the reference point. The IEKF is then developed based on this idea.

- Round-off error

The round-off error is caused by the limited number of significant digits supported by a processor. It is subject to the digital processors and hence will not be considered in this thesis.

### 4.1.2 Nonlinear Kalman filters without model approximation

Unlike the EKFs approximating the nonlinear model, some other approaches attempt to estimate the error distributions of the states using a set of representative points. These representative points will go through the actual nonlinear model, and then the mean value and the error covariance matrix can be calculated from the propagated representative points. These approaches are based on the assumption that the accuracy loss due to the model linearization might be larger than the accuracy loss due to the approximation of the Gaussian distribution (Simon 2006). Depending on the selection criteria of the representative points, we have the UKF and Monte-Carlo filter. In the UKF, the representative points are picked up in a deterministic way and always termed as “sigma points” (Julier et al. 2000). The way of collecting the sigma points determines that the UKF is dedicated to the systems with Gaussian form errors. The Monte-Carlo filter randomly generates the representative points so that it can theoretically fit any form of error distribution. Nevertheless, the excellent performance of Monte-Carlo filter relies on a great number of representative points, so the computational expense is remarkably increased and hence still challenges the real-time applications. We therefore mainly consider the UKF in this thesis.

## 4.2 Constant angular rate model

The PAMIR airplane always shows a relatively stable flying status, not only because of its own dynamic properties, but also due to the requirement of bistatic SAR experiments. Thus, we can use a constant angular rate model to approximate its attitude dynamics. According to this model, the state vector contains not only the Euler angles (yaw, pitch and roll) but also their corresponding angular rates:

$$\mathbf{x} = \begin{bmatrix} y & p & r & \dot{y} & \dot{p} & \dot{r} \end{bmatrix}^T \tag{4-5}$$

The discrete-time random-walk process can be expressed as:

$$\mathbf{x}_k = \mathbf{F}_{k-1}\mathbf{x}_{k-1} + \mathbf{G}_{k-1}\mathbf{w}_{k-1} \tag{4-6}$$

In order to evaluate the process noise, we can at first consider a one-dimensional case regarding the yaw angle for simplicity. In a constant angular rate model, the angular acceleration is treated as the noise, and hence it is also referred to as the white noise acceleration model (Bar-Shalom et al. 2001). The angular acceleration is related to the angle and angular rate in a discrete-time as follows:

$$\underbrace{\begin{bmatrix} y \\ \dot{y} \end{bmatrix}_k}_{\mathbf{x}_k} = \underbrace{\begin{bmatrix} 1 & \Delta t \\ 0 & 1 \end{bmatrix}}_{\mathbf{F}_{k-1}} \underbrace{\begin{bmatrix} y \\ \dot{y} \end{bmatrix}_{k-1}}_{\mathbf{x}_{k-1}} + \underbrace{\begin{bmatrix} 1/2 \cdot \Delta t^2 \\ \Delta t \end{bmatrix}}_{\mathbf{G}_{k-1}} \underbrace{\ddot{y}_{k-1}}_{\mathbf{w}_{k-1}} \tag{4-7}$$

where $\Delta t$ is the sampling interval. Expending (4-7) to three-dimensional Euler angles and ignoring the correlation between different angular accelerations of Euler angles we have:

$$\begin{gathered} \mathbf{Q}_k = diag\left(\sigma_{\ddot{y}}^2, \sigma_{\ddot{p}}^2, \sigma_{\ddot{r}}^2\right)_k \\ \mathbf{G}_k = \begin{bmatrix} \frac{1}{2}\Delta t^2 \cdot \mathbf{I}_{3\times3} \\ \Delta t \cdot \mathbf{I}_{3\times3} \end{bmatrix} \end{gathered} \tag{4-8}$$

In order to define **Q**, we need the *a priori* knowledge of the standard deviation of each angular acceleration.

## 4.3 An extended Kalman filter for dynamic attitude determination

The routine of an EKF starts with the linearization of the dynamic and measurement models. At epoch $k$, the dynamic model is linearized around the *a posteriori* state estimates at last epoch (denoted by $\hat{\mathbf{x}}_{k-1}^{+}$) and the measurement model is linearized around the *a priori* state estimates at current epoch (denoted by $\hat{\mathbf{x}}_{k}^{-}$), so that the nonlinear relation $f(\cdot)$ and $h(\cdot)$ can be replaced by the Jacobian matrices **F** and **H**, respectively. The time update and measurement update procedures can be formulated as follows (Simon 2006):

*Initialization:*

$$\hat{\mathbf{x}}_0^+ = E\left(\mathbf{x}_0\right) \tag{4-9}$$

$$\mathbf{P}_0^+ = E\left[\left(\mathbf{x}_0 - \hat{\mathbf{x}}_0^+\right)\left(\mathbf{x}_0 - \hat{\mathbf{x}}_0^+\right)^T\right] \tag{4-10}$$

*Time update:*

$$\hat{\mathbf{x}}_k^- = f_{k-1}\left(\hat{\mathbf{x}}_{k-1}^+\right) \tag{4-11}$$

$$\begin{aligned} \mathbf{F}_{k\text{-}1} &= \left.\frac{\partial f_{k-1}}{\partial x}\right|_{\hat{\mathbf{x}}_{k-1}^+} \\ \mathbf{P}_k^- &= \mathbf{F}_{k\text{-}1}\mathbf{P}_{k\text{-}1}^+\mathbf{F}_{k\text{-}1}^T + \mathbf{G}_{k-1}\mathbf{Q}_{k\text{-}1}\mathbf{G}_{k-1}^T \end{aligned} \tag{4-12}$$

*Measurement update:*

$$\begin{aligned} \mathbf{H}_k &= \left.\frac{\partial h_k}{\partial x}\right|_{\hat{\mathbf{x}}_k^-} \\ \mathbf{K}_k &= \mathbf{P}_k^-\mathbf{H}_k^T\left(\mathbf{H}_k\mathbf{P}_k^-\mathbf{H}_k^T + \mathbf{R}_k\right)^{-1} \end{aligned} \tag{4-13}$$

$$\begin{aligned} \hat{\mathbf{x}}_k^+ &= \hat{\mathbf{x}}_k^- + \mathbf{K}_k\left[\mathbf{z}_k - h_k\left(\hat{\mathbf{x}}_k^-\right)\right] \\ &= \hat{\mathbf{x}}_k^- + \mathbf{K}_k\mathbf{s}_k \end{aligned} \tag{4-14}$$

$$\mathbf{P}_k^+ = \left(\mathbf{I} - \mathbf{K}_k\mathbf{H}_k\right)\mathbf{P}_k^-\left(\mathbf{I} - \mathbf{K}_k\mathbf{H}_k\right)^T + \mathbf{K}_k\mathbf{R}_k\mathbf{K}_k^T \tag{4-15}$$

where **P** represents the covariance matrix of the states; **K** is the Kalman gain; **s** is the innovation vector. The formula (4-15) is the Joseph stabilized form of covariance measurement update. This form, however, can also be simplified to:

$$\mathbf{P}_k^+ = \left(\mathbf{I} - \mathbf{K}_k\mathbf{H}_k\right)\mathbf{P}_k^- \tag{4-16}$$

Both formulations are actually equivalent in mathematics. However, (4-15) guarantees that $\mathbf{P}_k^+$ is always symmetric positive definite, as long as $\mathbf{P}_k^-$ is symmetric positive definite (Simon 2006). In practice, the Kalman gain might have numerical errors from the computation, for example, due to the limited computational compatibility of the processor. In (4-16), numerical error of Kalman gain might lead $\mathbf{P}_k^+$ to be non-positive definite, even if the $\mathbf{P}_k^-$ is symmetric positive definite. For these reasons, (4-15) is more robust to the Kalman gain errors and hence can improve the stability.

When using a triple-antenna configuration, we have the corresponding parameters for the EKF:

$$\mathbf{H}_k = \begin{bmatrix} \dfrac{\partial(\mathbf{R}_c\mathbf{l}_2)}{\partial y} & \dfrac{\partial(\mathbf{R}_c\mathbf{l}_2)}{\partial p} & \dfrac{\partial(\mathbf{R}_c\mathbf{l}_2)}{\partial r} & \mathbf{O}_{3\times3} \\ \dfrac{\partial(\mathbf{R}_c\mathbf{l}_3)}{\partial y} & \dfrac{\partial(\mathbf{R}_c\mathbf{l}_3)}{\partial p} & \dfrac{\partial(\mathbf{R}_c\mathbf{l}_3)}{\partial r} & \mathbf{O}_{3\times3} \end{bmatrix}$$

$$\mathbf{x}_k = \begin{bmatrix} y & p & r & \dot{y} & \dot{p} & \dot{r} \end{bmatrix}_k^T \tag{4-17}$$

$$\mathbf{s}_k = \begin{bmatrix} \mathbf{R}_c\mathbf{l}_2 - \mathbf{b}_2 \\ \hdashline \mathbf{R}_c\mathbf{l}_3 - \mathbf{b}_3 \end{bmatrix}_k$$

where $\mathbf{R}_c$ is the rotation matrix computed at the *a priori* estimates of Euler angles. $\mathbf{R}_c$ should be distinguished from the measurement error covariance matrix **R** without the subscript. From the form of **H** it can be seen that the measurement model of the Kalman filter actually comes from the LSAD approach introduced in section 3.5.1.

Referring to (4-17), the measurement vector is the LLF coordinates of each slave antenna (El-Mowafy and Mohamed 2005; Wang 2003). Another form of the measurement vector directly employs the carrier phase measurements of all antennas (Hirokawa and Ebinuma 2009; Knedlik et al. 2009). This allows an easier design of the measurement error covariance matrix **R** since the carrier phase noise is usually considered as a time-uncorrelated Gaussian white noise. The system based on this model might possibly work with less than 4 common satellites and provides an integrity monitoring for GPS measurements. However, the matrices related to coordinate transformation will show up in the design matrix **H**. This will increase the dimension of design matrix **H**, leave difficulties for linearization and lead to increased computational time. Also, the coordinate transformation can be used in advance for ambiguity resolution before deriving matrix **H** (Park et al. 1996; Park and Kim 1998). In this case, it is then a duplicated operation to perform the coordinate transformation again in matrix **H**. In this thesis, we will focus on the use of model (4-17).

The measurement errors are contained in both ABF and LLF. The antenna position in the ABF can be precisely determined in the calibration procedure, and hence antenna position errors in the LLF are the dominant errors. The error covariance matrix of the antenna position in the LLF can be obtained by analyzing the error propagation from the GPS measurement domain to the position domain. Considering the structure of the thesis, this derivation will be the detailed in chapter 6 from Eq. (6-3) to Eq. (6-8). Thus, the associated content is not shown here. Assuming that the error covariance matrix of antenna 2 and antenna 3 are already obtained, **R** can be initialized by:

$$\mathbf{R}_{t_0} = \eta \begin{bmatrix} Cov(\mathbf{l}_2)\big|_{t_0} & \mathbf{O}_{3\times3} \\ \mathbf{O}_{3\times3} & Cov(\mathbf{l}_3)\big|_{t_0} \end{bmatrix} \tag{4-18}$$

where $\mathbf{l}_2$ and $\mathbf{l}_3$ represent the LLF coordinates of both slave antennas, respectively; $\eta$ is a multiplication factor slightly larger than 1, because **R** is normally conservatively estimated in order to avoid the filter divergence; $t_0$ implies that the results are obtained at the starting epoch. For a short trajectory, the matrix **R** can be considered as a fixed value calculated at the first epoch. For a long trajectory, the matrix **R** should be calculated in a more rigorous way either epoch by epoch or with a specific period.

Based on the hardware configuration used in chapter 3, we also conduct a dynamic experiment, where the rotation of antennas is controlled by the turn table. In this experiment, the antennas rotate with a constant angular rate. The GPS data are collected with 10 Hz sampling rate. We use the LSAD and the EKF, respectively, to calculate the yaw and pitch angles.

The following parameters are used to tune the filter. The standard deviation of carrier phase noise is 2 mm. The matrix **R** is calculated based on the satellite geometry and the position of the master antenna at the first epoch (see Figure 3-11). To set the **Q** we use $\sigma_{\ddot{y}} = \sigma_{\ddot{p}} = 0.2\left[\mathrm{deg}/\Delta\mathrm{epoch}^2\right]$. In order to initialize **P**, the standard deviation of yaw and pitch are set as 0.2 degrees and 0.3 degrees, respectively, and the standard deviations of angular rates are set as 0.5 [deg/Δepoch] for both Euler angles. The yaw and pitch estimates are initialized using the LSAD results at the first epoch. The initial angular rates are calculated by averaging the between-epoch variations of yaw and pitch angles during the entire observation session.

In Figure 4-1, the yaw angle obtained from the EKF and the LSAD are presented and compared.

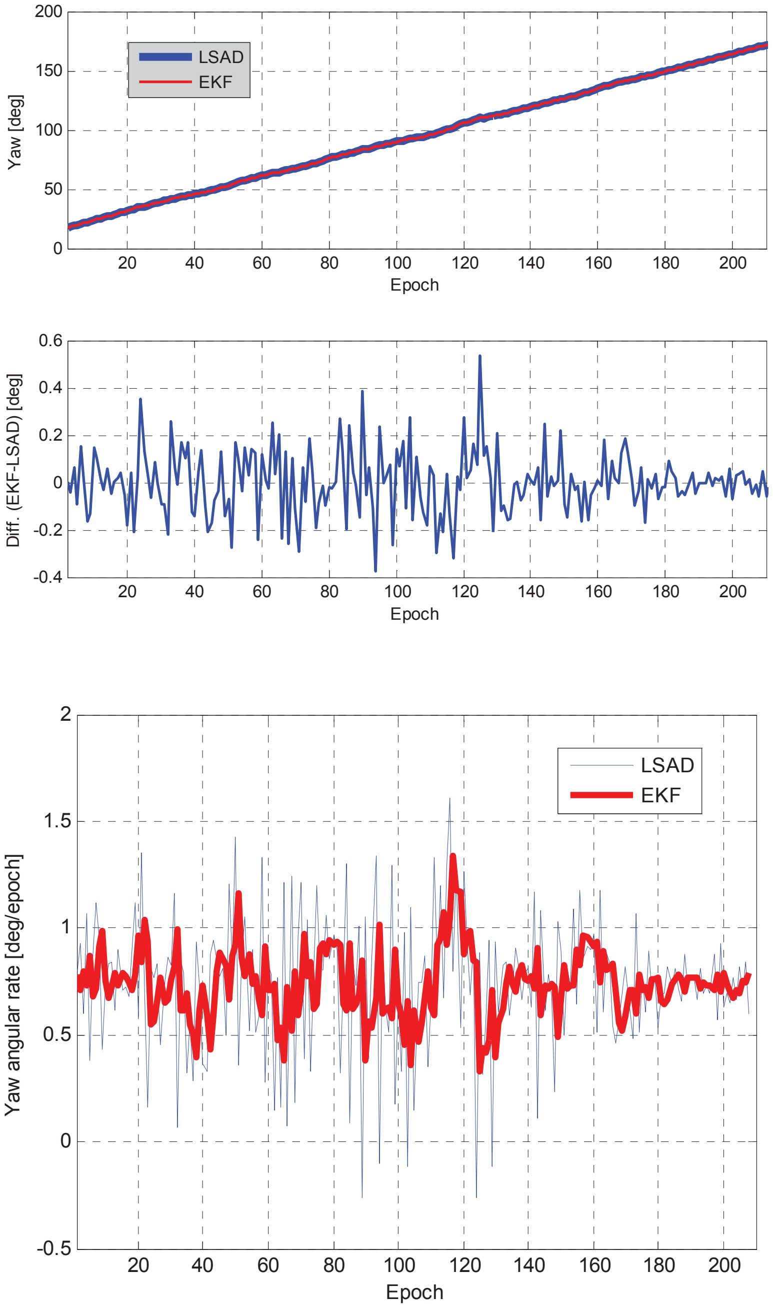

**Figure 4-1: Yaw angle and angular rates for the rotating frame**

In the upper figure, the differences in the estimated yaw angles are also presented in order to clearly distinguish the nearly overlapping curves. Figure 4-1 indicates that the angular rates obtained from the EKF are smoother than from the LSAD. It also implies the benefits of a constant angular rate model. In the experiment, the turn table also slightly vibrates in the vertical direction due to its mechanical properties, and consequently the pitch angle is not always a fixed value. We also present the estimated pitch angle and the angular rate in the following figures.

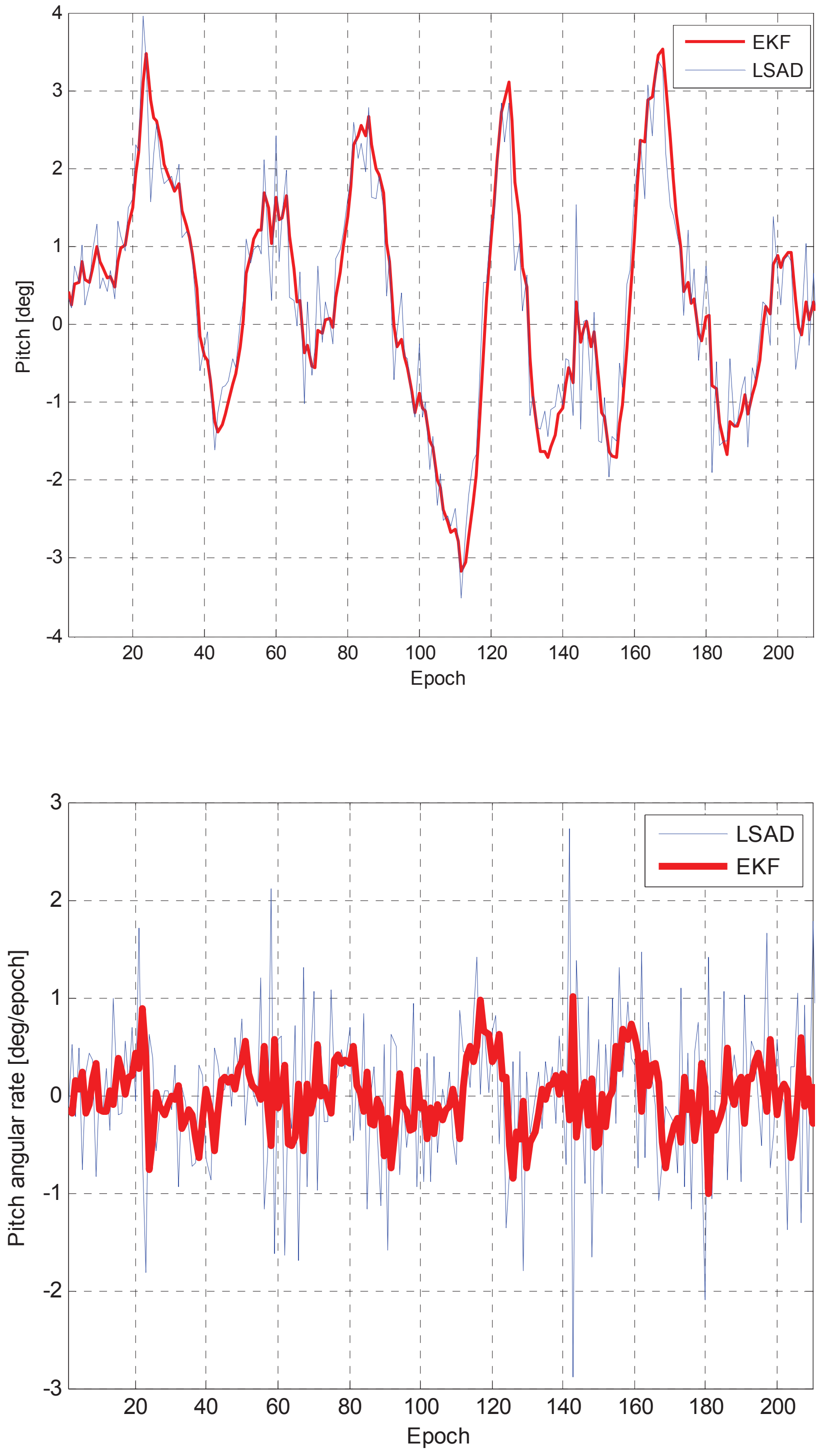

**Figure 4-2: Pitch angle and angular rates from the rotating frame**

The vibration of pitch can be clearly seen from the upper figure. From the lower figure it can be seen that the angular rate is fluctuating around zero. Also, the EKF offers smoother results than LSAD.

## 4.4 Other Kalman filters for nonlinear systems

The wide use of the EKF profits from its straightforward implementation, since the conventional Kalman filters can be applied after the nonlinear model has been linearized. Nevertheless, the error due to the linearization will degrade its accuracy and probably lead to a divergence. As shown before, the EKF truncates the Taylor series to the first order, whereas the IEKF and the SOEKF aim at reducing the linearization error and the UKF can avoid the linearization error by approximating the Gaussian error distribution using sigma-points. The application of these filters in GPS-based attitude determination systems will be presented in this section.

### 4.4.1 Iterated Extended Kalman Filter

The IEKF linearizes the nonlinear model iteratively around the updated *a posteriori* state estimates. The whole procedure is formulated below (Simon 2006):

*Initialization:*

$$\hat{\mathbf{x}}_0^+ = E\left(\mathbf{x}_0\right)$$
$$\mathbf{P}_0^+ = E\left[\left(\mathbf{x}_0 - \hat{\mathbf{x}}_0^+\right)\left(\mathbf{x}_0 - \hat{\mathbf{x}}_0^+\right)^T\right] \tag{4-19}$$

*Time update:*

$$\hat{\mathbf{x}}_k^- = f_{k-1}\left(\hat{\mathbf{x}}_{k-1}^+\right)$$
$$\mathbf{F}_{k\text{-}1} = \left.\frac{\partial f_{k-1}}{\partial x}\right|_{\hat{\mathbf{x}}_{k-1}^+} \tag{4-20}$$
$$\mathbf{P}_k^- = \mathbf{F}_{k\text{-}1}\mathbf{P}_{k\text{-}1}^+\mathbf{F}_{k\text{-}1}^T + \mathbf{G}_{k-1}\mathbf{Q}_{k\text{-}1}\mathbf{G}_{k-1}^T$$

*Measurement update:*

*Initialization of the iteration:*

$$\hat{\mathbf{x}}_{k,0}^+ = \hat{\mathbf{x}}_k^-$$
$$\mathbf{P}_{k,0}^+ = \mathbf{P}_k^- \tag{4-21}$$

*State updates (to be performed iteratively):*

for $i$=0,1,…$N$: (4-22)

$$\mathbf{H}_{k,i} = \left.\frac{\partial h_k}{\partial \mathbf{x}}\right|_{\hat{\mathbf{x}}_{k,i}^+}$$
$$\mathbf{K}_{k,i} = \mathbf{P}_k^-\mathbf{H}_{k,i}^T\left(\mathbf{H}_{k,i}\mathbf{P}_k^-\mathbf{H}_{k,i}^T + \mathbf{R}_k\right)^{-1}$$
$$\hat{\mathbf{x}}_{k,i+1}^+ = \hat{\mathbf{x}}_k^- + \mathbf{K}_{k,i}\left[\mathbf{z}_k - h_k\left(\hat{\mathbf{x}}_{k,i}^+\right) - \mathbf{H}_{k,i}\left(\hat{\mathbf{x}}_k^- - \hat{\mathbf{x}}_{k,i}^+\right)\right]$$

*Covariance updates (to be performed iteratively):*

$$\mathbf{P}_{k+1}^{+}=\left(\mathbf{I}-\mathbf{K}_{k,i}\mathbf{H}_{k,i}\right)\mathbf{P}_{k}^{-}\left(\mathbf{I}-\mathbf{K}_{k,i}\mathbf{H}_{k,i}\right)^{T}+\mathbf{K}_{k,i}\mathbf{R}_{k}\mathbf{K}_{k,i}^{T} \qquad (4\text{-}23)$$

*Estimates after the end of iteration:*

$$\begin{aligned}\hat{\mathbf{x}}_{k}^{+}&=\hat{\mathbf{x}}_{k,N}^{+}\\ \mathbf{P}_{k}^{+}&=\mathbf{P}_{k,N}\end{aligned} \qquad (4\text{-}24)$$

In Eq. (4-22) the iteration keeps running until the convergence criterion is fulfilled or the predefined maximal iteration number is reached. At the final stage, say *i*=*N*, the estimated states and error covariance at epoch *k* is given in (4-24). The IEKF will outperform the conventional EKF for high-quality measurements, as the update of the *a posteriori* estimates mainly relies on the measurement model. If significant errors of *a priori* state estimates are caused by an improper dynamic model, the IEKF can fully benefit from the measurement model to tune the linearization reference point, so that it can improve the accuracy of the *a posteriori* state estimates.

### 4.4.2 Second-Order Extended Kalman Filter

Both EKF and IEKF approximate the nonlinear model by truncating the Taylor expansion to the first order, whereas the SOEKF truncates to the second order. Although a higher order truncation is possible and theoretically better fit the nonlinear systems, the complexity of the filter implementation makes it impractical. In this study, the dynamic model is a linear relation, and hence the second-order derivative is only applied to the measurement model. Referring to a measurement vector with *m* elements, the second-order derivative of the measurement function with respect to the state vector can be written as:

$$\begin{aligned}\left[z_1 \mid z_2 \mid \cdots \mid z_m\right]_k^T &= \left[h_{1,k}\left(\mathbf{x}_k\right) \mid h_{2,k}\left(\mathbf{x}_k\right) \mid \ldots \mid h_{m,k}\left(\mathbf{x}_k\right)\right]^T \\ h_{i,k}\left(\mathbf{x}_k\right) &\approx h_{i,k}\left(\hat{\mathbf{x}}_k^-\right)+\left.\frac{\partial h_{i,k}}{\partial \mathbf{x}}\right|_{\hat{\mathbf{x}}_k^-}\left(\mathbf{x}-\hat{\mathbf{x}}_k^-\right)+\frac{1}{2}\left(\mathbf{x}-\hat{\mathbf{x}}_k^-\right)^T\left.\frac{\partial^2 h_{i,k}}{\partial \mathbf{x}^2}\right|_{\hat{\mathbf{x}}_k^-}\left(\mathbf{x}-\hat{\mathbf{x}}_k^-\right) \\ &\approx h_{i,k}\left(\hat{\mathbf{x}}_k^-\right)+\left.\frac{\partial h_{i,k}}{\partial \mathbf{x}}\right|_{\hat{\mathbf{x}}_k^-}\Delta\mathbf{x}_k+\frac{1}{2}tr\left[\left.\frac{\partial^2 h_{i,k}}{\partial \mathbf{x}^2}\right|_{\hat{\mathbf{x}}_k^-}\Delta\mathbf{x}_k\Delta\mathbf{x}_k^T\right]\end{aligned} \qquad (4\text{-}25)$$

where $\Delta\mathbf{x}_k$ denotes $\mathbf{x}_k-\hat{\mathbf{x}}_k^-$; *tr*(·) denotes the trace of a matrix. $h_{i,k}(\cdot)$ denotes the *i*-th measurement function at time *k*. As the value of $\Delta\mathbf{x}_k\Delta\mathbf{x}_k^T$ is not known, this term can be approximated by its expected value, namely the error covariance matrix of the states ($\mathbf{P}_k^-$), so that we have:

$$h_{i,k}\left(\mathbf{x}_k\right) \approx h_{i,k}\left(\hat{\mathbf{x}}_k^-\right)+\left.\frac{\partial h_{i,k}}{\partial \mathbf{x}}\right|_{\hat{\mathbf{x}}_k^-}\Delta\mathbf{x}_k+\frac{1}{2}tr\left[\left.\frac{\partial^2 h_{i,k}}{\partial \mathbf{x}^2}\right|_{\hat{\mathbf{x}}_k^-}\mathbf{P}_k^-\right] \qquad (4\text{-}26)$$

This formula applies to a single measurement equation. Referring to all measurements available, the second-order Taylor series expansion of measurement equations can be therefore written as:

$$h_k\left(\mathbf{x}_k\right) \approx h_k\left(\hat{\mathbf{x}}_k^-\right) + \mathbf{H}_k \Delta\mathbf{x}_k + \frac{1}{2}\sum_{i=1}^{m} \boldsymbol{\psi}_i tr\left[\mathbf{D}_{i,k}\mathbf{P}_k^-\right]$$

with

$$h_k\left(\mathbf{x}_k\right) = \left[h_{1,k}\left(\mathbf{x}_k\right) \mid h_{2,k}\left(\mathbf{x}_k\right) \mid \dots \mid h_{m,k}\left(\mathbf{x}_k\right)\right]^T$$

$$\mathbf{H}_k = \left[\left(\left.\frac{\partial h_{1,k}}{\partial \mathbf{x}}\right|_{\hat{\mathbf{x}}_k^-}\right)^T \mid \left(\left.\frac{\partial h_{2,k}}{\partial \mathbf{x}}\right|_{\hat{\mathbf{x}}_k^-}\right)^T \mid \dots \mid \left(\left.\frac{\partial h_{m,k}}{\partial \mathbf{x}}\right|_{\hat{\mathbf{x}}_k^-}\right)^T\right]^T \qquad (4\text{-}27)$$

$$\mathbf{D}_{i,k} = \left.\frac{\partial^2 h_{i,k}}{\partial \mathbf{x}^2}\right|_{\hat{\mathbf{x}}_k^-}$$

where **H** is Jacobin matrix as used in (4-13) for the conventional EKF. $\boldsymbol{\psi}_i$ is a column vector with all zero components except for the *i*-th entry being 1. This vector indicates the *i*-th measurement equation $h_i(\cdot)$. **D** is the Hessian matrix indicating the second-order partial derivative of a nonlinear function. Based on (4-27), we can write the measurement update procedure of a SOEFK as follows (Simon 2006):

$$\mathbf{K}_k = \mathbf{P}_k^- \mathbf{H}_k^T \left(\mathbf{H}_k \mathbf{P}_k^- \mathbf{H}_k^T + \mathbf{R}_k\right)^{-1}$$

$$\hat{\mathbf{x}}_k^+ = \hat{\mathbf{x}}_k^- + \mathbf{K}_k\left[\mathbf{z}_k - h_k\left(\hat{\mathbf{x}}_k^-\right)\right] - \boldsymbol{\pi}$$

$$\mathbf{P}_k^+ = \left(\mathbf{I} - \mathbf{K}_k\mathbf{H}_k\right)\mathbf{P}_k^-\left(\mathbf{I} - \mathbf{K}_k\mathbf{H}_k\right)^T + \mathbf{K}_k\mathbf{R}_k\mathbf{K}_k^T \qquad (4\text{-}28)$$

with

$$\boldsymbol{\pi} = \mathbf{K}_k \frac{1}{2}\sum_{i=1}^{m} \boldsymbol{\psi}_i tr\left(\mathbf{D}_{i,k}\mathbf{P}_k^-\right)$$

A detailed derivation of **D** in the multi-antenna attitude determination system is given in Appendix V.

### 4.4.3 Unscented Kalman Filter

The UKF calculates the mean and covariance of the state estimates by using a deterministic “sampling” approach, namely the unscented transformation (Julier et al. 2000; Van der Merwe and Wan 2001). The UKF first collects a set of sigma points around the estimated mean values of the states. These sigma points are then propagated through the actual nonlinear model. The estimated states and covariance are obtained from the propagated sigma points and the corresponding weights. The advantages of the UKF can be understood from the following aspects.

Firstly, the mean values of the state estimates can be accurate to the third-order of Taylor series expansion, which is higher than the EKF. The covariance estimated by the UKF is calculated to the second order accuracy, which is the same as the EKF (Julier and Uhlmann 1997; Simon 2006). Secondly, the calculation of the Jacobian matrix or Hessian matrix is needed by the EKFs. In some applications, these operations might bring severe computational complexity into the algorithm implementation. In some cases, these matrices are even not resolvable. The UKF does not rely on the model linearization and allows a simpler realization.

The routine of a discrete-time UKF can be formulated as follows (Simon 2006):

*Initialization:*

$$\begin{gathered} \hat{\mathbf{x}}_0^+ = E\left(\mathbf{x}_0\right) \\ \mathbf{P}_0^+ = E\left[\left(\mathbf{x}_0 - \hat{\mathbf{x}}_0^+\right)\left(\mathbf{x}_0 - \hat{\mathbf{x}}_0^+\right)^T\right] \end{gathered} \tag{4-29}$$

*Time update:*

$$\boldsymbol{\chi}_{k-1,i}^+ = \hat{\mathbf{x}}_{k-1}^+ + \left(\sqrt{n\mathbf{P}_{k-1}^+}\right)_i \qquad \boldsymbol{\chi}_{k-1,n+i}^+ = \hat{\mathbf{x}}_{k-1}^+ - \left(\sqrt{n\mathbf{P}_{k-1}^+}\right)_i \quad \text{for } i=1,2,\ldots n \tag{4-30}$$

$$\boldsymbol{\chi}_{k,i}^* = f_{k-1}\left(\boldsymbol{\chi}_{k-1,i}^+\right) \quad \text{for } i=1,2\ldots,2n \tag{4-31}$$

$$\hat{\mathbf{x}}_k^- = \frac{1}{2n}\sum_{i=1}^{2n}\boldsymbol{\chi}_{k,i}^* \tag{4-32}$$

$$\mathbf{P}_k^- = \frac{1}{2n}\sum_{i=1}^{2n}\left[\boldsymbol{\chi}_{k,i}^* - \hat{\mathbf{x}}_k^-\right]\left[\boldsymbol{\chi}_{k,i}^* - \hat{\mathbf{x}}_k^-\right]^T + \mathbf{G}_{k-1}\mathbf{Q}_{k-1}\mathbf{G}_{k-1}^T \tag{4-33}$$

*Measurement update:*

$$\boldsymbol{\chi}_{k,i}^- = \hat{\mathbf{x}}_k^- + \left(\sqrt{n\mathbf{P}_k^-}\right)_i \qquad \boldsymbol{\chi}_{k,n+i}^- = \hat{\mathbf{x}}_k^- - \left(\sqrt{n\mathbf{P}_k^-}\right)_i \quad \text{for } i=1,2,\ldots n \tag{4-34}$$

$$\boldsymbol{\zeta}_{k,i}^- = h_k\left(\boldsymbol{\chi}_{k,i}^-\right) \quad \text{for } i=1,2,\ldots 2n \tag{4-35}$$

$$\hat{\mathbf{z}}_k^- = \frac{1}{2n}\sum_{i=1}^{2n}\boldsymbol{\zeta}_{k,i}^- \tag{4-36}$$

$$\mathbf{P}_{\mathbf{z}_k,\mathbf{z}_k} = \frac{1}{2n}\sum_{i=1}^{2n}\left[\boldsymbol{\zeta}_{k,i}^- - \hat{\mathbf{z}}_k^-\right]\left[\boldsymbol{\zeta}_{k,i}^- - \hat{\mathbf{z}}_k^-\right]^T + \mathbf{R}_k \tag{4-37}$$

$$\mathbf{P}_{\mathbf{x}_k,\mathbf{z}_k} = \frac{1}{2n}\sum_{i=1}^{2n}\left[\boldsymbol{\chi}_{k,i}^- - \hat{\mathbf{x}}_k^-\right]\left[\boldsymbol{\zeta}_{k,i}^- - \hat{\mathbf{z}}_k^-\right]^T \tag{4-38}$$

$$\mathbf{K}_k = \mathbf{P}_{\mathbf{x}_k,\mathbf{z}_k}\mathbf{P}_{\mathbf{z}_k,\mathbf{z}_k}^{-1} \tag{4-39}$$

$$\hat{\mathbf{x}}_k^+ = \hat{\mathbf{x}}_k^- + \mathbf{K}_k\left(\mathbf{z}_k - \hat{\mathbf{z}}_k^-\right) \tag{4-40}$$

$$\mathbf{P}_k^+ = \mathbf{P}_k^- - \mathbf{K}_k \mathbf{P}_{\mathbf{z}_k,\mathbf{z}_k} \mathbf{K}_k^T \tag{4-41}$$

where the vector $\boldsymbol{\chi}$ contains the sigma points; the subscript $i$ indicates the $i$-th sigma points; $\left(\sqrt{\mathbf{P}}\right)$ is the matrix square root of **P** and can be obtained from the low-triangular matrix of the Cholesky factorization. It should be stressed that the UKF also relies on the measurement and process noises with Gaussian distributions, which can be seen from **Q** and **R** matrices in the UKF formulations.

## 4.5 Simulations with different nonlinear Kalman filters

In order to show the performance of stochastic systems, Monte-Carlo simulations are conducted. In this section, we simulate a straight flight trajectory to the east direction and assume that the airplane keeps a level flight at a constant speed of 110 m/s, as shown in Figure 4-3.

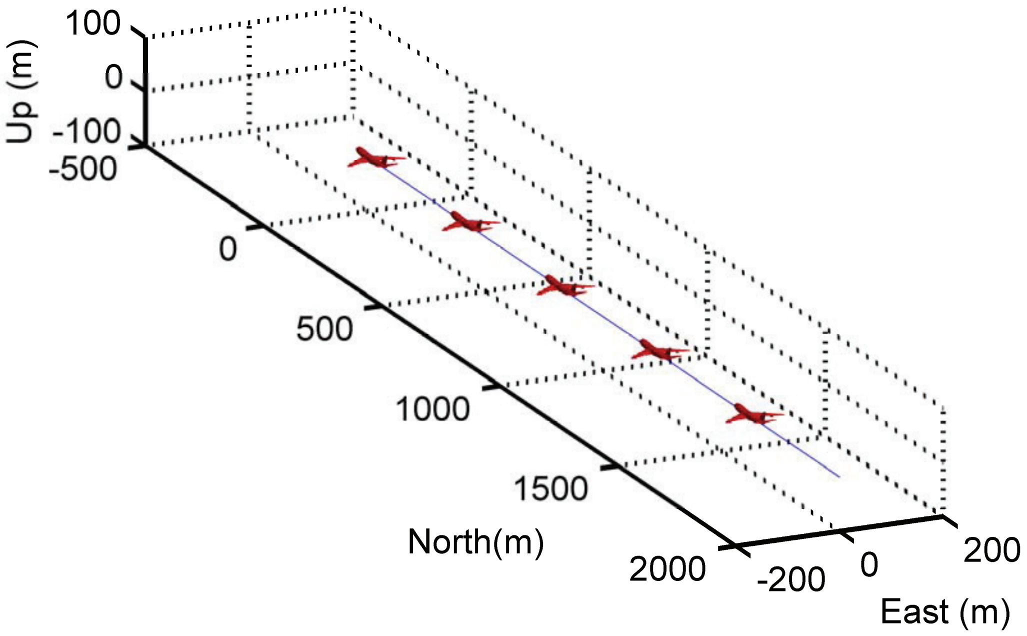

**Figure 4-3: Flight trajectory (level flight)**

The trajectory and the flight dynamics are simulated using the GPS software simulator SatNav Toolbox 3.0 for MATLAB® by GPSoft®. Parameters for generating the simulation scenarios are listed in Table 4-1. The position of the master antenna will be generated first. The ECEF coordinates of the other two slave antennas are calculated according to the position of the master antenna, the attitude parameters and the predefined ABF. The GPS errors are generated by the same mean like section 2.7. The measurement error covariance matrix **R** is determined using Eq. (4-18) at the first epoch, and the ABF errors are neglected for simplicity. Carrier phase ambiguities are set as zeros and no cycle-slips are added to the carrier phase measurements.

**Table 4-1: Parameters for level-flight simulation**

| | |
|---|---|
| **Sampling rate** | 5 Hz |
| **Number of common satellites** | 6 satellites |
| **Geometry of multiple antennas** | An equilateral triple-antenna configuration with 0.7 m baseline length. |
| **Ionospheric and tropospheric delay** | They are ignored due to the closely-spaced antennas. |
| **Satellite and receiver clock error** | They can be eliminated by differential positioning and hence will not be simulated herein. |
| **Multipath** | This is described below. |
| **Nominal attitude values** | yaw=90 [deg] pitch=0 [deg] roll=0 [deg] |
| **Thermal noise of carrier phase (for R)** | 2 mm |
| **Dynamics of attitude (for Q)** | $\sigma_{\ddot{y}} = 0.2\left[\text{deg}/\Delta\text{epoch}^2\right]$ $\sigma_{\ddot{r}} = \sigma_{\ddot{p}} = 0.3\left[\text{deg}/\Delta\text{epoch}^2\right]$ |
| **Initial value for state error covariance matrix $P_0$** | $\sigma_y = \sigma_p = \sigma_r = 0.5\left[\text{deg}\right]$ for small initialization errors<br>$\sigma_y = \sigma_p = \sigma_r = 5\left[\text{deg}\right]$ for large initialization errors<br>$\sigma_{\dot{y}} = \sigma_{\dot{p}} = \sigma_{\dot{r}} = 0.4\left[\text{deg}/\ \Delta\text{epoch}\right]$ |
| **Initial attitude values** | They are specified in the following sections. |
| **Initial attitude rates** | They are set as zeros. |

The multipath errors are generated by the same method as the low-multipath environment described in section 2.7. Note that a common satellite may lead to different multipath errors to different antennas. An example is given in Figure 4-4, where the multipath errors on L1 signal for a one-run simulation are depicted.

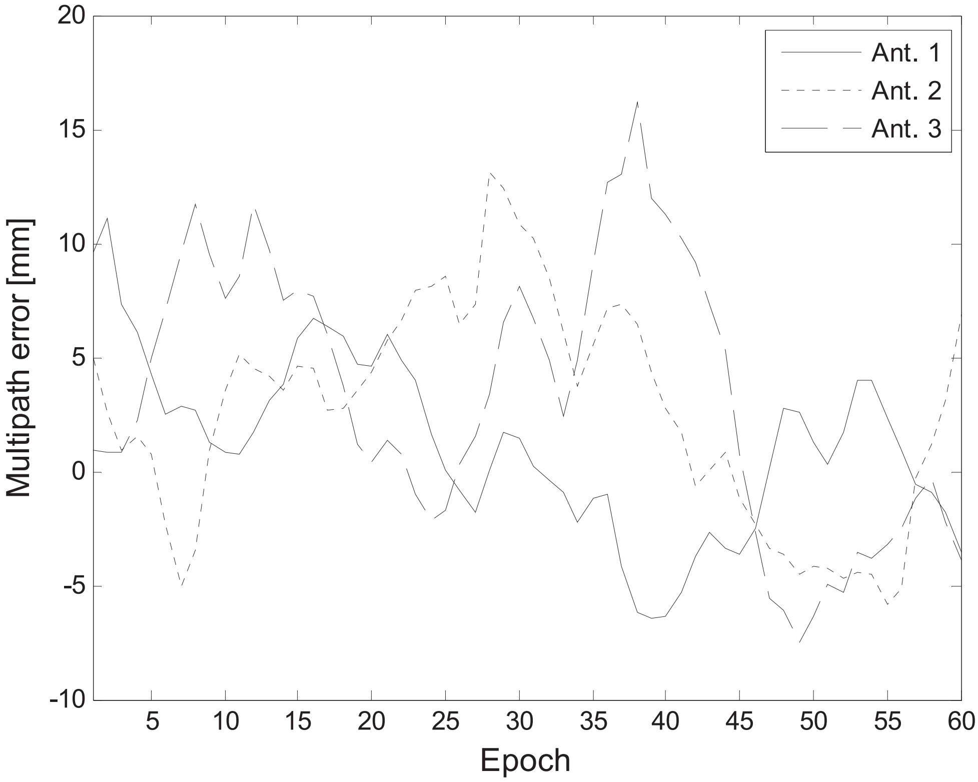

**Figure 4-4: Multipath errors for multiple antennas (an example)**

Comparisons in terms of accuracy between the estimated Euler angles from the EKF with respect to other nonlinear filters are given below. A Monte-Carlo simulation of 100 runs is carried out and the Root Mean Square Error (RMSE) is calculated. The performance of different filters under large initialization error and small initialization error will be compared. The computational burden will also be quantified. The flight starts at the GPS time 1000 so that the satellite geometry at the first epoch is identical for all simulations.

### 4.5.1 Large initialization error

At first, we consider a case with large initialization errors. As stated before, the carrier phase ambiguities are integer values. Before the integer values are resolved, we can obtain the float solutions by incorporating the code measurements. Once the integer ambiguities cannot be fixed, the float values can be used for positioning. The baselines estimated using the float ambiguities are less accurate than that based on the integer ambiguities, and hence the attitude accuracy will also be degraded. According to the test results, the estimated Euler angles obtained from float ambiguities can have an error of several degrees. We assume that the Euler angles at the first epoch are estimated using the float phase ambiguities. The integer ambiguities can be solved starting from the second epoch. The RMSE of Euler angles are depicted from Figure 4-5 to Figure 4-7. For a clear demonstration, the results at the first epoch are not shown. Note that the iteration of the IEKF is terminated when the squared norm of correction value is less than $10^{-7}$ degrees.

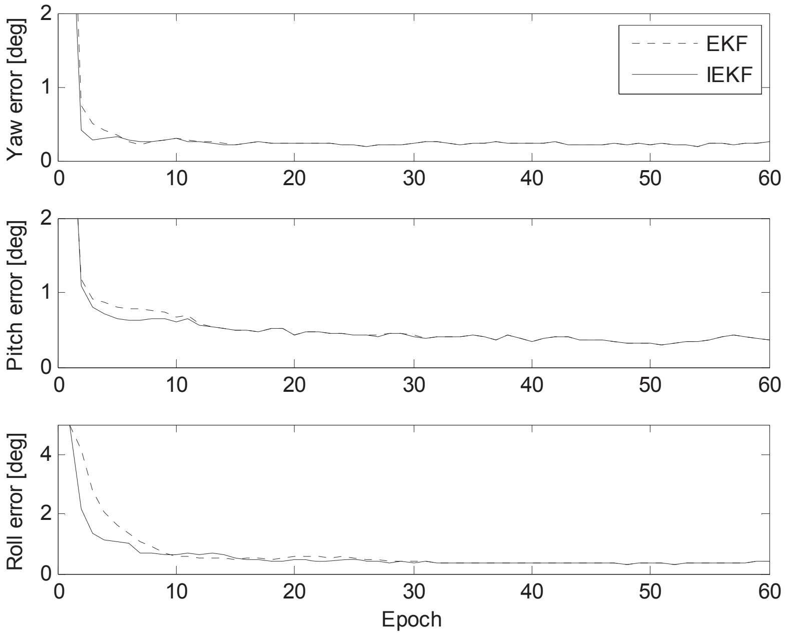

**Figure 4-5: RMSE with large initialization bias (IEKF and EKF)**

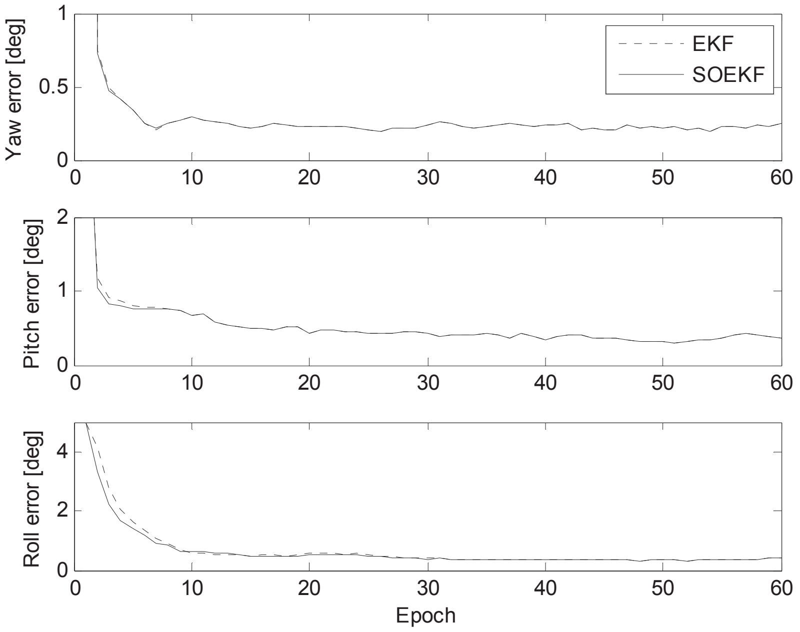

**Figure 4-6: RMSE with large initialization bias (SOEKF and EKF)**

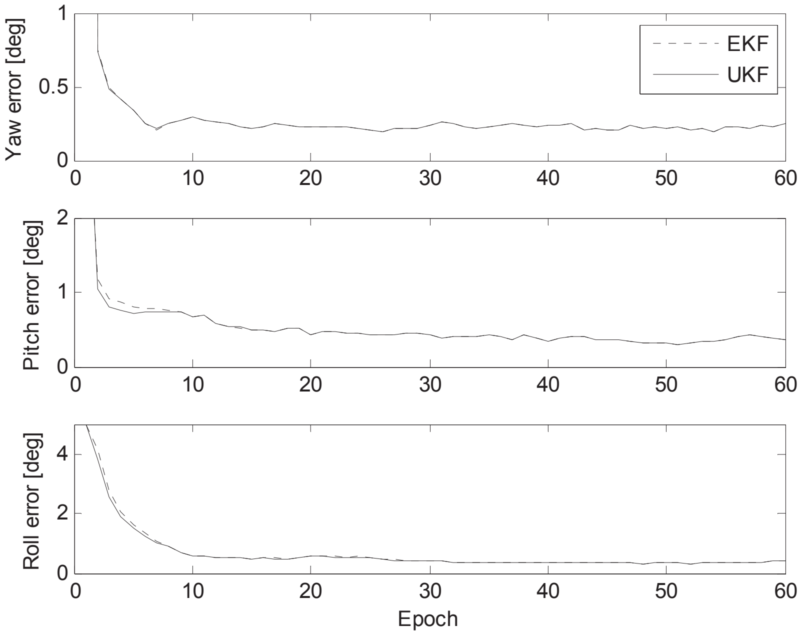

**Figure 4-7: RMSE with large initialization bias (UKF and EKF)**

From Figure 4-5 to Figure 4-7 it can be seen that the total 60 epochs can be divided into two phases. The first 20 epochs belong to the "converging phase", where the filter gradually approaches to the convergence from a large initialization error. From 21st epoch to the 60th epoch, the filter is in a steady-state. In order to evaluate the accuracy of an estimator within a specific range of epochs, we use the averaged RMSE. The averaged RMSE is calculated by dividing the sum of RMSE within the specific epochs by the total epoch number, which can be expressed as:

$$\overline{e} = \frac{1}{n}\sum_{i=1}^{n} e_{RMSE}\left(i\right) \tag{4-42}$$

Where $n$ is the total number of epochs; $e_{\mathrm{RMSE}}(i)$ is the RMSE at epoch $i$; $\overline{e}$ is the averaged RMSE. Table 4-2 presents the averaged RMSEs of different nonlinear filters in both "converging" phase and "steady-state" phase.

**Table 4-2: Averaged RMSE of Euler angles with large initialization bias**

(a) 1st – 20th epochs (filter is converging)

| Algorithm | Yaw error [deg] | Pitch error [deg] | Roll error [deg] |
|---|---|---|---|
| EKF | 0.538 | 0.888 | 1.280 |
| UKF | 0.536 | 0.864 | 1.220 |
| SOEKF | 0.535 | 0.872 | 1.227 |
| IEKF | 0.506 | 0.830 | 0.991 |

(b) 21st - 60th epochs (filter converged)

| Algorithm | Yaw error [deg] | Pitch error [deg] | Roll error [deg] |
|---|---|---|---|
| EKF | 0.228 | 0.374 | 0.359 |
| UKF | 0.229 | 0.374 | 0.358 |
| SOEKF | 0.228 | 0.374 | 0.358 |
| IEKF | 0.228 | 0.373 | 0.356 |

It can be seen that the IEKF offers the fastest convergence, followed by the UKF and the SOEKF. The EKF shows the worst converging performance. A large initialization error means that there is a significant deviation between the *a priori* state estimates and the corresponding true value, and hence the linearization error is large. The IEFK, SOEKF and UKF show the superiority in reducing the linearization error compared to the conventional EKF. After 20th epoch, all these filters show quite similar accuracies.

### 4.5.2 Small initialization error

We initialize the filter with attitude parameters estimated using correctly resolved integer ambiguities. According to the error analysis, the mean error of Euler angles will not be larger than 0.5 degrees in this case, implying a small initialization error. The averaged RMSE are shown below:

**Table 4-3: Averaged RMSE of Euler angles with small initialization bias**

| Algorithm | Yaw error [deg] | Pitch error [deg] | Roll error [deg] |
|---|---|---|---|
| EKF | 0.230 | 0.375 | 0.360 |
| UKF | 0.228 | 0.377 | 0.361 |
| SOEKF | 0.232 | 0.378 | 0.357 |
| IEKF | 0.227 | 0.370 | 0.355 |

Under small initialization errors, all these filters give comparable accuracies with differences at milli-degree level.

### 4.5.3 Computational complexity

A comparison of the processing time for the entire trajectory based on the EKF, SOEKF, IEKF and UKF is given below. The time needed for 100 runs of simulations are computed firstly under the system environment:

- CPU: Inter® Core2 Duo CPU E8400@ 3G(Hz)
- RAM: 3GB RAM
- Software: MATLAB® R2007a

After that, the processing time for one filter-routine can be calculated by dividing the total processing time by the number of runs. The processing time for a single filter-routine is given in Table 4-4.

**Table 4-4: Computational time of different filters**

| Algorithm | Average time for one run [ms] |
|---|---|
| EKF | 2.8 |
| SOEKF | 3.5 |
| UKF | 4.0 |
| IEKF (1 Iteration) | 3.1 |
| IEKF (2 Iteration) | 5.2 |
| IEKF (5 Iteration) | 12.1 |

The EKF offers the lowest computational burden, followed by the SOEKF and the UKF. The computational time of the IEKF depends on the number of iterations performed.

## 4.6 Conclusions

If a platform does not allow long baselines for multiple antennas, the accuracy of computed Euler angles can be improved by introducing a dynamic model. With a less-maneuvering platform and high data sampling rate, a constant angular rate model can approximate the attitude dynamics. If the GPS carrier phase integer ambiguities can be correctly resolved and a precise initialization for the filter can be carried out, different nonlinear filters offer comparable accuracies. With large initialization errors, the IEKF, SOEFK and UKF lead to a faster convergence than the conventional EKF. However, the conventional EKF has the lowest computational burden. Summarizing these discussions, the EKF under a precise initialization can be a proper choice for this application.

Besides the large initialization error, the mismodeling error of the dynamic model can also yield large innovation vectors to a Kalman filter. The performance of different filters under mismodeling errors will be presented in chapter 5.

# 5. Approaches to overcome the limitations of the introduced dynamic model

A constant angular rate model has been introduced as the dynamic model. The "***mismodeling error***" of the dynamic model can manifest itself in at least two aspects. Firstly, the constant angular rate model cannot fully reflect the model transition of an airplane. Secondly, the actual dynamic error of the airplane is unknown, and hence the Kalman filter should be able to automatically identify the changing dynamics. Both problems will be identified and solved in this chapter.

## 5.1 Problem description

The PAMIR airplane can undergo several "***motion models***" during a flight trajectory, for example (Federal-Aviation-Administration 2007):

- Straight and level flight, where pitch and roll angles are close to zero and the yaw angle is almost unchanged;
- Pitch (up or down) climb, where the pitch angle is gradually increasing or decreasing;
- Banked turn, where the airplane will change the direction in the horizontal plane by rolling an inclined angle, i.e. roll and yaw will change.

A constant angular rate model should be valid for each motion model due to the low maneuver output of the PAMIR airplane and high GPS data rate. Nevertheless, it cannot fully reflect the transition between different motion models. The shortcoming of the constant angular rate model in this case is shown by a simulated trajectory shown in Figure 5-1.

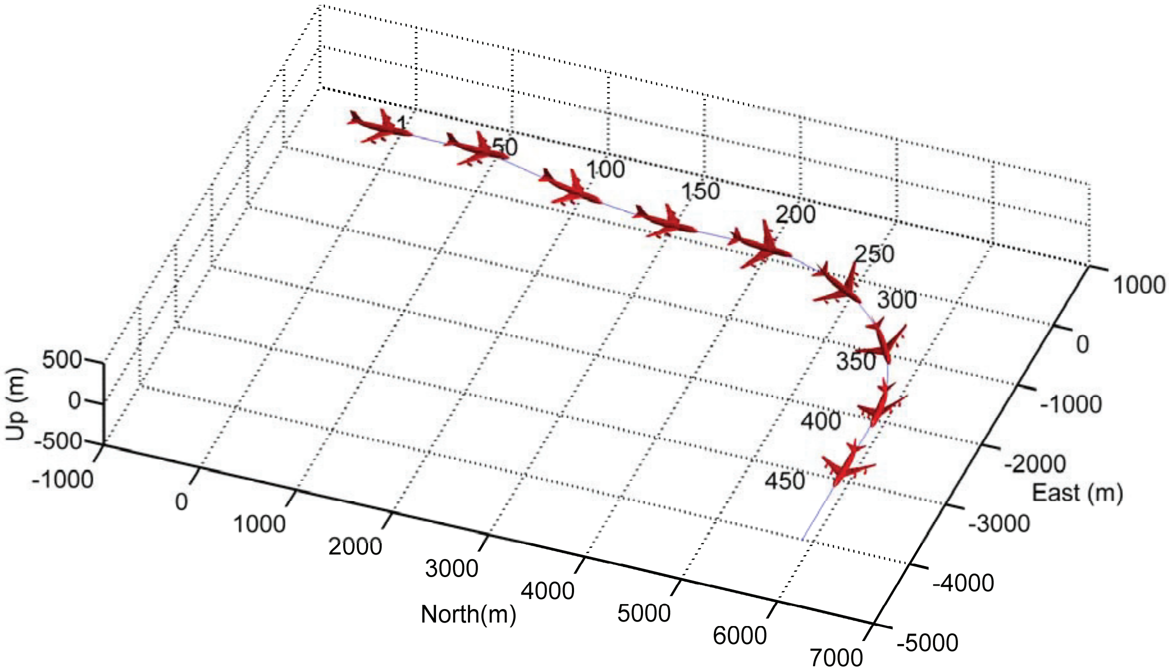

**Figure 5-1: Trajectory of the airplane under different motion models**

We term the phase when the airplane is transiting one motion model to another as "***model transition phase***". The phase in which the airplane maintains a certain motion model is termed as "***stable motion phase***". In Figure 5-1, the airplane starts with a straight level flight to the east direction at the speed of 110 m/s, followed by a "pitch down" climb, and then the airplane takes a banked turn of 90 degrees and finally returns to a straight level flight. The numbers marked along the trajectory represent the epochs. The GPS data sampling rate is 5 Hz. We assume that the airplane with three onboard GPS antennas is flying at the geodetic height of 1000 meters. The trajectory reflects the coordinates of the master GPS antenna. The three GPS antennas form an equilateral configuration with a baseline of 0.5 meters. There are 7 common GPS satellites in view during the flight. A low-multipath environment is simulated as presented in chapter 4. The ionospheric and tropospheric errors are ignored due to the short antenna baselines. The nominal attitude values are presented in Figure 5-2, where the red points represent the starting epochs of the model transition.

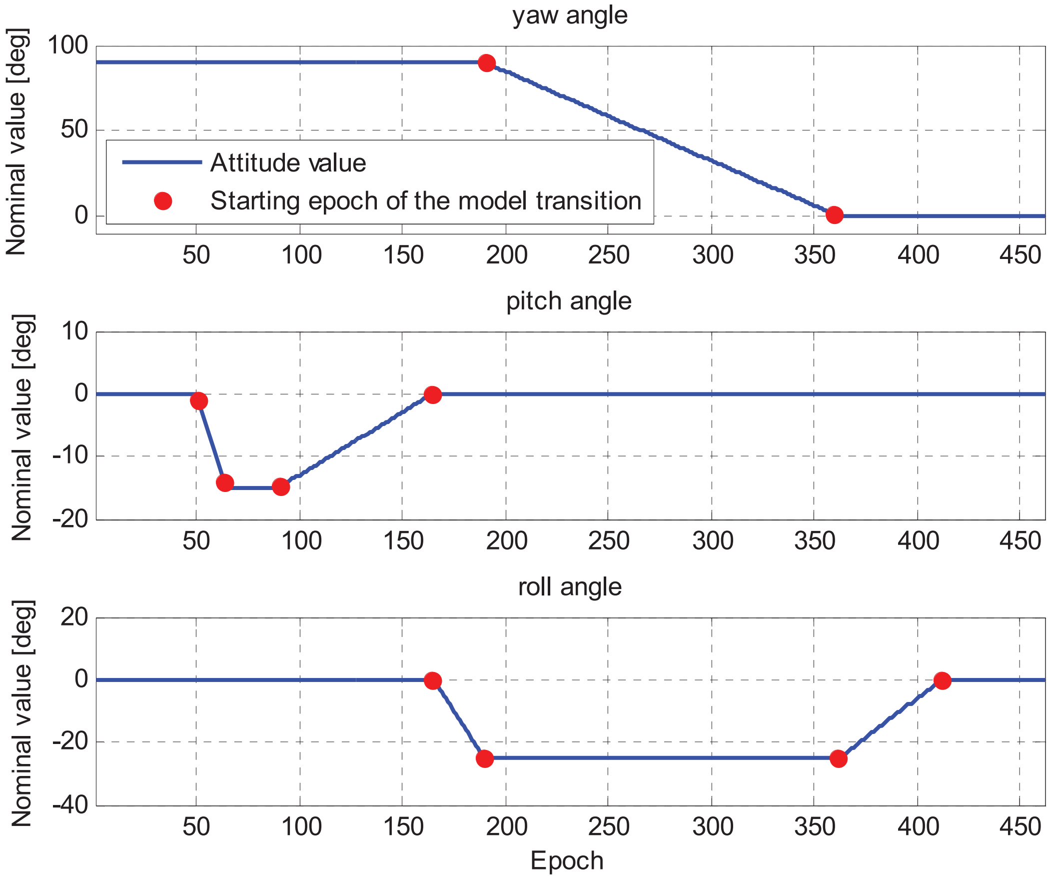

**Figure 5-2: Nominal attitude values**

We use two approaches to estimate the attitude results, the LSAD with merely the GPS carrier phase measurements and the EKF aided by the constant angular rate model. We use the attitude results estimated by the LSAD at the first epoch to initialize the EKF. The simulation is generated with smaller process noise, whereas the filter is initialized with larger process noise. These process noise parameters are set deliberately to show the benefit of adaptive Kalman filter introduced in the following sections. The parameters for running the EKF are listed in Table 5-1.

**Table 5-1: Parameters for simulation and filter initialization**

| | |
|---|---|
| **Thermal noise of carrier phase (for R)** | 2 mm |
| **Process noise parameters for generating the simulation (Q)** | $\sigma_{\ddot{y}} = 0.2\left[\mathrm{deg}/\Delta\mathrm{epoch}^2\right]$  $\sigma_{\ddot{r}} = \sigma_{\ddot{p}} = 0.3\left[\mathrm{deg}/\Delta\mathrm{epoch}^2\right]$ |
| **Process noise parameters for running the filter (Q)** | $\sigma_{\ddot{y}} = 0.35\,[\mathrm{deg}/\Delta\mathrm{epoch}^2]$  $\sigma_{\ddot{p}} = \sigma_{\ddot{r}} = 0.4\,[\mathrm{deg}/\Delta\mathrm{epoch}^2]$ |
| **Initial value for state error covariance matrix $\mathrm{P}_0^+$** | $\sigma_y = 0.4\left[\mathrm{deg}\right]$  $\sigma_p = \sigma_r = 0.6\left[\mathrm{deg}\right]$<br>$\sigma_{\dot{y}} = \sigma_{\dot{p}} = \sigma_{\dot{r}} = 0.4\left[\mathrm{deg}/\,\Delta\mathrm{epoch}\right]$ |
| **Initial attitude values** | LSAD at first epoch |
| **Initial attitude rates** | They are set as zeros. |

Figure 5-3 compares the RMSE of estimated attitude parameters from the EKF and the LSAD. The results are obtained based on Monte-Carlo simulations with 100 runs.

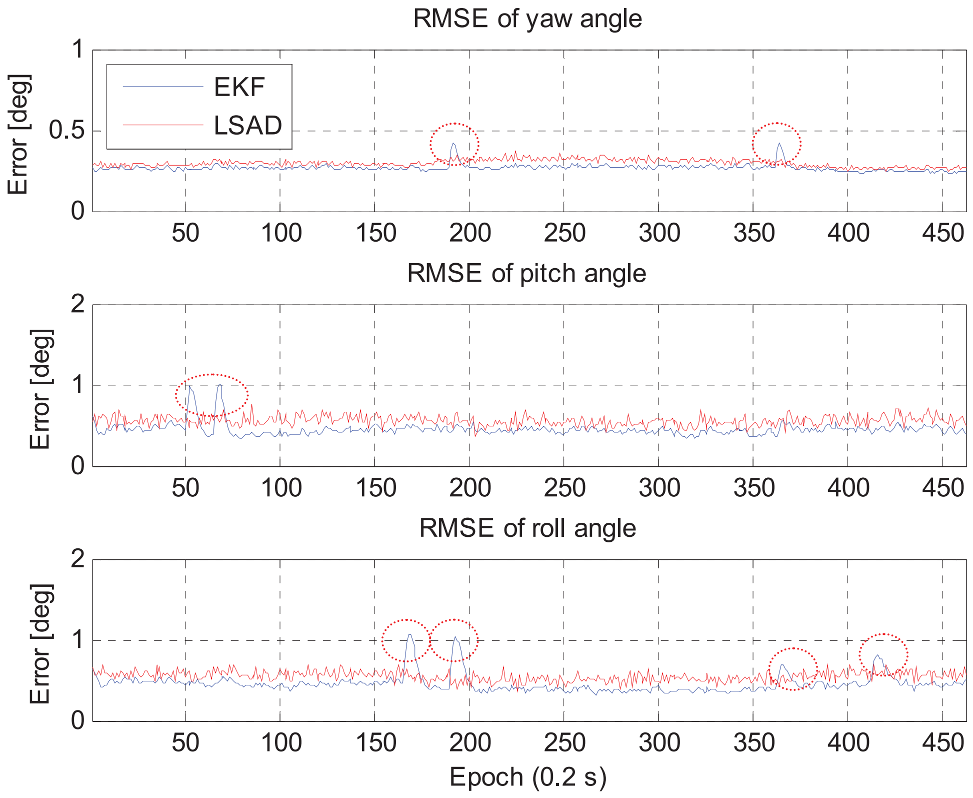

**Figure 5-3: RMSE of EKF and LSAD**

We can observe the following phenomena from Figure 5-3:

(1) The LSAD approach without the aid of the dynamic model offers a stable attitude

estimates during the entire trajectory.

(2) The errors caused by the model transition can be observed from the EKF results. The errors manifest themselves as peak values in the magnitude, which have been marked by red circles in the figure. There errors are termed as "***model transition errors***" in this thesis. Seeing again Figure 5-1, it can be observed that the model transition errors occur during the model transition phases. At the beginning of a model transition, the Euler angles might experience a sharp change whose magnitude might be larger than the associated process noise. In this case, the dynamic model cannot fully reflect the change of Euler angles and hence bring significant errors into the *a priori* state estimates.

(3) The filter outputs can gradually converge after the model transition, because the angular rates in each motion model obey a constant variation and hence the dynamic model still holds.

(4) Once the filter has converged, the EKF give more accurate attitude estimates than the LSAD due to the benefit of the dynamic model.

Besides the model transition errors, another type of mismodeling error is caused by a conservative initialization of process noise. The constant angular rate model is merely an approximation rather than a measure of the attitude dynamics. The process noise parameters fitting the entire trajectory are difficult to be determined, as they depend on the environments nearby, the application scenarios, the actual maneuver output, etc. In order to avoid filter divergence, the process noise covariance matrix is usually conservatively initialized in practice. This will, however, make the filter not fully benefit from the attitude dynamic information. It is necessary to design an adaptive algorithm to make the Kalman filter for an automatically identify the actual process noise parameters.

Summarizing the previous discussions, the solution to the mismodeling error is a two-fold task. On the one hand, the model transition errors need to be detected and reduced. On the other hand, the Kalman filter should have an online tuning function of the process noise.

## 5.2 Reducing model transition errors using different nonlinear Kalman filters

The failure of the dynamic model will bring large errors to the *a priori* state estimates. This will lead to large innovation vectors and significant linearization errors. As presented in chapter 4, the IEKF, SOEKF and UKF might reduce the linearization errors in comparison with the conventional EKF. The performances of these filters in the model transition phases will be demonstrated in this section. The results are obtained from a one-run simulation in the same scenario introduced in section 5.1.

The IEKF will iteratively update the linearization reference point using the *a posteriori* state estimates. This procedure will gradually shift the reference point closer to the true value and consequently lead to the accuracy improvement, which can be seen from the update of the *a posteriori* state estimates at the first several iterations. In Figure 5-4, the update values of the *a posteriori* Euler angle estimates at the first round iteration, namely $\hat{\mathbf{x}}_{k,1}^{+} - \hat{\mathbf{x}}_{k,0}^{+}$, are depicted at the left-hand side, and the update values at the second round iteration, namely $\hat{\mathbf{x}}_{k,2}^{+} - \hat{\mathbf{x}}_{k,1}^{+}$, are depicted at the right-hand side.

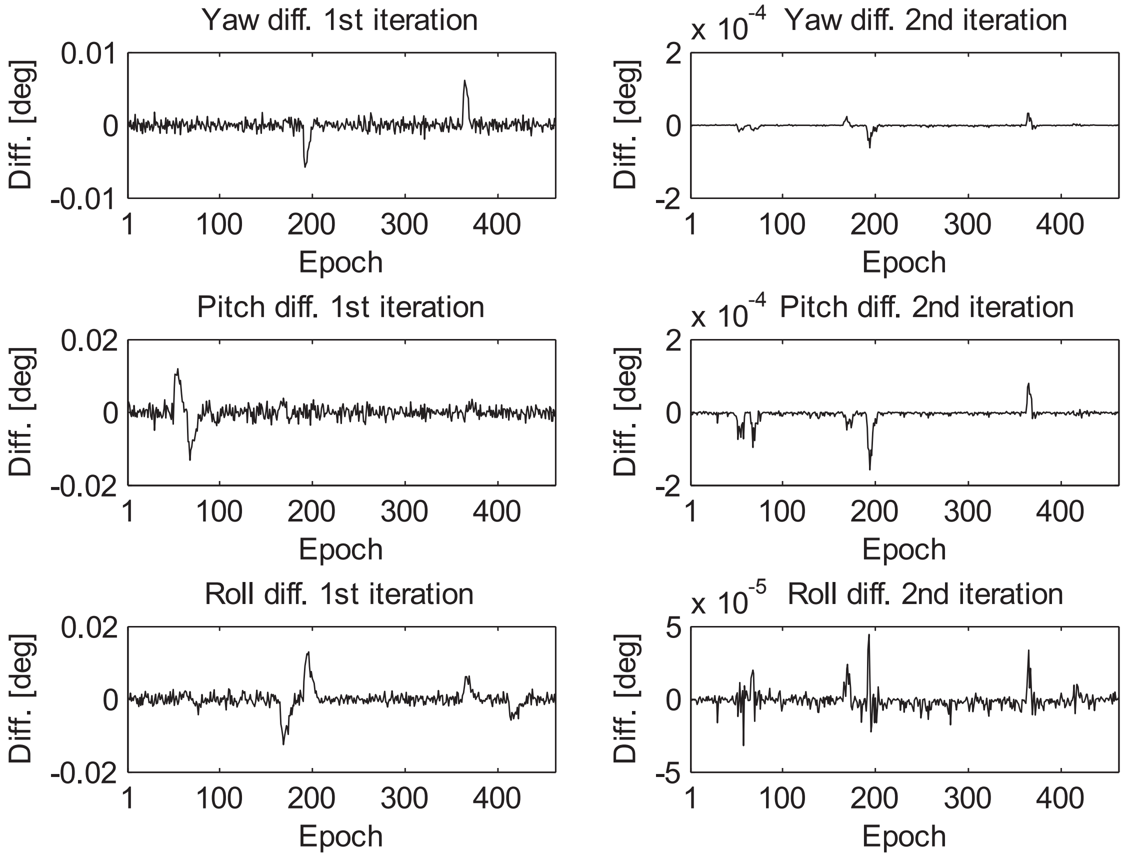

**Figure 5-4: The update of the *a posteriori* state estimates in IEKF**

At the most epochs, the magnitude of update values is small. However, some peak values can be observed. Looking back at Figure 5-2 we know that the peak values arise at the start of model transition phases. The occurrence of these peak values reflects that the linearization reference points are moving from the *a priori* state estimates towards to the true values, so that the linearization error will be reduced. By comparing the figures at left- and right-hand sides it can be seen that the first iteration implements much larger corrections to the linearization reference points. Due to the very small update values at the second round iteration, the third round iteration is normally not required.

The difference between the SOEKF and the conventional EKF lies in the term $\boldsymbol{\pi}$ of Eq.

(4-28). This term indicates the effects of the second-order Taylor series expansion. The corresponding components of Euler angles in vector $\boldsymbol{\pi}$ are depicted in Figure 5-5.

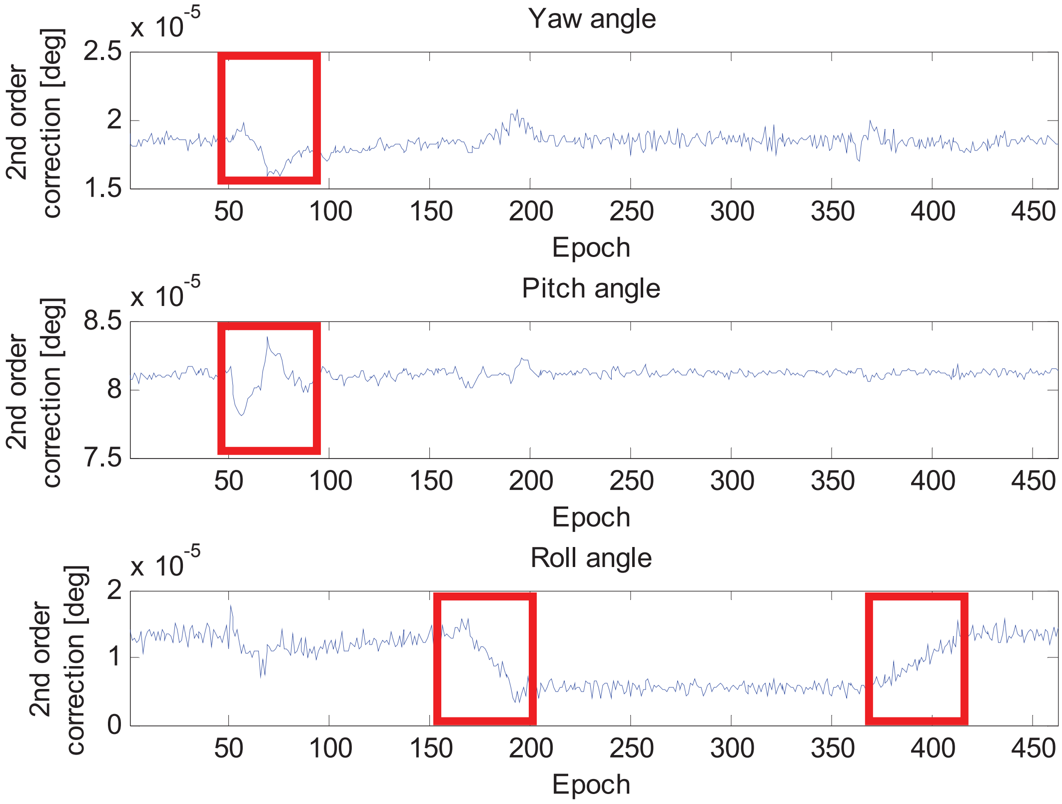

**Figure 5-5: The second-order correction in the SOEKF**

In Figure 5-5, some variations with large magnitude are marked. The epochs of these distinct variations can be related to the epochs of the peak values shown in Figure 5-4. These variations indicate the significant second-order initialization errors at the model transition phases.

Figure 5-6 shows different accuracies of Euler angles estimated by the EKF and the UKF. The curves represent Euler angle errors from the EKF minus that from the UKF, so that a positive value implies the outperformance of the UKF over the EKF in terms of accuracy.

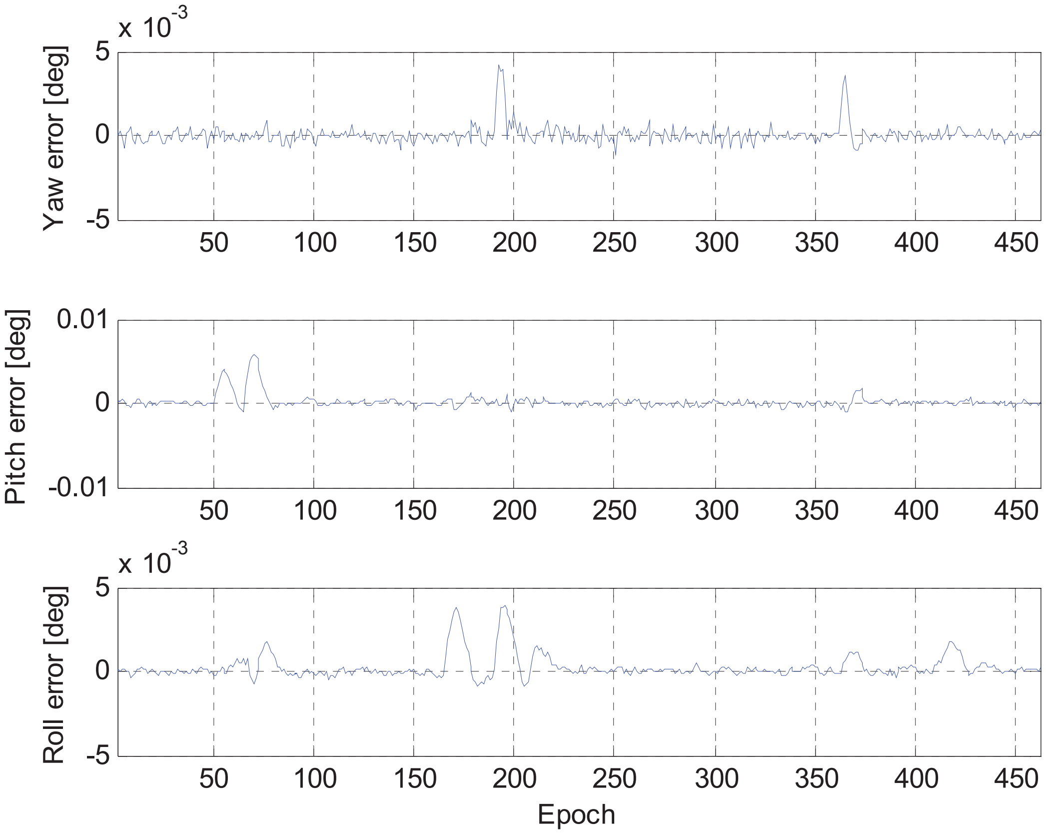

**Figure 5-6: Deviations between UKF and EKF under mismodeling error**

In the model transition phases, large positive peak values can be observed, meaning that the UKF offers higher accuracies in these cases. However, both filters present comparable accuracies of Euler angles at other epochs.

Although the IEKF, SOEKF and UKF outperform the conventional EKF during the model transition phases, the accuracy improvements benefited from the IEKF, SOEFK and UKF are small compared to the magnitude of peak values shown in Figure 5-3. We therefore need to seek for other solutions to solve this problem.

## 5.3 Solutions to the model transition errors

The propagation of the process noise is reflected in the following step of a Kalman filter routine:

$$\mathbf{P}_k^- = \mathbf{F}_{k-1}\mathbf{P}_{k-1}^+\mathbf{F}_{k-1}^T + \mathbf{G}_{k-1}\mathbf{Q}_{k-1}\mathbf{G}_{k-1}^T \tag{5-1}$$

The first term after the equal sign reflects the propagation of state errors from the past epochs to the current epoch. The second term reflects the influence of the process noise on the current epoch. In order to adapt the filter to the changing dynamics, we can tune either the first term or the second term. By tuning the first term, we have the fading-memory extended Kalman filter (FMEKF). Tuning the second term yields the adaptive extended Kalman filter (AEKF). Both techniques will be detailed in the following sections.

Another commonly used approach to overcome the dependence of a Kalman filter on modeling accuracies is the Interacting Multiple-Model (IMM) approach. This approach needs more than two filters running in parallel and outputs the weighted results from all sub-filters. In a sense of reducing the model transition errors, the IMM is more robust than the FMEKF and the AEKF. In order to make the IMM approach better fit the changing dynamics, we propose an approach to embed the adaptive tuning function into the IMM.

## 5.4 Fading-memory extended Kalman filter

The state estimates from Kalman filters are obtained by a weighted sum of the information from the past epochs and the current epoch. Once the model transition occurs, the Kalman filter should give more weight to the measurements of the current epoch and accordingly give less weight to the history (Simon 2006). This is the basic idea for the FMEKF. The key step of a FMEKF is presented by the following equation:

$$\mathbf{P}_k^- = \alpha \mathbf{F}_{k-1} \mathbf{P}_{k-1}^+ \mathbf{F}_{k-1}^T + \mathbf{G}_{k-1} \mathbf{Q}_{k-1} \mathbf{G}_{k-1}^T \tag{5-2}$$

where $\alpha$ is the scaling factor. Such a scalar factor reflects how responsive the Kalman filter is to the past measurement. The larger the scaling factor, the more weight the filter gives to the nearest measurement. If the scaling factor is a fixed value, a FMEKF can be equivalent to a conventional EKF. In order to adapt the FMEKF to the changing dynamics, a variant scaling factor is expected.

### 5.4.1 Calculation of the fading-memory factor

A variant scaling factor $\alpha$ can be derived for the innovation vector of a Kalman filter (Hu et al. 2003). The innovation vector can be calculated as:

$$\mathbf{s}_k = \mathbf{z}_k - h_k\left(\mathbf{x}_k^-\right) \tag{5-3}$$

After linearizing the measurement model, the error covariance matrix of the innovation reads:

$$\begin{aligned} Cov\left(\mathbf{s}_k\right) &= Cov\left(\mathbf{z}_k\right) + \mathbf{H}_k Cov\left(\mathbf{x}_k^-\right)\mathbf{H}_k^T \\ &= \mathbf{R}_k + \alpha \mathbf{H}_k \mathbf{F}_{k,k-1} \mathbf{P}_{k-1}^+ \mathbf{F}_{k,k-1}^T \mathbf{H}_k^T + \mathbf{H}_k \mathbf{G}_{k-1} \mathbf{Q}_{k-1} \mathbf{G}_{k-1}^T \mathbf{H}_k^T \end{aligned} \tag{5-4}$$

So that the following inequality holds true if $\alpha \geq 1$:

$$\begin{gathered} \mathbf{s}_k^T \mathbf{s}_k \leq \alpha \cdot Trace\left(\mathbf{R}_k + \mathbf{H}_k \mathbf{F}_{k,k-1} \mathbf{P}_{k-1}^+ \mathbf{F}_{k,k-1}^T \mathbf{H}_k^T + \mathbf{H}_k \mathbf{G}_{k-1} \mathbf{Q}_{k-1} \mathbf{G}_{k-1}^T \mathbf{H}_k^T\right) \\ \text{or in another form:} \\ \mathbf{s}_k^T \mathbf{s}_k \leq \alpha \cdot Trace\left[Cov\left(\overline{\mathbf{s}}_k\right)\right] \end{gathered} \tag{5-5}$$

where $\overline{\mathbf{s}}_k$ is the estimated innovation vector. For a steady-state Kalman filter, $\overline{\mathbf{s}}_k$ can be approximated by the normalized innovation sequence of the previous $N$ epochs, so that the trace of $\overline{\mathbf{s}}_k$ can be obtained by:

$$Trace\left[Cov\left(\overline{\mathbf{s}}_k\right)\right] \approx \frac{1}{N}\sum_{j=k-N}^{k-1} \mathbf{s}_j^T \mathbf{s}_j \tag{5-6}$$

Substituting (5-6) into (5-5) yields the following relation:

$$\alpha \geq \frac{\mathbf{s}_k^T \mathbf{s}_k}{\frac{1}{N}\sum_{j=k-N}^{k-1} \mathbf{s}_j^T \mathbf{s}_j} \tag{5-7}$$

We can use (5-7) to calculate the scaling factor $\alpha$. The scaling factor has two functions. The first function is to detect the occurrence of the model transition. If the scaling factor is larger than 1, it means that the norm of innovation vector at current epoch exceeds the average level of the past epochs. This also implies the occurrence of the model transition. Only in this case, the fading-memory function can be activated. Otherwise, the conventional EKF will be applied. The second function of the scaling factor is to determine the weight given to the current measurement. However, as is shown in (5-6), the averaged innovation sequence is only an approximation under a specific window size and hence needs to be added with a tolerance factor. For this purpose, the fading-memory function can be activated if the following relation holds:

$$\alpha \geq \eta \frac{\mathbf{s}_k^T \mathbf{s}_k}{\frac{1}{N}\sum_{j=k-N}^{k-1} \mathbf{s}_j^T \mathbf{s}_j} \tag{5-8}$$

where the multiplication factor $\eta$ reflects the tolerance and should be slightly larger than 1. If the relation (5-8) holds, the scaling factor $\alpha$ can be assigned with the minimal value of inequality (5-7), otherwise $\alpha$ is kept as 1.

### 5.4.2 Performance comparison of fading-memory and conventional extended Kalman filter

Figure 5-7 shows the RMSE of the estimated Euler angles from a conventional EKF and a FMEKF, where the window size $N$ is 10 epochs and the multiplication factor $\eta$ in (5-8) is 1.1. We use the same simulation scenario and initialization parameters as that used in section 5.1. The results are obtained from a 100-run Monte Carlo simulation.

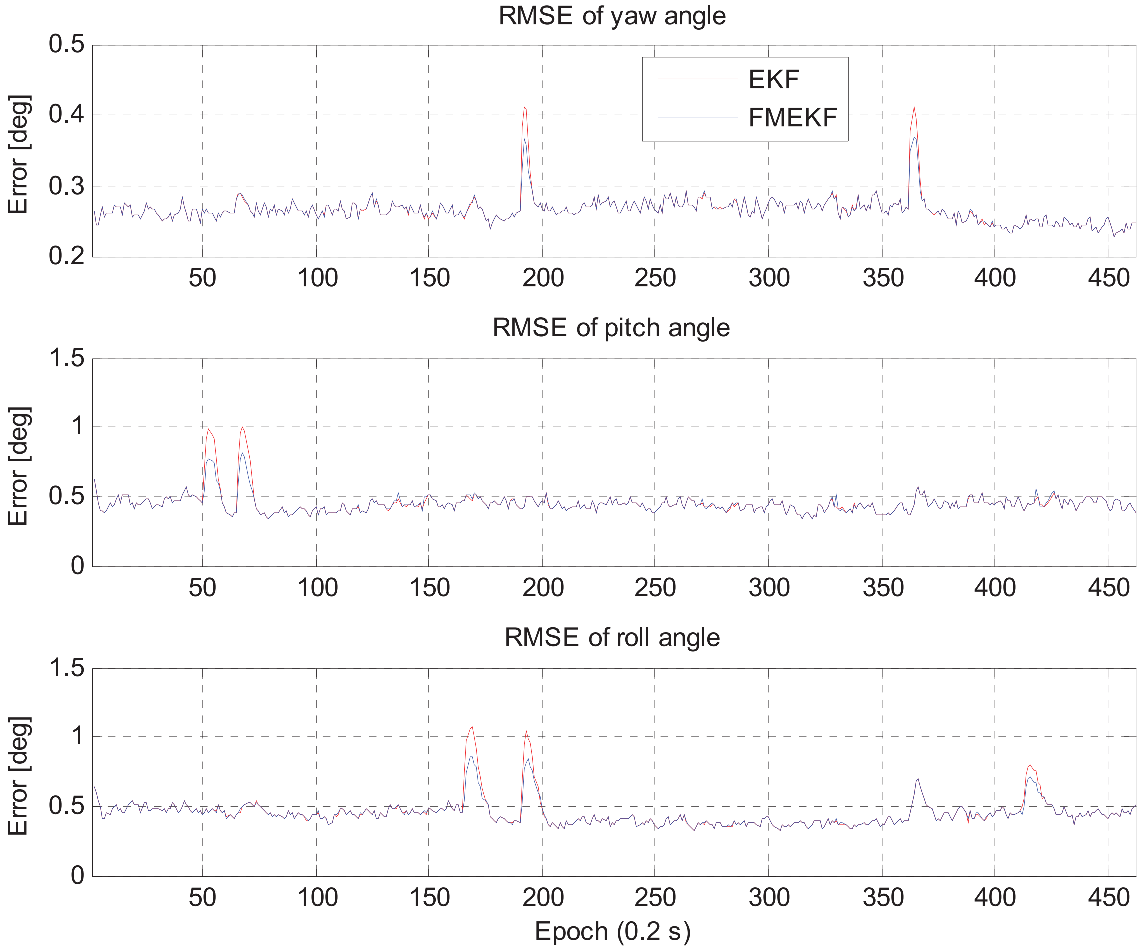

**Figure 5-7: RMSE of FMEKF and conventional EKF**

From Figure 5-7 we can see that the FMEKF shows its superiority during the model transition phases as it shows smaller magnitude of model transition errors and faster convergence. During the stable motion phases, the fading-memory function is inactive and the conventional EKF is resumed.

The variation of the fading-memory factor $\alpha$ calculated from a one-run simulation is illustrated in Figure 5-8.

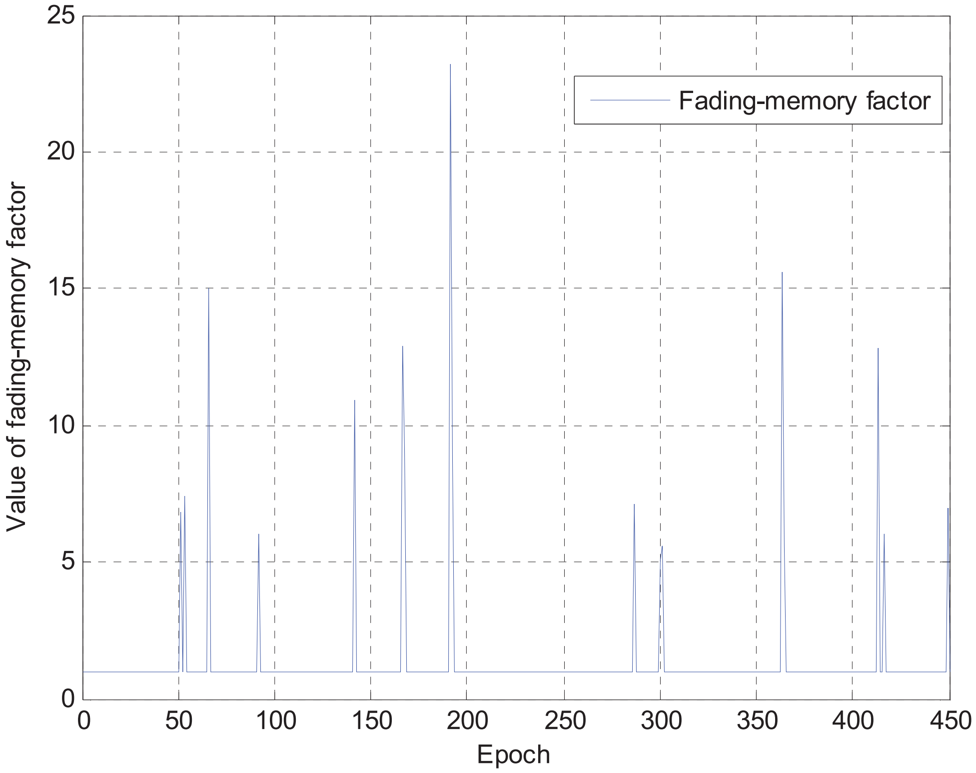

**Figure 5-8: Variation of the fading-memory factor**

The fading-memory factor experiences some peak values. By comparing with nominal attitude values given in Figure 5-2, we can see that these peak values normally appear at the beginning of model transition phases. The peak values reflect the significant increase of the norm of the innovation vector and hence indicate the occurrence of the model transition. In these cases, the fading-memory function is activated.

## 5.5 Adaptive tuning of process noise

The optimality of the Kalman filter setting is closely related to the quality of the *a priori* knowledge about the process noise and the measurement noise. The measurement noise can be referred to the product instructions provided by the manufacture. An appropriate *a priori* process noise is highly dependent on the application scenarios and vehicle dynamics, and hence it is difficult to be determined. The use of constant process noise parameters is a major drawback in a changing dynamic environment. In order to make the filter adaptively identify the changing dynamics, several algorithms are developed for online tuning of the process noise. These algorithms can be categorized into innovation-based approaches (Mohamed and Schwarz 1999) and residual-based approaches (Wang et al. 1999). The difference is that the former one relies on the measurements predicted by the *a priori* state estimates, whereas the latter one is based on the *a posteriori* state estimates. However, the calculation of *a posteriori* residuals is not an essential step in a Kalman filter routine and needs extra processing time. In this thesis, we only consider the innovation-based algorithms. Different algorithms are investigated to tune the parameters of process noise, or the parameters of measurement noise, or both simultaneously (Wang et al. 1997). In order to determine the technique to be applied, it is necessary to know which one contributes the major error. In our applications, the measurement model based on the multi-antenna system gives an accurate estimate of the attitude information, if no blunder like cycle-slips or loss of lock occurs. The cycle-slip detection and the integer ambiguity resolution have been discussed in chapter 2. As the antennas are closely distributed, the ionospheric and tropospheric errors can be cancelled by differential positioning. Consequently, the quality of the GPS double-differenced carrier phase measurements can be well assessed. In contrary, the changing dynamics of the airplane is difficult to be predicted. We therefore focus on the tuning of process noise parameters in this thesis. The tuning at epoch *k* can be expressed by (Hide et al. 2004; Mehra 1972):

$$\mathbf{G}_k \mathbf{Q}_k \mathbf{G}_k^T \approx \mathbf{K}_k \left( \frac{1}{N} \sum_{j=k-N+1}^{k} \left[ \mathbf{z}_j - h\left(\hat{x}_j^-\right) \right] \left[ \mathbf{z}_j - h\left(\hat{x}_j^-\right) \right]^T \right) \mathbf{K}_k^T \tag{5-9}$$

It is worth noting that this formula tunes the entire term for process error propagation rather than **Q** itself. The tuning takes place after the Kalman gain is obtained and will take effects at the next epoch.

The adaptive tuning of the process noise can be evaluated by using the simulation scenario and same filter initialization presented in section 5.1. As explained before, we use small process noise parameters to generate the simulation and large process noise parameters to initialize the filter. The variation of the associated process noise for each Euler angle is given in Figure 5-9. The length of time window is 8 epochs. For a clear illustration, we only present the first 80 epochs. The results are based on a one-run simulation.

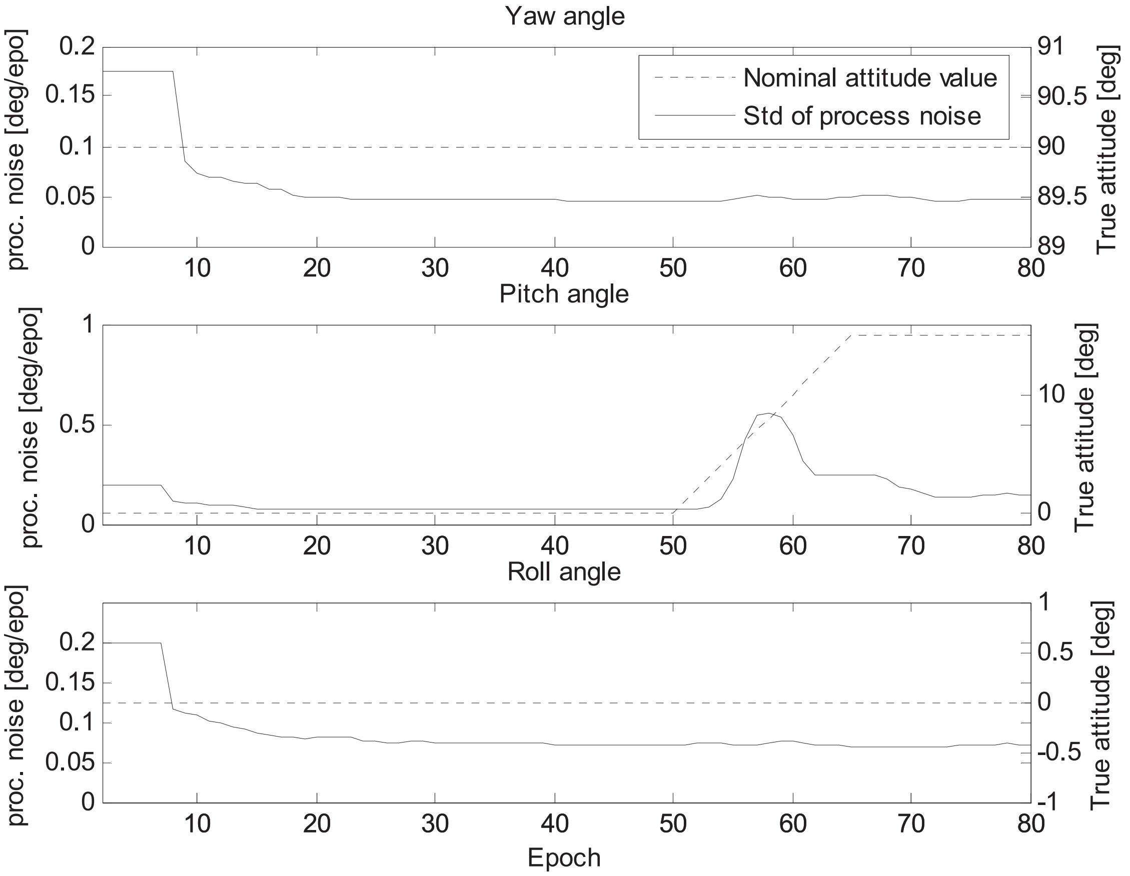

**Figure 5-9: Variation of process noise parameters**

The solid curve represents the standard deviation of the associated process noise parameter of each Euler angle. Using the notation M=$\mathbf{G}_k\mathbf{Q}_k\mathbf{G}_k^T$, we have $\sqrt{\mathbf{M}(1,1)}$ for yaw angle, $\sqrt{\mathbf{M}(2,2)}$ for pitch angle and $\sqrt{\mathbf{M}(3,3)}$ for roll angle. The dashed curves represent the nominal attitude values. At the first 8 epochs, the process noise parameters are not tuned because the adaptive processing will start after the innovation sequence is full. After that we can clearly observe a decrease of the process noise caused by the adaptive tuning function. A jump in the pitch angle can be observed from 50th epoch to 65th epoch, as the airplane transits from a level flight to a “pitch-up climb”. The process noise for pitch angle immediately increases, which implies that less weight is given to the dynamic model for estimating the pitch angle. The nominal yaw and roll values do not change in this case, so that their corresponding process noise parameters are not tuned significantly. After the 65th epoch, the airplane continues the pitch-up climb for several epochs with a fixed pitch angle, and therefore the constant angular rate model still holds and the filter gives the dynamic model increasing weight. As a result, the process noise of pitch is tuned down. The Euler angles estimated by the AEKF and the FMEKF are depicted in Figure 5-10.

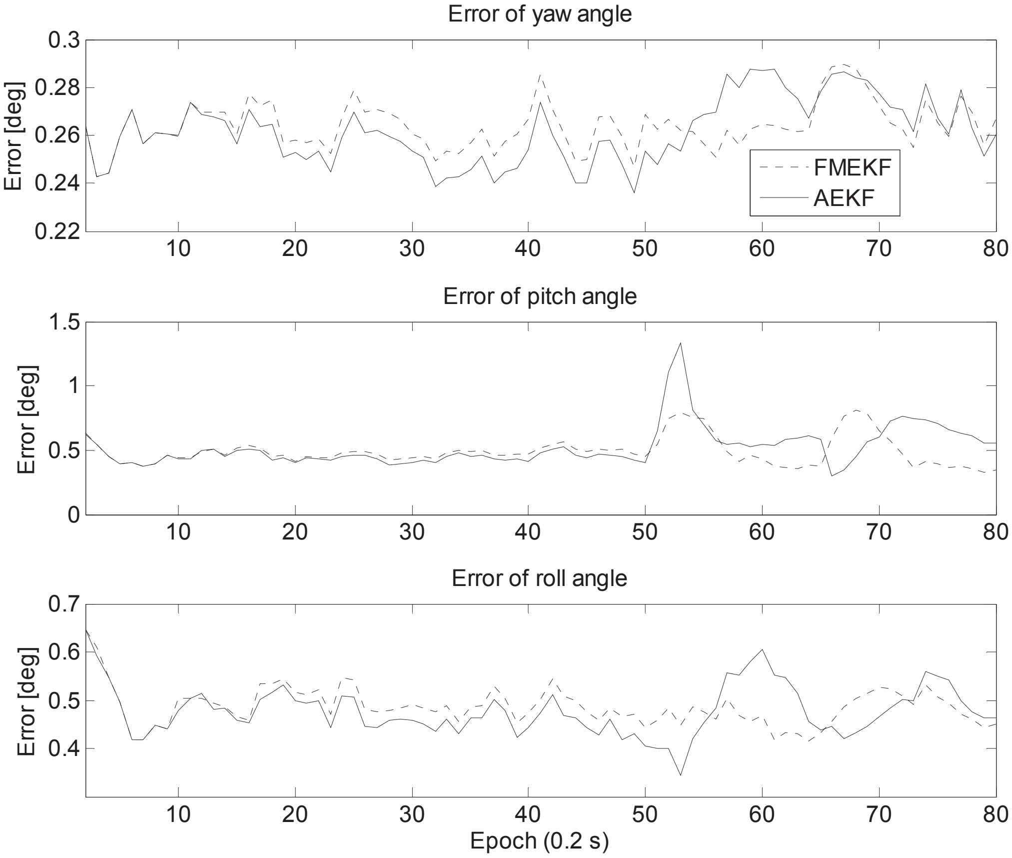

**Figure 5-10: RMSE of AEKF and FMEKF**

We can divide the results into two phases. The first phase ranges from the 1st epoch to the 50th epoch until the "pitch-up climb" occurs. Following that the second phase proceeds to the 80th epoch. As presented in Eq. (4-42), the averaged RMSEs for both phases are given in Table 5-2.

**Table 5-2: Averaged RMSE of AEKF and FMEKF**

(1st – 50th epochs)

| Algorithm | Yaw error [deg] | Pitch error [deg] | Roll error [deg] |
|---|---|---|---|
| FMEKF | 0.262 | 0.475 | 0.495 |
| AEKF | 0.252 | 0.447 | 0.466 |

(51st – 70th epochs)

| Algorithm | Yaw error [deg] | Pitch error [deg] | Roll error [deg] |
|---|---|---|---|
| FMEKF | 0.266 | 0.480 | 0.462 |
| AEKF | 0.274 | 0.614 | 0.472 |

The AEKF outputs more accurate attitude estimates in comparison with the FMEKF from

10th to 50th epochs, because the AEKF benefits more from the dynamic model. After 50th epoch, the model transition occurs and introduces the model transition errors. A serious problem is that the process noise at this time has been tuned down, making the Kalman filter give larger weight to the dynamic model. In this case, an underestimated process noise will contribute more errors on the state estimates. This phenomenon can be seen from 50th -70th epochs, where the Euler angle errors from the AEKF clearly show anomaly jumps. This reveals a significant disadvantage of the AEKF at the model transition. If the predefined stochastic dynamic model does not work properly, the adaptive tuning function can lead the filter to a divergence.

The length of the innovation sequence, also termed as window size, affects the performance of the FMEKF as well as the AEKF. The smaller the window size is, the more sensitive the filter is to the changing dynamics. However, a small window size might lead to a biased estimation, destabilization, even divergence (Mohamed 1999). Therefore, a trade-off needs to be made between the sensitivity and the stabilization. In Figure 5-11 the AEKF results under time windows of 8 and 20 epochs are presented, respectively.

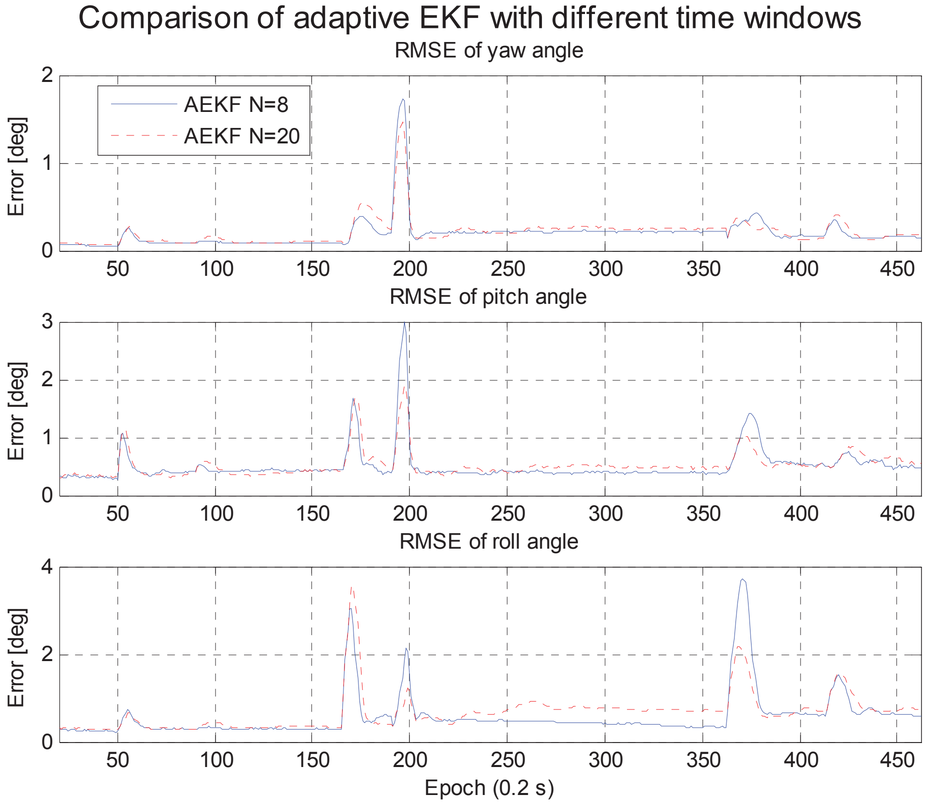

**Figure 5-11: RMSE of AEKF with different window lengths**

A shorter time window, on the one hand, outputs better attitude estimates during the stable motion phases. But on the other hand, it also yields higher magnitude of model transition errors. Figure 5-11 also shows that the model transition errors cannot be properly solved by the AEKF.

## 5.6 Interacting multiple model approach

Figure 5-3 shows that the model transition errors exhibited by the EKF normally exceed the error level of LSAD approach. It means that a failure of the dynamic model may result in larger errors than the measurement errors. A straightforward solution to this problem is to enlarge the process noise for the whole trajectory. However, the filter in this case will gain less benefit from the dynamic model. Meanwhile, when the dynamic model is adaptively tuned, a conservatively defined process noise can be tuned down, and consequently, even larger magnitude of model transition errors or filter divergence might occur at the model transition.

In recent years, multiple-model methods have drawn increasing attention in the navigation application for handling the motion mode uncertainties. The multiple-model approach is a hybrid system which needs a set of sub-filters running in parallel. Each sub-filter has its own particular dynamic model. The states are estimated by each sub-filter, and then an overall estimation is obtained by fusing the results from these sub-filters. Using the notations given in Eq. (4-1) and (4-2), each sub-filter can be described by:

$$\text{Dynamic model}: \mathbf{x}_k\left(M_i\right) = f_{k-1,M_i}\left[\mathbf{x}_{k-1}\left(M_i\right)\right] + g_{k-1,M_i}\left[\mathbf{w}_{k-1}\left(M_i\right)\right] \tag{5-10}$$

$$\text{Measurement model: } \mathbf{z}_k = h_{k,M_i}\left[\mathbf{x}_{k-1}\left(M_i\right)\right] + \mathbf{v}_k\left(M_i\right) \tag{5-11}$$

where $M_i$ indicates $i$-th model. The sub-filters share the same measurement vector.

An important limitation of the multiple-model methods in previous applications lies in the computational load caused by the filters running in parallel. However, the advance in processor technology allows the wide use of multiple-model approaches (Hide et al. 2003). The multiple-model approaches can be categorized into static multiple-model approaches and dynamic multiple-model approaches. Among different dynamic multiple-model approaches, the Interacting Multiple Model (IMM) estimator is one of the most efficient ones (Blom and Bar-Shalom 1988). Just as the name implies, there is an interaction step for calculating the initial conditions of each sub-filter. In the interaction step, the *a posteriori* estimates of all sub-filters are fused according to the model probabilities and model transition probabilities. A comparison between the static multiple-model approach and the IMM based on a dual-filter architecture is illustrated in Figure 5-12.

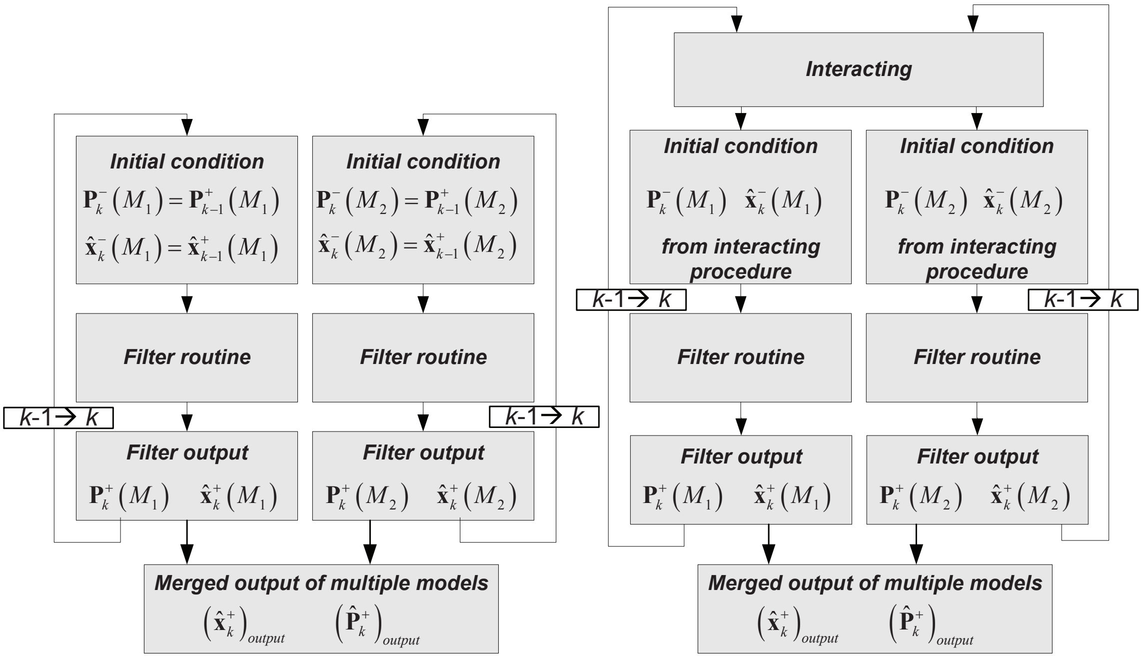

**Static multiple-model approach** **IMM approach**

Figure 5-12: Static and interacting multiple-model approaches

A good performance of a static multiple-model approach relies on the following prerequisites (Bar-Shalom et al. 2001). Firstly, the correct model should exist among the set of models. Secondly, each model should take effect and work properly during the whole observation session. The latter requirement will face a problem when the model transition occurs. In order to solve this problem, modifications must be made to the static multiple-model approaches. A commonly-used method is to add an empirical upper bound to the norm of the innovation vector. This upper bound indicates the occurrence of the temporary filter divergence, so that this model can be excluded from the set of running sub-filters in order to fulfill the prerequisites mentioned above. In the IMM, the interacting procedure is used to maintain the proper running of each sub-filter. The sub-filter with large innovation will be less weighted instead of being excluded. In this sense, the IMM better fits the model-switching scenarios than the static multiple-model approach.

### 5.6.1 Implementation of an interacting multiple model approach

Concerning our application, we can have two sub-filters running in parallel. One sub-filter mainly relies on the measurement model, i.e. it has a large process noise and is less affected by the mismodeling errors. The other sub-filter has a smaller process noise, like the EKF used in chapter 5.1. Both sub-filters can be merged using the IMM approach. A cycle of the IMM composed of two sub-filters is illustrated in Figure 5-13.

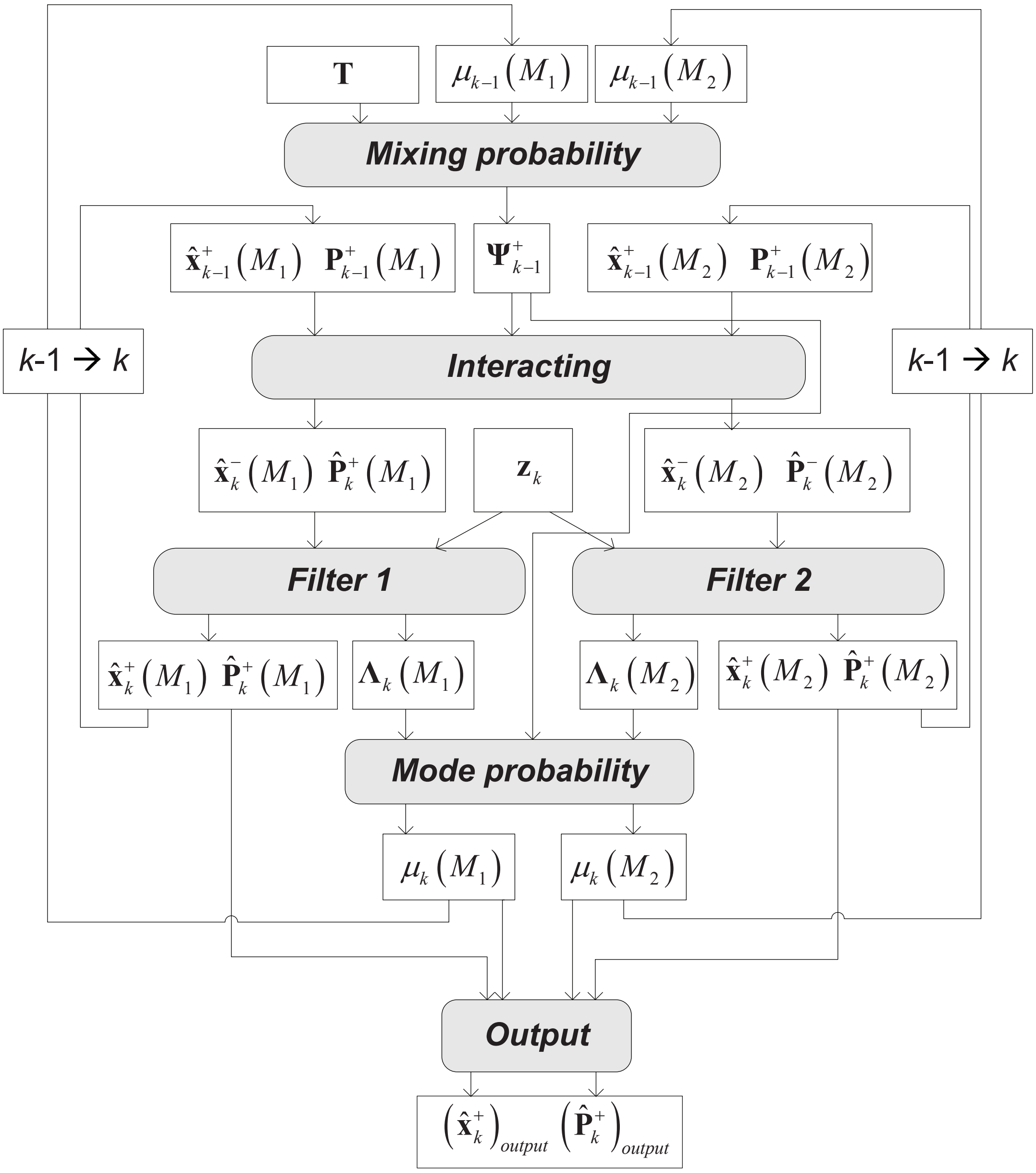

**Figure 5-13: Flowchart of an IMM**

The derivation of this algorithm can be found in (Bar-Shalom et al. 2001). The symbols shown in the flowchart are briefly explained below and detailed later in the following context:

| | |
|---|---|
| $\mathbf{P}_k^+(M_i)$ | State estimates and error covariance matrix at time *k* for sub-filter *i* |
| $\left(\hat{\mathbf{x}}_k^+\right)_{output}$ $\left(\hat{\mathbf{P}}_k^+\right)_{output}$ | State estimates and error covariance matrix for merged output |
| $\mathbf{T}$ | Model transition probability matrix |
| $\mu$ | Model probability |
| $\mathbf{z}$ | Measurement vector |

| | |
|---|---|
| $M_i$ | Sub-filter *i* |
| $\mathbf{\Psi}$ | Mixing probability matrix |
| $\Lambda$ | Model-matched likelihood |

**Step 1 : Initialization of IMM:**

Before applying the IMM, two probability terms should be initialized. The ***model transition probability*** matrix **T** indicates the probability of one model changing to another and is assumed to be time-invariant. With two sub-filters, matrix **T** has a form of

$$\mathbf{T} = \begin{bmatrix} \mathbf{T}(1,1) & \mathbf{T}(1,2) \\ \mathbf{T}(2,1) & \mathbf{T}(2,2) \end{bmatrix} \tag{5-12}$$

$$\text{with } \mathbf{T}(i,j) = \mu_{m_k | m_{k-1}, z_{k-1}} \left\{ M_j \middle| M_i, z_{k-1} \right\}$$

$\mathbf{T}(1,1)$ and $\mathbf{T}(2,2)$ represent the probability of sub-filter 1 and sub-filter 2 taking effects during the entire trajectory, respectively; $\mathbf{T}(1,2)$ and $\mathbf{T}(2,1)$ represent the probability of one filter switching to the other. The sum of each column and each row should be 1. The second probability term to be initialized is the ***model probability*** denoted by $\mu$, which indicates the weight of each filter taken for the merged output. This term will be updated epoch by epoch in each IMM cycle.

**Step 2 : Calculation of the mixing probability**

The ***mixing probability*** matrix $\mathbf{\Psi}$ is used for the interaction step. An associated component $\mathbf{\Psi}(i,j)$ reflects how the probability of model i at current epoch is affected by the given probability of model j of last epoch. To calculate $\mathbf{\Psi}$, both the model transition probability matrix and model probability $\mu$ are considered by applying the Bayes' theorem and total probability theorem (Bar-Shalom et al. 2001, Zhang 2010):

$$
\begin{aligned}
\boldsymbol{\Psi}_{k-1}^{+}\left(M_i \middle| M_j\right) &= \mu_{m_{k-1}|m_k,\mathbf{z}_{k-1}}\left\{M_i \middle| M_j,\mathbf{z}_{k-1}\right\} \\
&= \frac{\mu_{m_{k-1},m_k,\mathbf{z}_{k-1}}\left\{M_i, M_j,\mathbf{z}_{k-1}\right\}}{\mu_{m_k|\mathbf{z}_{k-1}}\left\{M_j,\mathbf{z}_{k-1}\right\}} \\
&= \frac{\mu_{m_k|m_{k-1},\mathbf{z}_{k-1}}\left\{M_j \middle| M_i,\mathbf{z}_{k-1}\right\}\mu_{m_{k-1}|z_{k-1}}\left\{M_i \middle| \mathbf{z}_{k-1}\right\}\mu_{z_{k-1}}\left\{\mathbf{z}_{k-1}\right\}}{\mu_{m_k|\mathbf{z}_{k-1}}\left\{M_j \middle| \mathbf{z}_{k-1}\right\}\mu_{\mathbf{z}_{k-1}}\left\{\mathbf{z}_{k-1}\right\}} \\
&= \frac{\mu_{m_k|m_{k-1},\mathbf{z}_{k-1}}\left\{M_j \middle| M_i,\mathbf{z}_{k-1}\right\}\mu_{m_{k-1}|\mathbf{z}_{k-1}}\left\{M_i \middle| \mathbf{z}_{k-1}\right\}}{\mu_{m_k|\mathbf{z}_{k-1}}\left\{M_j \middle| \mathbf{z}_{k-1}\right\}} \\
&= \frac{\mu_{m_k|m_{k-1},\mathbf{z}_{k-1}}\left\{M_j \middle| M_i,\mathbf{z}_{k-1}\right\}\mu_{m_{k-1}|\mathbf{z}_{k-1}}\left\{M_i \middle| \mathbf{z}_{k-1}\right\}}{\sum_{i=1}^{n}\mu_{m_k|m_{k-1},\mathbf{z}_{k-1}}\left\{M_j \middle| M_i,\mathbf{z}_{k-1}\right\}\mu_{m_{k-1}|\mathbf{z}_{k-1}}\left\{M_i \middle| \mathbf{z}_{k-1}\right\}}
\end{aligned}
\tag{5-13}
$$

where $n$ is the number of sub-filters. Denoting $\mu_{m_k|\mathbf{z}_k}\left\{M_i \middle| \mathbf{z}_k\right\}$ with $\mu_k\left(M_i\right)$ and using the time-invariant model transition probability $\mathbf{T}$ in (5-12) we have:

$$
\boldsymbol{\Psi}_{k-1}^{+}\left(M_i \middle| M_j\right) = \frac{\mathbf{T}(i,j)\,\mu_{k-1}\left(M_i\right)}{\sum_{a=1}^{n}\mathbf{T}(a,j)\,\mu_{k-1}\left(M_a\right)} \quad \text{for } i,j=1,2,\ldots n \tag{5-14}
$$

Note that the model probability $\mu$ obtained at time *k-1* allows the mixing at the beginning of each IMM cycle at time *k*.

**Step 3 : Interaction for the filter initial conditions**

The mixing probability can be fused with the *a posteriori* state estimates and the covariance matrices of all sub-filters at the last epoch to yield the initial condition for each sub-filter at current epoch:

$$
\hat{\mathbf{x}}_k^{-}\left(M_j\right) = \sum_{i=1}^{n}\hat{\mathbf{x}}_{k-1}^{+}\left(M_i\right)\boldsymbol{\Psi}_{k-1}^{+}\left(M_i \middle| M_j\right) \quad for\ j=1,2,\ldots n \tag{5-15}
$$

$$
\mathbf{P}_k^{-}\left(M_j\right) = \sum_{i=1}^{n}\boldsymbol{\Psi}_{k-1}^{+}\left(M_i \middle| M_j\right)\left\{\mathbf{P}_k^{-}\left(M_i\right) + \left[\hat{\mathbf{x}}_{k-1}^{+}\left(M_i\right) - \hat{\mathbf{x}}_k^{-}\left(M_i\right)\right]\left[\hat{\mathbf{x}}_{k-1}^{+}\left(M_i\right) - \hat{\mathbf{x}}_k^{-}\left(M_i\right)\right]^T\right\} \tag{5-16}
$$

$$
for\ j=1,2,\ldots n
$$

**Step 4 : Kalman filter routine with model-matched likelihood calculation**

Each sub-filter will be executed by taking the initial conditions obtained from Eq. (5-15) and Eq. (5-16) into the routine. Once the measurement at time *k* is available, the ***model-matched***

***likelihood*** function can be obtained from the innovation vector as follows:

$$\Lambda_k\left(M_j\right)=\frac{1}{\sqrt{\left(2\pi\right)^l\cdot\det\left[\mathbf{C}_k\left(M_j\right)\right]}}\exp\left\{-\frac{1}{2}\mathbf{s}_k^T\left(M_j\right)\left[\mathbf{C}_k\left(M_j\right)\right]^{-1}\mathbf{s}_k\left(M_j\right)\right\} \qquad \text{(5-17)}$$

$$for \quad j=1,2,\ldots n$$

where $l$ is the dimension of measurement vector; det$(\cdot)$ denotes the determinant of a matrix; **s** is the innovation vector; $\mathbf{C}_k$ is the error covariance matrix of the innovation vector and can be calculated by $\mathbf{C}_k=\mathbf{H}_k\mathbf{P}_k^-\mathbf{H}_k^T+\mathbf{R}_k$. The equation is valid under the assumption that the measurements have Gaussian noises and the measurement model has been linearized.

**Step 5 : Model probability update**

The model probability of sub-filter *j* can be related to the model-matched likelihood function Λ, the model transition probability matrix **T** and the previous model probabilities by the following equation:

$$\mu_k\left(M_j\right)=\frac{\Lambda_k\left(M_j\right)\sum_{i=1}^{n}\mathbf{T}\left(i,j\right)\mu_{k-1}\left(M_j\right)}{\sum_{a=1}^{n}\Lambda_k\left(M_a\right)\left[\sum_{i=1}^{n}\mathbf{T}\left(i,a\right)\mu_{k-1}\left(M_i\right)\right]} \quad for\, j=1,2,\ldots n \qquad \text{(5-18)}$$

Eq. (5-18) shows that the model probability of a sub-filter depends on its current model-matched likelihood function with respect to the likelihood functions of other sub-filters. Implied from term $\mu_{k-1}$ (model probability at last epoch), the history of the model probabilities from all sub-filters are taken into account. In other words, the model probability of a sub-filter depends on its relative performance with respect to the other sub-filters not only at the current epoch but also in the history.

**Step 6 : Calculation of the merged output**

The output from the IMM is a weighted sum of the *a posteriori* state estimates and covariance matrices of all sub-filters. The weight herein is determined by the model probabilities.

$$\left(\hat{\mathbf{x}}_k^+\right)_{output}=\sum_{j=1}^{n}\hat{\mathbf{x}}_k^+\left(M_j\right)\mu_k\left(M_j\right) \qquad \text{(5-19)}$$

$$\left(\mathbf{P}_k^+\right)_{output}=\sum_{j=1}^{n}\mu_k\left(M_j\right)\left\{\mathbf{P}_k^+\left(M_j\right)+\left[\left(\hat{\mathbf{x}}_k^+\right)_{output}-\hat{\mathbf{x}}_k^+\left(M_j\right)\right]\left[\left(\hat{\mathbf{x}}_k^+\right)_{output}-\hat{\mathbf{x}}_k^+\left(M_j\right)\right]^T\right\} \qquad \text{(5-20)}$$

It should be stressed that $\left(\hat{\mathbf{x}}_k^+\right)_{output}$ and $\left(\mathbf{P}_k^+\right)_{output}$ serve as merely the output to the users. They will not be fed back to the IMM at next time epoch.

### 5.6.2 Performance comparison of IMM and FMEKF

Concerning the reduction of model transition errors, the IMM outperforms the FMEKF, which can be demonstrated using simulations. The IMM is configured with the following parameters:

**Table 5-3: Initialization parameters for IMM**

| | |
|---|---|
| **Process noise for sub-filter 1** | $\sigma_{\ddot{y}} = 0.35\,[\text{deg}/\Delta\text{epoch}^2]$<br>$\sigma_{\ddot{p}} = \sigma_{\ddot{r}} = 0.4\,[\text{deg}/\Delta\text{epoch}^2]$ |
| **Process noise for sub-filter 2** | $\sigma_{\ddot{y}} = \sigma_{\ddot{p}} = \sigma_{\ddot{r}} = 1.5\,[\text{deg}/\Delta\text{epoch}^2]$ |
| **Thermal noise of carrier phase (for R) for both sub-filters** | 2 mm |
| **Initial state error covariance matrix $\mathbf{P}_0^+$ for both sub-filters** | $\sigma_y = 0.4\left[\text{deg}\right] \quad \sigma_p = \sigma_r = 0.6\left[\text{deg}\right]$<br>$\sigma_{\dot{y}} = \sigma_{\dot{p}} = \sigma_{\dot{r}} = 0.4\left[\text{deg}/\,\Delta\text{epoch}\right]$ |
| **Initial attitude values for both sub-filters** | LSAD at first epoch |
| **Initial angular rates for both sub-filters** | They are set as zeros. |
| **Model transition probability matrix** | $\mathbf{T} = \begin{bmatrix} \mathbf{T}(1,1) & \mathbf{T}(1,2) \\ \mathbf{T}(2,1) & \mathbf{T}(2,2) \end{bmatrix} = \begin{bmatrix} 0.9 & 0.1 \\ 0.1 & 0.9 \end{bmatrix}$ |
| **Initial model probability** | $\mu_0(M_1) = \mu_0(M_2) = 0.5$ |

The sub-filter with small process noise parameters has a dominant probability in matrix **T**, meaning that the constant angular model should take effects with large probability during the trajectory. Figure 5-14 shows the RMSE of estimated Euler angles using the IMM and the FMEKF with a time window of 8 epochs. The FMEKF is configured as in section 5.4.2:

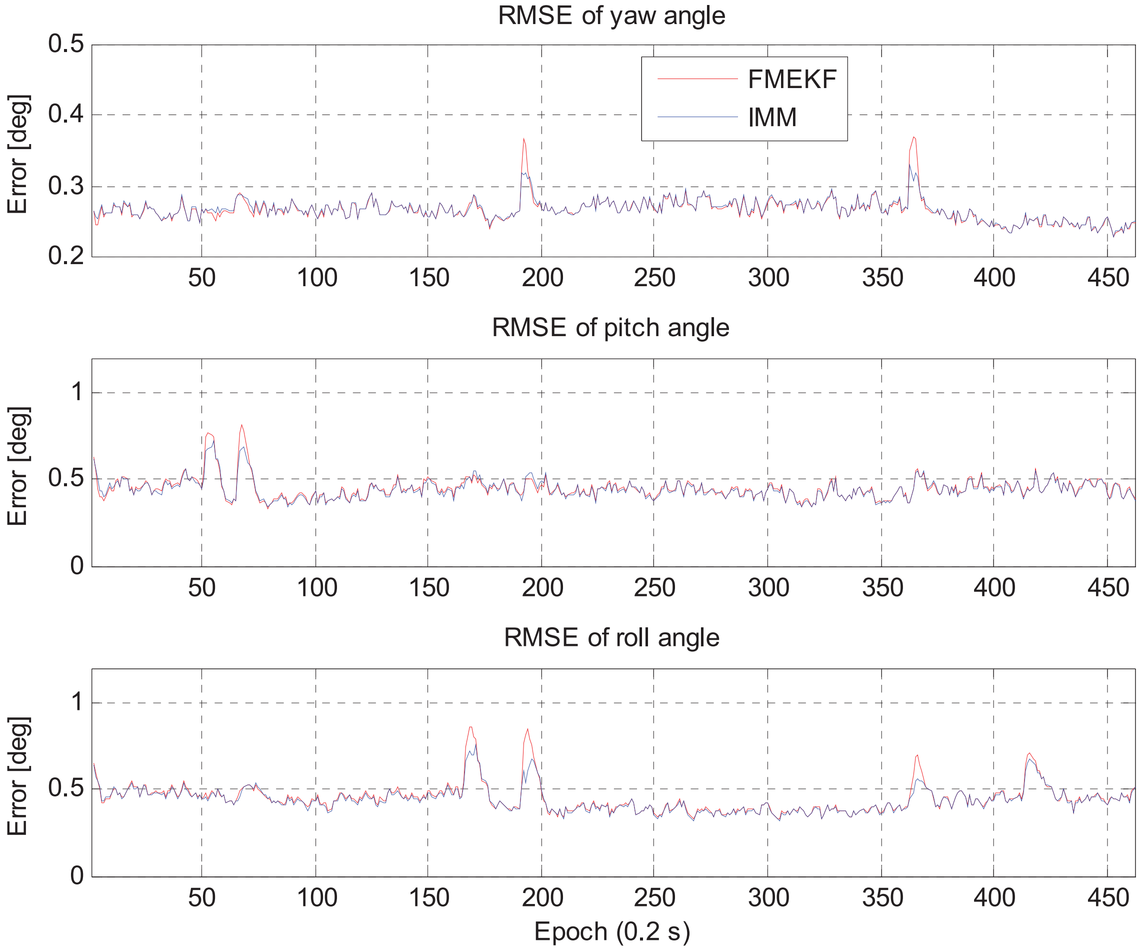

**Figure 5-14: RMSE of IMM and FMEKF**

The IMM and FMEKF offer similar accuracies if no model transition occurs. However, the model transition errors from the IMM are lower than those from the FMEKF during the model transition phases. Examples can be seen from 50th-70th epochs for pitch angle and from 160th-200th epochs for roll angle. This is due to the reduced model probability of the sub-filter with small process noise, which can be seen from Figure 5-15.

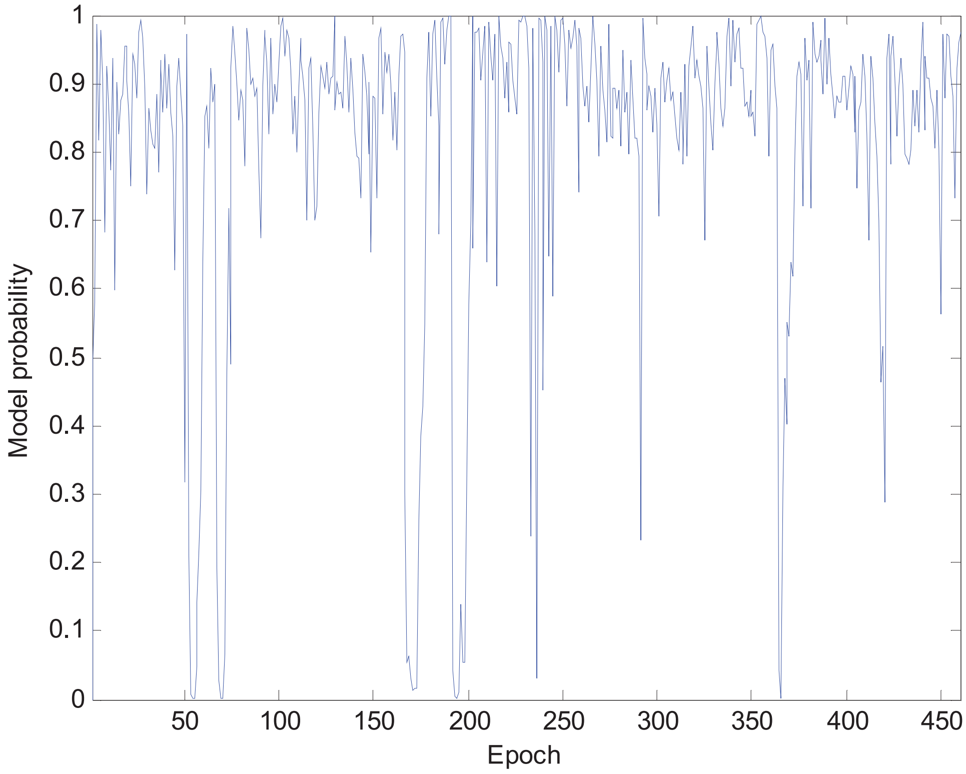

**Figure 5-15: Model probability of the sub-filter with small process noise**

In most epochs, the model probability of the sub-filter with small process noise is more than 60%. However, it can be remarkably reduced in some epochs, for example, 50th-70th epochs, 160th -200th epochs and 360th-380th epochs. Comparing with the Figure 5-3 it is clear that the model transitions take place during these epochs. In these cases, the merged output from an IMM mainly comes from the sub-filter with larger process noises.

## 5.7 Adaptive interacting multiple model approach

From the comparison given in Figure 5-14 it can be seen that the IMM does not offer higher accuracy in stable motion phases, as it has no adaptive tuning function to the process noise. By incorporating the adaptive tuning function into the IMM, we can have an adaptive IMM approach (AIMM). An AIMM consists of two sub-filters. One sub-filter has fixed and large process noise parameters and is robust to the mismodeling errors. The other sub-filter features an adaptive tuning function. A routine of AIMM can be seen in the following flowchart.

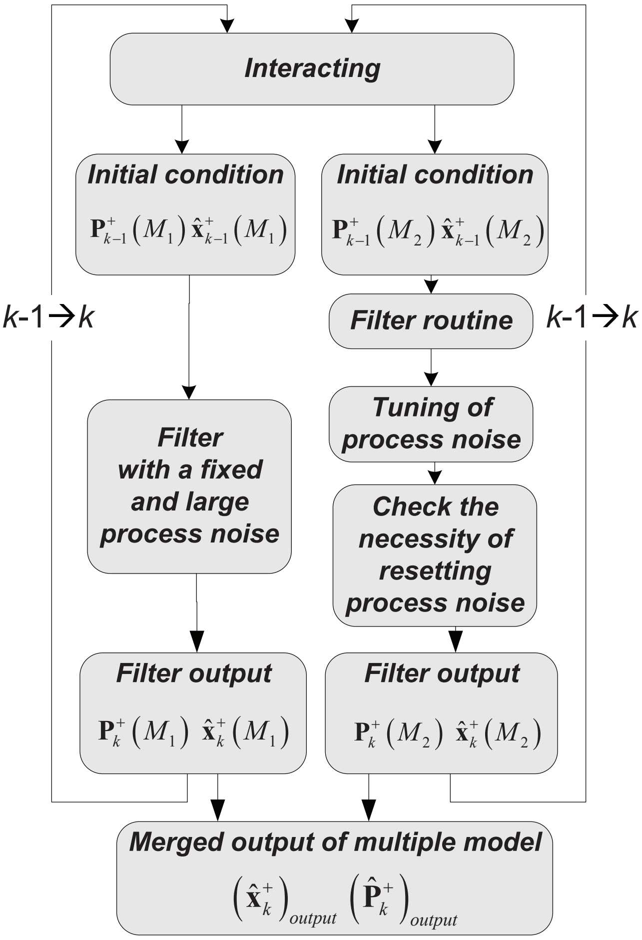

**Figure 5-16: Flowchart of an AIMM routine**

The difference between the AIMM and the IMM only lies in whether or not the adaptive tuning function is embedded into the sub-filter with small process noise. The adaptive tuning of process noise based on innovation vectors has been introduced in section 5.5. This technique can lead the filter to an instable status if an extraordinarily large innovation vector exists in the innovation sequence. To solve this problem, the tuning function of process noise parameters will be suspended if an innovation anomaly is detected. The tuning function will be restored once the sub-filter is in a steady-state. The innovation anomalies can be detected by the following methods:

- Check the norm of the innovation vectors of the current epoch. If it is significantly larger than the average value of previous innovation vectors inside the time window, a reset of process noise parameters will take place.
- Check the model probability of the sub-filter with small process noise. This value is very small during the model transition phases, which can be known from Figure 5-15.

Once one of the aforementioned conditions holds true, process noise parameters will be reset to their initial values given at the filter initialization and the innovation sequence is cleared. This operation aims at invoking the adaptive tuning function only if the sub-filter is running under the predefined stochastic conditions.

The RMSE of Euler angles estimated by the AIMM and the IMM are compared in Figure 5-17. The length of time window is 8 epochs, and the process noise parameters are reset if the model probability of sub-filter with small process noise is lower than 30%.

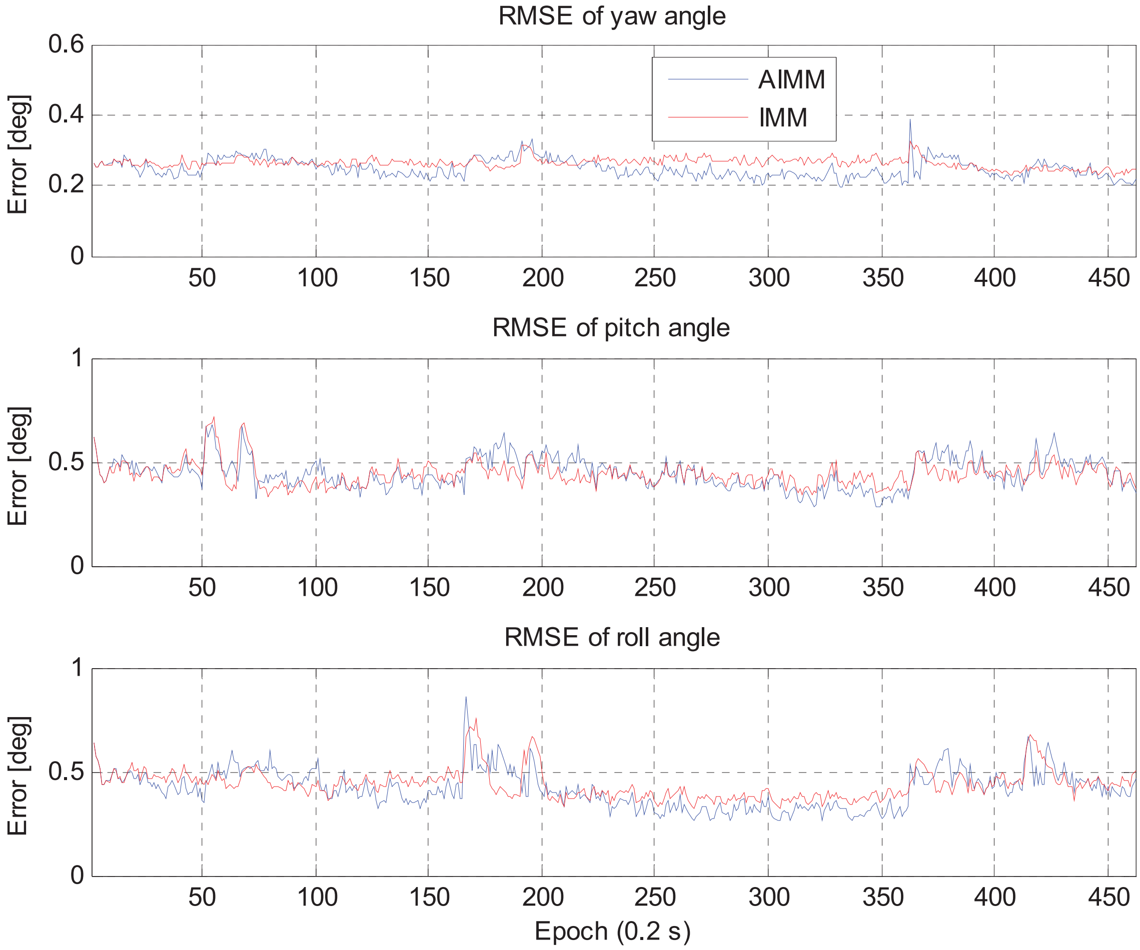

**Figure 5-17: RMSE of AIMM and conventional IMM**

From Figure 5-17 we can see that the AIMM outperforms the conventional IMM during the stable motion phases due to the adaptive tuning function, for example from 200th to 360th epoch. Although the magnitude of model transition errors obtained from the AIMM are slightly larger than the conventional IMM, they are still lower than the FMEKF.

At the beginning of this chapter we have presented the RMSE of the LSAD and the EKF. A comparison in terms of accuracy between the AIMM and both approaches is illustrated in Figure 5-18.

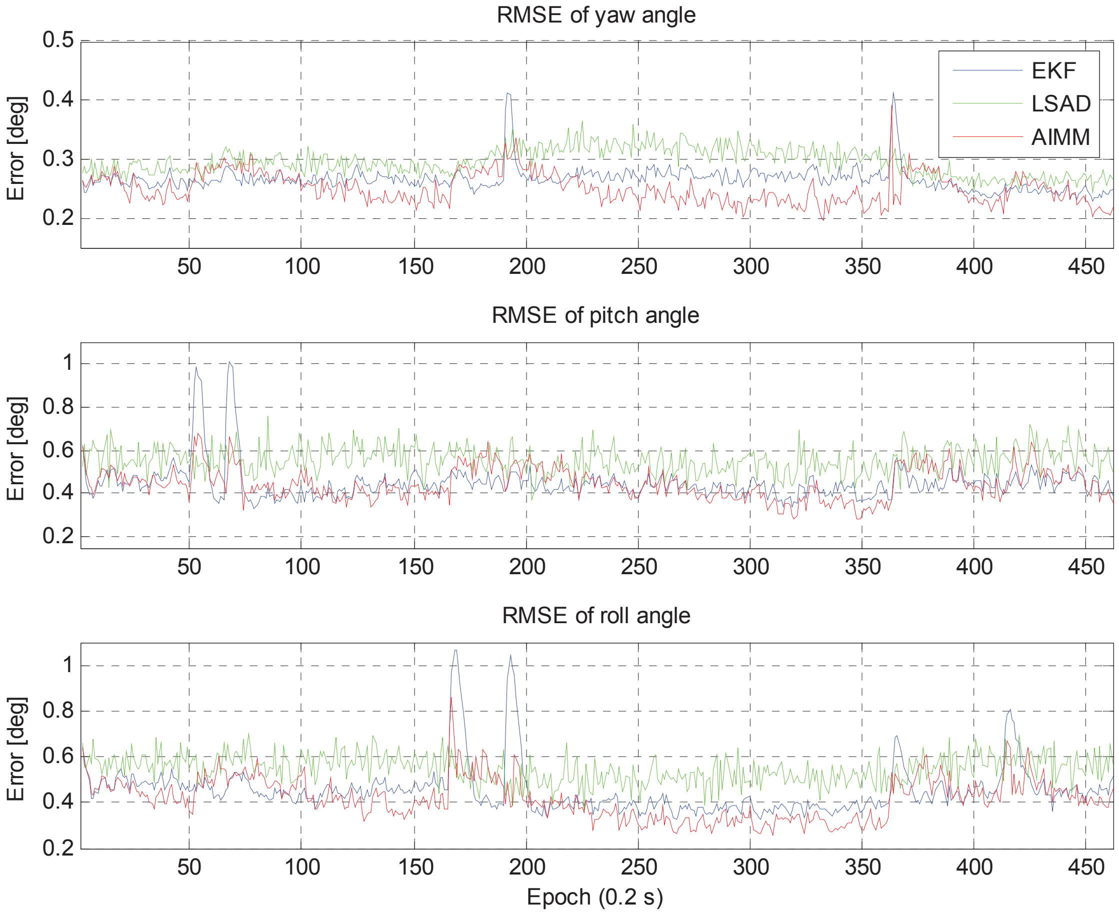

**Figure 5-18: RMSE of AIMM, EKF and LSAD**

At the model transition, the model transition errors from the EKF are clearly reduced by the AIMM. During the stable motion phases, the AIMM benefits more from the dynamic model and hence offers higher accuracy. The AIMM integrates the robustness to the model transition and adaptive tuning function of process noise, and therefore it can be adopted as a proper approach to handle the two-fold mismodeling errors introduced at the beginning of this chapter.

## 5.8 Computational complexity

The computational burden of the presented approaches is quantified in Table 5-4. The processing time of one cycle is obtained in the same computational environment and by the same method presented in section 4.5.3. The processing time of the FMEKF and the AIMM depends on the length of time window used.

Table 5-4: Computational time of different approaches

| Approach (N=length the time window) | Time needed per cycle [ms] |
|---|---|
| EKF | 3.5 |
| FMEKF (N=8 epochs) | 6.31 |
| FMEKF (N=20 epochs) | 6.49 |
| FMEKF (N=40 epochs) | 6.69 |
| IMM | 10.1 |
| Adaptive IMM (N=8 epochs) | 11.44 |
| Adaptive IMM (N=20 epochs) | 11.65 |
| Adaptive IMM (N=40 epochs) | 11.77 |

## 5.9 Conclusions

Using a constant angular model to approximate the attitude dynamics may bring in two kinds of mismodeling errors. The first type of mismodeling error takes place when the airplane changes the motion model, where the errors from EKF will show model transition errors. This kind of error can only be slightly reduced by using other nonlinear Kalman filters. The EKF with variant fading-memory factors can better handle the model transition errors. Furthermore, the IMM approach is more robust to the model transition than the FMEKF. The second type of mismodeling error lies in the fixed and conservatively initialized process noises. The AEKF with a tuning function of the process noise parameters is a suitable approach for this case. However, it might lead the filter to a divergence under the first kind of mismodeling error. An AIMM approach has been proposed to handle both mismodeling errors. Simulation results indicate that the AIMM offers higher accuracy in both stable motion phases and model transition phases compared to the conventional EKF.

# 6. Error analysis for position, attitude and SAR related parameters

The inaccurately estimated position of SAR Antenna Phase Center (APC) is a primary source of undesirable SAR phase errors. The errors during a SAR coherent integration time will introduce serious deterioration in the resolution and geometry of the final image. Besides that, an incorrect Doppler Centroid Frequency (DCF) might result in the misregistration and degradation in azimuth. In order to obtain the APC position and DCF, the position, velocity and attitude of the airplane are needed. These states can be obtained from GPS using the configuration given in Figure 6-1.

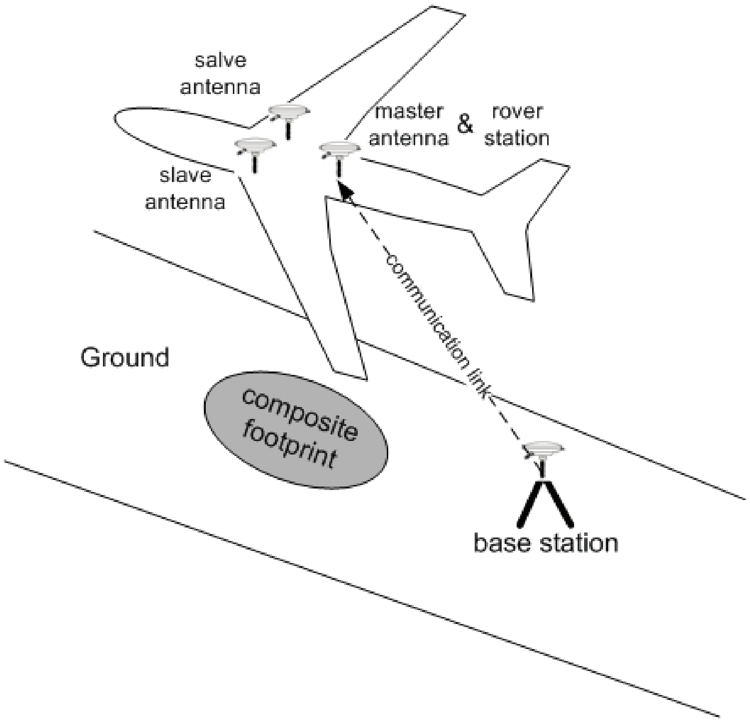

**Figure 6-1: Configuration of GPS devices for TerraSAR/PAMIR experiment**

A GPS multi-antenna system allows the attitude determination. A configuration of base and rover stations is used for precise positioning. In order to study the feasibility of using only GPS in SAR experiment, it is important to know the effects of the potential GPS errors on the motion compensation. For this purpose, the relation between the information obtained from GPS and the information required by the motion compensation will be established. An error analysis will be carried out as well.

## 6.1 Error propagation in position and attitude domain

The differential positioning technique is not only the technique for precise positioning, but also the basis for the attitude determination. The GPS carrier phase measurements are usually assumed to contain Gaussian white noise. For short baselines, especially for the multiple onboard antennas, atmospheric errors are normally eliminated and hence the thermal noise and the multipath error are the major remaining errors. In this chapter, we mainly consider the error propagation from thermal noise of GPS carrier phase measurements to the position and attitude parameters.

### 6.1.1 Error propagation from single to double-differenced measurements

At first, the double-differential positioning equation (1-15) is recalled here:

$$\lambda_{Li}\Delta\nabla\Phi_{u1-u2}^{s1-s2} = \Delta\nabla\rho_{u1-u2}^{s1-s2} + \lambda_{Li}\Delta\nabla N_{u1-u2}^{s1-s2}{}_{,Li} + \Delta\nabla e_{u1-u2}^{s1-s2} + \Delta\nabla M_{u1-u2}^{s1-s2} \tag{6-1}$$

The operator $\Delta\nabla$ denotes double-differencing; The subscripts *u1 and u2* identify the GPS receiver's antenna 1 and 2, respectively; the superscripts $s1$ and $s2$ identify the satellite 1 and satellite 2, respectively; the notation of $u1$-$u2$ and $s1$-$s2$ indicate that the differencing is made between two antenna and two satellites; $\lambda$ is the GPS signal wavelength; the subscript $L_i$ identifies the carrier signal; $\Phi$ is the carrier phase measurement; $\rho$ is the geometry distance from the GPS receiver's antenna to the GPS satellite; $N$ is the integer phase ambiguity; $e$ is the carrier phase thermal noise; $M$ is the multipath error. In order to analyze the error propagation from the single GPS carrier phase measurements onto the double-differenced carrier phase measurements, the term $\Delta\nabla\Phi_{u1-u2}^{s1-s2}$ can be detailed as:

$$\begin{aligned}\Delta\nabla\Phi_{u1-u2}^{s1-s2} &= \left(\Phi_{u1}^{s1} - \Phi_{u2}^{s1}\right) - \left(\Phi_{u1}^{s2} - \Phi_{u2}^{s2}\right) \\ &= \begin{bmatrix}1 & -1 & -1 & 1\end{bmatrix}\begin{bmatrix}\Phi_{u1}^{s1} & \Phi_{u1}^{s2} & \Phi_{u2}^{s1} & \Phi_{u2}^{s2}\end{bmatrix}^T\end{aligned} \tag{6-2}$$

Considering a two-antenna configuration with $n$ common satellites in view, the double-differenced carrier phase measurement $\Delta\nabla\boldsymbol{\Phi}$ can be formed as:

$$\begin{aligned}\Delta\nabla\boldsymbol{\Phi} &= \mathbf{A}_{DD}\begin{bmatrix}\Phi_{u1}^{s1} & \cdots & \Phi_{u1}^{sn} & \Phi_{u2}^{s1} & \cdots & \Phi_{u2}^{sn}\end{bmatrix}^T \\ \mathbf{A}_{DD} &= \begin{bmatrix}\mathbf{1}_{(n-1)\times 1} & -\mathbf{I}_{(n-1)\times(n-1)} & -\mathbf{1}_{(n-1)\times 1} & \mathbf{I}_{(n-1)\times(n-1)}\end{bmatrix}\end{aligned} \tag{6-3}$$

where the bold "**1**" indicates the vector with all components being one; **I** is the identify matrix. Note that the satellite 1 is chosen as the key satellite. We assume that the carrier phase measurements from different satellites have uncorrelated Gaussian white noise with a standard deviation $\sigma_\Phi$, so that the double-differenced carrier phase measurements have the error of:

$$Cov\left(\Delta\nabla\mathbf{\Phi}\right) = \mathbf{A}_{DD} \cdot \sigma_{\Phi}^{2} \cdot \mathbf{A}_{DD}^{T} \tag{6-4}$$

### 6.1.2 Error propagation from measurement domain to position domain

The linearized double-difference positioning model can be formulated as:

$$\begin{bmatrix} \lambda_{L1}\Delta\nabla\Phi_{u1-u2}^{s1-s2} - \lambda_{L1}\Delta\nabla N_{u1-u2}^{s1-s2} - \Delta\nabla\rho_{u1-u2}^{s1-s2} \\ \cdots \\ \lambda_{L1}\Delta\nabla\Phi_{u1-u2}^{s1-sn} - \lambda_{L1}\Delta\nabla N_{u1-u2}^{s1-sn} - \Delta\nabla\rho_{u1-u2}^{s1-sn} \end{bmatrix} = \underbrace{\begin{bmatrix} \mathbf{G}_2 \\ \cdots \\ \mathbf{G}_n \end{bmatrix}}_{\mathbf{G}} \underbrace{\begin{bmatrix} x_{ECEF} \\ y_{ECEF} \\ z_{ECEF} \end{bmatrix}}_{\mathbf{x}^{ECEF}} + \boldsymbol{\omega} \tag{6-5}$$

$$\text{with } \mathbf{G}_j = \left[ -\frac{x^{sj} - x_{u2}}{\rho_{u2}^{sj}} + \frac{x^{s1} - x_{u2}}{\rho_{u2}^{s1}} \quad -\frac{y^{sj} - y_{u2}}{\rho_{u2}^{sj}} + \frac{y^{s1} - y_{u2}}{\rho_{u2}^{s1}} \quad -\frac{z^{sj} - z_{u2}}{\rho_{u2}^{sj}} + \frac{z^{s1} - z_{u2}}{\rho_{u2}^{s1}} \right]$$

where the terms at the left-hand side have been introduced by Eq. (6-1); at the right-hand side, vector $\mathbf{x}^{ECEF}$ includes the ECEF coordinate of the rover antenna which is identified here by antenna *u2*; matrix **G** comprises the unit direction vectors with $\rho_{u2}^{sj}$ being the distance from satellite *j* to the rover antenna; *j* is the satellite number from 1 to total number of satellites; The vector $\boldsymbol{\omega}$ contains the thermal noises of the double-difference phase measurements and other remaining errors, including mainly the ionospheric error, tropospheric error and the multipath delay. The remaining ionospheric and tropospheric errors are highly dependent on the baseline between the base and rover antenna. Given a short-baseline (shorter than 10 km on the ground) between the base and rover antenna, the remaining ionospheric and tropospheric are negligible. We also ignore multipath errors for simplicity.

The DOP for single-point positioning has been introduced in 1.3.5 and detailed in the appendix. Similar to that, in the differential positioning, the effects of the satellite geometry in the position domain can also be quantified by DOP. For example, using the term G in (6-5), the PDOP in differential positioning can be calculated as (e.g. Nielsen 1997):

$$PDOP = \sqrt{trace\left(\left(\mathbf{G}^{\mathrm{T}}\mathbf{G}\right)^{-1}\right)} \tag{6-6}$$

### 6.1.3 Transformation from ECEF to LLF

The transformation from the ECEF ($\mathbf{x}^{ECEF}$) to the LLF ($\mathbf{x}^{LLF}$) can be formulated as:

$$\underbrace{\begin{bmatrix} x_l \\ y_l \\ z_l \end{bmatrix}}_{\mathbf{x}^{LLF}} = \underbrace{\begin{bmatrix} -\sin\lambda & \cos\lambda & 0 \\ -\sin\varphi\cos\lambda & -\sin\varphi\sin\lambda & \cos\varphi \\ \cos\varphi\cos\lambda & \cos\varphi\sin\lambda & \sin\varphi \end{bmatrix}}_{\mathbf{R}_{ECEF}^{LLF}} \underbrace{\begin{bmatrix} x_{ECEF} \\ y_{ECEF} \\ z_{ECEF} \end{bmatrix}}_{\mathbf{x}^{ECEF}} \tag{6-7}$$

where $\mathbf{R}_{ECEF}^{LLF}$ is the rotation matrix indicating the projection of a target point from the ECEF to the LLF; $\varphi$ and $\lambda$ denote the latitude and longitude of the reference point, respectively. The longitude and latitude can be derived from the known Cartesian coordinates (Hofmann-Wellenhof et al. 2001).

### 6.1.4 Error analysis for double-difference positioning in LLF

Equations from (6-3) to (6-7) indicate the sequential procedure for calculating the LLF coordinate. Since the carrier phase noise is assumed to be Gaussian white noise, the errors in the LLF coordinate $Cov\left(\mathbf{l}_i\right)$ can be derived by applying the error propagation law to the double-differenced carrier phase noise:

$$Cov\left(\mathbf{l}_i\right) = \mathbf{R}_{ECEF}^{LLF} \underbrace{\left(\mathbf{G}^T \left(\mathbf{A}_{\mathbf{DD}} \sigma_{\Phi}^2 \mathbf{A}_{\mathbf{DD}}^T\right)^{-1} \mathbf{G}\right)^{-1}}_{Cov\left(\mathbf{x}^{ECEF}\right)} \left(\mathbf{R}_{ECEF}^{LLF}\right)^T \tag{6-8}$$

## 6.2 Error analysis for attitude determination

Based on the LSAD model given in (3-11), the errors in the estimated Euler angles can be derived by:

$$Cov\left(att\right) = \left[\sum_{i=2}^{3} \mathbf{A}_i^T \left(\mathbf{R}_0^T Cov\left(\mathbf{l}_i\right) \mathbf{R}_0\right)^{-1} \mathbf{A}_i\right]^{-1} \tag{6-9}$$

where $Cov\left(att\right)$ indicates the error covariance matrix of the Euler angles. Here we assume that the ABF are precisely measured *a priori* so that its errors can be neglected. In Eq. (6-9), the geometry of antennas is involved in the rotation matrix $\mathbf{A}_i$ and will affect the attitude precision. The geometry is determined by the baseline lengths between the antennas. Figure 6-2 show the impacts of baseline length and carrier phase noise on the precision of yaw and pitch angles. The results are obtained by simulating a static scenario where the antennas form an equilateral triangle. In the simulation, the true values of Euler angles are all zeros. The standard deviation of yaw and pitch errors are obtained from (6-9). The baseline length reflects the distance between the phase centers of the antennas. Considering the antenna dimensions, baseline lengths larger than 0.2 m are taken into account.

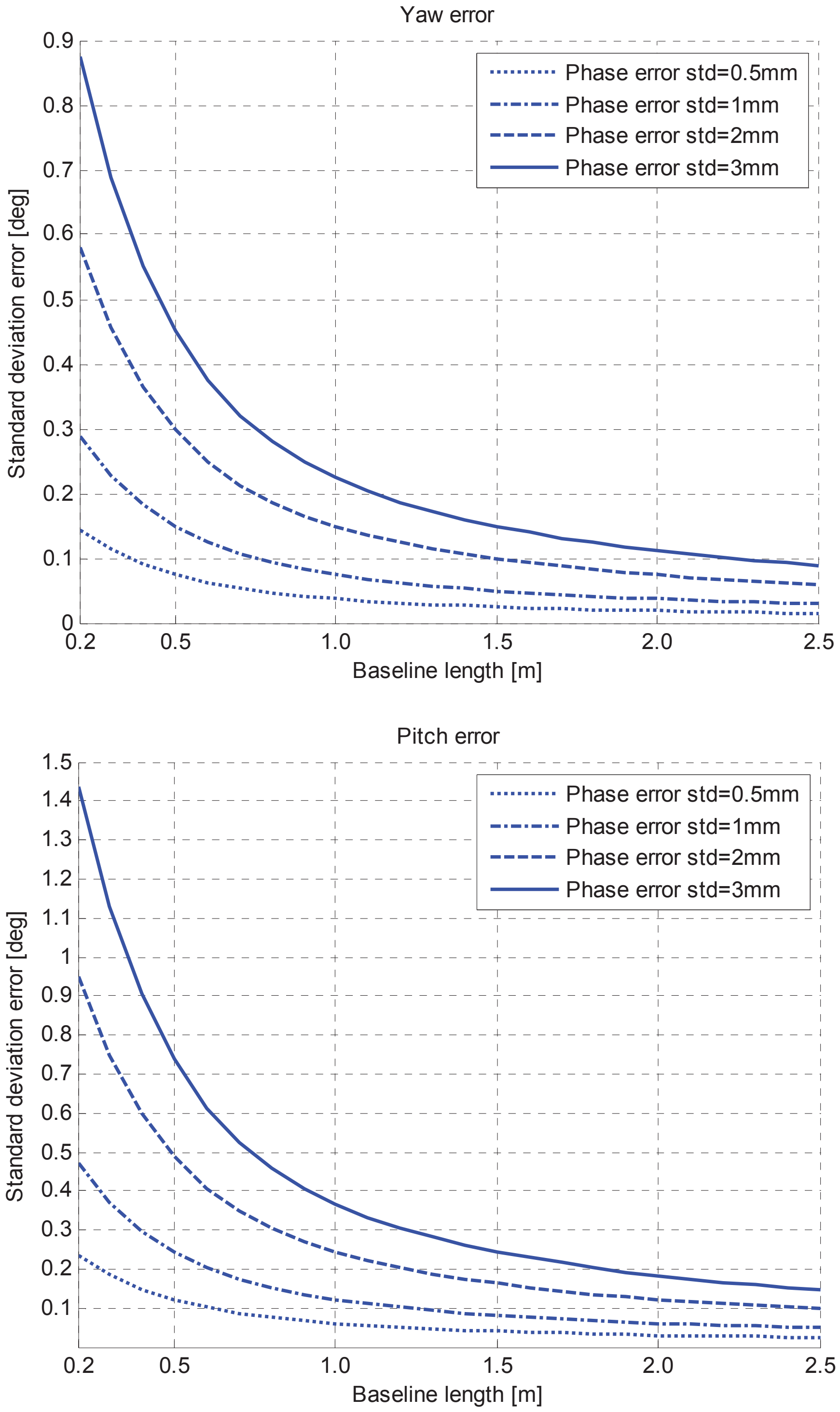

**Figure 6-2: Attitude precision under different baseline and carrier phase noise**

It can be seen that a longer baseline and a smaller phase noise yield a higher attitude precision. Note that the errors of each Euler angle will differ according to the satellite geometry, the antenna geometry and other factors. The results presented in Figure 6-2 only correspond to the specified simulation scenario and cannot generally reflect the precision of the attitude parameters.

## 6.3 SAR motion compensation using GPS

The SAR APC position derived from GPS is given in the LLF, whereas the analysis of receiver-to-target range is usually carried out in the frame related to the track directions. In the horizontal plane, the LLF coordinates of the APC should be projected into the Along-track/Cross-track/Up (ACU) frame, as shown in Figure 6-3. Both frames share the same up direction, namely Z-axis in the LLF. The angle $\alpha$ reflects the deviation in the cross-track direction and the X-axis of the LLF.

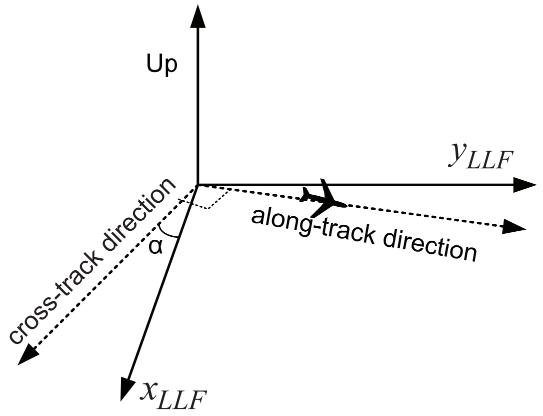

**Figure 6-3: LLF and along/cross-track frame**

### 6.3.1 APC and position parameters

The APC error is illustrated in Figure 6-4, where the nominal coordinate of the airplane is at the point APC' and the estimated coordinate is at the point APC. Point C is located at the midswath. $R_0$ is the true slant range and $R_1$ is the estimated slant range. Note that the APC position error needed for the motion compensation is actually $|R_0 - R_1|$ rather than the magnitude of $R_2$.

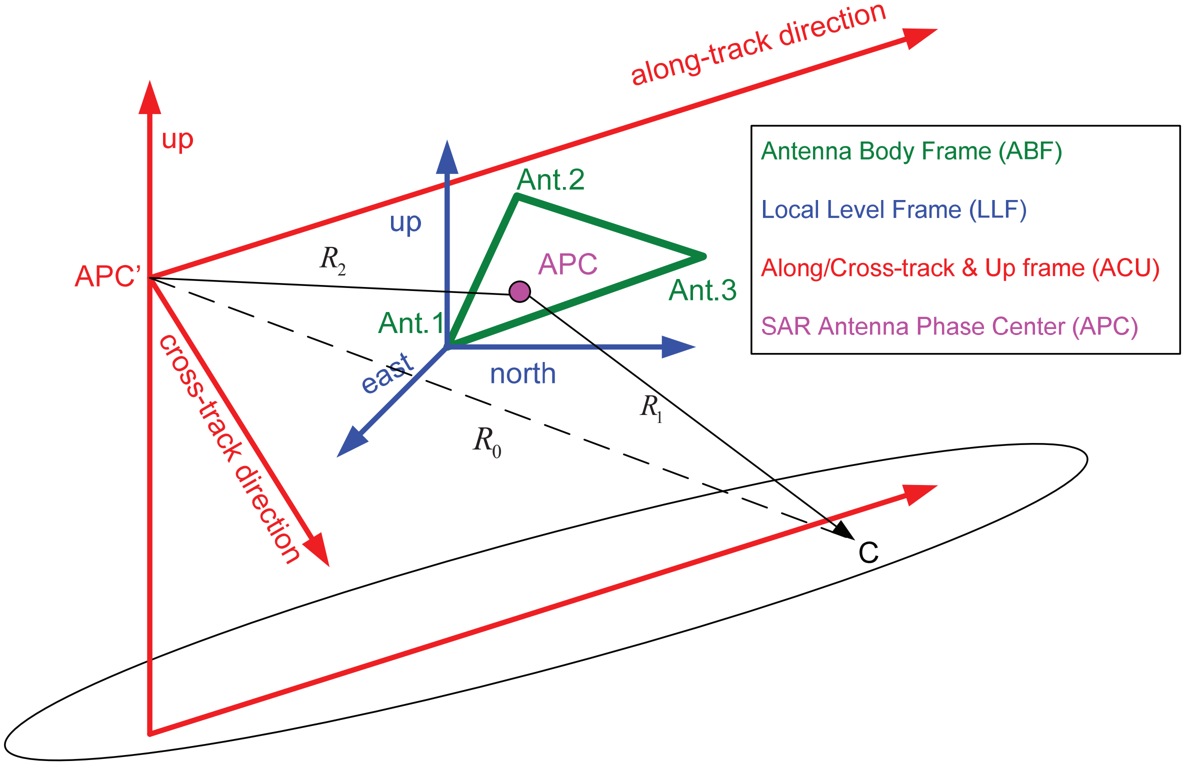

**Figure 6-4: An illustration of APC error in 3D space**

The GPS antennas and SAR antenna will be rigidly mounted on the airplane body, so that the coordinate of APC in the ABF ($\mathbf{x}^{ABF}$) can be fixed prior to the experiment. However, the calculation of the slant range is usually performed in the ACU frame. We therefore need to transform the APC coordinate from the ABF to the ACU frame. Applying Helmert formulation introduced in Eq. (3-1) yields:

$$\mathbf{x}^{ACU} = \mathbf{x}_{0,ABF}^{ACU} + \mathbf{R}_{ABF}^{ACU}\mathbf{x}^{ABF} \qquad (6\text{-}10)$$

where $\mathbf{x}^{ACU}$ is the coordinate of APC in the ACU frame; $\mathbf{x}_{0,ABF}^{ACU}$ is the origin of the ABF in the ACU frame; $\mathbf{x}^{ABF}$ is the coordinate of APC in the ABF. Note that the master antenna serve as the origin for both ABF and LLF, so that $\mathbf{x}_{0,ABF}^{ACU}$ is equivalent to $\mathbf{x}_{0,LLF}^{ACU}$. From GPS we can obtain the coordinate of the master antenna in the ECEF frame and the attitude parameter between the ABF and the LLF. Substituting these terms into (6-10) yields:

$$\mathbf{x}^{ACU} = \underbrace{\mathbf{R}_{LLF}^{ACU}\mathbf{R}_{ECEF}^{LLF}\mathbf{x}_{MA}^{ECEF}}_{\mathbf{x}_{0,ABF}^{ACU}} + \underbrace{\mathbf{R}_{LLF}^{ACU}\mathbf{R}_{ABF}^{LLF}\mathbf{x}^{ABF}}_{\mathbf{R}_{ABF}^{ACU}\mathbf{x}^{ABF}} \qquad (6\text{-}11)$$

where $\mathbf{R}_{LLF}^{ACU}$ reflect the rotation from the LLF to the ACU frame (see Figure 6-3); $\mathbf{R}_{ECEF}^{LLF}$ reflects the rotation from the ECEF to the LLF centered at the master antenna; The terms labeled under the brace are associated with Eq. (6-10) and represent the transition and rotation between the ABF and the ACU frames, respectively. $\mathbf{R}_{ECEF}^{LLF}$ is determined by the position of the master antenna. The position of master antenna in the LLF, even obtained through SPP, presents only millimeter-level errors (Lu 1995). In our experiment, the master antenna is positioned using RTK technique, and therefore the error in $\mathbf{R}_{ECEF}^{LLF}$ can be ignored. The term $\mathbf{x}_{MA}^{ECEF}$ is obtained from the GPS position determination. The term $\mathbf{R}_{ABF}^{LLF}$ is obtained from the attitude determination.

Eq. (6-11) shows that the positioning error of SAR APC in the ACU frame is affected by the attitude error and the positioning error. By ignoring the covariance between the position and attitude results we have:

$$Cov\left(\mathbf{x}^{ACU}\right) = Cov\left(\mathbf{R}_{LLF}^{ACU}\mathbf{R}_{ECEF}^{LLF}\mathbf{x}_{MA}^{ECEF}\right) + Cov\left(\mathbf{R}_{LLF}^{ACU}\mathbf{R}_{ABF}^{LLF}\mathbf{x}^{ABF}\right) \tag{6-12}$$

In (6-12) the first term of the right-hand side describes the effects of positioning error. It can be calculated from:

$$\begin{gathered} Cov\left(\mathbf{R}_{LLF}^{ACU}\mathbf{R}_{ECEF}^{LLF}\mathbf{x}_{MA}^{ECEF}\right) = \mathbf{R}_{LLF}^{ACU} Cov\left(\mathbf{x}^{LLF}\right)\left(\mathbf{R}_{LLF}^{ACU}\right)^T \\ \mathbf{R}_{LLF}^{ACU} = \begin{bmatrix} \cos\alpha & -\sin\alpha & 0 \\ \sin\alpha & \cos\alpha & 0 \\ 0 & 0 & 1 \end{bmatrix} \end{gathered} \tag{6-13}$$

where $\alpha$ is the included angle presented in Figure 6-3. In this case, the origin of LLF is the nominal APC position. The term $Cov(\mathbf{x}^{LLF})$ can be calculated from Eq. (6-8). The second term of the right-hand side of Eq. (6-12) indicates the influences of attitude error. This can be related to the attitude error derived in Eq. (6-9) by the following equation:

$$\begin{gathered} Cov\left(\mathbf{R}_{LLF}^{ACU}\mathbf{R}_{ABF}^{LLF}\mathbf{x}_{APC}^{ABF}\right) = \mathbf{R}_{LLF}^{ACU}\mathbf{\Omega} Cov\left(att\right)\mathbf{\Omega}^T\left(\mathbf{R}_{LLF}^{ACU}\right)^T \\ \mathbf{\Omega} = \begin{bmatrix} \dfrac{\partial \mathbf{R}_{ABF}^{LLF}\mathbf{x}^{ABF}}{\partial y} & \dfrac{\partial \mathbf{R}_{ABF}^{LLF}\mathbf{x}^{ABF}}{\partial p} & \dfrac{\partial \mathbf{R}_{ABF}^{LLF}\mathbf{x}^{ABF}}{\partial r} \end{bmatrix} \end{gathered} \tag{6-14}$$

Where $Cov(att)$ is the error covariance matrix of the Euler angles calculated from Eq. (6-9).

From Figure 6-4 it can be seen that the APC error is actually obtained from the three-dimensional space. However, the position error in the along-track direction can be accurately compensated by re-sampling procedures (Fornaro 1999), and hence the cross-track direction is the only error source in the horizontal plane. Consequently, we can project the APC error into a two-dimensional plane. Shown in Figure 6-5 is the two-dimensional plane formed by the cross-track and up directions, where B represents estimated APC position in the two dimensional plane and A is the nominal position of the APC.

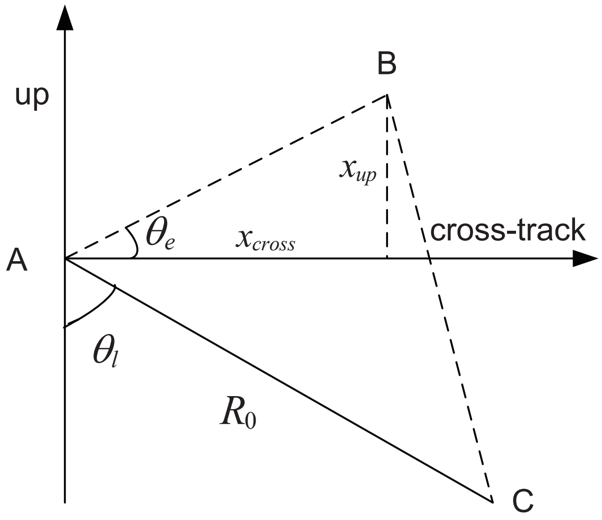

**Figure 6-5: An illustration of APC error in 2D plane**

The APC position error is expressed by |*AC*-*BC*|. The true slant range *AC* with the magnitude of $R_0$ can be considered free of error, so that the APC position error (denoted by $f_{APC}$) can be calculated from the actual slant range *BC* as follows:

$$
\begin{aligned}
f_{APC} &= \sqrt{R_0^2 + \left[\left(x^{up}\right)^2 + \left(x^{cross}\right)^2\right] - 2\frac{x^{up}}{\sin\theta_e} R_0 \sin\left(\theta_l - \theta_e\right)} \\
&= \sqrt{R_0^2 + \left[\left(x^{up}\right)^2 + \left(x^{cross}\right)^2\right] - 2R_0\left(x^{cross}\sin\theta_l - x^{up}\cos\theta_l\right)}
\end{aligned}
\qquad (6\text{-}15)
$$

where $R_0$ is the true slant range to the target point and can be obtained from $z^{LLF}/\theta_l$ with $z^{LLF}$ being the nominal position of APC in the up direction; $x^{up}$ and $x^{cross}$ are the actual APC coordinates in up and cross-track directions, respectively; $\theta_e$ can be expressed by $\theta_e = \tan^{-1}\left(x^{up}/x^{cross}\right)$ as depicted in Figure 6-5; $\theta_l$ is the look angle. From Eq. (6-15) we have the APC position error:

$$
Cov\left(f_{APC}\right) = \mathbf{a}_{CU} Cov\left(\mathbf{x}^{CU}\right)\mathbf{a}_{CU}^{T}
$$

$$
\mathbf{a}_{CU} = \begin{bmatrix} \dfrac{\partial f_{APC}}{\partial \mathbf{x}^{up}} & \dfrac{\partial f_{APC}}{\partial \mathbf{x}^{cross}} \end{bmatrix}
$$

$$
\begin{aligned}
\frac{\partial f_{APC}}{\partial x^{up}} &= -\frac{x^{up} + R_0\cos\theta_l}{\sqrt{R_0^2 + \left[\left(x^{up}\right)^2 + \left(x^{cross}\right)^2\right] - 2R_0\left[\sin\theta_l x^{cross} - \cos\theta_l x^{up}\right]}} \\
\frac{\partial f_{APC}}{\partial x^{cross}} &= -\frac{x^{cross} - R_0\sin\theta_l}{\sqrt{R_0^2 + \left[\left(x^{up}\right)^2 + \left(x^{cross}\right)^2\right] - 2R_0\left[\sin\theta_l x^{cross} - \cos\theta_l x^{up}\right]}}
\end{aligned}
\qquad (6\text{-}16)
$$

where $Cov(\mathbf{x}^{CU})$ is the error covariance matrix of the APC position in up and cross-track directions. $Cov(\mathbf{x}^{CU})$ can be extracted from $Cov(\mathbf{x}^{ACU})$ of Eq. (6-12). The SAR image processing needs an APC position error lower than 1/8 SAR wavelength (Wang et al. 2009).

### 6.3.2 DCF and attitude parameters

The Doppler Centroid Frequency (DCF) and attitude parameters are related by:

$$f_{DC} = \left(\sin\theta_l \sin y + \cos\theta_l \sin p\right) v_{along} / \lambda_{SAR} \tag{6-17}$$

where $f_{\mathrm{DC}}$ stands for the DCF; $v_{along}$ refers to the velocity of the airplane in the along-track direction; $\theta_l$ denotes the look angle of the APC; $y$ represents the yaw angle of the PBF (plane body frame introduced in chapter 3) and $p$ is the pitch angle of the PBF; $\lambda_{SAR}$ refers to the SAR signal wavelength used in this bistatic SAR experiment, namely 0.031 m. Except for the yaw angle and pitch angle, the velocity term $v_{along}$ is also an unknown parameter in (6-17). Applying the error propagation law to (6-17) and neglecting the variance between the attitude parameters and the velocity yield:

$$\begin{gathered} Cov\left(f_{DC}\right) = \frac{1}{\lambda_{SAR}^2} \mathbf{a}_{DCF} Cov\left(\mathbf{x}^{AV}\right) \mathbf{a}_{DCF}^T \\ Cov\left(\mathbf{x}^{AV}\right) = \begin{bmatrix} \sigma_y^2 & \sigma_y \sigma_p & 0 \\ \sigma_y \sigma_p & \sigma_p^2 & 0 \\ 0 & 0 & \sigma_{v_{along}}^2 \end{bmatrix} \\ \mathbf{a}_{DCF} = \begin{bmatrix} \left(\sin\theta_l \cos y + \cos\theta_l \sin p\right) v_{along} \\ \left(\sin\theta_l \sin y + \cos\theta_l \cos p\right) v_{along} \\ \left(\sin\theta_l \sin y + \cos\theta_l \sin p\right) \end{bmatrix}^T \end{gathered} \tag{6-18}$$

In the covariance matrix $Cov(\mathbf{x}^{AV})$, the variance and covariance of the yaw and pitch angles can be obtained from Eq. (6-9). The calculation of velocity will be discussed in section 6.3.3. The DCF error should not exceed 5% of the Pulse Repetition Frequency (PRF).

### 6.3.3 Phase and velocity parameters

As discussed before, the positioning error in the along-track direction can be compensated by a re-sampling procedure. The re-sampling procedure depends on the velocity information in the along-track direction. This can be seen in Figure 6-6.

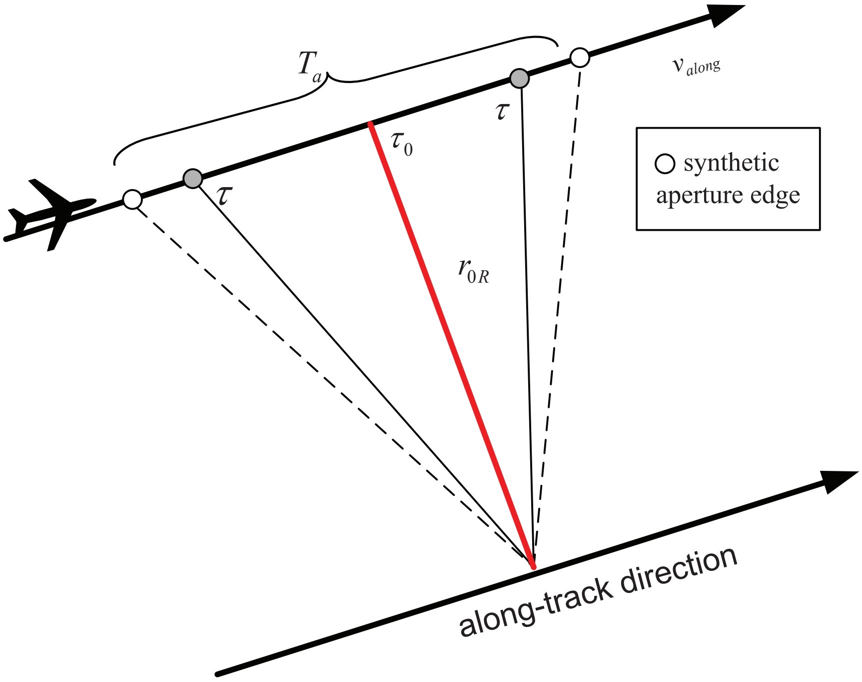

**Figure 6-6: Re-sampling in along-track direction**

In Figure 6-6, the synthetic aperture edge is marked by a hollow circle; $T_a$ is the composite exposure time; τ is the azimuth time variable and $\tau_{0R}$ denotes the zero-Doppler time; $r_{0R}$ is the zero-Doppler slant range; $v^{along}$ represents the nominal along-track velocity of the SAR receiver.

The slant range history of receiver is defined as:

$$\Phi_{SR} = 2\pi \sqrt{r_{0R}^2 + \left[\left(\tau - \tau_{0R}\right) v^{along}\right]^2} \Big/ \lambda_{SAR} \qquad (6\text{-}19)$$

where $\Phi_{SR}$ is the SAR phase in units of cycles. The velocity in the along-track direction ($v^{along}$) can be obtained from various sensors, for example by the embedded speed sensor of the airplane, by the inertial sensors or by GPS measurements. In this study, we focus on the velocity determination with GPS. Doppler measurements or carrier phase rates are usually employed for velocity determination in single-point positioning (Serrano et al. 2004). However, Doppler measurements under high dynamics are not known with sufficient accuracy (Lipp and Gu 1994) and therefore its error model is difficult to be established. If RTK solutions are available, the velocity can be obtained by differentiating the precise positions with time. This is always used as reference values to evaluate other velocity determination systems (Ding and Wang 2011). The drawback mainly lies in the low data rate of GPS output, so that a constant velocity has to be assumed between the two adjacent GPS position outputs. Denoting the GPS sampling frequency as $f_s$, the velocity can be calculated by:

$$v^{along} = \left[ \mathbf{x}_t^{along} - \mathbf{x}_{t-1}^{along} \right] f_s \tag{6-20}$$

By neglecting the correlation of position errors between two adjacent epochs, the velocity error in the along-track direction can be related to the position error by:

$$Std\left(v^{along}\right) = \sqrt{2} f_s \, Std\left(\mathbf{x}^{along}\right) \tag{6-21}$$

where $f_s$ is the output rate of the GPS measurement; *Std* is the short-hand notation of standard deviation. The GPS output rate usually ranges from 1 Hz to 20 Hz. From Eq. (6-19) the phase error $\Phi_{SR}$ caused by the velocity error is given by:

$$Std\left(\Phi_{SR}\right) = 2\pi \frac{v^{along}\left(\tau - \tau_{0R}\right)^2}{\lambda_{SAR}\sqrt{r_{0R}^2 + \left(\tau - \tau_{0R}\right)^2 \left(v^{along}\right)^2}} Std\left(v^{along}\right) \tag{6-22}$$

where the time dependence $\tau$ is a SAR related parameter and its relation with respect to the GPS output is hard to be constructed, we therefore need to simplify the error analysis by replacing this time dependence. As is known, the maximal error appears at the synthetic aperture edge, and hence we treat the composite exposure time $T_a$ as the upper bound. Substituting $T_a$ into (6-22) yields:

$$Std\left(\Phi_{SR}\right) \le \frac{2\pi}{\lambda_{SAR}} \frac{v^{along}\left(T_a/2\right)^2}{\sqrt{r_{0R}^2 + \left(T_a/2\right)^2 \left(v^{along}\right)^2}} Std\left(v^{along}\right) \tag{6-23}$$

For SAR focusing, the SAR phase error on the synthetic aperture edge should be lower than $\pi/4$.

## 6.4 Factors affecting the position and attitude accuracies

From the above discussions we can summarize the affecting factors for the position and attitude errors:

1. Receiver quality. It is mainly reflected by the carrier phase errors.
2. Satellite geometry. This is shown by the matrix **G** in Eq. (6-5).
3. Trajectory of the airplane. This affects the position of the master antenna and furthermore changes the matrix $\mathbf{R}_{ECEF}^{LLF}$ in Eq. (6-11). But the trajectory is usually pre-defined according to the experiment scenario and hence its effects are always ignored.
4. Geometry and separation of the antennas. Both terms are involved in the computation of the LLF coordinates of slave antennas. A longer baseline results in an improved precision but will delay the carrier phase ambiguity resolution. An orthogonal configuration of antennas is optimal for attitude determination (Comp 1993). However, it is usually not practical to set up long baselines with an orthogonal geometry due to the limited space of the fuselage.

Considering the architecture of the Transall C-160 aircraft, we have the following possible locations to mount GPS antennas, which are marked from A to G.

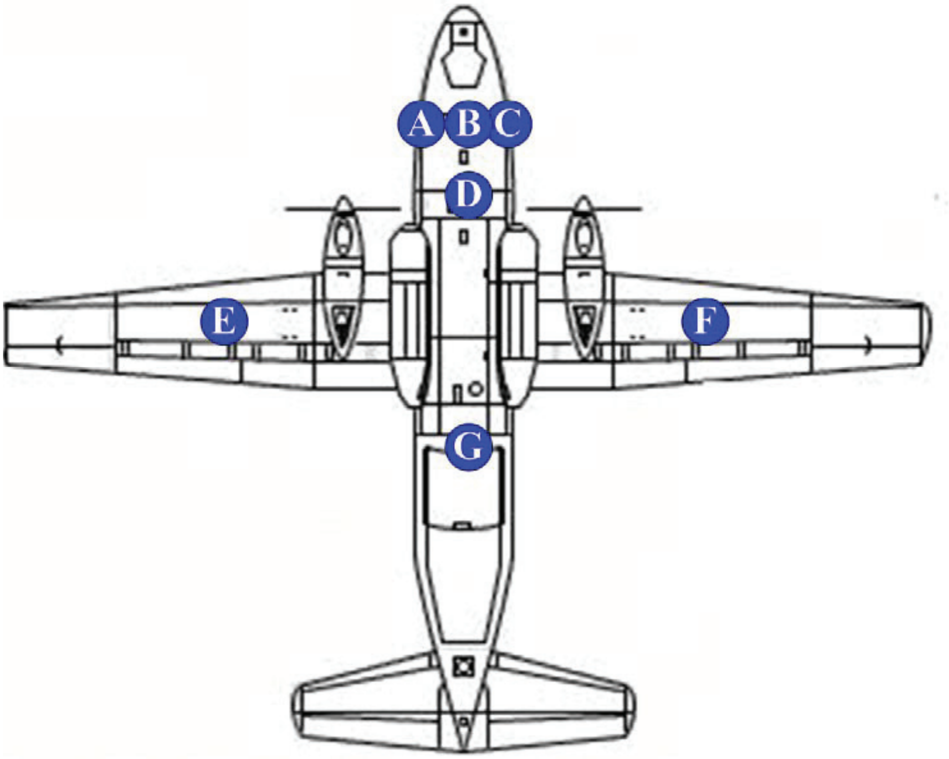

**Figure 6-7: Possible locations for mounting antennas on Transall C-160**[2]

According to Figure 6-7 we have the following antenna configurations:

(a) B-E-F. This is a combination of long baselines and orthogonal geometry. However, as identified in section 3.5.4, mounting the antennas on the wings is not recommended as the wing flexure might significantly degrade the accuracy of the attitude parameters.

(b) A-D-C. This is an equilateral configuration with short baselines (maximal 2.5 m). In the real application, multiple GPS antennas are usually mounted on a rigid frame, and then the frame is fixed on the vehicle body. For this reason, such a configuration can simplify the installation of the antennas. If the required accuracy is achievable by short baselines, this configuration is recommended in the experiment.

(c) A-G-C. Such a non-orthogonal configuration contains long baselines between A-G and C-G, yielding an improved precision of yaw and pitch over (b), but a fast ambiguity resolution for single-frequency GPS receivers is then challenging.

---

[2] The origin of the figure comes from the reference document US-Army. (1996). *FM 44-80 Visual Aircraft Recognition*. Department of the US Army, Washington, DC,.

## 6.5 Simulation

We assume that the airplane is flying in the east direction at the geodetic height of 3000 m starting from the position with latitude being 50° and longitude being 8° with a constant velocity of 110 m/s. According to the flying direction, $\mathbf{R}_{LLF}^{ACU}$ turns out to be an identity matrix. During the flight, there are 8 satellites in view, leading to a PDOP of 1.6. A ground station is located in the middle of the flight trajectory and at the geodetic height of 360 m. We assume that the phase integer ambiguities are correctly resolved and no phase cycle-slip occurs during the flight. By default, the GPS receivers mounted on the airborne keep tracking the GPS signals and output the data at 5 Hz. The observation session takes 1 min. Other relevant parameters for performing the simulation are presented in Table 6-1.

**Table 6-1: Parameters for simulating bistatic SAR experiment**

| Parameter | Indication | Value |
|---|---|---|
| $\theta_l$ | look angle | 70º |
| $\lambda_{SAR}$ | SAR wavelength | 0.031 m |
| $T_a$ | composite exposure time | 2.2 s |

In the previous sections, we have introduced the accuracy requirements for parameters used in the SAR motion compensation. These values are actually the recommended maximal errors. Besides that, we have also derived the standard deviation errors of each parameter. It should be stressed that the standard deviation cannot be directly related to the maximal errors since it covers only 68.2% confidence level. A 3σ standard deviation (99.7% confidence level) is adopted here to approximate the maximal error.

### 6.5.1 GPS positioning error and APC position error in cross-track direction

We will firstly analyze the effects of different receiver qualities on the APC position errors in the cross-track direction. The 3σ APC position errors in the cross-track direction based on different carrier phase noises are depicted below:

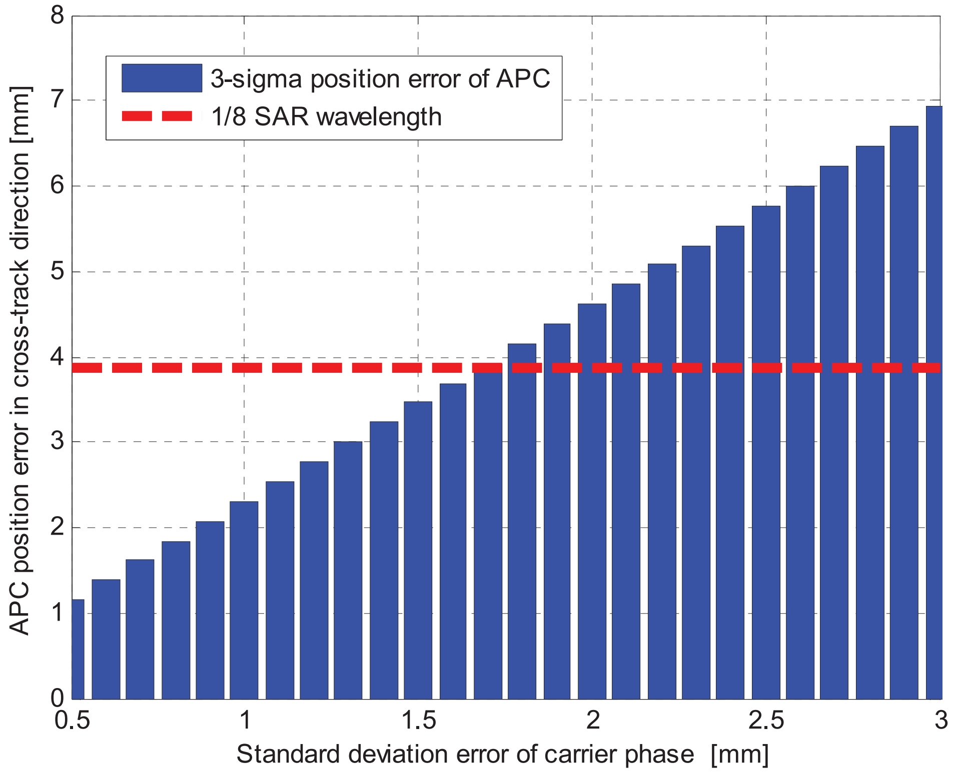

**Figure 6-8: APC position error under different the carrier phase noise**

From Figure 6-8 we can see that the standard deviation of carrier phase measurements should not be larger than 1.7 mm in order to guarantee that the position error will not exceed the threshold of 1/8 SAR wavelength (3.1 cm). Figure 6-9 shows the APC position error during the flight based on the receiver with 1.5 mm carrier phase noise.

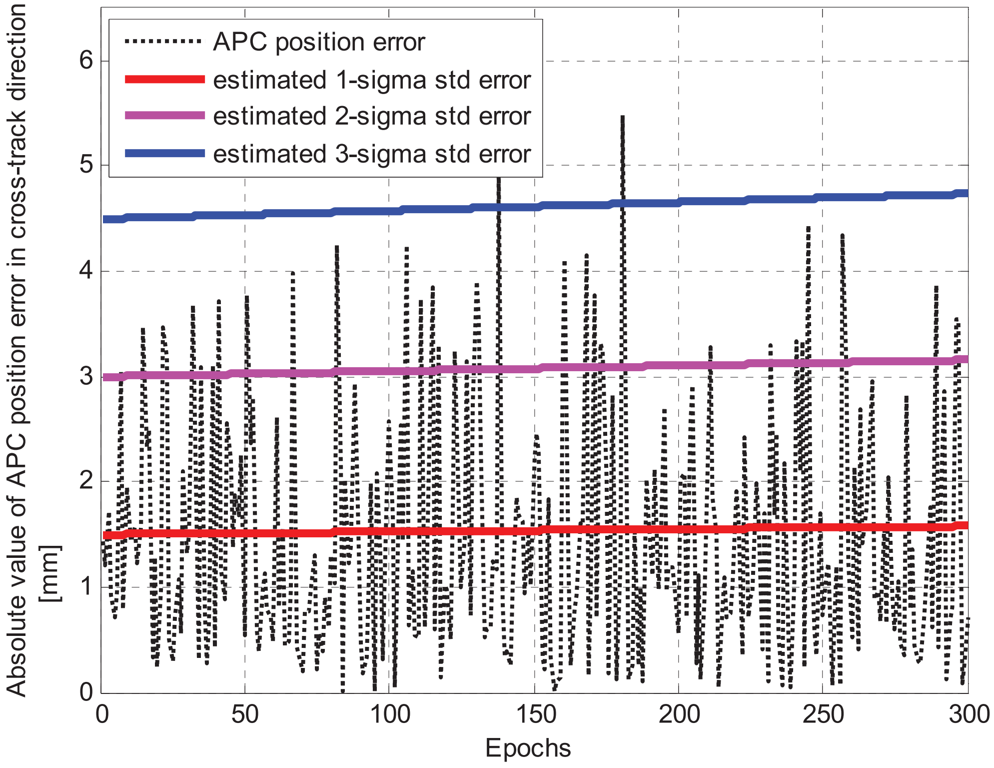

**Figure 6-9: APC position error during the flight**

Figure 6-9 shows that the APC position errors are almost lower the estimated 3σ error (99.7% confidence level) except for two exceptional epochs. The outages satisfy the fact that there might be 0.03% data out of the confidence level.

### 6.5.2 GPS attitude error and APC position error in cross-track direction

The coordinate of the SAR APC in the ABF can be determined at the calibration procedure. To do this, the distance from the SAR APC to the phase center of each GPS antenna needs to be measured. Such a lever-arm affects error propagation from the attitude domain to the position domain. A longer lever-arm will increase the positioning error of SAR APC in the cross-track direction. It has been interpreted that the attitude precision depends on the baselines between onboard multiple GPS antennas. In Figure 6-10, these baselines are depicted, where the blue solid line is the baseline between GPS antennas and the red dashed line indicates the baseline (also lever-arm) from the SAR APC to each GPS antennas.

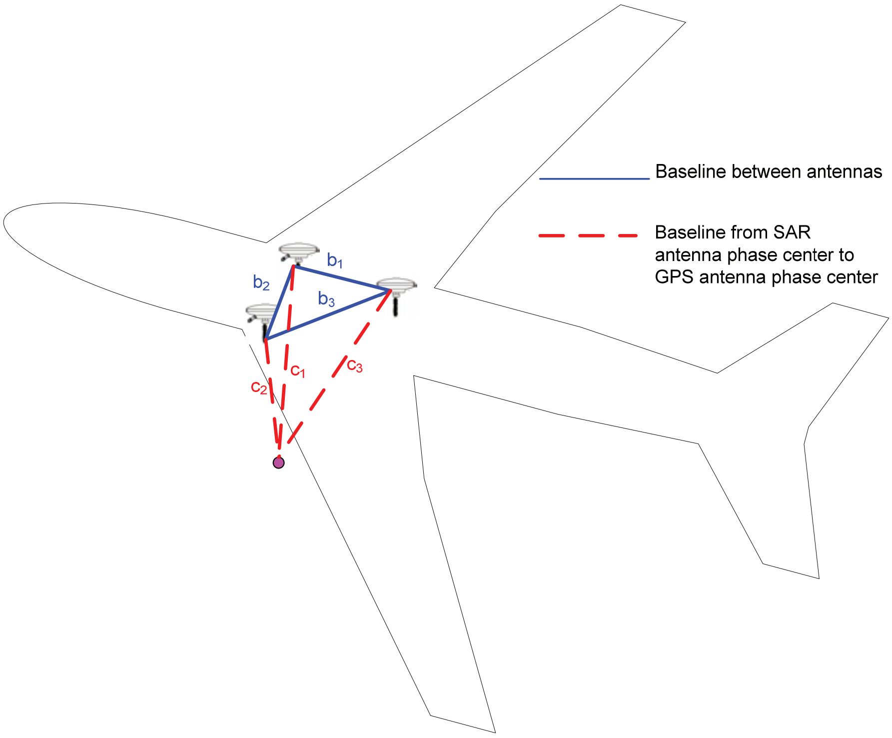

**Figure 6-10: Locations of SAR antenna and GPS onboard antennas**

For simplicity we assume that the GPS antennas have the same baseline length between each other, also the baseline from SAR APC to each GPS antenna are of the same magnitude, i.e. $b_1=b_2=b_3$ and $c_1=c_2=c_3$. Based on Eq. (6-12) and Eq. (6-16) the effects of different baselines on the positioning error of SAR APC in the cross-track direction can be demonstrated in Figure 6-11. The standard deviation of the carrier phase noise is 2 mm.

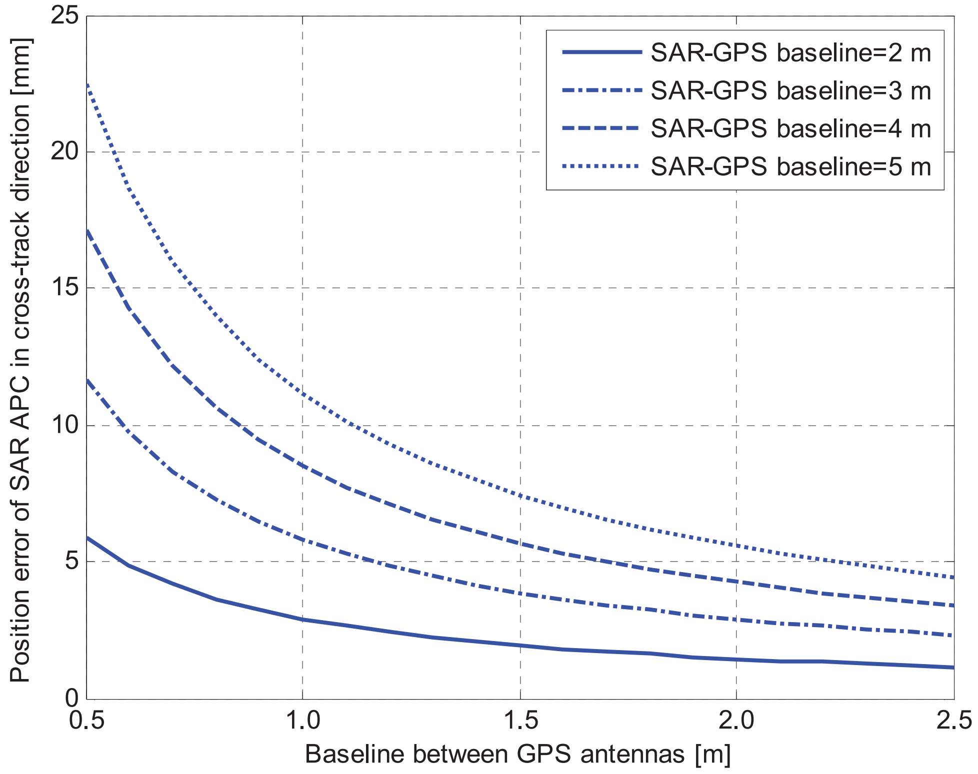

**Figure 6-11: Baseline effects on the estimated SAR APC positioning error**

Figure 6-11 indicates the significance of lever-arm effects. Although accurate attitude information can be provided by multiple GPS antennas, the lever-arm effects can magnify the influence of attitude errors in the estimated SAR APC position. A large lever-arm of 5 meters will result in a centimeter-level error in the position domain. The SAR antenna is usually mounted at the bottom or on a side of the airplane to receive the echoed signals, therefore the distance from the SAR APC to the GPS antenna is mainly dependent on the height of the airplane body. A large lever-arm is a significant limitation of GPS-based attitude determination technique in SAR applications.

### 6.5.3 Velocity error and APC positioning error in along-track direction

As investigated before, the GPS receivers with the standard phase error smaller than 1.7 mm should be used in order to meet the APC positioning accuracy. The velocity of the airplane is derived from the position parameters in the along-track direction. From Eq. (6-23) it can be seen that the threshold of the velocity measuring error depends on the magnitude of the velocity parameter as well. Such a relation is depicted in Figure 6-12. Here we use a zero-Doppler slant range ($r_{0R}$) of 8770 m.

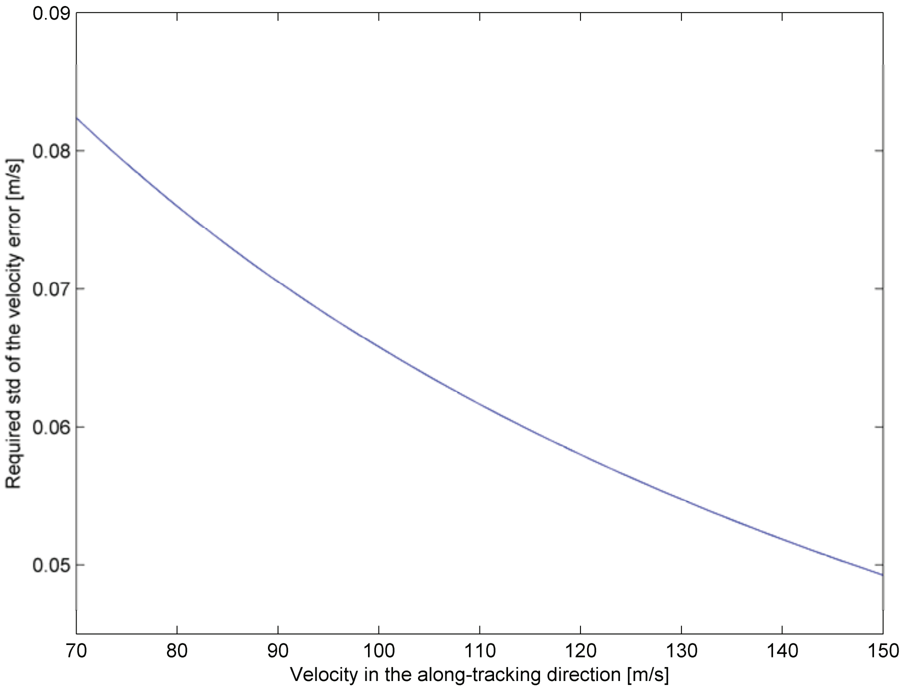

**Figure 6-12: Velocity error caused by the SAR phase error**

As indicated by Figure 6-12, a lower velocity error is required when a higher velocity is to be reached. With a GPS carrier phase noise of 1.7 mm, the velocity can be accurate to 0.05 m/s at 5 Hz sampling rate. According to Figure 6-12 such a velocity error threshold is subject to a velocity of 150 m/s. The nominal velocity of PAMIR airplane in the bistatic SAR experiments is 110 m/s, and therefore the required velocity accuracy is achievable.

### 6.5.4 DCF error and the GPS attitude error

The DCF error is determined by the attitude error and the velocity error. We will at first consider the attitude error by treating the velocity as a constant value. Different configurations of on-board antennas have been presented in Figure 6-7. For configuration (b), there can be different baselines in the fuselage area. The DCF errors associated to different carrier phase errors and different baselines are illustrated in Figure 6-13.

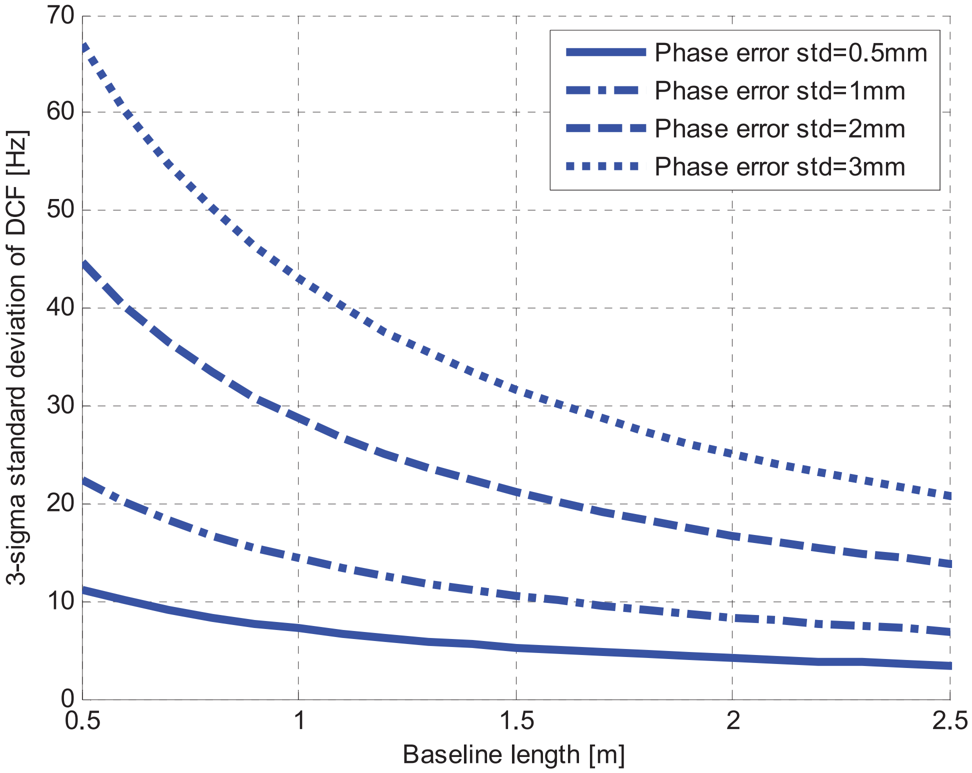

**Figure 6-13: DCF error under different carrier phase noises and baseline lengths**

Figure 6-13 shows that a long baseline and a high receiver quality lead to a higher DCF precision, we therefore use the maximal baseline of 2.5 m. In this case, even a receiver having a phase error of 3 mm can still provide a DCF error which is much lower than 5% PRF (assuming that PRF>3000 Hz). Figure 6-14 shows the actual and estimated DCF errors during the flight trajectory in the same scenario, where the standard deviation of carrier phase thermal noise is 3 mm and baseline length is 2.5 m.

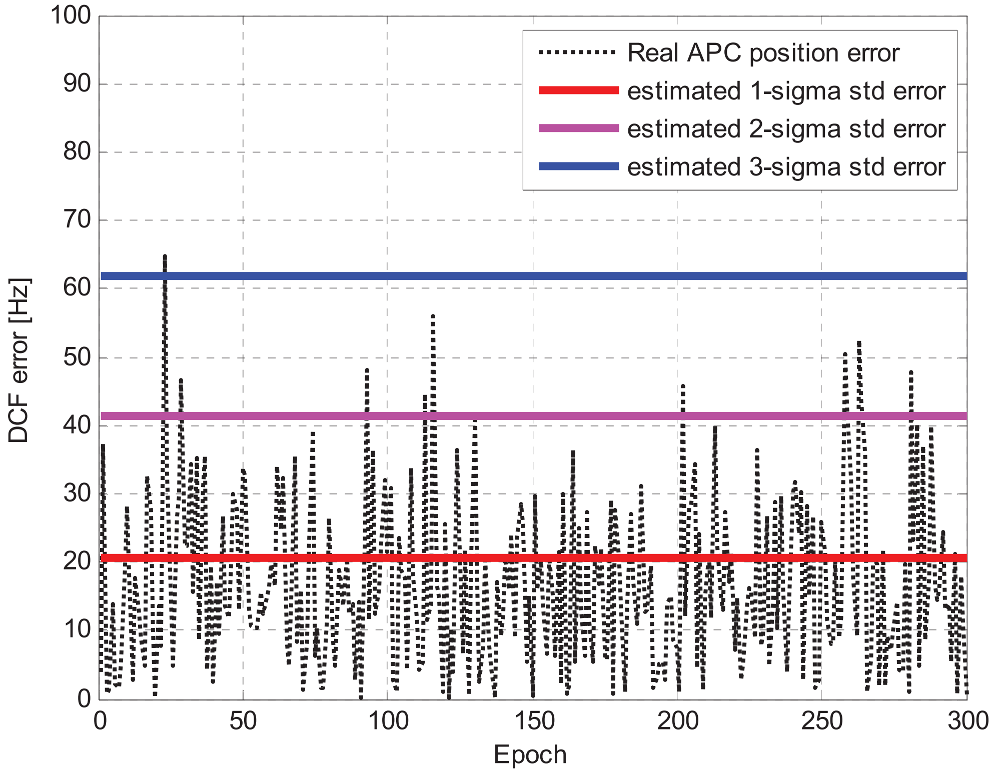

**Figure 6-14: Estimated DCF error during the trajectory**

Figure 6-13 and Figure 6-14 indicate a fact that the attitude error will not challenge the DCF quality. Besides the attitude error, the velocity is another error source for DCF. From the calculation it can be proven that a velocity error at decimeter-per-second level can fulfill the accuracy requirement of the DCF. Considering a poor case where the baseline between onboard antenna is 0.5 m and standard deviation of GPS carrier phase noise is 3mm, the derived standard deviation error of the yaw angle is 0.45 [deg] and of pitch angle is 0.70 [deg]. With these attitude errors, once the velocity in along-track direction has an error of 0.5 m/s, the outcoming DCF errors are depicted in Figure 6-15. The horizontal plane indicates the different combinations of yaw and pitch errors. The vertical axis represents the associated DCF error.

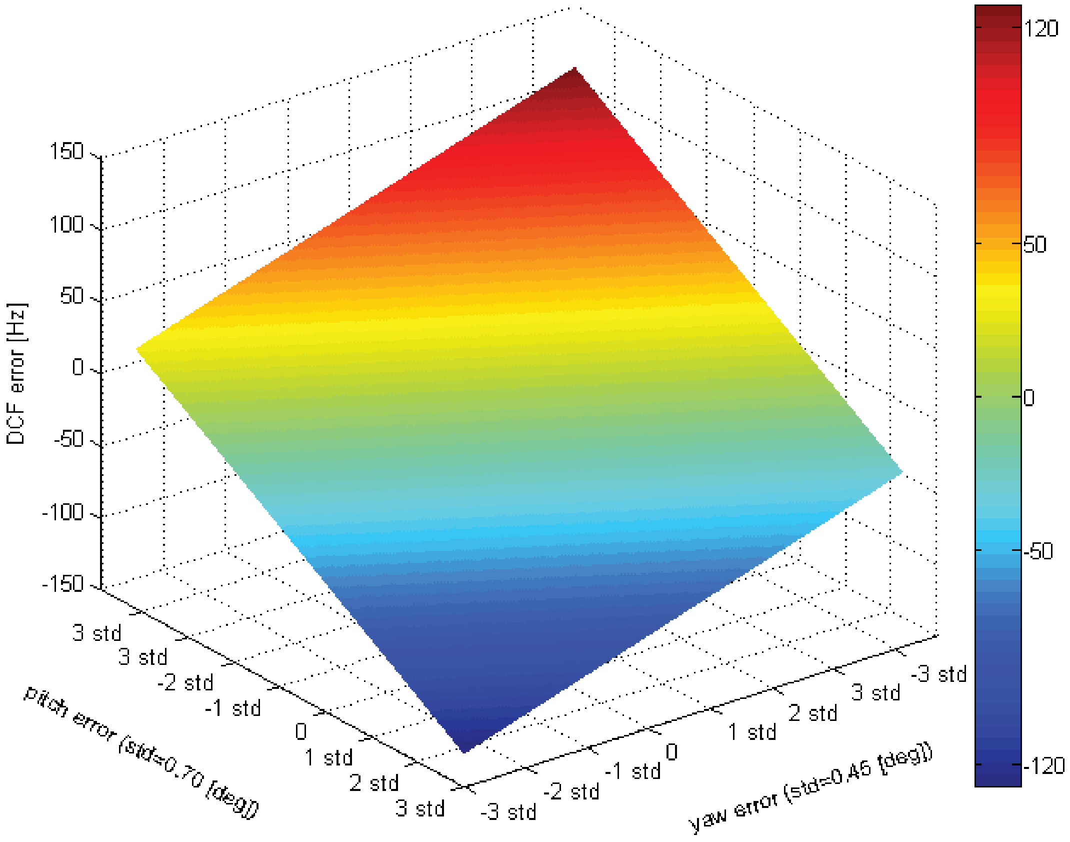

**Figure 6-15: DCF error under different velocity and attitude errors**

Assuming that the PRF is 3000 Hz, the acceptable DCF error should be lower than 5% of PRF, namely 150Hz. Figure 6-15 shows that the DCF errors are lower than this threshold. It means that even velocity errors at decimeter-per-second level will not introduce significant errors to DCF results. With RTK solutions and a high GPS sampling rate, better velocity accuracies can be achieved, and therefore velocity errors will not degrade the DCF quality.

## 6.6 Conclusions

In this section, the error propagation from the GPS phase noise to the positioning results and results has been analyzed at first. Baselines between antennas are important impacting factors for the attitude precision. The analysis of positioning error of the SAR APC can be carried out in along-track and cross-track directions. GPS positioning and attitude errors are involved in the cross-track direction. Considering only the GPS positioning error, a GPS phase thermal noise less than 1.7 mm can fulfill the accuracy requirement. This is not a challenge for current GPS receivers. However, as the GPS antenna and SAR antenna are mounted on the upside and underside of an airplane, respectively, the potential large lever-arm will introduce significant errors. This can be seen as a major drawback of using GPS multi-antenna systems in Terra/SAR PAMIR experiment. In the along-track direction, meeting the required accuracy of the DCF is not an issue.

Another factor needed by the SAR motion compensation is the DCF, which is related to the attitude and velocity parameters. Based on a GPS multi-antenna system with 2.5 m baseline and the velocity determined by differential positioning, meeting the accuracy of the DCF is not an issue.

# Concluding remarks and future work

This thesis has discussed four major aspects around the attitude determination using a GPS multi-antenna system, including (1) the pre-processing of GPS carrier phase measurements; (2) the mathematic model and the implementation of a multi-antenna system (3) the integration of GPS measurements and attitude dynamics through nonlinear Kalman filters and the solutions to mismodeling errors; (4) the error analysis for position and attitude parameters as well as the parameters related to the SAR motion compensation.

In the pre-processing of GPS carrier phases, the cycle-slip detection, determination and validation for triple-frequency GPS have been highlighted. The cycle-slip detection is implemented using two geometry-free phase combinations constructed by the scalars (-1, -1, 2) and (-1, 4, -3). This approach can detect all cycle-slips except for the most insensitive ones and well fit the low- and high-multipath environments. However, with sampling interval larger than 30 seconds, the cycle-slip detection might not work properly due to the potential large variation of the ionospheric error within the sampling period. The cycle-slip determination relies on the adaptive use of predicated phase measurements and code measurements. The LAMBDA technique is employed to provide the highest success rate. The cycle-slip validation is embedded into the cycle-slip determination to filter out the incorrect cycle-slip candidates. The above-mentioned algorithms are dedicated for stand-alone GPS receivers and suitable for real-time static or dynamic applications.

Multiple GPS antennas can form an attitude determination system. For this application, a software toolbox has been developed in MATLAB to process the GPS raw data in a post-processing. A key step of the attitude determination is the estimation of baseline vectors between antennas using the RTK technique. Two dedicated approaches have been presented for attitude determination. The LSAD approach needs a predefined ABF and gives an optimal solution. The direct attitude computation does not rely on knowing the ABF in advance and hence simplifies the implementation. However, it employs only part of the measurements and leads to a sub-optimal solution. A reliable pre-processing of carrier phase measurements is the prerequisite of precise attitude solutions.

The attitude dynamics can be incorporated with GPS measurements in order to improve the accuracy. If the airplane undergoes low maneuver and inertial sensors are not available, a constant angular rate model can be used to approximate the attitude dynamics under a high GPS sampling rate. A successful ambiguity resolution of carrier phase measurements enables precise attitude estimation, and hence there are small nonlinearity errors within the measurement model. In this case, the EKF is a proper technique to fuse the measurement model and the dynamic model due to its lower computational complexity than other nonlinear

Kalman filters. However, a constant angular model is only an approximation rather than an exact description of the attitude dynamics, and hence it might cause mismodeling errors. One type of mismodeling error occurs if the actual attitude dynamics is out of the error range described by the process noise parameters. In this case, the model mismatch will bring large errors into the *a priori* state estimates and cause model transition errors. The IEKF, SOEKF and UKF lead to smaller magnitude of model transition errors than the conventional EKF. However, using these nonlinear filters in this case does not improve the estimation accuracy to a sufficient extent. Instead, an IMM approach composed of a common measurement model and two filters running in parallel with different dynamic models can remarkably reduce the magnitude of model transition errors. In the IMM, one sub-filter is given large process noise and therefore mainly subject to the measurement model, whereas the other sub-filter gives more weight to the dynamic model. Another type of mismodeling error is due to the fact that a fixed process noise covariance matrix cannot describe the changing attitude dynamics. The innovation-based adaptive tuning of process noise can overcome this shortcoming. By embedding the adaptive tuning function into the IMM, an AIMM has been proposed to handle both kinds of mismodeling errors.

The theoretical error ranges of the position and attitude results have been derived from the GPS carrier phase noise by analyzing the error propagation. The baseline length is a central factor for the attitude precision. In order to determine the distribution and distance of the multiple antennas, the following factors should be considered, including the receivers used, the accuracy requirement, the locations for the antenna installation, and whether or not the baseline information is needed by the pre-processing of carrier phases. The bistatic SAR motion compensation needs the position, attitude and velocity information obtained by GPS. In the cross-track direction, the desired positioning accuracy of the SAR APC requires a standard GPS carrier phase noise smaller than 1.7 mm. However, lever-arm effects might introduce significant errors from attitude domain into position domain. In the along-track direction, the velocity accuracy can theoretically fulfill the requirement of the experiment. Referring to the Doppler centroid frequency, the attitude and velocity parameters derived from GPS can limit the errors within the allowable range.

Continuing with the presented works, future studies can be carried out at least in the following aspects:

1. The fixed baseline length between onboard multiple GPS antennas has been employed for ambiguity resolution. Similarly, it can also be used in cycle-slip determination or validation. For cycle-slip determination, the baseline length can be transformed into the measurement domain to aid the search of cycle-slip candidates.
2. The cycle-slip issue can be handled with respect to each double-differenced phase measurement instead of each single antenna-satellite measurement, so that presented algorithms can be simply applied to the differential positioning. The difference is that the

*a priori* measurement noise should be enlarged since four single measurements are combined into a double-differenced measurement.

3. The proposed AIMM approach can also be applied to other navigation applications where an appropriate model of vehicle dynamics is hard to be found.
4. The motion compensation for TerraSAR-X/PAMIR experiment requires position and attitude parameters at a high sampling frequency. A significant disadvantage of the GPS system lies in the low data output rate. In order to have position, velocity and attitude information in high data rate, we can apply the interpolation technique in a post-processing or integrate GPS with inertial sensors. The error analysis for both cases needs to be investigated.

# Appendix I: Dilution of precision for single-point positioning

The geometry of satellites is an important factor for the precision of the positioning results. The Dilution Of Precision (DOP) is a measure of the instantaneous geometry of satellites (Hofmann-Wellenhof et al. 2003). As already presented in Eq. (1-9), the single-point positioning is formulated by:

$$\begin{aligned}
&\sqrt{\left(x^{s1}-x_u\right)^2+\left(y^{s1}-y_u\right)^2+\left(z^{s1}-z_u\right)^2}-t_r\cdot c=r_u^{s1}+e_u^{s1}\\
&\sqrt{\left(x^{s2}-x_u\right)^2+\left(y^{s2}-y_u\right)^2+\left(z^{s2}-z_u\right)^2}-t_r\cdot c=r_u^{s2}+e_u^{s2}\\
&\qquad\qquad\vdots\\
&\sqrt{\left(x^{sn}-x_u\right)^2+\left(y^{sn}-y_u\right)^2+\left(z^{sn}-z_u\right)^2}-t_r\cdot c=r_u^{sn}+e_u^{sn}
\end{aligned} \tag{A-I}$$

where all terms are related to a certain epoch so that the time dependence is dropped from the equation; *x*, *y* and *z* are the ECEF coordinate; the subscript *u* denotes the user position (namely the antenna position); the superscript $s_n$ denotes the *n*-th satellite position; $t_r$ is the receiver clock error; *r* is the original or corrected pseudorange measurement; *e* contains the remaining errors of the pseudorange measurements; *c* is the speed of light. The unknown values to be estimated include the ECEF coordinate of the user position (the antenna position) and the receiver clock error. The least-squares adjustment can be carried out after the linearization around an approximated antenna position *u0*, so that we have:

$$\mathbf{A}\cdot\mathbf{x}=\mathbf{l}$$

$$\mathbf{A}_{n\times4}=\begin{bmatrix}
-\dfrac{x^{s1}-x_{u0}}{\rho_{u0}^{s1}} & -\dfrac{y^{s1}-y_{u0}}{\rho_{u0}^{s1}} & -\dfrac{z^{s1}-z_{u0}}{\rho_{u0}^{s1}} & c\\
-\dfrac{x^{s2}-x_{u0}}{\rho_{u0}^{s2}} & -\dfrac{y^{s2}-y_{u0}}{\rho_{u0}^{s2}} & -\dfrac{z^{s2}-z_{u0}}{\rho_{u0}^{s2}} & c\\
\vdots & \vdots & \vdots & \vdots\\
-\dfrac{x^{sn}-x_{u0}}{\rho_{u0}^{sn}} & -\dfrac{y^{sn}-y_{u0}}{\rho_{u0}^{sn}} & -\dfrac{z^{sn}-z_{u0}}{\rho_{u0}^{sn}} & c
\end{bmatrix} \tag{A-II}$$

$$\rho_{u0}^{si}=\sqrt{\left(x^{si}-x_{u0}\right)^2+\left(y^{si}-y_{u0}\right)^2+\left(z^{si}-z_{u0}\right)^2}\quad \text{for } i=1,2\ldots n$$

$$\mathbf{l}_{n\times1}=\left[r_u^{s1}-\rho_{u0}^{s1}\;\vdots\;r_u^{s2}-\rho_{u0}^{s2}\;\vdots\;\ldots\;\vdots\;r_u^{sn}-\rho_{u0}^{sn}\right]^T$$

$$\mathbf{x}_{4\times1}=\left[\Delta x_u\quad \Delta y_u\quad \Delta z_u\quad t_r\right]^T$$

where the state vector **x** includes the increment of coordinate parameters and the receiver clock error; **l** contains the difference between the estimated measurements and actual measurements; $\rho_{u0}^{si}$ is the pseudorange calculated by the *i*-th satellite position and the antenna coordinate estimated in the current round of least-squares adjustment; **A** is the design matrix.

Assuming the measurement error has a zero-mean Gaussian distribution, the error covariance matrix of vector **x** can be calculated by rearranging (A-II) and applying the error propagation law:

$$\begin{aligned} \mathbf{x} &= \underbrace{\left(\mathbf{A}^T\mathbf{A}\right)^{-1}\mathbf{A}^T}_{\mathbf{G}}\mathbf{l} \\ Cov(\mathbf{x}) &= \mathbf{G}Cov(\mathbf{l})\mathbf{G}^T \end{aligned} \tag{A-III}$$

It can be seen that, the precision of the states are determined by two factors. The first factor is the measurement qualities described by the covariance matrix of the pseudorange measurements *Cov*(**l**). The other factor is reflected by the matrix **G** which describes the effects of satellite geometry. In order to focus on the analysis of satellite geometry, the cofactor matrix $\mathbf{Q_x}$ of the estimated parameters can be calculated by extracting **G** items from (A-III) and rearranging in form of matrix **A**:

$$\begin{aligned} \mathbf{Q}_{\mathbf{x},ECEF} &= \mathbf{G}\mathbf{G}^T = \left(\mathbf{A}^T\mathbf{A}\right)^{-1} \\ &= \begin{bmatrix} q_{xx} & q_{xy} & q_{xz} & q_{xt} \\ q_{yx} & q_{yy} & q_{yz} & q_{yt} \\ q_{zx} & q_{zy} & q_{zz} & q_{zt} \\ q_{tx} & q_{ty} & q_{tz} & q_{tt} \end{bmatrix} \end{aligned} \tag{A-IV}$$

The DOPs are defined by the diagonal components of $\mathbf{Q}_{\mathbf{x},ECEF}$, for example

$$\begin{aligned} &\text{Geometry Dilution of Precision:} && GDOP = \sqrt{q_{xx}+q_{yy}+q_{zz}+q_{tt}} \\ &\text{Position Dilution of Precision:} && PDOP = \sqrt{q_{xx}+q_{yy}+q_{zz}} \\ &\text{Time Dilution of Precision:} && TDOP = \sqrt{q_{tt}} \end{aligned} \tag{A-V}$$

The DOPs can also be calculated in the equatorial system, namely in the Local Level Frame (LLF) or East/North/Up (ENU) frame. It allows the determination of the DOPs in horizontal plane and vertical direction. To do this, cofactor matrix $\mathbf{Q_x}$ should be transformed from ECEF into LLF by employing the rotation matrix. The rotation matrix can be expressed as:

$$\underbrace{\begin{bmatrix} x_l \\ y_l \\ z_l \end{bmatrix}}_{\mathbf{x}^{LLF}} = \underbrace{\begin{bmatrix} -\sin\lambda & \cos\lambda & 0 \\ -\sin\varphi\cos\lambda & -\sin\varphi\sin\lambda & \cos\varphi \\ \cos\varphi\cos\lambda & \cos\varphi\sin\lambda & \sin\varphi \end{bmatrix}}_{\mathbf{R}_{ECEF}^{LLF}} \underbrace{\begin{bmatrix} x_{ECEF} \\ y_{ECEF} \\ z_{ECEF} \end{bmatrix}}_{\mathbf{x}^{ECEF}} \tag{A-VI}$$

where $\mathbf{R}_{ECEF}^{LLF}$ is the rotation matrix indicating the projection of a target point from the ECEF to the LLF; $\varphi$ and $\lambda$ denote the latitude and longitude of the reference point, respectively. Based on the rotation matrix, the cofactor matrix in the LLF can be calculated by:

$$\begin{aligned}\mathbf{Q}_{\mathbf{x},LLF} &= \mathbf{R}_{ECEF}^{LLF}\mathbf{Q}_{\mathbf{x},ECEF}\left(\mathbf{R}_{ECEF}^{LLF}\right)^{T} \\ &= \begin{bmatrix} q_{ee} & q_{en} & q_{eu} \\ q_{ne} & q_{nn} & q_{nu} \\ q_{ue} & q_{un} & q_{uu} \end{bmatrix}\end{aligned} \tag{A-VII}$$

Horizontal Dilution of Precision: $HDOP = \sqrt{q_{ee} + q_{nn}}$

Vertical Dilution of Precision: $VDOP = \sqrt{q_{uu}}$

The DOPs could help in the planning of a survey, interpretation of the processed baseline vector and projection of errors from measurement domain to the position domain (Hofmann-Wellenhof et al. 2003). A satellite geometry with PDOP less than 3 and HDOP less than 2 is generally said to be a good geometry.

# Appendix II: Jacobian matrix for three-dimensional Euler angles

Three-dimensional attitude parameters can be determined using the following model:

$$\begin{bmatrix} x_b \\ y_b \\ z_b \end{bmatrix} = \underbrace{\begin{bmatrix} c(r)c(y)-s(r)s(p)s(y) & c(r)s(y)+s(r)s(p)c(y) & -s(r)c(p) \\ -c(p)s(y) & c(p)c(y) & s(p) \\ s(r)c(y)+c(r)s(p)s(y) & s(r)s(y)-c(r)s(p)c(y) & c(r)c(p) \end{bmatrix}}_{\mathbf{R}} \begin{bmatrix} x_l \\ y_l \\ z_l \end{bmatrix} \tag{A-VIII}$$

where subscripts $b$ and $l$ indicate the ABF and LLF, respectively; direction cosine matrix **R** representing the rotation from the LLF to ABF; $c(\cdot)$ and $s(\cdot)$ are the cosine and sine operators, respectively. $r$, $p$, $y$ represent roll, pitch and yaw angles. In order to apply the least-squares adjustment to solve Eq. (A-VIII), we should expand the right-hand side and linearize it with respect to Euler angles, yielding the matrix $\mathbf{A}_i$ as follows:

$$\mathbf{A}_i = \begin{bmatrix} \frac{\partial f_1}{\partial y} & \frac{\partial f_1}{\partial p} & \frac{\partial f_1}{\partial r} \\ \frac{\partial f_2}{\partial y} & \frac{\partial f_2}{\partial p} & \frac{\partial f_2}{\partial r} \\ \frac{\partial f_3}{\partial y} & \frac{\partial f_3}{\partial p} & \frac{\partial f_3}{\partial r} \end{bmatrix} \tag{A-IX}$$

where $f_1, f_2, f_3$ can be obtained from:

$$\begin{aligned} f_1 &= \mathbf{R}_{11}x_l + \mathbf{R}_{12}y_l + \mathbf{R}_{13}z_l \\ f_2 &= \mathbf{R}_{21}x_l + \mathbf{R}_{22}y_l + \mathbf{R}_{23}z_l \\ f_3 &= \mathbf{R}_{31}x_l + \mathbf{R}_{32}y_l + \mathbf{R}_{33}z_l \end{aligned} \tag{A-X}$$

The components of matrix **A** are then calculated as follows:

$$\begin{aligned}
A_{11} &= \frac{\partial f_1}{\partial y} = \left[-c(r)x_l - s(r)s(p)y_l\right]s(y) + \left[-s(r)s(p)x_l + c(r)y_l\right]c(y) \\
A_{12} &= \frac{\partial f_1}{\partial p} = \left[s(r)z_l\right]s(p) + \left[-s(r)s(y)x_l + s(r)c(y)y_l\right]c(p) \\
A_{13} &= \frac{\partial f_1}{\partial r} = \left[-c(y)x_l - s(y)y_l\right]s(r) + \left[-s(p)s(y)x_l + s(p)c(y)y_l - c(p)z_l\right]c(r) \\
A_{21} &= \frac{\partial f_2}{\partial y} = \left[-c(p)y_l\right]s(y) - \left[c(p)x_l\right]c(y) \\
A_{22} &= \frac{\partial f_2}{\partial p} = \left[s(y)x_l - c(y)y_l\right]s(p) + \left[z_l\right]c(p) \\
A_{23} &= \frac{\partial f_2}{\partial r} = 0 \\
A_{31} &= \frac{\partial f_3}{\partial y} = \left[-s(r)x_l + c(r)s(p)y_l\right]s(y) + \left[c(r)s(p)x_l + s(r)y_l\right]c(y) \\
A_{32} &= \frac{\partial f_3}{\partial p} = \left[-c(r)z_l\right]s(p) + \left[c(r)s(y)x_l - c(r)c(y)y_l\right]c(p) \\
A_{33} &= \frac{\partial f_3}{\partial r} = \left[-s(p)s(y)x_l + s(p)c(y)y_l - c(p)z_l\right]s(r) + \left[s(y)y_l + c(y)x_l\right]c(r)
\end{aligned} \tag{A-XI}$$

# Appendix III: Jacobian matrix for a dual-antenna configuration

For a dual-antenna configuration, only yaw and pitch angles can be determined. This procedure is quite similar like the three-dimensional attitude determination given in Appendix II. The mathematic model for a dual-antenna configuration can be related to the rotation matrix **R** by:

$$\begin{bmatrix} x_b \\ y_b \\ z_b \end{bmatrix} = \underbrace{\begin{bmatrix} c(y) & s(y) & 0 \\ -s(y)c(p) & c(p)c(y) & s(p) \\ s(y)s(p) & -c(y)s(p) & c(p) \end{bmatrix}}_{\mathbf{R}} \begin{bmatrix} x_l \\ y_l \\ z_l \end{bmatrix} \tag{A-XII}$$

The notations can be referred to (A-VIII). An expected linearized form can be expressed by:

$$\begin{bmatrix} x_b \\ y_b \\ z_b \end{bmatrix} = \begin{bmatrix} \frac{\partial f_1}{\partial y} & \frac{\partial f_1}{\partial p} \\ \frac{\partial f_2}{\partial y} & \frac{\partial f_2}{\partial p} \\ \frac{\partial f_3}{\partial y} & \frac{\partial f_3}{\partial p} \end{bmatrix} \begin{bmatrix} \Delta yaw \\ \Delta pitch \end{bmatrix} = \mathbf{A} \begin{bmatrix} \Delta yaw \\ \Delta pitch \end{bmatrix} \tag{A-XIII}$$

where $f_1, f_2, f_3$ correspond to:

$$\begin{aligned} f_1 &= \mathbf{R}_{11}x_l + \mathbf{R}_{12}y_l + \mathbf{R}_{13}z_l \\ f_2 &= \mathbf{R}_{21}x_l + \mathbf{R}_{22}y_l + \mathbf{R}_{23}z_l \\ f_3 &= \mathbf{R}_{31}x_l + \mathbf{R}_{32}y_l + \mathbf{R}_{33}z_l \end{aligned} \tag{A-XIV}$$

Each component of matrix **A** reads:

$$\begin{aligned} \mathbf{A}_{11} &= \frac{\partial f_1}{\partial y} = -s(y)x_l + c(y)y_l \\ \mathbf{A}_{12} &= \frac{\partial f_1}{\partial p} = 0 \\ \mathbf{A}_{21} &= \frac{\partial f_2}{\partial y} = -c(p)c(y)x_l - c(p)s(y)y_l \\ \mathbf{A}_{22} &= \frac{\partial f_2}{\partial p} = s(p)s(y)x_l - s(p)c(y)y_l + c(p)z_l \\ \mathbf{A}_{31} &= \frac{\partial f_3}{\partial y} = s(p)c(y)x_l + s(p)s(y)y_l \\ \mathbf{A}_{32} &= \frac{\partial f_3}{\partial p} = c(p)s(y)x_l - c(p)c(y)y_l - s(p)z_l \end{aligned} \tag{A-XV}$$

# Appendix IV: Error of local level frame coordinate due to the positioning error of the origin

The transformation of a target point from the ECEF to the LLF centered at a reference point is expressed as follows:

$$\begin{bmatrix} x_l \\ y_l \\ z_l \end{bmatrix} = \begin{bmatrix} -\sin\lambda & \cos\lambda & 0 \\ -\sin\varphi\cos\lambda & -\sin\varphi\sin\lambda & \cos\varphi \\ \cos\varphi\cos\lambda & \cos\varphi\sin\lambda & \sin\varphi \end{bmatrix} \begin{bmatrix} x_{ECEF} \\ y_{ECEF} \\ z_{ECEF} \end{bmatrix} \tag{A-XVI}$$

where *x*, *y* and *z* represent the coordinates of the target point. Subscript *l* and *ECEF* indicate the LLF and ECEF, respectively; $\lambda$ and $\varphi$ represent the latitude and longitude of the reference point, respectively. The reference point is the common center of LLF and ECEF, and its positioning error in ECEF will also affect the LLF coordinate of the target point. In order to analyze this relation, (A-XVI) should be differentiated with respect to the latitude and longitude of the reference point. Expanding the right-hand side yields:

$$\begin{bmatrix} x_l \\ y_l \\ z_l \end{bmatrix} = \underbrace{\begin{bmatrix} -\sin\lambda\cdot x_{ECEF} + \cos\lambda\cdot y_{ECEF} \\ -\sin\varphi\cdot\cos\lambda\cdot x_{ECEF} - \sin\varphi\cdot\sin\lambda\cdot y_{ECEF} + \cos\varphi\cdot y_{ECEF} \\ \cos\varphi\cdot\cos\lambda\cdot x_{ECEF} + \cos\varphi\cdot\sin\lambda\cdot y_{ECEF} + \sin\varphi\cdot z_{ECEF} \end{bmatrix}}_{\mathbf{m}} \tag{A-XVII}$$

Differentiating the vector **m** with respect to $\lambda$ and $\varphi$ we have:

$$\begin{bmatrix} x_l \\ y_l \\ z_l \end{bmatrix}_{3\times1} = \begin{bmatrix} \dfrac{\partial\mathbf{m}}{\partial\varphi} & \dfrac{\partial\mathbf{m}}{\partial\lambda} \end{bmatrix}_{3\times2} \begin{bmatrix} \Delta\varphi \\ \Delta\lambda \end{bmatrix}_{2\times1}$$

$$\frac{\partial\mathbf{m}}{\partial\varphi} = \begin{bmatrix} 0 \\ -\cos\varphi\cdot\cos\lambda\cdot x_{ECEF} - \cos\varphi\cdot\sin\lambda\cdot y_{ECEF} - \sin\varphi\cdot z_{ECEF} \\ -\sin\varphi\cdot\cos\lambda\cdot x_{ECEF} - \sin\varphi\cdot\sin\lambda\cdot y_{ECEF} + \cos\varphi\cdot z_{ECEF} \end{bmatrix} \tag{A-XVIII}$$

$$\frac{\partial\mathbf{m}}{\partial\lambda} = \begin{bmatrix} -\cos\lambda\cdot x_{ECEF} - \sin\lambda\cdot y_{ECEF} \\ \sin\varphi\cdot\sin\lambda\cdot x_{ECEF} - \sin\varphi\cdot\cos\lambda\cdot y_{ECEF} \\ -\cos\varphi\cdot\sin\lambda\cdot x_{ECEF} + \cos\varphi\cdot\cos\lambda\cdot y_{ECEF} \end{bmatrix}$$

We use a latitude of 50 degrees and a longitude 8 degrees (near Siegen) to test the error range of the LLF coordinate. Providing that the single-point positioning can cause up to an error of 0.001 degrees in latitude as well as longitude, the absolute three-dimensional errors in the LLF coordinate are illustrated in Figure A-I.

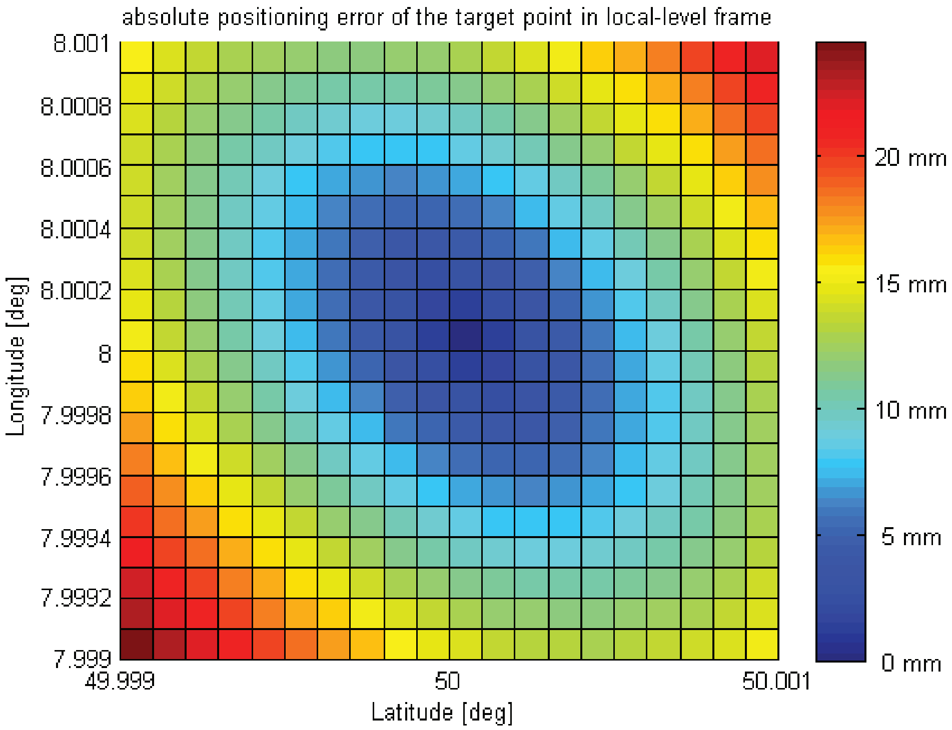

Figure A-I: Absolute positioning error of the target point in LLF

In order to give a clearer demonstration, we also present the three-dimensional positioning error of the reference point in the Cartesian coordinate system (e.g. ECEF in meters).

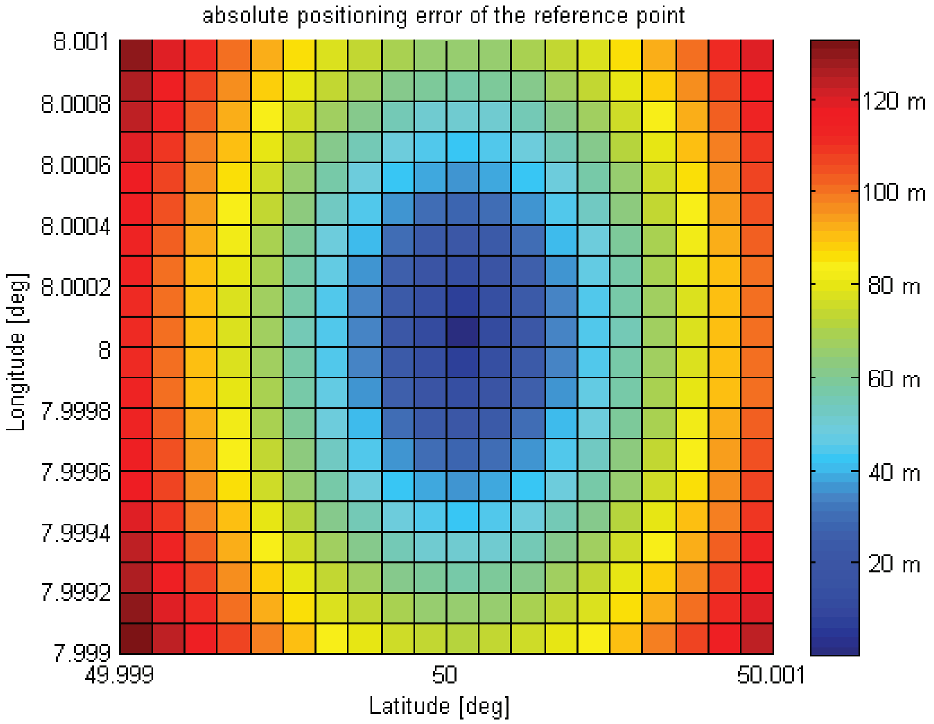

Figure A-II: Absolute positioning error of the reference point in ECEF

From both of Figure A-I and Figure A-II we can see that, if the absolute positioning error of the reference point is lower than 20 m in ECEF, the corresponding error in the LLF coordinate of the target point is smaller than 5 mm.

# Appendix V: Hessian matrix for SOEKF

In order to apply the SOEKF, the Hessian matrix **D** in (4-28) needs to be determined. The Hessian matrix can be obtained by differentiating Jacobian matrix with respect to the Euler angles. A Hessian matrix is associated to a row vector of the Jacobian matrix. Denoting $[\mathbf{A}_1\ \mathbf{A}_2\ \mathbf{A}_3]^T$ as the row vectors of the Jacobian matrix **A** given in (A-XI), the Hessian matrices $\mathbf{D}_1$, $\mathbf{D}_2$ and $\mathbf{D}_3$ are detailed as follows:

$$
\begin{aligned}
\mathbf{D}_{1,11} &= \frac{\partial \mathbf{A}_{11}}{\partial y} = \left[-c(r)c(y)+s(r)s(p)s(y)\right]x_l + \left[-c(r)s(y)-s(r)s(p)c(y)\right]y_l \\
\mathbf{D}_{1,12} &= \frac{\partial \mathbf{A}_{11}}{\partial p} = -s(r)c(p)c(y)x_l - s(r)c(p)s(y)y_l \\
\mathbf{D}_{1,13} &= \frac{\partial \mathbf{A}_{11}}{\partial r} = \left[s(r)s(y)-c(r)s(p)c(y)\right]x_l + \left[-s(r)c(y)-c(r)s(p)s(y)\right]y_l \\
\mathbf{D}_{1,21} &= \frac{\partial \mathbf{A}_{12}}{\partial y} = -s(r)c(p)c(y)x_l - s(r)c(p)s(y)y_l \\
\mathbf{D}_{1,22} &= \frac{\partial \mathbf{A}_{12}}{\partial p} = s(r)s(p)s(y)x_l - s(r)s(p)c(y)y_l + s(r)c(p)z_l \\
\mathbf{D}_{1,23} &= \frac{\partial \mathbf{A}_{12}}{\partial r} = -c(r)c(p)s(y)x_l + c(r)c(p)c(y)y_l + c(r)s(p)z_l \\
\mathbf{D}_{1,31} &= \frac{\partial \mathbf{A}_{13}}{\partial y} = \left[s(r)s(y)-c(r)s(p)c(y)\right]x_l - \left[s(r)c(y)+c(r)s(p)s(y)\right]y_l \\
\mathbf{D}_{1,32} &= \frac{\partial \mathbf{A}_{13}}{\partial p} = -c(r)c(p)s(y)x_l + c(r)c(p)c(y)y_l + c(r)s(p)z_l \\
\mathbf{D}_{1,33} &= \frac{\partial \mathbf{A}_{13}}{\partial r} = \left[-c(r)c(y)+s(r)s(p)s(y)\right]x_l - \left[c(r)s(y)+s(r)s(p)c(y)\right]y_l \\
&\qquad + s(r)c(p)z_l
\end{aligned}
\tag{A-XIX}
$$

$$
\begin{aligned}
\mathbf{D}_{2,11} &= \frac{\partial \mathbf{A}_{21}}{\partial y} = c\left(p\right)s\left(y\right)x_l - c\left(p\right)c\left(y\right)y_l \\
\mathbf{D}_{2,12} &= \frac{\partial \mathbf{A}_{21}}{\partial p} = s\left(p\right)c\left(y\right)x_l + s\left(p\right)s\left(y\right)y_l \\
\mathbf{D}_{2,13} &= \frac{\partial \mathbf{A}_{21}}{\partial r} = 0 \\
\mathbf{D}_{2,21} &= \frac{\partial \mathbf{A}_{22}}{\partial y} = s\left(p\right)c\left(y\right)x_l + s\left(p\right)s\left(y\right)y_l \\
\mathbf{D}_{2,22} &= \frac{\partial \mathbf{A}_{22}}{\partial p} = c\left(p\right)s\left(y\right)x_l - c\left(p\right)c\left(y\right)y_l - s\left(p\right)z_l \\
\mathbf{D}_{2,23} &= \frac{\partial \mathbf{A}_{22}}{\partial r} = 0 \\
\mathbf{D}_{2,31} &= \frac{\partial \mathbf{A}_{23}}{\partial y} = 0 \\
\mathbf{D}_{2,32} &= \frac{\partial \mathbf{A}_{23}}{\partial p} = 0 \\
\mathbf{D}_{2,33} &= \frac{\partial \mathbf{A}_{23}}{\partial r} = 0
\end{aligned}
\tag{A-XX}
$$

$$
\begin{aligned}
\mathbf{D}_{3,11} &= \frac{\partial \mathbf{A}_{31}}{\partial y} = \left[-s\left(r\right)c(y) - c\left(r\right)s\left(p\right)s(y)\right]x_l + \left[-s\left(r\right)s(y) + c\left(r\right)s\left(p\right)c(y)\right]y_l \\
\mathbf{D}_{3,12} &= \frac{\partial \mathbf{A}_{31}}{\partial p} = c\left(r\right)c\left(p\right)c\left(y\right)x_l + c\left(r\right)c\left(p\right)s\left(y\right)y_l \\
\mathbf{D}_{3,13} &= \frac{\partial \mathbf{A}_{31}}{\partial r} = \left[-c\left(r\right)s(y) - s\left(r\right)s\left(p\right)c(y)\right]x_l + \left[c\left(r\right)c(y) - s\left(r\right)s\left(p\right)s(y)\right]y_l \\
\mathbf{D}_{3,21} &= \frac{\partial \mathbf{A}_{32}}{\partial y} = c\left(r\right)c\left(p\right)c\left(y\right)x_l + c\left(r\right)c\left(p\right)s\left(y\right)y_l \\
\mathbf{D}_{3,22} &= \frac{\partial \mathbf{A}_{32}}{\partial p} = -c\left(r\right)s\left(p\right)s\left(y\right)x_l + c\left(r\right)s\left(p\right)c\left(y\right)y_l - c\left(r\right)c\left(p\right)z_l \\
\mathbf{D}_{3,23} &= \frac{\partial \mathbf{A}_{32}}{\partial r} = -s\left(r\right)c\left(p\right)s\left(y\right)x_l + s\left(r\right)c\left(p\right)c\left(y\right)y_l + s\left(r\right)s\left(p\right)z_l \\
\mathbf{D}_{3,31} &= \frac{\partial \mathbf{A}_{33}}{\partial y} = \left[-c\left(r\right)s(y) - s\left(r\right)s\left(p\right)c(y)\right]x_l + \left[c\left(r\right)c(y) - s\left(r\right)s\left(p\right)s(y)\right]y_l \\
\mathbf{D}_{3,32} &= \frac{\partial \mathbf{A}_{33}}{\partial p} = -s\left(r\right)c\left(p\right)s\left(y\right)x_l + s\left(r\right)c\left(p\right)c\left(y\right)y_l + s\left(r\right)s\left(p\right)z_l \\
\mathbf{D}_{3,33} &= \frac{\partial \mathbf{A}_{33}}{\partial r} = \left[-s\left(r\right)c(y) - c\left(r\right)s\left(p\right)s(y)\right]x_l + \left[-s\left(r\right)s(y) + c\left(r\right)s\left(p\right)c(y)\right]y_l \\
&\quad - c\left(r\right)c\left(p\right)z_l
\end{aligned}
\tag{A-XXI}
$$

# Bibliography

Abidin, H. Z. (1993). "On the construction of the ambiguity searching space for on-the-fly ambiguity resolution." *Navigation: Journal of The Institute of Navigation*, vol. 40, no. 3, pp. 321-338.

Bar-Shalom, Y., Li, X.-R., and Kirubarajan, T. (2001). *Estimation with applications to tracking and navigation*, New York: John Wiley and Sons.

Barrows, A. K., Gebre-Egziabher, D., Hayward, R., Renxin, X., and Powell, J. D. "GPS-based attitude and guidance displays for general aviation." *Presented at IEEE Conference on Emerging Technologies and Factory Automation (EFTA)*, Hawaii, USA, 1996, pp. 423-428.

Beutler, G., Davidson, D., Langley, R., Santerre, R., Vaníček, P., and Wells, D. E. (1984). "Some theoretical and practical aspects of geodetic positioning using carrier phase difference observations of GPS satellites". Technical Report, University of New Brunswick, Canada.

Bisnath, S., and Langley, R. B. "Automated cycle-slip correction of dual-frequency kinematic GPS data." *Presented at 47th Annual Conference of the Canadian Aeronautics and Space Institute*, Ottawa, 2000, pp. 121-125.

Blewitt, G. (1990). "An automatic editing algorithm for GPS data." *Geophysical research letters*, vol. 17, no. 3, pp. 199-202.

Blom, H. A. P., and Bar-Shalom, Y. (1988). "The interacting multiple model algorithm for systems with Markovian switching coefficients." *IEEE Transactions on Automatic Control*, vol. 33, no. 8, pp. 780-783.

Borre, K. (2003). "The Easy Suite - Matlab code for the GPS newcomer." *GPS Solutions*, vol. 7, no. 1, pp. 47-51.

Braasch, M. S. (1999). *Satellite Navigation (SatNav) Toolbox 3.0 for MATLAB*. GPSoft LLC.

Cohen, C. (1992). *Attitude Determination Using GPS*, PhD Thesis, Stanford University, Albuquerque,.

Comp, C. J. "Optimal antenna configuration for GPS-based attitude determination." *Presented at the 6th International Technical Meeting of the Satellite Division of the ION*, Salt Lake City , USA, 1993, pp. 773-779.

Dai, Z., Knedlik, S., and Loffeld, O. "Real-time cycle-slip detection and determination for multiple frequency GNSS." *Presented at 5th Workshop on Positioning, Navigation and Communication (WPNC)*, Hannover, Germany, 2008, pp. 37-43.

Dai, Z., Knedlik, S., and Loffeld, O. (2009a). "Instantaneous Triple-Frequency GPS Cycle-Slip Detection and Repair." *International Journal of Navigation and Observation*, vol. 2009.

Dai, Z., Knedlik, S., and Loffeld, O. (2009b). "A Matlab toolbox for attitude determination with GPS multi-antenna systems." *GPS solutions*, vol. 13, no. 3, pp. 241-248.

De Jong, C. D. (1998). "Real-time integrity monitoring, ambiguity resolution and kinematic positioning with GPS"*2nd European Symposium on Global Navigation Satellite Systems*. City: Toulouse, France, pp. VIII07/1-VIII07/7.

Ding, W., and Wang, J. (2011). "Precise Velocity Estimation with a Stand-Alone GPS Receiver." *Journal of Navigation*, vol. 64, no. 2, pp. 311-325.

El-Mowafy, A., and Mohamed, A. (2005). "Attitude Determination from GNSS Using Adaptive Kalman Filtering." *The Journal of Navigation*, vol. 58, no. 1, pp. 135-148.

Fan, J., Wang, F., and Guo, G. (2006). "Automated Cycle-slip Detection and Correction for GPS Triple-frequency Undifferenced Observables." *Science of surveying and mapping*, vol. 31, no. 5, pp. 24-36.

Federal-Aviation-Administration. (2007). *Pilot's Encyclopedia of Aeronautical Knowledge*, New York: Skyhorse

Publishing.

Fornaro, G. (1999). "Trajectory deviations in airborne SAR: analysis and compensation." *IEEE Transactions on Aerospace and Electronic Systems*, vol. 35, no. 3, pp. 997-1009.

Frei, E., and Beuler, G. (1990). "Rapid static positioning based on the fast ambiguity resolution approach "FARA": theory and first results." *Manuscripta Geodaetica*, vol. 15, no. 4, pp. 325-356.

Grass, F. V., and Braasch, M. (1991). "GPS interferometric attiude and heading determination: Initial flight test results." *Journal of Institude of Navigation* vol. 38, no. 4, pp. 297-316.

Gustafsson, K., McCarthy, F., and Paulraj, A. (1996 ). "Mitigation of wing flexure induced errors for airborne direction-finding applications." *IEEE Transactions on Signal Processing*, vol. 44, no. 2, pp. 296-304.

Han, S., and Rizos, C. "The impact of two additional civilian GPS frequencies on ambiguity resolutions strategies." *Presented at ION National Technical Meeting*, San Diego, Calif, USA, 1999, pp. 315-321.

Hatch, R. "The synergism of GPS code and carrier measurements." *Presented at International Geodetic Symposium on Satellite Doppler Positioning*, Las Cruces, NM, 1982, pp. 1213-1231.

Hatch, R. "Instantaneous ambiguity resolution." *Presented at KIS' 90*, Banff, Canada, 1990, pp. 299-308.

Hatch, R. (1996). "Promise of a third frequency." *GPS World,*, vol. 7, no. 5, pp. 55-58.

Hide, C., Moore, T., and Smith, M. (2003). "Adaptive Kalman Filtering for Low-cost INS/GPS." *The Journal of Navigation*, vol. 56, no. 1, pp. 143-152.

Hide, C., Moore, T., and Smith, M. "Adaptive Kalman filtering algorithms for integrating GPS and low cost INS." *Presented at Position Location and Navigation Symposium (PLANS)*, 2004, pp. 227-233.

Hirokawa, R., and Ebinuma, T. (2009). "A Low-Cost Tightly Coupled GPS/INS for Small UAVs Augmented with Multiple GPS Antennas." *Journal of Institude of Navigation*, vol. 56, no. 1, pp. 35-44.

Hofmann-Wellenhof, B., Legat, K., and Wieser, M. (2003). *Navigation principles of positioning and guidance*, Wien, NewYork: Springer Verlag.

Hofmann-Wellenhof, B., Lichtenegger, H., and Collins, J. (2001). *GPS: Theory and practice,* Wien: Springer Verlag.

Horemuž, M., and Sjöberg, L. E. (2002). "Rapid GPS ambiguity resolution for short and long baselines." *Journal of Geodesy*, vol. 76, no. 6-7, pp. 381-391.

Hu, C., Chen, W., Chen, Y., and Liu, D. (2003). "Adaptive Kalman filtering for vehicle navigation." *Journal of Global Positioning Systems*, vol. 2, no. 1, pp. 42-47.

Jia, P., and Wu, L. (2001). "An algorithm for detecting and estimating cycle slips in single-frequency GPS." *Chinese Astronomy and Astrophysics*, vol. 25, no. 4, pp. 515-521.

Julien, O., Cannon, M. E., Alves, P., and Lachapelle, G. (2004). "Triple Frequency Ambiguity Resolution Using GPS/Galileo." *European Journal of Navigation*, vol. 2, no. 2, pp. 51-57.

Julier, S., Uhlmann, J., and Durrant-Whyte, H. F. (2000). "A new method for the nonlinear transformation of means and covariances in filters and estimators." *IEEE Transactions on Automatic Control*, vol. 45, no. 3, pp. 477-482.

Julier, S. J., and Uhlmann, J. K. "A new extension of the Kalman filter to nonlinear systems." *Presented at Society of Photo-Optical Instrumentation Engineers (SPIE) Conference Series*, 1997, pp. 182-193.

Kaplan, E. D., and Hegarty, C. (2006). *Understanding GPS : principles and applications*, Boston: Artech House.

Kim, D., and Langley, R. B. "GPS Ambiguity Resolution and Validation: Methodologies, Trends and Issues." *Presented at 7th GNSS Workshop and International Symposium on GPS/GNSS*, Seoul, Korea, 2000, pp. 213-221.

Kim, D., and Langley, R. B. "Instantaneous real-time cycle-slip correction of dual frequency GPS data." *Presented at International Symposium on Kinematic Systems in Geodesy, Geomatics and Navigation*, Banff, Alberta, 2001, pp. 255-264.

Knedlik, S., Zhou, J., and Loffeld, O. (2009). "On Position and Attitude Estimation for Remote Sensing with Bistatic SAR", *Geoscience and Remote Sensing*. Rijeka, Croatia: InTech.

Kuipers, J. B. (2002). *Quaternions and rotation sequences*, Princeton: Princeton University Press.

Leick, A. (2004). *GPS satellite surveying*, New York: John Wiley & Sons Inc.

Lipp, A., and Gu, X. "Cycle-slip detection and repair in integrated navigation systems." *Presented at IEEE/ION Position Location and Navigation Symposium, 1994*, pp. 681-688.

Lu, G. (1995). *Development of a GPS Multi-Antenna System for Attitude Determination* PhD Thesis, University of Calgary, Calgary.

Lu, G., Cannon, M. E., Lachapelle, G., and Kielland, P. (1994). "Attitude determination using dedicated and nondedicated multiantenna GPS sensors." *IEEE Transactions on Aerospace and Electronic Systems*, vol. 30, no. 4, pp. 1053-1058.

Markley, F. L. (1988). "Attitude Determination Using Vector Observations and the Singular Value Decomposition." *Journal of the Astronautical Sciences*, vol. 36, no. 3, pp. 245-258.

Markley, F. L. (1993). "Attitude determination from vector observations: a fast optimal matrix algorithm." *Journal of the Astronautical Sciences*, vol. 41, no. 2, pp. 261-280.

McDonald, K. D. (2002). "The Modernization of GPS: Plans, New Capabilities and the Future Relationship to Galileo." *Journal of Global Positioning Systems,* vol. 1, no. 1, pp. 1-17.

Mehra, R. (1972). "Approaches to adaptive filtering." *IEEE Transactions on Automatic Control*, vol. 17, no. 5, pp. 693-698.

Mohamed, A. H. (1999). *Optimizing the estimation procedure in INS/GPS integration for kinematic applications*, Ph.D. Thesis, University of Calgary, Calgary.

Mohamed, A. H., and Schwarz, K. P. (1999). "Adaptive Kalman Filtering for INS/GPS." *Journal of Geodesy*, vol. 73, no. 4, pp. 193-203.

Nielsen, R. O. (1997). "Relationship between dilution of precision for point positioning and for relative positioning with GPS." *IEEE Transactions on Aerospace and Electronic Systems*, vol. 33, no. 1, pp. 333-338.

Park, C., Ilsun, K., Jang Gyu, L., and Gyu-In, J. "Efficient ambiguity resolution using constraint equation." *Presented at IEEE/ION Conference on Position Location and Navigation Symposium (PLANS)*, Atlanta, USA, 1996, pp. 277-284.

Park, C., and Kim, I. "Integer ambiguity resolution for GPS based attitude determination system." *Presented at The 37th SICE Annual Conference International Session* Chiba 1998, pp. 1115 - 1120

Ray, J. K. (2000). *Mitigation of GPS Code and Carrier Phase Multipath Effects Using a Multi-Antenna System*, PhD thesis, University of Calgary, Calgary.

Serrano, L., Kim, D., and Langley , R. B. "A GPS Velocity Sensor: How Accurate Can It Be? – A First Look." *Presented at ION National Technical Meeting*, San Diego, USA, 2004, pp. 875-885.

Simon, D. (2006). *Optimal State Estimation*, New Jersey: John Wiley & Sons.

Simsky, A. (2006). "Three's the Charm. Triple-Frequency Combinations in Future GNSS." *Inside GNSS*, vol. 1, no. 5, pp. 38-41.

Sutton, E. "Optimal Search Space Identification for Instantaneous Integer Cycle Ambiguity Resolution." *Presented at International Technical Meeting of the Satellite Division of ION*, Kansas City, 1997, pp. 313-322.

Teunissen, P. J. G. (1995). "The least-squares ambiguity decorrelation adjustment: a method for fast GPS integer ambiguity estimation." *Journal of Geodesy*, vol. 70, no. 1, pp. 65-82.

Teunissen, P. J. G. (1999). "An optimality property of the integer least-squares estimator." *Journal of geodesy*, vol. 73, no. 11, pp. 587-593.

Teunissen, P. J. G., and Kleusberg, A. (1998). *GPS for Geodesy*, Berlin, Heidelberg: Springer Verlag, pp. 361-363, 368-373.

US-Army. (1996). *FM 44-80 Visual Aircraft Recognition*. Department of the US Army, Washington, DC,.

Van der Merwe, R., and Wan, E. A. "The square-root unscented Kalman filter for state and parameter-estimation." *Presented at IEEE International Conference on Acoustics, Speech, and Signal Processing* 2001, pp. 3461-3464.

Verhagen, S. (2004). "Integer ambiguity validation: an open problem?" *GPS Solutions*, vol. 8, no. 1, pp. 36-43.

Wahba, G. (1965). "A Least Squares Estimate of Satellite Attitude." *SIAM Review*, vol. 7, no. 3, pp. 409-409.

Wang, C. (2003). *Development of a Low-Cost GPS-Based Attitude Determination System*, Master Thesis, University of Calgary, Calgary.

Wang, J., Stewart, M., and Tsakiri, M. "Kinematic GPS positioning with adaptive filtering techniques." *Presented at IAG Scientific Assembly*, Rio de Janeiro, Brazil, 1997, pp. 389-394.

Wang, J., Stewart, M., and Tsakiri, M. "Online stochastic modelling for INS/GPS integration." *Presented at 12th International Technical Meeting of the Satellite Division of ION*, Nashville, USA, 1999, pp. 1887-1895.

Wang, R., Loffeld, O., Nies, H., Knedlik, S., and Ender, J. (2009). "Chirp-Scaling Algorithm for Bistatic SAR Data in the Constant-Offset Configuration." *IEEE Transactions on Geoscience and Remote Sensing*, vol. 47, no. 3, pp. 952-964.

Wang, Z., Wu, Y., Zhang, K., and Meng, Y. (2005). "Triple-Frequency Method for High-Order Ionospheric Refractive Error Modelling in GPS Modernization." *Journal of Global Positioning Systems*, vol. 4, no. 1, pp. 291-295.

Wells, D., Beck, N., Delikaraoglou, D., and Kleusberg, A. (1986). *Guide to GPS positioning*, Fredericton, New Brunswick: Canadian GPS Associates.

Wertz, J. R. (1978). *Spacecraft Attitude Determination and Control*: Kluwer Academic Publishers.

Yang, Z. (1998). *Joint Time Frequency Analysis of Global Positioning System (GPS) Multipath Signals*, Master Thesis, Ohio University.

Zhang, M. (2010). *Data Fusion for Ground Target Tracking in GSM Networks,* PhD Thesis, University of Siegen.